9. Glow Discharge Instabilities and Their Consequences

9.1 Causes and Consequences of Instabilities

The homogeneous state of the glow discharge positive column is quite often unstable, especially if the discharge is maintained in large volume, or at high pressure, when current is high and Joule heat is intensively released. Random perturbations grow catastrophically and the plasma switches to a different, spatially inhomogeneous state. The inhomogeneous modes caused by *instabilities* have been known for a long time: *striations*, that is, when the positive column is formed of bright and dark layers alternating along the current direction, and *contraction* of the plasma into a bright *current filament*. In fact, these effects have recently attracted special attention owing to the difficulties that they cause for the development of high-power gas lasers: instabilities destructively affect the laser generation. The suppression of the tendency to the *filamentation* of discharge constitutes the central, and the most difficult, problem in the development of high-power electrical discharge lasers (Chap. 14). High stability can be efficiently achieved only if the nature of discharge processes and the mechanisms of instabilities are well understood. Recent efforts in this field have essentially expanded our knowledge concerning such a classical object as glow discharge.[1]

9.1.1 Phenomenological Attribute of Stability (or Instability)

Quite often, plasma instability is apparent under visual observation. Differences in luminosity are caused, first of all, by unequal electron density. Consequently, the factors that cause inhomogeneity are related to the processes that control the density of electrons, their production, removal, and spatial transfer. The symbolic equation of kinetics of electrons is

$$\frac{dn_e}{dt} = Z_+ - Z_- \,. \tag{9.1}$$

In the steady state, the production and removal rates are equal: $Z_+ = Z_-$. The rates depend on n_e and other parameters: electron temperature, field, density of negative ions and excited atoms, and so on; the dependence may be given by

[1] Inevitably, we can dwell only briefly on the most general, key aspects of this extensive topic. Further discussion may be found in the reviews [9.1–5], where a detailed bibliography can be found.

differential equations, such as (8.28). Therefore, only a qualitative picture of the functional relationship between Z_+, Z_- and n_e can be outlined in the general case. The point of intersection of symbolic functions $Z_+(n_e)$ and $Z_-(n_e)$ (see Fig. 9.1) corresponds to a steady-state electron density $n_e^{(0)}$ which is ultimately deermined by external conditions: e.m.f. of power supply unit, geometry, and the resulting magnitude of the discharge current.

The stability of the steady state can be deduced on the basis of the mutual arrangement of curves in its neighbourhood. The state is stable if the removal curve Z_- passes above the production curve when $n_e > n_e^{(0)}$ and below it when $n_e < n_e^{(0)}$ (see Fig. 9.1a) because the system returns to equilibrium in response to an accidental deviation. Otherwise the state is unstable (shown in Fig. 9.1b): if n_e fluctuates upward, production becomes greater than removal and the number of electrons grows still further. The important factor is the mutual arrangement of the Z_+ and Z_- curves, not their absolute positions.

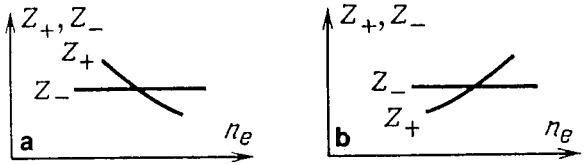

Fig. 9.1. Qualitative of electron production and removal rates in the neighborhood of (a) stable and (b) unstable states

9.1.2 Stabilizing and Destabilizing Factors

The above arguments allow the construction of a qualitative classification of the effects of various factors on stability. Let free electrons be created in the ionization of atoms from the ground state by electron impact, the electron temperature being insensitive to n_e; in this case, $Z_+ = \nu_i(T_e)n_e \sim n_e$. The bulk recombination $Z_- = \beta n_e^2$ helps stabilize the discharge, since it imparts to the removal rate a stronger, quadratic dependence on n_e. The discharge is stabilized by the external resistance: if n_e and the current increase, the voltage, electron temperature, and hence, ionization frequency ν_i all decrease. Owing to this chain of relations, the function $Z_+(n_e)$ increases with n_e less steeply than in proportion to n_e. For this reason, a homogeneous discharge controlled by ambipolar diffusion (so that $Z_- = \nu_d n_e \sim n_e$) is stable unless destabilized by factors to be discussed below. The same is true of discharges controlled by recombination in the bulk. Diffusion and heat conduction help level off the inhomogeneities in particle densities and temperature and are thus among the stabilizing factors.

Gas heating is a destabilizing factor. As the pressure levels off quickly in a gas, a local increase in gas temperature is accompanied with a drop in density (thermal expansion). This effect does not directly influence field strength, but the ratio E/N and electron temperature that depends on E/N both increase. The result is enhanced ionization and locally increased conductivity, current density, and Joule heat release. The gas is therefore heated even more. This is the so-

called *thermal instability*; it is the most dangerous and wide-spread instability in gas lasers.

Stepwise ionization and accumulation of metastable atoms and molecules also destabilize the discharge. As n_e increases, more excited particles are created and ionization from the ground state is supplemented with ionization of excited particles which is an easier process (owing to a smaller electron binding energy). Therefore, the ionization rate Z_+ grows with n_e steeper than $\nu_i(T_e)n_e$. Later we will introduce some other mechanisms of discharge destabilization. In fact, a state is stable or unstable depending on which of the stabilizing and destabilizing factors comes out the winner.

9.1.3 Longitudinal and Transverse Instabilities and Effects They Produce

The growth of instability (i.e., a catastrophic increase of an initially small perturbation) is a nonsteady process. It must lead to something. Two possibilities can be suggested – and are indeed realized. (1) The system comes to a new, more stable state. (2) Steady state is never achieved; however, a nonsteady process cannot evolve eternally in one direction, so that a periodically changing state is established.[2]

Chains of causual links between various processes involved in the evolution of perturbations and their final results depend on the orientation of inhomogeneities with respect to a chosen direction in the discharge space, namely, the electric field and current vector. If the discharge parameters, say, electron density, vary along the field (Fig. 9.2), case (2) is realized: striations are formed, with regions of increased and reduced n_e and other discharge parameters alternating in space and time. Sometimes *domains* are formed, that is, individual regions with modified parameters (e.g., strong field domains) that are periodically generated and propagate along the current direction. The growth of perturbations perpendicular to the field (Fig. 9.2) results in discharge contraction and in formation of filaments with sharply increased current density. The discharge current mostly flows in these filaments, and increases. In tubes, symmetry results in a single axial filament; in plane channels, there may be several filaments (which often "dance").

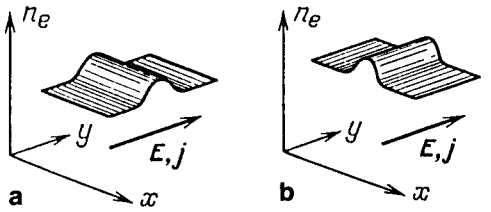

Fig. 9.2. Longitudinal (a) and transverse (b) perturbations of electron density

[2] In principle, irregular (stochastic) periodicity is also possible.

9.1.4 Principles of Stability Analysis

As a rule, it is extremely difficult to monitor the behavior of a discharge from a small perturbation to the final result of its evolution. Even the formulation of an adequate physical system of equations is often a tough proposition, to say nothing of the mathematical difficulties of solution. Typically, one is satisfied with a much less ambitious task: to find a region of the values of parameters of the steady state that correspond to stable and unstable states, and to calculate the initial rate of growth of small perturbations in the *linear approximation.* Sometimes it is possible to analyze independently the final, steady or periodic, inhomogeneous state. In fact, the solution of the former problem supplies considerable information, because, in general, the initial rate of evolution gives an idea of the time scale of transition to the final state via a nonlinear stage.

Let a homogeneous steady state of a discharge system correspond with the parameters $n_e^{(0)}$, $T_e^{(0)}$, etc. For stability analysis, the equations describing the behaviour of n_e, T_e, ... are linearized by substituting expressions of type $n_e = n_e^{(0)} + \delta n_e$, ... for parameters and assuming the perturbations δn_e to be small. The solution of the linear system is sought in the form of a plane wave, $\delta n_e = (\delta n_e)_a \exp[i(\omega t - \boldsymbol{K} \cdot \boldsymbol{r})]$, ..., where the wave vector $\boldsymbol{K}$ is assumed to be oriented along or normally to the field (oblique waves can be decomposed as vectors). Physically, this allows the following interpretation. Let us be interested in the response of the discharge to a perturbation of spatial size Λ and a given orientation (Fig. 9.2). By virtue of the linearity of the equations, a perturbation can always be written as a Fourier integral in plane waves, and each component can be analyzed independently. Clearly, the wave vectors $\boldsymbol{K}$ are then directed along the coordinates along which change n_e, T_e, ... ; the wavelengths best represented in the integral are of order Λ, or $K \sim \Lambda^{-1}$.

The substitution of wave solutions into linearized equations yields a system of m homogeneous algebraic equations for m amplitudes $(\delta n_e)_a$, $(\delta T_e)_a$, ... Setting the determinant of the system to zero yields the dispersion equation that relates ω to $\boldsymbol{K}$. If at least one of its m complex roots is such that $\Omega = \mathrm{Re}\, i\omega > 0$, perturbations grow exponentially, as $\exp(\Omega t)$. If there are several such roots, the instability growth rate is the greatest among Ω. The characteristic time of instability development is $\tau = \Omega_{max}^{-1}$. Usually, long-wave perturbations grow at the fastest rate: they are less prone to levelling off by diffusion and heat conduction. The upper bound on wavelengths is imposed by the smallest dimensions of the discharge volume (tube diameter, channel height).

9.2 Quasisteady Parameters

9.2.1 Fast and Slow Processes

The state of the plasma, especially in an electronegative molecular gas, is described by a considerable number of parameters: n_e, n_-, n_+, T_e, T, vibrational temperature T_V (which may differ from the translational gas temperature T as

a result of delayed vibrational relaxation), N, E, and the density N^* of excited molecules. The parameters obey nonstationary equations which are in general interrelated [one example is a reduced system (8.28)]. An analysis of the required determinant of order m for $m \sim 10$ would be unthinkable. The problem is alleviated by the fact that some plasma processes are fast and some are slow. When considering instability due to a specific process, developing over a time τ, we can approximately treat faster processes as relaxing instantaneously, that is, as quasisteady, and treat slower processes as frozen, that is, as processes not developing when the specified perturbations grow.

9.2.2 Time Scales of Various Processes

These are illustrted in Table 9.1. The spreading of space charge $\varrho = e(n_+ - n_e - n_-)$ in a medium of constant conductivity σ is defined by the continuity, electrostatics, and Ohm's equations:

$$\frac{\partial \varrho}{\partial t} + \operatorname{div} \boldsymbol{j} = \frac{\partial \varrho}{\partial t} + \sigma \operatorname{div} \boldsymbol{E} = \frac{\partial \varrho}{\partial t} + 4\pi\sigma\varrho = 0 \,, \qquad (9.2)$$
$$\varrho(t) = \varrho(0) \exp(-t/\tau_\sigma) \,, \quad \tau_\sigma = 1/4\pi\sigma \,.$$

The time τ_σ of space-charge decay is called the *plasma relaxation* or *Maxwell time*. The pumping time of molecular vibrations is similar to the gas heating time, provided the vibrational heat capacity c_V and the density of molecules N_M are introduced. The vibrational relaxation is characterized by the time of energy transfer between vibrational and translational degrees of freedom, τ_{VT}. Pressure levels off in space at the velocity of sound c_s. The electron thermal conductivity in weakly ionized gas is approximately equal to $\lambda_e \approx (5/2)kn_eD_e$; the corresponding thermometric conductivity is $\chi_e \approx D_e$.

9.2.3 Quasisteady Behavior of Current

The main instabilities of discharge plasma are connected with the kinetics of production and removal of electrons, changes in gas temperature, and excitation of electronic and vibrational levels of atoms and molecules. Table 9.1 shows that these processes are much slower than the space-charge decay. The latter process can therefore be regarded as fast. Assume that n_e and σ are somehow redistributed in space in the course of the evolution of the instability with a characteristic time $\tau \gg \tau_\sigma$. Generalizing (9.2) to the case of variable σ, we have

$$\partial\varrho/\partial t + 4\pi\sigma\varrho + \boldsymbol{E} \cdot \nabla\sigma = 0 \,. \qquad (9.3)$$

The space charge ϱ that is absent in the homogeneous stationary state is itself a perturbation. As all other perturbations, it changes at the rate of violation of homogeneity in the plasma. Hence, the first term in (9.3) is of order ϱ/τ, much less than the second term, ϱ/τ_σ. The last two terms, both of large magnitude, add up to $\operatorname{div} \boldsymbol{j}$; they compensate each other up to a relatively small quantity ϱ/τ.

Table 9.1. Time scales of various discharge processes under conditions typical of discharge in cw CO_2 lasers ($CO_2 + N_2 + He$); $p \sim 10$–100 Torr, $N \sim 10^{18}\,10^{-3}$, $T \sim 300$–500 K, $E/p \sim 10$ V/(cm·Torr), $T_e \approx 1$ eV, $T_V \approx 2000$–5000 K, $n_e \sim 10^{10}$ cm^{-3}, $\Lambda \sim 1$ cm [a)]

Process	Characteristic time	Duration, s
1. Space-charge relaxation	$\tau_\sigma = 1/4\pi\sigma$	10^{-10}–10^{-9}
2. Collisional energy transfer		
(1) electron tempeature relaxation	$\tau_u = 1/\nu_m\delta_1$	10^{-9}–10^{-8}
(2) gas heating	$\tau_T = Nc_{p1}T/\sigma E^2$	10^{-3}–10^{-2}
(3) pumping of molecular vibrations	$\tau_V = N_M c_V T_V/\sigma E^2$	10^{-3}–10^{-2}
(4) vibrational relaxation	τ_{VT}	10^{-4}–10^{-2}
3. Collision kinetics		
(1) ionization	$\tau_i = (k_i N)^{-1}$	10^{-5}–10^{-4}
(2) attachment	$\tau_a = (k_a N)^{-1}$	10^{-6}–10^{-5}
(3) detachment	$\tau_d = (k_d N)^{-1}$	10^{-6}–10^{-5}
(4) electron excitation	$\tau^* = (k^* N)^{-1}$	10^{-6}–10^{-4}
(5) electron-ion recombination	$\tau_{rec}^e = (\beta_e n_+)^{-1}$	10^{-4}–10^{-3}
(6) ion-ion recombination	$\tau_{rec}^- = (\beta_- n_+)^{-1}$	10^{-4}–10^{-3}
4. Transport processes		
(1) pressure levelling (sound)	$\tau_s = \Lambda/c_s$	10^{-5}–10^{-4}
(2) heat conduction of the gas	$\tau_\chi = \Lambda^2/\chi$	10^{-2}
(3) ambipolar diffusion	$\tau_{da} = \Lambda^2/D_a$	10^{-2}
(4) electron heat conduction	$\tau_\chi^e = \Lambda^2/\chi_e$	10^{-5}

[a)] Taken from [9.1]. More realistic values are given in some places

Hence, the derivative $\partial\varrho/\partial t$ in (9.3) can be neglected, and we can set $\operatorname{div} \boldsymbol{j} = 0$ at each moment of time, just as in truly steady-statse conditions.

In one-dimensional cases, current density is always spatially homogeneous and depends only on time. The electric circuit is not closed in the direction perpendicular to $\boldsymbol{E}$; hence, the transverse current cannot flow even if the conductivity in this direction undergoes a change (as in the case of filamentation). The transverse current is zero because the drift and diffusion components cancel out (Sect. 2.6). The latter component is not included in (9.2, 3).

In the case of longitudinal inhomogeneities (striations), $\boldsymbol{j}$ remains constant along the field. If we impose on longitudinal perturbations the plane wave form, then $\boldsymbol{K}\delta\boldsymbol{j} = 0$. If $\boldsymbol{K} \parallel \boldsymbol{E}$, $K \neq 0$, then $\delta\boldsymbol{j} \equiv 0$, that is, the current is constant both in space and in time.

9.2.4 Quasisteady Behavior of Electron Temperature

The attainment of mean electron energy due to collisions is one of the fastest processes, especially in molecular gases. Table 9.1 shows that only the space-charge relaxation is a faster process. As a result, the electron temperature remains quasi-steady during the development of most instabilities. It tracks the slower

variations of other quantities. In the simplified energy balance equation for the electron, (2.12) [taking into account (2.17)], we have $d\varepsilon/dt \sim T_e/\tau$. If $\tau \gg \tau_u$, then large terms (of order T_e/τ_u) in the right-hand side cancel out with high accuracy. Therefore, T_e is related to E/N by an expression implied by (2.12), provided the electron energy is quasisteady. Formula (2.15) is again derived, although here we do not assume ν_m and δ to be independent of T_e:

$$E/N = \left(3mkT_e\tilde{\nu}_m\tilde{\nu}_u/2e^2\right)^{1/2} , \quad \tilde{\nu}_{m,u}(T_e) = \nu_{m,u}/N . \tag{9.4}$$

To avoid confusion, in this chapter we denote the fraction of energy lost by an electron by δ_1.

9.2.5 Violation of the Condition of Quasisteady T_e

This occurrence is possible if the field varies appreciably over one electron temperature relaxation length Λ_u, (2.18). In order to find when this may happen, we compare the orders of magnitude of various terms in the general equation for the electron energy (2.52), where the spatial inhomogeneity was taken into account, in contrast to (2.12). Let us compare the convective term in dT_e/dt that contains $v_d\nabla T$ (the electron pressure term has the same order of magnitude), the heat conduction transfer rate in an electron gas, and the rate of energy transfer to molecules. As $kT_e \approx eE\Lambda_u$, the ratios of these terms are $1 : \Lambda_u/\Lambda : \Lambda/\Lambda_u$. Very small-scale inhomogeneities, with $\Lambda \ll \Lambda_u$, level off via heat conduction quite rapidly. If $\Lambda \gg \Lambda_u$, local energy transfer to molecules is dominant, and T_e is quasistationary. This occurs in molecular laser discharges (at $p = 30$ Torr, the electron path length is $l \sim 10^{-3}$ cm, $\delta_1 \sim 10^{-2}$, $\Lambda_u \sim 10^{-2}$ cm, and $\Lambda \sim 1$ cm). If, however, $\Lambda \sim \Lambda_u$ and all three terms are of the same order of magnitude, no local quasisteady relation exists between T_e and E. The electron temperature varies along the direction of E with a delay, owing to the relatively slow relaxation. This situation is typical for striations in inert gases when $l \sim 10^{-2}$ cm, $\delta_1 \sim 10^{-4}$–10^{-5}, $\Lambda_u \sim 1$ cm, and Λ is on the order of the tube diameter (~ 1 cm).

9.3 Field and Electron Temperature Perturbations in the Case of Quasisteady-State T_e

9.3.1 Existence of the Potential of the Field

A nonsteady process may generate variable magnetic fields connected with changes in the electric field and possible changes in conduction current. It is not difficult to estimate, using Maxwell's equations (3.13, 14) and the data of Table 9.1, that the induced *vortex* electric field constitutes a negligible fraction of perturbations δE. The perturbed electric field has a *potential* and satisfies to a very good approximation the stationary equation $\operatorname{curl} \boldsymbol{E} = 0$. As follows from this equation, only the component $\boldsymbol{E}$ along the direction of change of all parameters can vary in space in one-dimensional cases. This is not surprising.

Field perturbations are caused by space charges and the polarization field is oriented along the direction of displacement of charges. For plane waves, we have $[\boldsymbol{K} \times \delta\boldsymbol{E}] = 0$, whence $\delta\boldsymbol{E} \parallel \boldsymbol{K}$ for $K \neq 0$.

9.3.2 Transverse Inhomogeneities

If $\boldsymbol{K} \perp \boldsymbol{E}$, then $\delta\boldsymbol{E} \perp \boldsymbol{E}$. A perturbation of the field magnitude,

$$\delta|E| = \sqrt{\boldsymbol{E}^2 + (\delta\boldsymbol{E})^2} - E \approx (\delta\boldsymbol{E})^2/2E ,$$

is of second order of smallness, and can be safely ignored. All parameters are invariable along the drift direction and nothing impedes the establishment of T_e. The electron temperature is quasistationary. The field magnitude being practically constant, T_e may change only as a result of changes in gas density N. This also takes place when the gas is heated. Both electron temperature and ionization rate increase in response to thermal expansion.

According to (8.4), a perturbation in T_e is related to the perturbation in density by the formula

$$\delta T_e/T_e = -\xi\delta N/N , \quad \xi = 2/(1 + \hat{\nu}_m + \hat{\nu}_u) , \quad \hat{\nu} \equiv d \ln \nu/d \ln T_e . \tag{9.5}$$

The numerical coefficient ξ is always positive; its value is of order unity. If $l(T_e) = \text{const}$ and $\delta_1(T_e) = \text{const}$, then $\nu_{m,u} \propto \sqrt{T_e}$, $\xi = 1$.

9.3.3 Relation Between Longitudinal Perturbations of T_e, E, and n_e

In the case of longitudinal inhomogeneities, the field is perturbed so that $\delta\boldsymbol{E} \parallel \boldsymbol{E}$, but the current remains unaffected. Therefore, $\delta E/E = -\delta\sigma/\sigma$.[3] As a rule, longitudinal instabilities develop via nonthermal mechanisms which act much faster than any processes changing temperature or density in the gas. Hence, N is a frozen parameter in this case. As follows from (9.4),

$$\delta T_e/T_e = \xi\delta E/E \tag{9.6}$$

and the temperature T_e is higher where the field is stronger. By varying $\sigma = e^2 n_e/m\nu_m$ at $N = \text{const}$,

$$\delta\sigma/\sigma = \delta n_e/n_e - \hat{\nu}_m \delta T_e/T_e = -\delta E/E ,$$

and eliminating $\delta E/E$ via (9.6), we obtain a relation between electron temperature and density [9.1]:

$$\delta T_e/T_e = -(2/\hat{\nu}'_u)\delta n_e/n_e , \quad \hat{\nu}'_u \equiv 1 + \hat{\nu}_u - \hat{\nu}_m . \tag{9.7}$$

The factor $(2/\hat{\nu}'_u) = 2/(1 + \hat{\delta}_1)$ is definitely positive and is of order unity. Therefore, the field and electron temperature are reduced at points of increased

[3] We neglect the electron diffusion current j_{dif}, because if $\Lambda \gg \Lambda_u$ and T_e is quasisteady, j_{dif} is small in comparison with the drift current. Indeed, (2.41, 24, 19) imply that $j_{dif}/\sigma E \sim \Lambda_u/\Lambda \ll 1$.

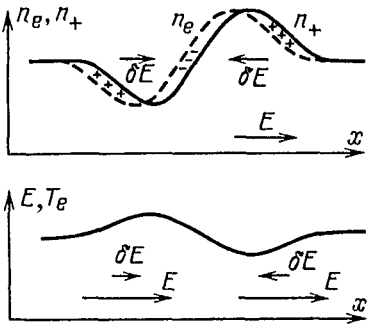

Fig. 9.3. Reduction of E and T_e where n_e increases

electron density, and vice versa. The physical mechanism producing this effect is illustrated in Fig. 9.3. It is assumed that the size of inhomogeneity, Λ, is much greater than the Debye radius d (at $T_e \approx 1$ eV and $n_e \approx 10^{10}\,\mathrm{cm}^{-3}$, $d \approx 10^{-2}$ cm) so that the densities n_e and n_+ are perturbed "in synchrony". The shift of n_e (dashed curve) with respect to n_+ (solid curve) is caused by drifting of electrons. The polarization field δE adds to the external field E in the region of the dip in n_e. The field δE is subtracted from E in the region of the crest.

9.4 Thermal Instability

This instability constitutes a universal mechanism which perturbes homogeneous discharges at elevated pressures and sufficiently high currents in atomic and molecular gases, both in tubes and in plane channels. It results in discharge contraction, and in the formation of current filaments in which the degree of ionization and the gas temperature are much higher than in ordinary glow discharges. The instability develops from transverse inhomogeneities. The field E remains homogeneous along the current direction; its magnitude changes only because the voltage at the electrodes decreases (as a result of current increase and increased voltage drop across the external resistor).

Thermal instability was first studied before the high-power laser problem arose; it was analyzed in discharges controlled by diffusion of charges to the tube walls [9.6].

The instability mechanism clarified in Sect. 9.1.2 is reflected in the following closed chain of causal links that can be started at any one step:

$$\delta n_e \uparrow\rightarrow \delta(jE) \uparrow\rightarrow \delta T \uparrow\rightarrow \delta N \downarrow\rightarrow \delta(E/N) \uparrow\rightarrow \delta T_e \uparrow\rightarrow \delta n_e \uparrow \ . \qquad (9.8)$$

Upward (downward) directed arrows symbolize an increase (decrease) in a quantity. The rate of growth of perturbations is limited by the slowest step, namely, the heating of the gas. The electron density, electron temperature, and also the relation of gas temperature to density at constant pressure, $p = NkT = \mathrm{const}$, can be considered quasisteady, corresponding to the instantaneous value of E/N.

9.4.1 Threshold and Growth Rate

We will determine the critical (threshold) conditions for the appearance of instability and evaluate its growth rate. The crucial parameter is the gas temperature T, which obeys the energy balance equation. The balance equation (8.23) is written for space-averaged quantities but this is not an obstacle. Small-scale spatial inhomogeneitiess are not very "dangerous" because heat conduction dissipates them rapidly. Perturbations of wavelength Λ of the order of the volume size are especially dangerous. Heat loss from the entire volume is nevertheless taken into account in (8.23) (this is a stabilizing factor).

An equation for perturbations δT is most easily constructed by varying (8.23) against the background of steady state (8.24). The mass conservation law (constancy of the rate of flow) implies that $N\nu_F \propto Nu = \text{const}$ in the case of convective transport. Also $\nu_T \propto \chi \propto 1/N$ in the case of heat conduction. The product $N\nu_{T,\mathrm{F}}$ is not perturbed in either case. In the term $jE = \sigma E^2$, we will vary only the factor that varies most steeply, n_e. The collision frequency is assumed to be approximately constant, because, according to (9.5), the variations of factors in the varied product $\nu_m = N\tilde{\nu}_m(T_e)$ have opposite signs and partially cancel each other out. Assuming after varying that $\delta T \sim \exp(\Omega t)$, we find

$$\Omega = \nu_T^0 \frac{\delta \ln n_e}{\delta \ln T} - \nu_{T,\mathrm{F}}\,, \quad \nu_T^0 = \frac{\sigma E^2}{N c_{p1} T} = \frac{\gamma - 1}{\gamma}\frac{\sigma E^2}{p}\,, \tag{9.9}$$

where $\nu_T^0 = \tau_T^{-1}$ is the inverse of the characteristic time of doubling the gas temperature at a nonperturbed value of T, and γ is the adiabatic exponent. In order to relate n_e to T, we describe the removal of electrons in terms of an effective recombination coefficient (8.32). The electron density n_e is quasisteady, because the production and removal of electrons are processes that are fast in comparison with gas heating:

$$n_e = \nu_i \left[T_e(E/N)\right] / \beta'_{\mathrm{eff}}\,, \quad N = p/kT\,. \tag{9.10}$$

Let us vary these equalities assuming $\beta'_{\mathrm{eff}}(T_e) = \text{const}$; this is quite legitimate. In view of (9.5), we have

$$\frac{\delta \ln n_e}{\delta \ln T} = -\hat{\nu}_i \frac{\delta \ln T_e}{\delta \ln N} = \xi \hat{\nu}_i\,, \quad \hat{\nu}_i = \frac{d \ln \nu_i}{d \ln T_e}\,. \tag{9.11}$$

The electron density is much more sensitive to heating than T_e because $\hat{\nu}_i$, in contrast to ξ, is a large number. Its physical meaning is quite clear in the case of the Maxwell distribution of electrons, when

$$\nu_i \propto \exp(-I/kT_e)\,, \quad \hat{\nu}_i = I/kT_e \approx 5 - 10\,. \tag{9.12}$$

Substituting (9.11) into (9.9) and assuming for the sake of brevity $\xi = 1$, we obtain a very simple and clear formula:

$$\Omega = \nu_T^0 \hat{\nu}_i - \nu_{T,\mathrm{F}}\,, \quad \hat{\nu}_i = d \ln \nu_i / d \ln (E/N)\,. \tag{9.13}$$

The above definition of $\hat{\nu}_i$ is valid if we assume $T_e \propto E/N$. This is convenient when $\nu_i(E/N)$ is approximated by Townsend's function.

According to (9.13), an instability develops ($\Omega > 0$) only when the current and heat output exceed a certain threshold:

$$jE > Nc_{pl}T\nu_{T,F}/\hat{\nu}_i \approx (0.1 - 0.2)Nc_{pl}T\nu_{T,F} . \tag{9.14}$$

According to (8.24), this threshold corresponds to heating the gas by 10 to 20 %. As a result of a sharp dependence of ionization frequency on $T_e \propto E/N \propto T$, this very increase in temperature produces a strong enhancement of the ionization rate (by a factor of $\bar{e}$), thereby "launching" the system. Heat removal stabilizes the process: if increased, it raises the instability threshold. In the case of the heat conduction mechanism of cooling, as in tubes, we have $\nu_T \equiv \tau_\chi^{-1} \propto p^{-1}$, and the threshold $(jE)_{cr}$ is independent of pressure. Since $E/p \approx$ const, the threshold current is $j_{cr} \propto p^{-1}$. Experiments confirm this result: a homogeneous discharge is hard to obtain at high pressures, and at smaller currents the column contracts to the axis of the tube. In convective heat transfer, $(jE)_{cr} \propto p$ and the threshold current $j_{cr}(p) \approx$ const. The threshold is higher, the higher the flowrate of the pumped gas. When the energy release rate is appreciably greater than the threshold, the instability growth rate $\Omega \approx \nu_T^0 \hat{\nu}_i \sim 10^3$–$10^4\ s^{-1}$ (Table 9.1), that is, the thermal instability develops over 10^{-4}–10^{-3} s. The same conclusion follows from an analysis of the nonlinear stage of filament evolution [9.3].

9.4.2 Molecular Gas with Retarded Vibrational Relaxation

One example is nitrogen. In such cases, thermal expansion is delayed. Joule heat is first accumulated in vibrational degrees of freedom of molecules; as perturbations grow (provided the appropriate threshold has been exceeded), this heat transforms at an accelerating rate into the translational energy of the gas, because the vibrational relaxation accelerates with increasing temperature. The ionization rate also intensifies. What happens resembles a thermal explosion in which the chemical reaction goes faster and faster as temperature grows, so that the growth of temperature is constantly accelerated [9.4].

9.4.3 Stabilizing Effect of Ionization Produced by External Sources

The current and energy input into a discharge may be substantially increased without producing thermal instability by using a non-self-sustaining discharge in which the gas is ionized by an external source (especially by a fast electron beam) – see Chap. 14. The stabilizing effect stems from a sharp weakening of the inverse dependence of the rate of "self-sufficient" ionization on gas density.[4] Let an external source produce S pairs of ions per $cm^3 s$ in the volume. Now the balance equation for the number of electrons (9.10) takes the form

$$S + \nu_i\left[T_e(E/N)\right] n_e = \beta'_{eff} n_e^2 , \quad N = p/kT . \tag{9.15}$$

[4] A linear theory of stability of a non-self-sustaining discharge was first formulated in [9.7].

Let us vary these equalities, setting for brevity $T_e \propto E/N$ and $\xi = 1$. Let $S \sim N$, as is typical for ionization by an electron beam. We obtain

$$\frac{\delta \ln n_e}{\delta \ln T} \approx \frac{\hat{\nu}_i - S/\nu_i n_e}{1 + 2S/\nu_i n_e} < \hat{\nu}_i .$$

Now, the electron density is less sensitive to heating; in the limit $S \gg \nu_i n_e$ when $n_e \approx \sqrt{S/\beta'_{eff}}$, it even decreases in response to heating as $N^{1/2} \propto T^{-1/2}$. In the expression for the growth rate

$$\Omega = \nu_T^0 \frac{\hat{\nu}_i - S/\nu_i n_e}{1 + 2S/\nu_i n_e} - \nu_{T,F} = \frac{\nu_T^0 \hat{\nu}_i}{1 + 2S/\nu_i n_e} - \frac{S\nu_T^0}{2S + \nu_i n_e} - \nu_{T,F} , \qquad (9.16)$$

the first, destabilizing term has decreased in comparison with (9.13). In addition to the heat removal term, $\nu_{T,F}$, another stabilizing term (the second in the last expression) appears in the formula. If $S \gg \nu_i n_e$, that is, if the discharge is strongly non-self-sustaining, the threshold values of current and energy input (i.e., ν_T^0) are greater for the same heat removal $\nu_{T,F}$ than in the self-sustaining discharge. Actually, instability may arise when the rate of external ionization becomes almost equal to that of ordinary ionization, that is, when the non-self-sustaining discharge becomes nearly self-sustaining. If $S \ll \nu_i n_e$, (9.16) transforms into (9.13).

9.4.4 Enhanced Stability of Discharge in Oscillating Fields

Other conditions being equal, a *high-frequency capacitance discharge* (Chap. 13) is more stable with respect to thermal instability than a constant current discharge; this is an experimental fact. As a result of the steep dependence of ν_i on E, ionization in oscillating fields occurs at the moment of field maxima. When the field is weaker, the plasma mostly decays. The balance of charge production and removal in a steady-state discharge is maintained only when averaged over a period. The electron density then slightly oscillates around the steady-state mean value $\bar{n}_e$. Thermal instability can develop only during ionization. At these moments, the field is higher than the constant field that would produce a constant density n_e equal to the mean density $\bar{n}_e$ in the oscillating field. Indeed, the stronger ionizing field must compensate for insufficient ionization at the moments of weak field. In fact, the slope of the function $\nu_i(E)$ and the value of $\hat{\nu}_i$ are smaller in stronger fields [see (9.12)]. According to (9.14), the threshold energy release (called *maximum energy input*) is correspondingly higher.

The energy threshold for instabilities is found to be even higher in the constant current non-self-sustaining discharge in which the gas is ionized by *short repeated high-voltage pulses* and the energy is supplied by the dc current. The stabilizing factor is the same, but the effect is better pronounced because the amplitudes of pulses separated with relatively long pauses must be even higher in order to maintain the same mean electron density. By using this principle of discharge sustainment, it is possible to raise the energy input by an order of

magnitude without disturbing its homogeneity, and thus develop a high-power laser (Sect. 14.4.5). The above arguments on stability improvement are supported by calculations [9.8].

9.5 Attachment Instability

9.5.1 Stability of Attachment-Controlled Discharges

Attachment as such does not lead to instability. The attachment frequency ν_a increases with E/N not as steeply as ionization frequency, and $\hat{\nu}_a < \hat{\nu}_i$. In the case of longitudinal inhomogeneities, E/N and T_e depend on n_e inversely (Sect. 9.3.3), so that the stable situation of Fig. 9.1a holds for pure attachment. Indeed, neglecting spatial inhomogeneity and varying the electron kinetics equation $\partial n_e/\partial t = (\nu_i - \nu_a)n_e$ about the point of steady state $\nu_i = \nu_a$, and assuming $\delta n_e \propto \exp(\Omega t)$, we find

$$\Omega = \left(\frac{\partial \nu_i}{\partial T_e} - \frac{\partial \nu_a}{\partial T_e}\right) n_e \frac{\delta T_e}{\delta n_e} = \frac{\delta \ln T_e}{\delta \ln n_e}(\nu_i \hat{\nu}_i - \nu_a \hat{\nu}_a) \ , \quad \nu_i = \nu_a \ . \tag{9.17}$$

For instance, the ν_i and ν_a curves of the mixture $CO_2 : N_2 : He = 1 : 7 : 12$ intersect at $T_e = 1.6\,eV$ (Fig. 8.19). The ionization potential $I_{CO_2} = 13.3\,eV$. The frequency of dissociative attachment of an electron to a CO_2 molecule is $\nu_a \sim \exp(-U/kT_e)$, where $U = 3.85\,eV$ (Sect. 4.4.1). At the intersection point, $\hat{\nu}_i = 8.3$, $\hat{\nu}_a = 2.4$. In accordance with (9.7, 17), $\Omega < 0$. Perturbations damp out quite rapidly: $|\Omega| \sim 10\nu_a$.

Let a transverse perturbation appear. Heating and thermal expansion are considerably slower than the ionization-attachment kinetics so that the gas density N can be considered frozen. As a result, $\delta \ln T_e/\delta \ln n_e = 0$ (Sect. 9.3.2), and $\Omega = 0$ in (9.17). This uncertain equilibrium is stabilized by external resistance (Sect. 9.1.2). The stability of attachment-controlled discharges is confirmed by the experiment [9.9] described in Sect. 8.8.1.

9.5.2 Mechanism of Instability

The attachment instability can be appreciable only if detachment compensates for attachment to a considerable degree. The electron temperature of the steady state is then substantially lower than that at which $\nu_i = \nu_a$ because ionization must compensate for only a small difference between attachment and detachment. The longitudinal perturbations may grow because the detachment rate is independent of T_e. Let the electron density increase slightly at some point in the discharge. The electron temperature at this point decreases. The ionization rate obviously decreases, but this factor may affect the balance of the numbers of electrons less than the weakening of attachment. The latter factor leaves the (unchanged) detachment uncompensated and electrons keep entering the plasma from decaying

negative ions. The number of electrons increases, and E and T_e decrease still further. This effect is represented by a chain of causal links:

$$\delta n_e \uparrow \rightarrow \delta T_e \downarrow \rightarrow \nu_a \downarrow \rightarrow (Z_+ - Z_-) \uparrow \rightarrow \delta n_e \uparrow \ . \tag{9.18}$$

9.5.3 Growth Rate

The unsteady process of interest is described by a system of two kinetics equations from (8.28), for n_e and n_-. The third equation is equivalent to the charge neutrality condition $n_+ = n_e + n_-$. Their joint analysis [9.1, 2] leads to very complicated expressions. Let us take an essentially simpler case where positive ions recombine much more slowly than attachment and detachment proceed and than the instability develops [9.10]. In this case the parameter n_+ can be regarded as frozen, $\delta n_- = -\delta n_e$, so that only one kinetics equation, that for n_e, survives from (8.28). By varying it under the assumption of spatial homogeneity, as in Sect. 9.5.1, we find the instability growth rate:

$$\Omega = \frac{\delta \ln T_e}{\delta \ln n_e} (\nu_i \hat{\nu}_i - \nu_a \hat{\nu}_a) - (\nu_a + \nu_d) \ , \quad \frac{\delta \ln T_e}{\delta \ln n_e} < 0 \ , \tag{9.19}$$

where $\nu_d = k_d N$ is the negative ion detachment frequency. Taking into account (9.7) and an approximate equality of attachment and detachment velocities, $\nu_a n_e \approx \nu_d n_-$, we can rearrange Ω in the form

$$\Omega \approx \nu_a \left[\frac{2\hat{\nu}_a}{\hat{\nu}'_u} \left(1 - \frac{dk_i/dT_e}{dk_a/dT_e} \right) - \frac{n_+}{n_-} \right] \ . \tag{9.20}$$

The form of the first term in (9.19) coincides with that of (9.17) but now $\nu_i \ll \nu_a$ so that it can be positive. As follows from (9.20), this is possible only if $dk_i/dT_e < dk_a/dT_e$. In the mixture $CO_2 : N_2 : He = 1 : 7 : 12$, this inequality holds if $T_e < 1.05\,eV$ [9.2, 11] (Fig. 8.19). If T_e is considerably lower than this value, the first term in (9.19, 20) is a sufficiently large positive quantity and may become greater than the second term which is proportional to n_+/n_-. It is necessary, however, that the ratio n_+/n_- (it determines the stabilizing effect) be not too high.

Calculations [9.2, 11] have determined the boundaries of the instability region for the mixture given above: $n_e < 10^{10}\,cm^3$, $10^{-1} < n_-/n_e < 10$, $T_e < 1\,eV$. Recombination, which always plays a stabilizing role, is too strong for the instability to occur if $n_e > 10^{10}$ (Sect. 9.1.2). If $n_-/n_e < 10^{-1}$, that is $n_+/n_- > 10$, then the reservoir of bound negative charges whose release by detachment could result in destabilization is too small. If $n_-/n_e > 10$, the number of positive ions at the given electron density is too high, recombination is strong, and a high ionization rate is required to compensate for it, at $T_e > 1\,eV$. The destabilizing effect is thereby eliminated. According to (9.20), the time scale of the evolution of instability, if it occurs, is of the order of the attachment time $\tau_a = \nu_a^{-1}$.

9.5.4 Domains

The attachment instability typically results in domain formation. If a fluctuation $\delta n_e > 0$ or $\delta T_e < 0$ occurs in an unstable state with a relatively high number of negative ions, these ions immediately start to decay. Numerous electrons appear, the conductivity sharply increases, and the field at this spot decreases. The result is a *weak field domain*. If a fluctuation $\delta n_e < 0$ or $\delta T_e > 0$ occurs in an unstable state with relatively low n_-, attachment increases just as irresistibly, the conductivity drops, and the field increases. A *strong field domain* is thus formed. Domains move towards the anode with a phase velocity which may be several orders of magnitude lower than the electron drift velocity. Effects of spatial inhomogeneity must be taken into account. The manifestations of these effects will be discussed in Sect. 9.7, when considering the motion of striations. As a rule, domains are periodically initiated, travel, and then disappear. They are not visually detectable, but instruments do record current oscillations. No domains are observed in pure Ar, He, and N_2, where no attachment occurs.

9.6 Some Other Frequently Encountered Destabilizing Mechanisms

9.6.1 Stepwise Ionization

We will demonstrate this effect with the diffusion-controlled discharge. We again drop for the sake of simplification and brevity, the terms that take into account the spatial inhomogeneity of plasma, and write the kinetics equations for the densities of electrons and excited atoms:

$$dn_e/dt = k_i N n_e + k_i^* N^* n_e - \nu_{da} n_e \ , \quad k_i = k_i(T_e) \ , \tag{9.21}$$

$$dn^*/dt = k^* N n_e - k_2 N^* n_e - \nu_d^* N^* \ , \quad k^* = k^*(T_e) \ . \tag{9.22}$$

Here $k_i = \nu_i/N$, $k^* = \nu^*/N$ are the rates of ionization and excitation of atoms from the ground state, k_i^* and k_2 are the rates of ionization and deexcitation of excited metastable atoms, and ν_d^* is the frequency of losses of excited atoms not caused by electron impact (losses due to diffusion toward the walls and deactivation by collisions with atoms). Equation (9.22) takes into account that $k_i^* \ll k_2$ because an electron needs sufficient energy for ionization but does not need it for deactivation. If the instability develops more slowly than the excited atoms decay (in fact, this is a typical situation), the density N^*, being quasisteady, tracks the growth of n_e:

$$N^* \approx N^*[n_e(t)] \approx k^* N n_e/(k_2 n_e + \nu_d^*) \ . \tag{9.23}$$

Let us take the variations of (9.21, 23) at the steady-state point, neglecting the dependence of k_i^* and k_2 on T_e in comparison with that of k_i and k^*. Assuming $n_e \propto \exp(\Omega t)$, we find

$$\Omega = \frac{\nu_d^* k_i^* N^{*2}}{\nu^* n_e} + \frac{\delta \ln T_e}{\delta \ln n_e} \left(\hat{\nu}_i \nu_i + \hat{\nu}^* k_i^* N^* \right) . \tag{9.24}$$

The first positive term $\Omega^{(+)}$, reflecting the ionization of the accumulating excited atoms, is quadratic in N^*; it results in the destabilizing effect of the stepwise ionization. Considered as a function of n_e, it reaches maxima at the values

$$(n_e)_{opt} = \nu_d^*/k_2 , \quad (N^*)_{opt} = k^* N/2k_2 = N_{eq}^*/2 \tag{9.25}$$

that are optimal for instability to occur. Here N_{eq}^* is the equilibrium Boltzmann density of excited atoms, corresponding to T_e. It satisfies the detailed balance principle $k^* N n_e = k_2 N_{eq}^* n_e$. The quantity

$$\Omega_{max}^{(+)} = k_i^* k^* N/4k_2 = k_i^* (N^*)_{opt}/2 = k_i^* N_{eq}^*/4 \tag{9.26}$$

gives the upper bound to the instability growth rate. Instability would evolve at this rate under the most favorable conditions, if no stabilizing factors were at work. Far from the boundaries of the stability region, however, Ω is of the order of $\Omega_{max}^{(+)}$ even if such factors are present.

In order to evaluate the orders of magnitude of the quantities of interest, consider an example, Let $p = 3\,\text{Torr}$, $N = 10^{17}\,\text{cm}^{-3}$. In a tube of radius $R = 1\,\text{cm}$, the frequency of ambipolar diffusion of charges towards the walls (this diffusion controls the discharge in inert gases) is $\nu_{da} \approx 5 \cdot 10^3\,\text{s}^{-1}$. Therefore, the ionization frequency is also close to this value: $\nu_i \approx \nu_{da}$. The excitation frequency $\nu^* \approx 10^5\,\text{s}^{-1}$ is greater than ν_i because $E^* \approx 3I/4$; $k_i^* \sim 10^{-9}\,\text{cm}^3/\text{s} \gg k_i \approx 5 \cdot 10^{-14}\,\text{cm}^3/\text{s}$ because the binding energy of excited atoms $I - E^* \approx I/4$; $k_2 \approx 10^{-8}\,\text{cm}^3/\text{s}$, $N_{eq}^* \approx 10^{13}\,\text{cm}^{-3}$, $\nu_d^* \approx 3 \cdot 10^3\,\text{s}^{-1}$. Hence, $(n_e)_{opt} \approx 3 \cdot 10^{11}\,\text{cm}^{-3}$, $(N^*)_{opt} \approx 5 \cdot 10^{12}\,\text{cm}^{-3}$, $\Omega_{max}^{(+)} \approx 3 \cdot 10^3\,\text{s}^{-1}$. The growth rate is of the order of $\nu_{da} \approx \nu_i$.

As for the second ionization term in (9.24), it is negative for longitudinal perturbations, as in (9.17, 19), and its effect is stabilizing. This effect has to be overcome for instabilities to occur; hence, the region of possible occurrence of instability is correspondingly limited. Additional analysis of the stabilizing effect of ionization is given in Sect. 9.7.2. The effect disappears in the case of transverse perturbations, when T_e is related to n_e only through thermal expansion.

9.6.2 "Maxwellization" of Electrons

Electrons lose large amounts of energy when colliding with atoms and exciting (or ionizing) them. The result is a considerable depletion of the spectrum in the range of energies sufficient for ionization, and a reduction of the ionization frequency per electron. At greater concentrations, electrons begin interacting with one another, exchanging large portions of energy. The spectrum tends to a maxwellian form in which the fraction of fast electrons is larger than when electrons collide only with atoms and gain no energy from them. The ionization frequency increases, the electron density grows, and the spectrum becomes even

more maxwellian. If n_e is sufficiently high, at higher currents, this instability may lead to contraction and striation formation, just as stepwise ionization does.

9.7 Striations

9.7.1 Observations

The positive column of discharge in tubes is striated (Fig. 9.4) much more often than is detectable by the naked eye. As a rule, striations are travelling. In inert gases, they move at velocities $v_{ph} \sim 100\,\text{m/s}$ (at $p \sim 10^{-1}$–$10\,\text{Torr}$) from the anode to the cathode. The intensity of light emission oscillates at frequencies of about 1 kHz, so that the eye cannot resolve the oscillations and the column appears homogeneous. Striations may not be moving, revealing the alternation of bright and dark layers along the tube, which is how they were discovered. Striations appear fixed when the discharge incorporates a local, permanent source of strong perturbations, for example, a probe at high negative potential or a sharp change in tube cross section. Sometimes the region adjacent to the cathode

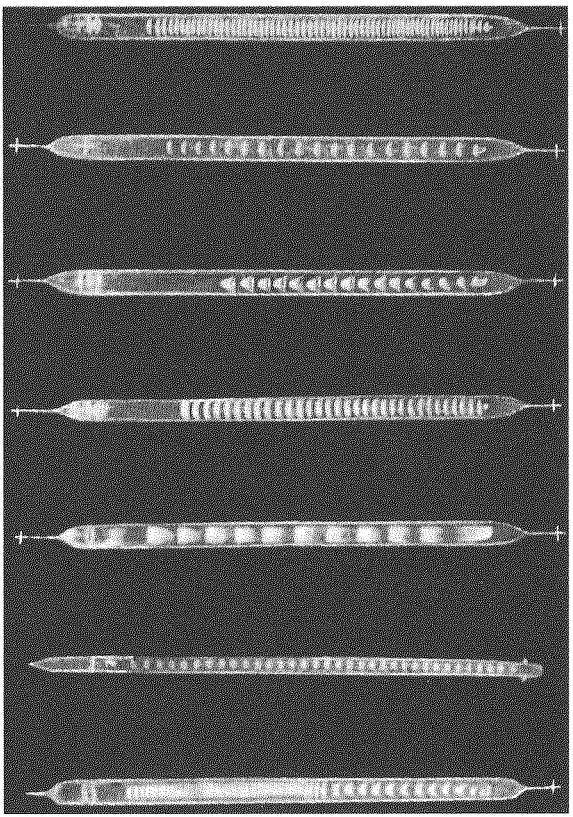

Fig. 9.4. General appearance of striated discharge

plays the role of such a perturbation. Fixed striations build up away from the perturbation point towards the anode and are gradually damped out. Sometimes only the first few striations fade out at the cathode, while the remaining ones are preserved. Typically, the length of one striation, that is, the distance between the corresponding points of neighbouring striations, equals several tube radii. This is true both for fixed and for running striations.

Striations survive in a limited range of current values, gas species, pressure, and tube radius. The amplitude of luminosity oscillations, striation wavelength, and the velocity of striation propagation depend on the same parameters. The amplitude of luminosity oscillations, that to some extent reflects the amplitude of electron density oscillations, is not high at the boundary of the existence region. The oscillations are very nearly sinusoidal. The realtionship between small- and large-amplitude striations is almost the same as between acoustic and strong nonlinear waves in gas dynamics. Beyond the region of existence of striations, the positive column is stable and homogeneous, although external perturbation agents can generate striations in a small neighbourhood beyond the natural region of existence. Extensive experimental data on striations can be found in the reviews [9.12–15].

9.7.2 Conditions of Occurrence

Striations are manifestations of ionization oscillations and waves. This means that periodic changes in electron density are caused not by redistribution of a fixed number of electrons (as in plasma waves), but by alternation of regions of predominant production and removal of electrons. Instability mechanisms leading to striation originate with ionization processes. A striated discharge may be caused by stepwise ionization, the maxwellization of the electron distribution function (Sect. 9.6), and by any agent causing enhancement in longitudinal inhomogeneities. Stepwise ionization is effective only at moderate currents, when the metastable atoms produced by electron impact decay as a result of diffusion to the walls. At greater currents (at $i \gtrsim 100\,\mathrm{mA}$ in inert gases), n_e becomes so high that metastables are destroyed by electron impact. As follows from (9.23), their density then stops growing with increasing n_e; hence, instability will definitely develop in response to the nonlinear dependence of the gas ionization rate on n_e. In this process, stepwise ionization is replaced by maxwellization or some other mechanism.

Running striations constitute a wave process in which the decisive role is played by spatial plasma inhomogeneities (namely, longitudinal). An important length scale inherent in plasmas is the relaxation length of electron temperature (energy spectrum) in the field: $\Lambda_u = v_d \tau_u \approx l/\sqrt{\delta}$. It is this scale, in addition to another geometric scale, namely, the tube radius R, that largely dictates the occurrence of spatial inhomogeneities and their scales. Actually, this situation arises because the steep increase of ionization rate with T_e in the case of longitudinal perturbations is a stabilizing factor [see (9.24) and the remark at the end of Sect. 9.6.1]. Indeed, since j is constant, the field drops at points where

n_e increases (Sect. 9.3.3). If T_e decreases together with E, the ionization rate is reduced and the positive increment of n_e is damped out.

The electron temperature reaches the value dictated by the given field over a relaxation length Λ_u. This stabilizing factor (the quasisteady behaviour of T_e in response to varying E) is at its most effective in the case of long waves or small wave numbers K, $K\Lambda_u \ll 1$. According to (9.7), $\delta \ln T_e/\delta \ln n_e \approx -2$ and the stabilizing factor in (9.24) ($\approx 2\hat{\nu}_i\nu_i$) is substantially greater than $\Omega^{(+)}_{max}$ given by (9.26). Destabilization caused by stepwise ionization cannot overcome the stabilization due to ionization. Stabilization due to ionizations weakens at short wavelengths, $K\Lambda_u > 1$, because T_e does not have enough time to decrease to the value corresponding to the reduced field. If the wavelength is very short ($K\Lambda_u \gg 1$), T_e is completely insensitive to oscillations in E, and ionization does not lead to stabilization. This mechanism bounds the striation wavelength from above by the electron energy relaxation length. Striations always have $K\Lambda_u$ greater than one. However, wavelengths are bounded from below as well. Waves which are too short in comparison with the tube radius R cannot survive either, because perturbations in n_e are actively destroyed by longitudinal ambipolar diffusion. As a result, striations can exist only in a certain interval of wavelengths. The most favourable conditions for striations in inert gases are $K\Lambda_u \approx 5$–10, $KR \sim 1$.

In molecular gases, where the fraction δ_1 of energy transferred to a molecule by a colliding electron is quite high, the relaxation length Λ_u is very short. The dimensions of those disturbances in n_e, which are not stabilized by ionization, are too small. Hence these disturbances may easily be destroyed by diffusion, and the formation of striations is obstructed. The situation with monatomic inert gases is different since $\delta_1 = 2m/M$ is a very small quantity and the length Λ_u is large, especially at low pressures in the range 10^{-2}–10 Torr. The case of Λ_u exceeding R is favourable for the occurrence of large-scale spatial inhomogeneities. Indeed, striated discharges are typical for inert gases, although narrow striations are also observed in hydrogen. Note that the study of striations started at the beginnning of this century, but the insight into the true nature of this widespread phenomenon was not gained until the 1960s.

9.7.3 Theory of Low-Amplitude Ionization Waves

The theory is based on linearizing the equations describing the behaviour of the electron gas in a plasma. In the hydrodynamics approximation, these equations are (2.44) for n_e, (2.52) and (2.53) for T_e, and (2.54) for E. These equations must contain a destabilizing factor, and if this factor is the stepwise ionization, the right-hand side of (9.21) [with N^* according to (9.23)] can be used as the charge source in (2.44). The dispersion relation for $\omega(K)$ is found as explained in Sect. 9.1.4, with the waves regarded as directed along $\boldsymbol{E}$. This calculation was consistently carried to the final result in [9.13, 16]. The calculation [9.17], involving maxwellization as the destabilization mechanism at elevated currents, gave not only a qualitative but also a good quantitative fit to the measured de-

pendence of striation wavelength on frequency and to the boundaries of striation existence in argon.

The system of equations (2.44, 52, 54) are of second order in t, so that a quadratic equation is obtained for ω. If, however, the wave solution is substituted for δT_e into (2.52), one finds that the temporal and convective terms are in the ratio $3\omega/5Kv_e \approx 3v_{ph}/5v_d$. Here $v_{ph} = \omega/K$ is by definition the phase velocity of the wave. The experimental data and the solution that follows demonstrate that the velocity of motion of striations is much lower than the drift velocity of electrons, so that there is every reason to drop the term with $\partial T_e/\partial t$. The dispersion relation then becomes of first order. As follows from (2.44), in the case of a stepwise ionization mechanism, it differs from (9.24) only in the term due to the ambipolar diffusion in the plasma. This diffusion tends to level off the disturbances and exerts a stabilizing influence, so that the contribution to $i\omega$ is

$$i\omega = \Omega^{(+)} + (\delta \ln T_e/\delta \ln n_e)\left(\hat{\nu}_i \nu_i + \hat{\nu}^* k_i^* N^*\right) - D_a K^2 . \tag{9.27}$$

The destabilizing term $\Omega^{(+)}$ has already been discussed in Sect. 9.6.1.

Let us introduce several simplifications, in order to avoid a cumbersome relation between δT_e and δn_e in (9.27). Let ν_m, μ_e, $\nu_u = \delta_1 \nu_m$ be independent of T_e (in a monatomic gas, $\delta_1 = 2m/M$ = const). We neglect the ambipolar diffusion flux in (2.54) because $D_a \ll D_e$. Then $n_e v_e = -j/e$ = const and we need not vary the product $n_e v_e$ (Sect. 9.2.3). Let us ignore the loss of energy spent on ionization in comparison with energy transfer to atoms. This is true if $\nu_i \ll \nu_u$, that is, if pressure is not too low, because $\nu_i \approx \nu_{da} \propto p^{-1}$ and $\nu_u \propto p$. Taking variations of (2.54, 52) (with $\partial T_e/\partial t = 0$) around the point of uniform steady state and taking account of $kT_e \approx eE\Lambda_u$ via (2.19), we find the relation between the complex perturbation amplitudes:

$$\delta E/E = (-1 + iK\Lambda_u)\delta n_e/n_e , \tag{9.28}$$

$$\left[(5/2)K^2\Lambda_u^2 + 1 + i(5/2)K\Lambda_u\right] \delta T_e/T_e = \delta E/E - \delta n_e/n_e , \tag{9.29}$$

$$\frac{\delta \ln T_e}{\delta \ln n_e} = \frac{-2 + iK\Lambda_u}{(5/2)K^2\Lambda_u^2 + 1 + i(5/2)\cdot K\Lambda_u} . \tag{9.30}$$

These formulae are significant and support the qualitative conclusions of Sect. 9.7.2. The relations become practically quasisteady in the limit $K\Lambda_u \ll 1$. They transform to those given by (9.6, 7) ($\hat{\nu}_m = 0$, $\hat{\nu}'_u = 1$, $\xi = 2$). The stabilization due to ionization in (9.27), where $\delta \ln T_e/\delta \ln n_e \approx -2$, is very strong. Long waves are damped out. In the general case, the waves of δn_e, δE, and δT_e are shifted in phase with respect to each other. We will presently see that these phase shifts ensure the motion of the waves. For the sake of simplification, consider the limiting case $K\Lambda_u \gg 1$ (the only one that can be realized experimentally in monatomic gases), and separate the real and imaginary parts of (9.30):

$$\frac{\delta \ln T_e}{\delta \ln n_e} = -\frac{2}{5K^2\Lambda_u^2} + i\frac{2}{5K\Lambda_u} . \tag{9.31}$$

The real negative term which is proportional to the stabilizing factor becomes very small, so that undamped waves become possible. The imaginary part determines the frequency, proportional to wavelength: $\omega \propto K^{-1}$. The stabilization due to ionization, proportional to K^{-2}, becomes weaker, the shorter the wavelength. However, excessively short waves are stabilized quite well by diffusion, whose effect is proportional to K^2 [see (9.27)]. Therefore, the overall stabilizing factor denoted here by $\Omega^{(-)}(K)$ has a minimum at a certain K_{opt}. If $\Omega^{(+)} > \Omega^{(-)}_{\text{min}}$, the waves are allowed and the equation $\Omega^{(+)} = \Omega^{(-)}(K)$ limits the interval of possible wavelengths around K_{opt} on both sides.[5] The formulae derived from (9.27, 31) give the following wave number K_{opt} that is optimal for driving the oscillations:

$$K_{\text{opt}} \Lambda_D \approx (\Lambda_D/\Lambda_u)^{1/2} (2\hat{\nu}_i/5)^{1/4} ,$$

where $\Lambda_D = R/2.4$ is the diffusion length for a tube of radius R. In monatomic gases at $p \sim$ 1–10 Torr and R = 1 cm, $\Lambda_u \sim l/\sqrt{\delta_1} \approx$ 1–10 cm, $\Lambda_D \approx 0.3$ cm, and $\hat{\nu}_i \approx 10$. The optimal striation wavelength comes to several tube diameters, in agreement with experiments; at the same time, $K_{\text{opt}} \Lambda_u \approx$ 5–10, which justifies the approximation $K\Lambda_u \gg 1$.

9.7.4 Why Do Striations Move?

Let us clarify the physical reason for the motion of striations, which typically run from the anode to the cathode. Density gradients in real, relatively short waves are considerable. The relative separation of charges that exists, despite a high degree of charge neutrality, is determined not by drift but by diffusion (Fig. 9.5). On the slopes where n_e decreases towards the cathode (as x increases), the arising polarization field δE is added to the constant nonperturbed field E. On the slopes where n_e increases as x increases, δE is subtracted from E. For this reason, the δE wave is shifted by one quarter of a wavelength to the cathode with respect to the δn_e wave [Fig. 9.5, formula (9.28)]. The energy release in the electron gas, jE, has the same distribution as E, because j = const. This means that the maxima of jE coincide with those of E and are shifted by a quarter of a wavelength with respect to the maxima of n_e.

Among the various components of the electron energy balance (Sect. 9.2.5), heat conduction plays the dominant role for short waves with $K\Lambda_u \gg 1$. Electronic heat from an enhanced source $\delta(jE) = j\delta E$ spreads in both directions and the T_e profile very nearly repeats those of the heat and E source. The δT_e wave is almost in phase with the δE wave [this is clear from (9.28–31) also]. The ionization rate $\nu_i(T_e)n_e$ is also almost in phase with it because it is much more

[5] The conclusion that the instability growth rate Ω is positive in some narrow interval of short wavelengths with $K\Lambda_u \gg 1$ was made in a well-known review [9.12] for a similar problem, disregarding stepwise ionization or any other destabilizating mechanism. It was repeated in the review [9.18], citing [9.12]. This conclusion was a result of neglecting electronic heat conduction which causes damping of short-wave perturbations.

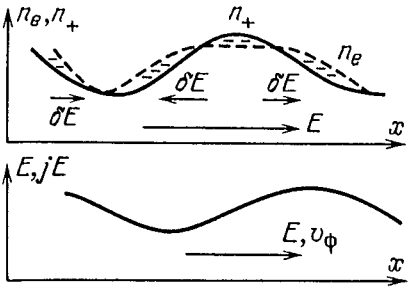

Fig. 9.5. Electron density and energy deposition distributions in moving striations: the case of short waves, when electron diffusion dominates the drift

sensitive to T_e than to n_e. Hence, ionization is most intensive at the piont of instantaneous equilibrium of n_e on the x axis, where $\delta n_e \approx 0$ and E is maximal. A quarter of a period later δn_e increases to the maximum value, that is, the crest of n_e moving in the direction of E arrives at this point.

9.7.5 Evaluation of the Velocity and Frequency of Striations

This is easier done not in a formal way, by extending the calculations of Sect. 9.7.3, but directly, on the basis of the arguments given above. The essence of the phenomenon is then better understood. Very short δn_e and δE waves are shifted by a quarter of a period. The relation between these parameters in complex representation is purely imaginary. According to (9.28),

$$\delta E/E \approx \mathrm{i} K \Lambda_u \delta n_e / n_e \,. \tag{9.32}$$

From the balance of the additional heat release and heat spreading due to heat conduction in (2.50, 51), we find $j\delta E \approx K^2 \lambda_e \delta T_e$. Substituting $j = e n_e \mu_e E$, $\lambda_e = (5/2) k n_e D_e$, and $T_e = E\Lambda_u$, we obtain

$$\frac{\delta T_e}{T_e} \approx \frac{2}{5K^2\Lambda_u^2}\frac{\delta E}{E} \approx \mathrm{i}\frac{2}{5K\Lambda_u}\frac{\delta n_e}{n_e} \,. \tag{9.33}$$

Owing to the temperature leveling via heat conduction, the relative change in T_e is much smaller than that of the field. It is also smaller than the change in plasma density, although here the difference is less pronounced.

The additional ionization rate due to enhanced heating is

$$\delta(\nu_i n_e) \approx n_e (d\nu_i/dT_e)\delta T_e = n_e \hat{\nu}_i \nu_i (\delta T_e/T_e) \,.$$

In a quarter of a period, that is, in a time $t \approx (K v_{ph})^{-1}$ where $v_{ph} = \omega/K$ is the phase velocity of the wave, n_e grows by a quantity δn_e of the order of the amplitude: $\delta(\nu_i n_e)t \approx \delta n_e$. Hence,

$$v_{ph} \approx \hat{\nu}_i \nu_i K^{-1} |\delta \ln T_e / \delta \ln n_e| \,.$$

After substituting here (9.33), we obtain the velocity and frequency of striations:

$$v_{ph} \approx \tfrac{2}{5}\hat{\nu}_i \nu_i / K^2 \Lambda_u \,, \quad \omega \approx \tfrac{2}{5}\hat{\nu}_i \nu_i / K \Lambda_u \,. \tag{9.34}$$

The frequency of oscillations of n_e and of other quantities in striations is proportional to the wavelength, and the velocity is proportional to the wavelength squared. The ionization frequency serves as frequency scale because striations are typically characterized by $K\Lambda_u \approx 10$ and $\hat{\nu}_i \approx I/kT_e \approx 10$. If the pressure in inert gases is not high, electrons are mainly removed to the walls by ambipolar diffusion, so that $\nu_i \approx \nu_{da} = D_a/\Lambda_D^2 \sim D_a/R^2$. Hence, ω is of the order of the diffusion frequency. In more rigorous solutions [9.13, 17], the qualitative core of the expressions for $\omega(K)$ and v_{ph} is the same as in (9.34). For argon in a tube of $R = 1.5\,\text{cm}$, at $p = 0.5\,\text{Torr}$ and $i = 3.6\,\text{mA}$, experiments and calculations [9.17] show that as the frequency $\omega/2\pi$ increases from 1.4 to 2 kHz, the striation wavelength $2\pi/K$ increases from 6 to 9 cm, and the velocity v_{ph}, from 80 to 180 m/s. Estimates yield correct orders of magnitude.

It is worthy of note that the group velocity of striations $v_{gr} = \partial\omega/\partial K < 0$, that is, v_{gr} points against the phase velocity and (in the framework of the chosen approximation) has equal magnitude. Therefore, any marking feature, such as a brighter region due to a pulsed local disturbance, runs towards the anode, in contrast to the striations themselves. Low-amplitude waves obeying linear theory typically survive under conditions that correspond to moderate penetration into the instability region. The stabilizing factors are still strong there and slow down by buildup of amplitude. Well-developed nonlinear waves of high amplitude can also arise far from the boundaries.

9.7.6 High-Amplitude Striations

Now we can conclude that striations are *ionization waves* moving through the gas, that is, alternating regions of enhanced and weakened ionization originating with the waves of enhanced and weakened field. In general, the processes in high-amplitude striations are the same as in weak-field waves but assume a greater role. High-field regions grow into abrupt potential jumps, and the field in more distant (on the anode side) regions may not just vanish, but may even become negative.

Ionization in high-field regions becomes so intensified that the electron density increases by an order of magnitude. This very bright, relatively narrow zone is known as the striation *head*. Ionization stops beyond it and electrons vanish owing to diffusion to the walls. Their density gradually decreases by the same order of magnitude until the next striation head. This dark zone is much longer than the bright one because electrons disappear at a slower rate than they are produced. As n_e falls off, the field is restored [$j(x) \propto n_e E = \text{const}$] and the process repeats itself. Qualitatively, this picture is similar to the stationary structure around cathode region of a static discharge (Sect. 8.5.3 and footnote 9 on p. 193). The cathode layer with negative glow corresponds to the striation head, and the Faraday dark space, to the extended region up to the next head. Instead of such a head, the positive column with moderate field and emission intensity is formed (provided the column is not striated).

9.7.7 Experiment and Its Interpretation

Figure 9.6 shows the results of probe measurement of the instantaneous distributions of n_e, T_e, and potential φ along the x axis of a strongly striated discharge tube [9.19]. The distribution of E, obtained by differentiating the $\varphi(x)$ curve, is also plotted. Measurements were carried out along the axis of a long tube. Striations move from the anode to the cathode at a velocity $v_{ph} = 60\,\text{m/s}$. The above distributions move as a whole from left to right at this velocity. The length of one striation is $d = 5.5\,\text{cm}$. The distribution of light intensity approximately follows that of n_e. Estimation of the space charge using double differentiation of the $\varphi(x)$ curve shows that the degree of charge neutrality is high even at points of high gradients: $|n_e - n_+| \lesssim 10^{-4} n_e$. On the average, $\langle E/p \rangle = 0.22\,\text{V/(cm·Torr)}$ along the striation and the column as a whole.

The maximum of E and of the ionization rate is localized at the point of steepest drop in n_e, on the right-hand slope of the crest. For this reason, the peak of $(n_e)_{max}$ and the entire striations moves to the right, to the cathode. The electron diffusion current is very high on the right-hand slope of n_e: $eD_e|dn_e/dx| \approx 530\,\text{mA/cm}^2$ ($D_e \approx 2.5 \cdot 10^6\,\text{cm/s}$); it is directed against the actual current i. With the Bessel radial profile $n_e(r)$ taken into account, the current density on the tube axis is $j = 2.3i/\pi R^2 = 77\,\text{mA/cm}^2$. The diffusion current is exceeded by the drift current $e\mu_e n_e E = 530 + 77 \approx 610\,\text{mA/cm}^2$ by just the amount necessary to supply the required density of j. Hence, for $\mu_e = 1.7 \cdot 10^5\,\text{cm}^2/(\text{s·V})$ we find $(E/p)_{max} \approx 8\,\text{V/(cm·Torr)}$, which is 36 times the average $\langle E/p \rangle$. When the

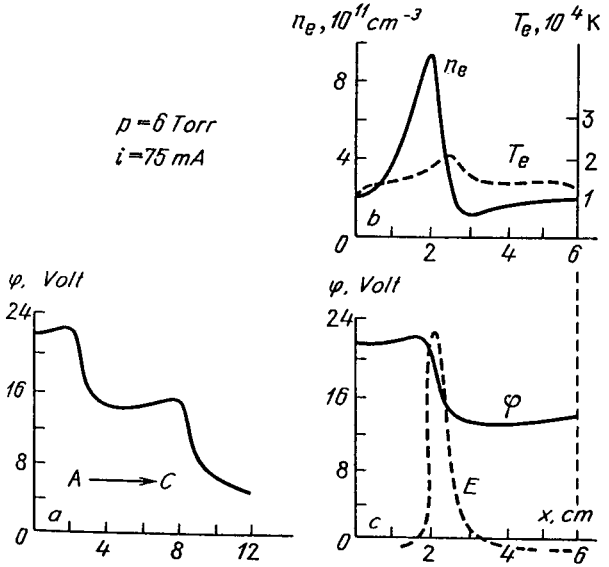

Fig. 9.6. High-amplitude striations in argon in a tube of radius $R = 0.85\,\text{cm}$ at $p = 6\,\text{Torr}$ and $i = 75\,\text{mA}$. **(a)** Potential distribution along the axis; $A \rightarrow C$ is the direction from anode to cathode, **(b)** distribution of n_e and T_e within one period, **(c)** potential distribution on the same scale as in **(b)**, superposed on the coordinate axis with the **(b)** curve. Dashed curve is the field obtained by differentiating the potential [9.19]

mechanism of removal of electrons is their diffusion to the walls, their density beyond the striation head (where production is impeded) must fall off obeying the formula $v_{ph} dn_e/d|x| = -\nu_{da} n_e$. Hence,

$$d \approx (v_{ph}/\nu_{da}) \ln (n_{e,max}/n_{e,min}) . \tag{9.35}$$

In the experiment, $\mu_+ \approx 250\,\mathrm{cm^2/(s \cdot V)}$, $T_e \approx 1.3\,\mathrm{eV}$, $D_a = \mu_+ T_e = 320\,\mathrm{cm^2/s}$, $\nu_{da} = 2.4^2 D_a/R^2 = 2.6 \cdot 10^3\,\mathrm{s^{-1}}$. The measured values of v_{ph}, d, and density drop $n_{e,max}/n_{e,min} \approx 10$ are in perfect agreement with estimate (9.35); hence the picture obtained experimentally is deciphered quantitatively. It must be emphasized that the electron distribution function in strong-field striations with abrupt field jumps, and also in weak-field striations with $K\Lambda_u \gg 1$, is of a nonlocal type, that is, it is determined not just by the local instantaneous field E, but also depends on the behaviour of potential in the space-time neighbourhood (as in the cathode layer, Sect. 8.4.10). This effect can in itself lead to a striated discharge and may affect the structure of strong-field striations [9.20].

9.7.8 Why Is the Striated State Favored?

A layered state must lead to some gains, since the positive column, which has the unequivocal possibility of being homogeneous (this state would ensure that all the conservation laws hold), nevertheless "prefers" a layered state. The gain is that the voltage V and power output iV in a striated column are lower, at the same current, than in a homogeneous column. The production and removal of electrons in high-amplitude striations are separated both in space and in time and are balanced only when averaged over the entire length of a striation, or over a period t_1 of oscillations in a given cross section of the tube. The slope of the function $\nu_i(E)$ is so steep that if the field is strong but acts for only a short time, a lower value of the integral $\int E\,dt$ is required over a period t_1 in order to produce a certain number of electrons to compensate for their removal. The voltage drop ΔV over the length d of a striation is

$$v_{ph} \int_0^{t_1} E\,dt = \int_0^d E\,dx = \Delta V ,$$

which is less than the drop over the same length of a homogeneous column with constant field.

The "usefulness" of a striated discharge resembles the usefulness of concentrating the entire function of discharge sustainment in the cathode layer (Sect. 8.4.1). The following clarification can be given: It is easier for an electron to gain the energy necessary for ionization if it crosses the required potential difference over a short path in a strong field. It will then take part in a smaller number of collisions obstructing its acceleration. From this standpoint, it is more profitable to distribute the potential over a set of abrupt steps than spread it over the same length at a constant gradient. The phenomenon of striations satisfies the principle of minimal power (Sect. 8.4.8). In fact, it was given an indepen-

dent, more profound interpretation based on analyzing the processes themselves. Striations are formed because under certain conditions the homogeneous state becomes unstable.

9.8 Contraction of the Positive Column

A systematic study of the transition of a diffuse glow discharge to a contracted state has been carried out only for cylindrical tube geometry. In working with plane channels, measurements are typically limited to recording the critical current at which the homogeneous "burning" of the discharge discontinues. Conditions for studying discharge in plane channels are very unfavourable: the filament geometry is not always reproducible in successive experiments, the spot where a filament will form is not known in advance, and the filaments "dance". The ideal symmetry of tubes imposes rigid constraints on the process. It can be hypothesized, however, that the main properties of filaments are the same regardless of discharge geometry.

9.8.1 Experimental Results

Let us look at the results of one study [9.21] where fairly complete information on the phenomenon was obtained. The discharge was sustained in neon at p = 75–100 Torr in a tube of radius R = 2.8 cm. The field strength was measured by probes, the radial distribution of electron density was found from the bremsstrahlung produced by the scattering of electrons by neutral atoms, which is proportional to $n_e N$. The radial gas density profile $N(r)$, related to the gas temperature distribution $T(r)$ via constant pressure $p = NkT$, was taken into account. This is important because the gas was heated quite strongly. To find $T(r)$, the heat conduction equation for the true distribution of heat sources $j(r)E$ was solved. The temperature of the tube controlled, its wall being kept at T_0 = 300 K. The electron temperature on the axis was found from the measured field and from $N(0)$ using (4.13), which describes the electron energy balance. The momentum transfer cross section for neon depends quite weakly on energy and equals approximately $\sigma_m \approx 2.3 \cdot 10^{-16}$ cm^2; the gas is monatomic, $\delta_1 = 2m/M$.

Figure 9.7 shows the $V-i$ characteristic of the positive column. The left-hand part (up to the jump) corresponds to the diffuse discharge that fills the entire tube at the degree of homogeneity typical of a diffusion-controlled discharge for which $n_e(r) \sim J_0(2.4r/R)$ (Sect. 8.6.2). The $V-i$ curve is of "dropping" type; this is characteristic of diffusion-controlled discharges at relatively high current, which strongly heats the gas (Sect. 8.7.4). The field and voltage decrease in jumps at the critical current which corresponds to the sudden transition of a homogeneous column to a contracted mode. A brightly luminous filament appears at the axis, while the rest of the tube volume gets darker. The transition occurs at a current density, averaged over the tube cross section, of about 5.3 mA/cm^2. The critical current density at the axis is 2.3 times greater, 12 mA/cm^2, in accord with the

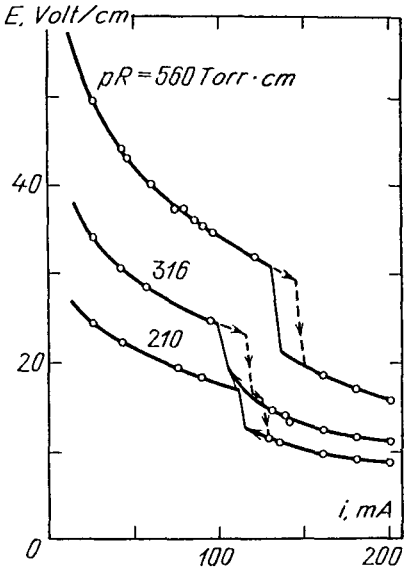

Fig. 9.7. $V - i$ characteristic of discharge in a tube containing neon in the region of transition from diffuse to contracted form. Tube radius $R = 2.8$ cm; *(1)* $pR = 210$ Torr·cm; *(2)* $pR = 316$; *(3)* $pR = 560$. The solid curve in the region of the jump was recorded as current was decreased, and the dashed curve, as it was raised [9.21]

Bessel $j(r)$ profile. The critical electron density at the axis $n_e(0) \approx 10^{11}$ cm^{-3}. A hysteresis is observed: The transition to the contracted discharge during current increase takes place at a somewhat greater current than the transition to diffuse current during current reduction. This is an indication of the double-valuedness of states in the region of the jump transition and of their possible metastability.[6]

Figure 9.8 shows radial distributions of n_e, and Table 9.2 lists discharge parameters at the axis, all at $p = 113$ Torr. Note how the current channel is sharply contracted, judging by its conductivity or n_e, and how the degree of

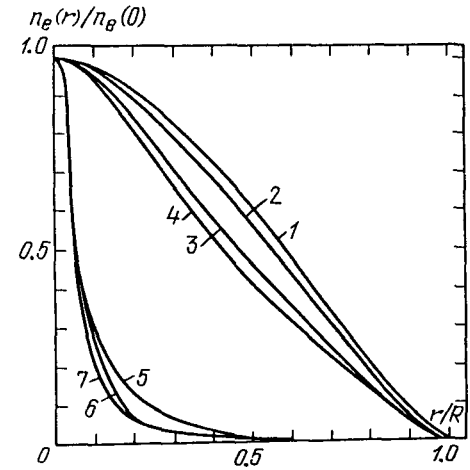

Fig. 9.8. Profiles of n_e measured under the conditions of Fig. 9.7. *(1)* $i/R = 4.8$ mA/cm; *(2)* 15.4; *(3)* 26.8; *(4)* 37.5; *(5)* 42.9; *(6)* 57.2; *(7)* 71.5 mA/cm. The transition from diffuse to contracted state occurred in the region between *(4)* and *(5)*

[6] We may recall the liquid-vapor phase transition (superheated liquid, supercooled vapor).

Table 9.2. Discharge parameters in a $R = 2.8$ cm tube at $p = 113$ Torr; the transition occurs at a current of 105–115 mA [9.21]

i, mA	$T_e(0)$, eV	$T(0)$, K	$n_e(0)$, 10^{11} cm^{-3}
13.5	3.0	440	0.12
43	3.3	650	0.39
75	3.6	840	0.93
96	3.7	930	1.2
120	3.0	1200	54
160	2.6	1300	72
200	2.5	1400	93

ionization jumps up by nearly two orders of magnitude. The effective filament radius [at the $n_e = n_e(0)/2$ level] is less than the tube radius by a factor of 20. The gas temperature at the axis is increased in the transition, and its fall-off from the axis is steeper in the contracted discharge than in the diffuse mode. The half-maximum point of the temperature drop between the axis and the walls lies at the point (0.7–0.8) R for a diffuse discharge and at the point $0.5R$ for the contracted discharge. This is natural: in the latter case, heat sources are concentrated at the axis. Upon contraction, the electron temperature slightly decreases because the field decreases. A very similar picture was also observed in argon.

The behaviour is somewhat different when a molecular gas is added to the inert host (Fig. 9.9) [9.22]. As usual, the $V - i$ curve first falls owing to gas heating, but then starts to rise. This is apparently related to the transition from diffusional to recombination losses as n_e increases. The $V - i$ characteristic of a bulk recombination-controlled discharge is typically rising (Sect. 8.6.3). The diffusion mode corresponds to very low values of $E/p \approx 0.12$ V/(cm·Torr). It appears that this is a result of (stepwise) ionization of metastable nitrogen atoms, since the production of electrons is thereby facilitated. After the jump,

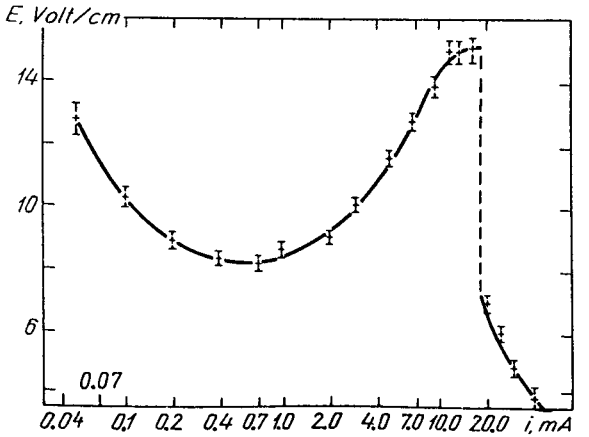

Fig. 9.9. $V - i$ characteristic of discharge in a tube of $R = 5$ cm in Xe + 0.12 % Ne, $p = 120$ Torr [9.22]

in contracted mode, a current filament of 0.5 mm radius is formed at the axis. An admixture of nitrogen somehow stabilizes the discharge in pure xenon: the transition occurs at much lower current, 1 mA instead of 19 mA, in the xenon-nitrogen mixture.

9.8.2 What Is Necessary for Contraction Onset

For the majority of electrons to be concentrated in a narrow channel in the vicinity of the axis (or at the spot where the filament was formed in a plane channel), at least two conditions must be met. *First*, electrons must be produced mostly where their density is high, i.e., there must be some *nonlinearly increasing* dependence of production rate on n_e, steeper than the usual one, $\nu_i n_e$ with $\nu_i(E) \approx$ const. The ionization frequency ν_i must fall appreciably from the axis to the periphery. If ν_i is independent of radius r, as we find for diffuse discharges, electron sources are uniformly distributed in volume in proportion to n_e, and electrons themselves fill the cross section more or less uniformly. Let us emphasize that only the dependence on n_e can produce the fall-off of ν_i away from the axis. Contraction leaves the longitudinal field homogeneous over the cross section, because curl $\boldsymbol{E} = 0$.

Second, the removal of electrons must be of *bulk* type, and it must be sufficiently fast for electrons liberated in a filament not to diffuse far laterally. Otherwise the diffusion (ambipolar) would make the electrons fill up the volume, even if the sources were concentrated on the axis. Electrons must disappear close to the place of production. As a result, contraction occurs only at sufficiently high currents and high n_e, when bulk recombination has a higher rate than recombination at the walls. The filament radius is determined by the greater of two lengths: the radius of the region where electron production sources are concentrated, and the distance

$$R_{max} \approx \sqrt{D_a \tau_{rec}} \approx \sqrt{D_a/\beta n_e}\,, \quad \text{or} \quad R_{max} \approx \sqrt{D_a \tau_a}$$

to which an electron can travel by diffusion during the recombination or attachment lifetime. The condition for contraction to be possible is that $R_{max} \ll R$. This gives the estimate $n_e > 10^{11}\,\mathrm{cm}^{-3}$, which is supported by experimental data. The fact that contraction occurs in pure inert gases points to the formation of molecular ions such as Ne_2^+ and Ar_2^+, otherwise recombination would be too slow.

9.8.3 Mechanisms of Nonlinear Production

These are the same mechanisms that result in diffuse discharge instabilities: thermal instability, stepwise ionization, Maxwellization. All three ensure that the ionization frequency, that is, the ionization rate per electron, increases with n_e. This behaviour was explained in Sect. 9.6 for the case of stepwise ionization and Maxwellization. For the thermal mechanism, ν_i as a function of n_e is given by

$$\nu_i \propto \exp(-I/kT_e) \propto \exp\left[-\mathrm{const}/(T_0 + \mathrm{const}\, n_e\right]\,,$$

where T_0 is the gas temperature in the case of very weak current (room temperature). This formula is implied by the relations: $T_e \propto E/N \propto T$ at $p \propto NT = \text{const}$, and $T - T_0 \propto \sigma E^2 \propto n_e$. All three mechanisms manifest themselves at densities n_e greater than about $10^{11}\,\text{cm}^{-3}$; it is fairly difficult to choose the main one among them. They may even act simultaneously, although experiments identify one predominant mechanism in some specific cases. Thus the thermal mechanism was not included in the interpretation of the experiments in neon (and argon) described in Sect. 9.8.1, although the overheating of the gas was tremendous, by a factor of 3.

The hysteresis observed in the transition from the diffuse to the contracted phase and back (Fig. 9.7) is a consequence of the two-valuedness of states in the transition zone. There are two ways to realize a given current i : it can be distributed at a low density over the entire cross section, or it may be concentrated at the axis in a small fraction of the cross section. In both cases, the heat transfer is balanced out by the heat released by the current. The transition from one state to the other is delayed because it starts only at a rather considerable penetration into the two-valued region, where one of the states is unstable. This is the case in which the instability growth rate is sufficiently large and the transition is triggered by a small fluctuation (see footnote 6 on p. 240).

9.8.4 Contraction of Discharge in Gas Flow

A discharge in plane channels with an intensive through-put of laser mixture clearly manifests the dependence of the maximum energy input, at which filamentation sets in, on the stream velocity u. The higher u, the shorter the residence time of a particle in the discharge zone, the shorter the time available for gas heating, and for the evolution of the instability, the more stable the discharge, and the higher the current can be increased before its homogeneous distribution breaks down. A clear-cut correlation of the homogeneity breakdown and gas temperature at the plane channel outlet is observed in a longitudinal discharge in plane channels (Fig. 8.1b). Contraction was observed each time the temperature rose by approximately 100° C. (These are the arguments in favour of the thermal nature of contraction under these conditions [9.23].)

A clear picture of filamentation under such conditions is shown in a unique photograph in Fig. 14.6. The methods of suppressing contraction developed for high-power laser design are described in Sect. 14.3, 14.4.

9.8.5 Filament and Arc

Although the contraction of glow discharges is often referred to as "arcing", the filament plasma is different from the typical equilibrium plasma of arc discharges with $T_e \approx T \approx 6000$–$10\,000\,\text{K}$. The characteristics of a filament lie between those of the strongly nonequilibrium plasma of diffuse glow discharges and the equilibrium plasma of arc discharges. The temperatures T_e and T in a filament differ appreciably: $T_e \approx (1-3)\cdot 10^4\,\text{K}$, $T \approx (2-3)\cdot 10^3\,\text{K}$; greater differences exist, however, in a glow discharge. The electron density $n_e \sim 10^{13}$–$10^{14}\,\text{cm}^{-3}$,

and the current density is greater than in the glow discharge but lower than in the arc. The field strength is lower than in the glow discharge but higher than in arcs. One feature in common with an arc discharge is the coexistence of the current region and currentless surrounding region, the longitudinal field being the same in both regions. In this sense, the thin column of the arc is also "contracted".

10. Arc Discharge

10.1 Definition and Characteristic Features of Arc Discharge

The discharge known as "the arc" is, as a rule, self-sustaining, with a relatively low cathode potential fall (of the order of the ionization or excitation potential of atoms, that is, about 10 eV). This characteristic distinguishes the arc discharge from the glow discharge, in which the cathode fall is hundreds of volts. The small cathode fall results from cathode emission mechanisms that differ from those in the glow discharge. These mechanisms are capable of supplying a greater electron current from the cathode, nearly equal to the total discharge current. This factor eliminates the need for considerable amplification of the electron current, which is the function fulfilled by the high cathode fall in glow discharges. Arc cathodes emit electrons as a result of *thermionic, field electron, and thermionic field emission.* More complex, combined processes of electron production at the cathode may also exist.

The arc discharge is characterized by large currents, $i \sim 1\text{–}10^5$ A, much greater than the typical currents of glow discharges, $i \sim 10^{-4}\text{–}10^{-1}$ A. The cathode current density is also greater than in glow discharges. It may be 10^2–10^4 A/cm^2 for some modes of arc discharge and 10^4–10^7 A/cm^2 for other modes. Note for comparison that the normal current density of 155 A/cm^2 on a copper cathode in air at a pressure $p = 1$ atm, (this is high for a glow discharge) corresponds to the lower limit of the arc range. As a rule, arcs burn at low voltage: not exceeding 20–30 V for short arcs, and as low as several volts in some cases. In many cases, but not always, $V - i$ characteristics of arcs are of the falling type.

Arc cathodes receive large amounts of energy from the current and reach high temperature, either over the entire cathode area or just locally, usually for short time intervals. They are *eroded* and suffer vaporization. The emission spectrum of the cathode region of a glow discharge coincides with the spectrum of the gas in which the discharge burns, but arc spectra show the lines of vapor of the electrode material. In fact, *vacuum arcs* burn in the vapor of the vaporized metal. As for the state of the plasma in the positive column, that is, the region between the layers adjacent to the electrodes, arc plasma may be in thermal *equilibrium* but quite often it may be *nonequilibrium.* (Thermal equilibrium of plasma is to be discussed in Sect. 10.11.) This characteristic depends on gas pressure. We can

say that equilibrium plasma is found only in arcs, but nonequilibrium plasma is characteristic both of glow and arc discharges, the latter burning at low pressure.

10.2 Arc Types

Almost all forms of dc discharge, except the glow discharge, can be subsumed under the definition of the arc, as the discharge with low cathode fall. Consequently, quite a few discharge modes are classified as arcs. The classification may be based on the characteristics of cathode processes, plasma state in the positive column, or the medium (gas or vapor of cathode materials) in which the current is sustained.

10.2.1 Arc with Hot Thermionic Cathode

The cathode of such arcs gets heated as a whole to a temperature about 3000 K, or even higher, so that the high current of the arc is simply the result of intense thermionic emission. The current flows through a comparatively large area on the cathode and its density is $j_C \sim 10^2$–10^4 A/cm^2. The arc is anchored at a fixed spot on the cathode surface and the current spot is stationary. Only refractory materials, which vaporize with great difficulty, can withstand this high temperature: carbon (graphite, coal, carbon black), which does not melt at all at normal pressure (its boiling temperature $T_{\text{boil}} \approx 4000$ K), tungsten, which is especially widespread in practical devices ($T_{\text{melt}} \approx 3700$ K, $T_{\text{boil}} \approx 5900$ K), molybdenum, zirconium, tantalum, etc. Arcs with hot tungsten cathodes are employed in apparatus (often high-pressure units) requiring long service life (low erosion) of electrodes such as plasmatrons, welding machines, and certain types of arc furnaces.

10.2.2 Arcs with External Cathode Heating

This is a particular case of hot thermionic cathode, with the cathode heated not by the discharge current, but by an external source. The discharge is therefore *non-self-sustaining*. The required temperature is lowered by employing *activated* cathodes, as in electron tubes. An arc with external heating differs from a vacuum diode in that the gap is filled with a conducting gaseous medium. As the current increases and heats the cathode more intensively than the supply of external energy, the discharge may switch to the self-sustaining mode. Arcs of this type are employed in some low-pressure devices, and in thermionic converters of thermal energy into electric energy.

10.2.3 Arcs with Cold Cathode and Cathode Spots

In such arcs, the current flows through one or more spots that appear and disappear, and move rapidly and randomly on the cathode surface. The current density within a spot is very high, $j_C \sim 10^4$–10^7 A/cm^2. The metal at the point of short-

time localization of a spot heats up greatly and is eroded and vaporized, but the cathode as a whole (and the spot's neighborhood) remain relatively cold. Spots always form on low-melting-point metal cathodes (copper, iron, silver, liquid mercury, etc.), which would not withstand the temperature required to work in the hot thermionic cathode mode (for Cu, $T_{\text{melt}} \approx 2570\,\text{K}$). At weak currents and low pressures, however, spots appear on refractory metals (W, Mo, etc.), as well. The main mechanism of electron emission of *cathode spots* seems to be thermionic field emission.

10.2.4 Vacuum Arc

This is an arc with cathode spots, initiated between electrodes in vacuum but burning in the metal vapor produced by intense erosion and vaporization of electrodes and immediately filling the discharge gap. Vacuum arcs are used in vacuum circuit breakers for high-current electrical equipment an important area of application of arc discharges.

10.2.5 High-Pressure Arc

By high pressure we mean pressures above $p \sim 0.1$–$0.5\,\text{atm}$, at which the plasma of the positive column is typically in equilibrium. Especially frequent among arcs of this type are arcs at atmospheric pressure, including those in open air. The column of the atmospheric pressure arc is a typical and widespread example of a *dense low-temperature equilibrium plasma* sustained by electric field. The temperature is usually $T \approx 6000$–$12{,}000\,\text{K}$, although higher temperatures, up to $50{,}000\,\text{K}$, are achieved under special conditions (Sect. 10.2.8).

10.2.6 Very-High-Pressure Arc:

$p \gtrsim 10\,\text{atm}$. This mode, belonging to the group of high-pressure arcs, deserves special attention. A plasma of such high density emits so intensively that up to 80–90 % of the released Joule heat is converted into radiation in the arc column. The yield of radiation is much lower at, say, atmospheric pressure. This property found an important application: the development of (super) high-pressure lamps. In these lamps, the arc burns in xenon or mercury vapors, which have optimal radiative characteristic and high efficiency of electroc-to-light power conversion.

10.2.7 Low-Pressure Arcs

These arcs burn at $p \sim 10^{-3}$–$10^{0}\,\text{Torr}$, so that the plasma in the positive column is strongly nonequilibrium, not differing in principle from the glow discharge plasma both with respect to "temperature gap" ($T_e \gg T$) and to the degree of ionization (which is much lower than the equilibrium value). The ionization is, however, higher than in glow discharge, because arcs burn at much higher current.

10.2.8 Special Modes

This group includes highly unusual modes, such as the so-called *Gerdien* arc found in 1922. This arc burns in a water vortex that squeezes the current channel away from a narrow diaphragm through which the channel passes. As a result of water evaporation, the arc is practically burning in water vapor. The highest temperature ever observed in an arc discharge, 50,000 K, was obtained at the channel axis of an improved Gerdien arc at a current of 1.5 kA and diaphragm diameter 2.5 mm.

10.3 Arc Initiation

10.3.1 Methods of Arc Initiation

The easiest way to start an arc is to connect the electrodes to a suitable power supply capable of providing sufficiently high current, bring the electrodes into contact, and then separate them. The electrodes may become red-hot at the point of contact, partly vaporize, and produce emission, so that at the moment of separation the arc strikes in the vapor, which is usually ionized more easily than the gas. The vapor is subsequently replaced by the gas (if it is there).

To initiate a high-current arc, an auxiliary anode can be employed. It is inserted between the main electrodes so as to touch the cathode, and is rapidly removed after applying the initial voltage.

When the cloud of ionized vapor, formed at the moment of short-circuit, reaches the main anode, the arc starts burning.

It is also possible to apply a high voltage sufficient for gas breakdown through the arc gap to stationary electrodes. In this case, the power supply and the external circuit must allow the burning of the arc discharge in accordance with the general $V - i$ curve (Fig. 8.4) and the loading curve. Normally, the usual mains voltage of 220 V is adequate for starting low-pressure arcs and mercury lamps in this manner. In the latter, a high pressure builds up gradually as the mercury evaporates; the first stage is a glow discharge that grows into an arc as the cathode heats up.

10.3.2 Transition from Glow to Arc Discharge

The transition is described by the segment FG of the $V - i$ curve in Fig. 8.4. The transition is caused by cathode heating as the current gradually increases and raises the current density of the abnormal glow discharge. With refractory (thermionic) cathodes, the transition is more or less smooth. If the cathode is made of a low-melting-point metal that behaves in the arc as a cold material, the glow discharge is suddenly transformed into an arc and cathode spots appear instantaneously. This occurs at lower currents ($i \sim 0.1$–1 A) than for thermionic cathodes ($i \sim 10$ A).

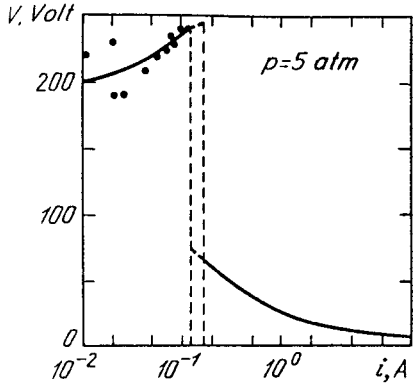

Fig. 10.1. $V - i$ characteristic of a xenon lamp, p = 5 atm., in the region of transition from glow to arc discharge [10.1]

Figure 10.1 shows the $V - i$ characteristic of the discharge in xenon lamp at $p = 5$ atm, at the transition stage [10.1]. At this high pressure, the glow discharge was stabilized by a high additional external resistance. At $i \approx 10^{-2}$–10^{-1} A, an abnormal glow discharge burns. At $i \approx 0.1$–0.2 A, it becomes unstable and is converted to an arc. The voltage at the electrodes then falls abruptly, while the current increases. In the unstable transition region, the same discharge current ($i \approx 0.2$ A) requires 250 V if the sustaining mechanism is secondary emission and multiplication of electrons in the cathode fall, but only 70 V if arc emission mechanisms are at work. The latter mechanism is more "economical", so that a spontaneous jump to arc discharge occurs; this is a clear illustration of instability manifestation (in this case, of the cathode process; see Chap. 9).

10.3.3 Short-Term Interruption of Current

Arcs with hot or cold cathodes behave quite differently when the current is interrupted. In the former case, the discharge can be restruck after a relatively long interval (up to 1 s for carbon electrodes) without the need to bring the electrodes together. In the latter case, even a very short interruption produces an irreversible effect. An arc with copper electrodes does not recover after a break of 10^{-3} s, and a mercury cathode arc, after 10^{-8} s.

10.4 Carbon Arc in Free Air

This is a classical example of the arc discharge. This mode, the first to be discovered (Sect. 1.4), is known as the voltaic arc. A moderate-current carbon arc is started by separating the initially contacting carbon electrodes, and a high-current arc is started using an auxiliary electrode (Sect. 10.3.1). This discharge was given the name "arc" because if the electrodes are arranged horizontally, the heated current channel bends upward since its central part floats owing to the Archimedean (buoyancy) force. The carbon arc at atmospheric pressure belongs to the class of high-pressure hot-cathode arcs. Figure 10.2a is a photograph of a vertically arranged arc which is axisymmetric.

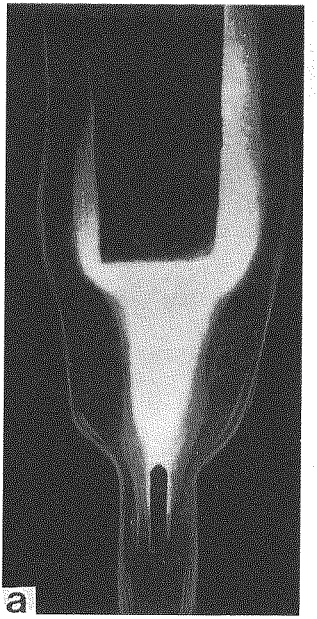

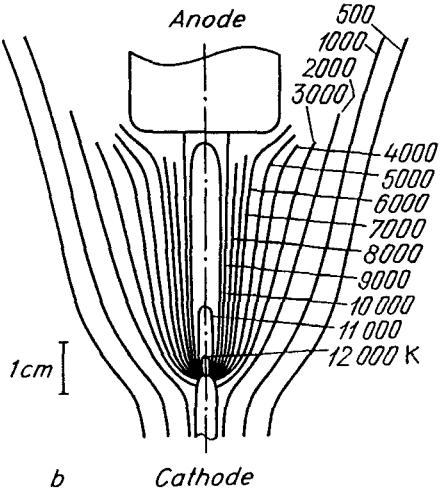

Fig. 10.2. Carbon arc in air at a current of 200 A: **(a)** a Toepler photograph, **(b)** measured temperature field [10.1]

$V - i$ characteristics of a carbon arc are shown in Fig. 10.3. The cathode fall was approximately 10 V, the anode fall about 11 V, that is, 21 V together, the rest falling across the positive column. With the separation between electrodes $L > 0.5$–1 cm, the arc burning voltage increases linearly with L, indicating a constant longitudinal potential gradient in the column. For instance, for $i = 7$ A, the field strength in a long homogeneous column is $E \approx 22$ V/cm. The field decreases with increasing current. At a certain current, the arc voltage drops to a lower level, the $V - i$ curve becomes almost horizontal, and a characteristic

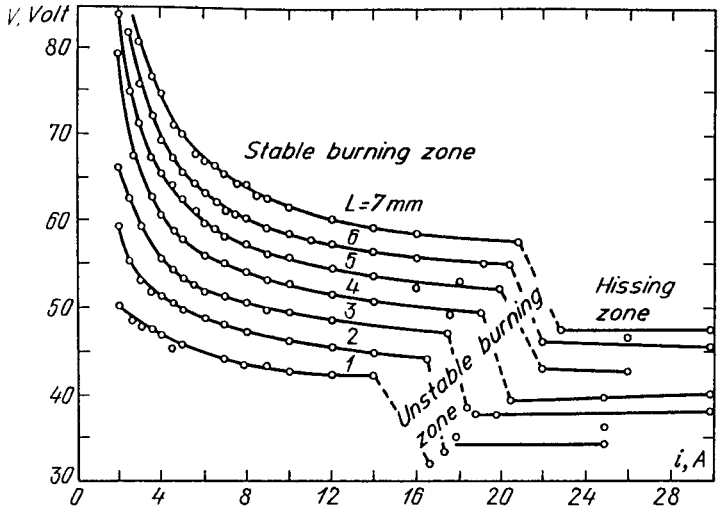

Fig. 10.3. $V-i$ characteristic of carbon arc in air. Values of L indicate the distance between electrodes [10.1]

hissing noise is heard. The sound is caused by intense vaporization of the anode in rapdily moving anode spots where the current density is high.

The plasma column in atmospheric-pressure air is in quasi-equilibrium. Figure 10.2b shows the recorded temperature distribution in the arc shown in Fig. 10.2a; $L = 4.6\,\text{cm}$, $i = 200\,\text{A}$. In the axial region, $T \approx 10,000\,\text{K}$, and at the maximum near the cathode, $T \approx 12,000\,\text{K}$. The radius of the high-temperature (hence, ionized and mostly electrically conducting) channel is about 0.5 cm; the channel slightly diverges toward the anode. The cathode temperature $T_C \approx 3500\,\text{K}$ and that of the anode, $T_A \approx 4200\,\text{K}$ (prior to "hissing"). The arc is anchored to the tip of the tapered cathode. The current density at small currents, $i \sim 1$–$10\,\text{A}$, is $j_C \approx 470\,\text{A/cm}^2$ at the cathode and $j_A \approx 65\,\text{A/cm}^2$ at the anode. As the current increases, j_C increases to $5 \times 10^3\,\text{A/cm}^2$at $i \approx 400\,\text{A}$, but further growth of current does not increase the cathode current density: the area of the cathode spot increases accordingly.

10.5 Hot Cathode Arc: Processes near the Cathode

10.5.1 Functions of the Cathode Layer

In principle, the cathode layer's functions are the same is in a glow discharge. In the absence of external heating, the cathode layer creates conditions for the *self-sustainment* of the current (in this particular case, a strong current). But this function is fulfilled in a different manner. The number of pairs of charges produced in the cathode layer of a glow discharge is such that their reproduction is ensured by the secondary emission due to the ionic flux. In the case of thermionic

emission, the ions produced in the cathode layer must supply the cathode with the energy required to maintain the proper temperature. This method of extracting electrons from the cathode by ions, not by knocking them out individually, but by heating the metal, is more efficient. Secondary emission produces only $\gamma \sim 10^{-3}$–10^{-1} electrons per ion, so that the farction of ionic current at the cathode in a glow discharge is slightly less than unity, $1/(1+\gamma)$, and that of electronic current is $\gamma/(1+\gamma) \sim 10^{-3}$–$10^{-1}$. Analysis shows that thermionic emission in a hot cathode arc provides $S \approx 0.7$–0.9 of the total current, and ions carry to the cathode $1 - S \approx 0.1$–0.3 of this current. Hence, $S/(1-S) \approx 2$–9 electrons are emitted by the cathode per ion. This high efficiency of ions can be achieved only with a high current that greatly heats the cathode.

The difference in the value of cathode fall V_C is a result of the large difference in the ratios of the electronic and ionic currents at the cathode in glow and arc discharges. Practically the entire current in the electrically neutral plasma that follows the cathode layer is carried by electrons. Several generations of electrons must be produced in the cathode layer of a glow discharge in order to raise the fraction of electronic current from $\gamma/(1+\gamma) \sim 10^{-3}$–$10^{-1}$ to unity, and this calls for a voltage of hundreds of volts, because 30 to 50 V are needed on average to produce a pair of ions in a weakly ionized gas. The fraction of electronic current in the cathode layer of an arc discharge must be raised by only $1 - S \approx 10$ to 30 %. Not even one additional generation is required here. As a result, the arc cathode fall is of the order of, or even lower than, the ionization potential. At the same time, the cathode layer is unavoidable. The ionic fraction of current in the electrically neutral plasma of the positive column is negligibly small, $\mu_+/(\mu_e + \mu_+) \sim 10^{-2}$. This weak ionic current could not heat up the cathode even together with the purely thermal energy flux. Indeed, the fraction of the current carried by the ions is enhanced in the layer from very nearly zero to 10–30 %.

The arc cathode layer serves its function mostly as the region where ions are copiously produced and where the ions acquire from the field the kinetic energy that they carry to the cathode and add to the energy from other sources, namely, the potential energy of ion neutralization and the heat flux from the plasma. This is not the only role of the layer. It also serves other purposes, all of them interrelated. The gas temperature at the cathode surface coincides with the metal temperature and is at most half that in the positive column (Fig. 10.4). Charges cannot be produced here at all if only *thermal* ionization is at work. Note that the production rate in the layer must be even higher than in the column because a strong ionic current must be generated. The effect is achieved in the cathode layer via a nonthermal mechanism of imparting energy to the emitted electrons. Furthermore, the strong electric field produced at the cathode surface reduces the work function through the Schottky effect and hence facilitates thermionic emission. Both the field and the cathode fall arise, in their turn, in response to an enhanced ion production rate in the layer and the accumulation of positive space charge owing to different removal rates of electrons and ions.

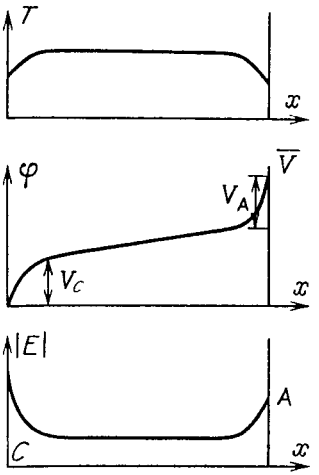

Fig. 10.4. Distributions of temperature, potential, and field in the arc from cathode to anode

10.5.2 Structure of the Cathode Layer

The main feature involved is the high current density at the cathode. A very high positive space charge is formed at the cathode. It entails a rather abrupt drop of field and potential in a very thin layer whose thickness is even less than one free path length of ions and electrons. This collisionless layer consumes a considerable fraction of the cathode potential fall, and its surface is separated from the positive column by a more extended intermediate layer of quasineutral plasma where the field is much weaker than at the cathode and where enhanced ionization of atoms by electron impact takes place. The electrons are accelerated in the collisionless layer to at least a considerable fraction of the ionization potential (Fig. 10.5). The remaining energy is gained in the region of collisions with other electrons. Here lies the main source of the production of ions that carry the current towards the cathode.

The electronic and ionic components of the total current remain unchanged, and equal to the cathode values, in the collisionless layer containing no charge sources. The fraction of the electronic current increases in the adjacent part of the cathode layer from S to $\mu_e/(\mu_e + \mu_+) \approx 1$, while the fraction of the ionic current falls from $1 - S$ to $\mu_+/(\mu_e + \mu_+) \ll 1$. Charge densities $n_e \approx n_+$ increase toward the positive column, as a result of intensive charge production. Electrons here undergo scattering collisions and some of them are returned to the cathode, forming a small *back current*. Although decelerated in the collisionless layer, these electrons partly reach the cathode. This effect resembles the electron flux from the plasma to a negatively charged probe. The magnitude of the back current is described by the same formula due to Langmuir (6.2).

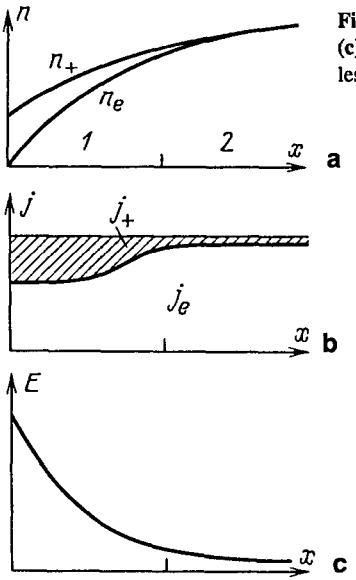

Fig. 10.5. Distributions of (**a**) charge density, (**b**) current, and (**c**) field in the cathode layer of an arc discharge. *(1)* collisionless layer; *(2)* quasineutral layer

10.5.3 Field at the Cathode

Consider the collisionless layer at the cathode. The x axis is directed from the cathode to the anode. The electronic and ionic current densities in the layer are constant and equal to

$$j_e = Sj = en_e v_e \ , \quad j_+ = (1 - S)j = en_+ v_+ \ . \tag{10.1}$$

Assume that the entire cathode potential fall V_C is concentrated across the collisionless layer. The field E_1 at the boundary with the plasma is much lower than the field E_C at the cathode boundary. The energies and velocities of charges are determined by the potential difference they fall through:

$$v_e = (2eV/m)^{1/2} \ , \quad v_+ = \left[2e(V_C - V)/M\right]^{1/2} \ . \tag{10.2}$$

We substitute (10.1, 2) into Poisson's equation

$$-\frac{d^2V}{dx^2} = 4\pi e(n_+ - n_e) = \frac{4\pi j}{\sqrt{2e}}\left[\frac{(1-S)\sqrt{M}}{\sqrt{V_C - V}} - \frac{S\sqrt{m}}{\sqrt{V}}\right] \ . \tag{10.3}$$

Remarking that $d^2V/dx^2 = (1/2)d(E^2)/dV$, integrating (10.3) once with the boundary condition $E = E_1 \approx 0$ at $V = V_C$, and determining the field at the cathode boundary where $V = 0$, we find that it has a value given by

$$E_C^2 = \frac{16\pi j}{\sqrt{2e}}\left[(1-S)\sqrt{M} - S\sqrt{m}\right]\sqrt{V_C} \ . \tag{10.4}$$

This formula was derived by ***McKeown*** in 1929.

The positive space charge due to ions helps enhance the field at the cathode. The negative charge of electrons partly compensates for this effect. However, the degree of compensation is very small for $S \approx 0.7$–0.9 which is realistic for any arc. The second term in (10.4), describing the effect of electrons, comes to at most several per cent of the first and thus can be safely dropped. In numerical form,

$$E_C = 5.7 \cdot 10^3 \, A^{1/4}(1 - S)^{1/2} V_C^{1/4} j^{1/2} , \quad h = 4V_C/3E_C , \tag{10.5}$$

where A is the atomic mass of the ion; E_C [V/cm]; V_C [V]; j [A/cm^2]; and h is the thickness of the layer under discussion. We easily find h by integrating (10.3) twice without the electron term. The situation in the collisionless part of the cathode layer is similar to the process in the vacuum diode (Sect. 6.6.1) and (10.5) corresponds to the "three-halves power" law (6.15). The role of charge emitter in this "diode" is played not by the cathode but by the plasma adjacent to the layer; as in the case of a negative probe (Sect. 6.6.2), this plasma supplies the layer with positive ions.[1]

Equalities (10.4) or (10.5), which are in fact valid for the cathode spot as well, form a unified set of equations together with other relations describing processes at the cathode. However, for purposes of evaluation, unknown values can be taken from experiments. For example, with the parameters typical for hot-cathode arcs $j = 3 \times 10^3$ A/cm^2, $S = 0.8$, $V_C = 10$ V, $A = 28$ (nitrogen) we obtain $E_C = 5.7 \times 10^5$ V/cm, $h = 2.3 \cdot 10^{-5}$ cm. By Schottky's formula (4.13), this field reduces to work function by $e\Delta\varphi = 0.27$ eV. At $T = 3000$ K, the thermionic emission rate increases by a factor of $\exp(e\Delta\varphi/kT) \approx 3$.

10.5.4 Energy Balance at the Cathode and the Fraction of Ionic Current

The cathode temperature, which is the main factor determining the thermionic emission current, and the ratio of ionic to electronic components are found from the system of equations describing the energy balance at the cathode, the charge production in the cathode layer, (10.4), etc. Calculations of this type [10.2] are highly imperfect, because the processes are complex and numerous, and the data on important parameters are incomplete. The results obtained are mostly of qualitative value. A representative estimate of one of the most interesting quantities, S, can be obtained by constructing the energy balance in a simplified manner.

Each ion carries to the cathode the kinetic energy required in the cathode fall V_C. A part of it, β_1, is transferred to the cathode upon impact; β_1 is known as

[1] The behavior shown by (10.5) is typical of currents so strong that the space-charge layer is very thin and ions move there without collisions. If the current is weak and the layer is extended, with ions in drift, then $dE/dx = 4\pi j_+/\mu_+ E$. Hence, $E_C \approx (8\pi j_+ h/\mu_+)^{1/2}$, $V_C \approx 2E_C h/3$. Instead of (10.5), we obtain $E_C = (12\pi j_+ V_C/\mu_+)^{1/3}$, and the current in a "gas-filled" diode, being space-charge limited, is given, instead of (6.15), by $j_+ \approx (9\mu_+/32\pi)V^2/h^3$, as in the cathode layer of a glow discharge [see (8.14)].

the *accommodation coefficient*. When an ion is neutralized, the energy released is equal to the ionization potential I of the resultant atom, minus the work function φ which is spent on removing the neutralizing electron from the metal. A part of it, β_2, is also transferred to the cathode. The fractions $1 - \beta_1$ and $1 - \beta_2$ of energy remain with the outgoing atom. Not much is known about the accomodation coefficients β_1 of kinetic and β_2 of potential energy but certain similarities and indirect arguments make it possible to assume that both are of order unity. With each emitted electron, the cathode loses the energy $e\varphi$ (plus a small energy $2kT_C$ carried by the emitted electron).

If we assume that the energy supplied by ions to the cathode is completely spent on electron emission, and set $\beta_1 = \beta_2 = 1$, we find [10.1]

$$j_e\varphi = j_+(V_C + I - \varphi)\ , \quad S = \frac{j_e}{j_e + j_+} = \frac{V_C + I - \varphi}{V_C + I}\ . \tag{10.6}$$

For example, for $I = 14\,\text{V}$, $V_C = 10\,\text{V}$, and $\varphi = 4\,\text{V}$, we have $S = j_e/j = 0.83$, $j_+/j = 0.17$. These are reasonable values that do not contradict other data. However, the actual energy balance has other components as well. The cathode receives from the plasma the heat conduction flux Q_T due to the temperature difference between plasma ($T \approx 6000$–$12{,}000\,\text{K}$) and cathode ($T_C \approx 3000\,\text{K}$). Another component is the radiant flux Q_{rad}. The heat entering the emitting surface of the cathode is transported into the metal by the heat conduction flux Q_H because the opposite part of the cathode body is colder (owing to cooling). Some part $Q_{\text{rad,C}}$ is radiated away by the cathode.

The dimension of Q is that of power [W]. Dividing Q by arc current i [A], we denote $q = Q/i$ [V]. The meaning of each respective q is the energy per electron charge transported by the electric current (numerically, it is energy in eV). The energy balance at the cathode, calculated per unit transported charge, is (for $\beta_1 = \beta_2 = 1$)

$$q_H = (1 - S)(V_C + I - \varphi) + q_T + q_{\text{rad}} - S\varphi - q_{\text{rad,C}}\ . \tag{10.7}$$

When all these factors are taken into account, the value of S remains of the same order of magnitude as the estimate in (10.6). Detailed calculations of the balance, involving other equations for quantities in (10.7), demonstrated that as the arc current increases, the temperature and current density at the cathode grow but the cathode fall, the field at the cathode, and the fraction of ionic current are all reduced [10.2].

Note that when the fraction of ionic current is calculated, one often evaluates energy balance not at the cathode itself, via (10.6), but in the cathode layer [10.2]. It is assumed that the entire energy gained by electrons within the cathode fall goes into ionization, that is, into the production of ions that subsequently reach the cathode. This gives

$$j_eV_C = j_+I\ , \quad S = \frac{I}{I + V_C}\ , \quad \frac{j_+}{j} = \frac{V_C}{I + V_C}\ . \tag{10.8}$$

The same numerical values that were taken to evaluate S via (10.6) now yield $S = 0.58$, $j_+/j = 0.42$. Presumably, (10.8) gave an overestimate of the value of the ionic current because, in view of exciting collisions, the production of one pair of ions consumes more energy, on the average, than one ionization potential.

10.5.5 Results of Measurements

Figure 10.6 plots the cathode fall measured by different methods (tungsten cathode, helium at $p = 1$ atm) as a function of arc current i. The calorimeter method consists in measuring calorimetrically the heat flux (power) transported by heat conduction from the cathode surface into the metal, Q_H [W]. The cathode fall V_C is obtained from this measurement and from the known current i by employing theoretical considerations concerning the energy balance at the cathode. Figure 10.6 also shows the measured ratio $q_H = Q_H/i$ known as the *voltaic equivalent of heat flux* into the cathode. It is related to V_C by the energy balance formula (10.7). In another method, one measures the decrease in voltage across electrodes when they are brought closer together. It is assumed that immediately before the moment of shorting, after which the voltage drops abruptly to a fraction of one volt (this corresponds to the contact resistance), the positive column disappears completely and the voltage equals simply the sum of the cathode and anode falls. The latter fall is measured separately and is subtracted. All methods point to a reduction in V_C as the current increases, although numerical results sometimes quantitatively disagree. It seems that the result of probe measurements is the most reliable.

Figure 10.7 shows the radial temperature distributions at the end-face current surface of a tungsten rod-shaped cathode 0.6 cm in diameter and 2.5 cm long. The temperature increases to 4000 K at the center. Note how the high-temperature current area grows as the current increases. The surface temperature is mostly measured by measuring surface brightness. The current density at the tungsten cathode is 10^3–10^4 A/cm^2. These parameters are found from the known total current and measured temperature distribution, which indicates the area occupied by the cathode current. The calculation is checked with the thermionic emission current formula. The fraction of ionic current cannot be measured directly. It is

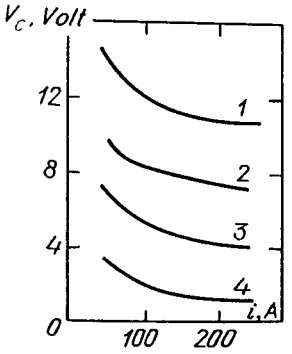

Fig. 10.6. Cathode fall of potential V_C as a function of arc current using tungsten cathode in helium atmosphere, $p = 1$ atm.. Measured by *(1)* probe, *(2)* calorimetric method, and *(3)* by bringing electrodes close together. Curve *(4)* is the voltaic equivalent of the thermal flux into the cathode, q_H [10.2]

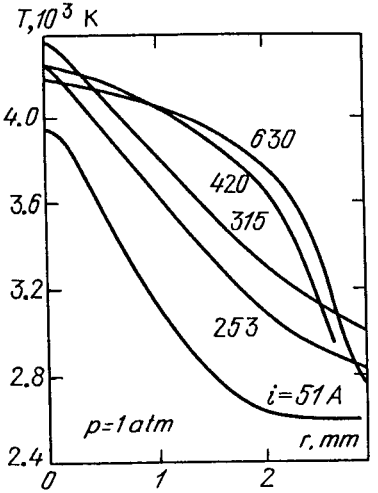

Fig. 10.7. Temperature distribution along the radius of the end-face surface of a tungsten rod cathode in argon at 1 atm. [10.2]

extracted by analyzing the energy balance and other measured quantities. The analysis gives $1 - S \approx 0.1$–0.3.

One of the problems that are very important for exploiting high-power electric arc devices is that of *erosion* of electrodes, especially cathodes. Even refractory metals undergo destruction and vaporization. The presence in the gas of small amounts of oxygen and water vapor, even in concentrations as low as 0.1 %, leads to oxidization and sharply enhances erosion. This is especially true for such widespread arc environment as air. The cathode resistance to erosion is characterized by the *specific erosion*, defined as the mass lost per coulomb of charge passed through the arc. The specific erosion depends on a number of conditions. For tungsten rod cathodes in inert gases at currents of hundreds of amperes and moderate-to-high pressures, it is of order 10^{-7} g/C. For example, this means that a cathode loses 0.1 g per hour at a current of 300 A.

10.5.6 Hollow Cathode

At low pressures, $p \lesssim 1$ Torr, cathode spots are formed even on tungsten (Sect. 10.6), with material in a spot being eroded much more strongly than in the hot cathode mode. Consequently, rod cathodes of refractory metals are used in practical devices only at high pressures. Designs based on the hollow cathode principle are used at low pressures. A *hollow cathode* in its simplest form is a segment of a tube to whose inner surface the arc is anchored, in similarity to a glow discharge (Sect. 8.5.4). Very high durability of refractory-metal cathodes has been achieved in arc devices with a gas blown through a hollow cathode, creating a specific gas environment inside it [10.2]. Such devices manifest record-low specific erosion of 10^{-9}–10^{-10} g/C.

10.6 Cathode Spots and Vacuum Arc

Highly localized current centers appear on the cathode when it is necessary to carry a considerable current, but the cathode cannot, for one reason or another, be heated as a whole to a high temperature. Such reasons may lie in low melting point of the metal (this is a typical situation), in a relatively low current that can cause emission from the cathode only when concentrated to a small area, or in low ambient pressure,. In the latter case, it is necessary to inject into the gap some number of atoms (vapor) of cathode material, otherwise there can be no ionic flux transporting energy to the cathode and the cathode emission cannot be sustained. However, a high concentration of energy is at the same time the condition for efficient vaporization of the metal. Indeed, if (roughly) $i < 1$–10 A, $p < 1$ Torr, cathode spots are formed even on refractory metals, which behave as thermionic cathodes at higher currents and pressures (as described in Sect. 10.5). In contrast to anchoring to a spot, the latter effect is known as *diffuse anchoring* of the arc to the cathode. In the case of low-melting-point metal cathodes, spots are formed at any pressure and any current.

10.6.1 Basic Experimental Facts

a) Evolution of spots. At the earliest stage of the discharge, small, fast spots moving randomly and independently of one another are formed on the cathode. Their size $r \sim 10^{-4}$–10^{-2} cm, and velocities are from 10^3 to 10^4 cm/s. They cause negligible, presumably nonthermal, erosion of the surface. It has been suggested that erosion is caused by microscopic explosions of tiny protrusions on the surface, in response to current concentration in the metal itself. The arrangement of spots changes in a time of about 10^{-4} s. Small spots merge into larger and less mobile spots moving at velocities of about 10–10^2 cm/s. The erosion in such enlarged spots is considerably more intense and is of thermal nature because it is caused by heating and vaporization of macroscopic segments of the surface at the expense of the energy injected by the ionic current originating from the vapor plasma.

b) Threshold current and spot multiplication. The current through an individual spot cannot be too low. There is a minimum, threshold current for a spot, and hence for the arc as a whole: $i_{\min} \sim 0.1$–1 A. As the current decreases to $i_{\min}$, it becomes concentrated in a single spot; if $i < i_{\min}$, the arc burns out. It was empirically found that for many nonferromagnetic materials, $i_{\min} \approx 2.5 \times 10^{-4} T_{\text{boil}} \sqrt{\lambda}$ [A], where λ [W/cmK] is the heat conduction coefficient; and T_{boil} is in degrees Kelvin [K]. The physical meaning of this relation is not yet clear; this is also the case for much in the behavior of cathode spots. On the average, the current through a single spot is from 1 A (on liquid mercury) to 300 A (on tungsten). As the discharge current increases, the number of spots grows. As a rule, the spots do not appear on fresh places, but multiply by "splitting". The spot lifetime with respect to splitting depends on current growth rate. If $di/dt \sim 10^5$–10^7 A/s, it is on the order of 10^{-5} s. Sometimes a spot may decay and vanish.

c) Current density. If the current through a spot $i \approx 10$ A and the spot radius $r \approx 10^{-3}$ cm, the current density is $j \approx i/\pi r^2 \approx 3 \times 10^6$ A/cm^2. Spot current densities reported by different authors lie in the range $j \sim 10^4$–10^7 A/cm^2, and even reach 10^8 A/cm^2 for copper. The data on j are extremely uncertain, imprecise, and contradictory. Typically, j is measured when only one spot survives, with known spot current i, but the difficulty lies in determining the spot size. When high-speed photography is used, the current spot size is identified with that of the luminous region, even though this is doubtful. The spot size may be found after switching the arc off from the erosion left on the cathode surface (autograph technique); here again, one cannot be sure that identification is unambiguous.

d) Vaporization. Cathode spots that receive the high-concentration energy flux transported by the ionic current become sources of intensitve vapor jets. Jet velocities are of the order 10^5–10^6 cm/s. The specific erosion within large spot clusters on copper reaches 10^{-4} g/C. We have already mentioned that erosion is much less intense in individual spots at the early stages of the discharge; for example, 5×10^{-7} g/C has been reported for copper.

e) Temperature and number densities of particles. The data on metal surface temperature within a spot are very contradictory. The temperature is found either by measuring brightness or by evaluating the pressure and density of vapor at the surface. The values reported for spots on mercury range from 700 to 2000 K, and on copper, from 2400 to 3700 K. The vapor density evaluated on the basis of saturation pressure is about 10^{17}–10^{19} cm^{-3} (calculations for Cu give T closer to 3700 K, and n_e closer to 10^{19} cm^{-3}). The concentration of neutrals, determined by measuring the attenuation of a probe electron beam in the vacuum arc at an iron cathode, was found to be 10^{16}–10^{17} cm^{-3}. Measurements of charged particle number density over cathode spots (by Stark broadening and by the ratio of intensities of the spectral lines of copper atoms and ions) gave $n_e \approx 5 \times 10^{17}$ cm^{-3}, which is typical of dense low-temperature plasma. Hence, the vapor density and the degree of ionization are quite high. Similar measurements lead to the value of electron temperature $T_e \approx 1$–2 eV.

f) Cathode fall. There are two ways to measure cathode fall: by probes, and by "bringing electrodes together" (Sect. 10.5.5), including the recording of the burning voltage of a short vacuum arc. It is assumed that the anode fall of a vacuum arc is small. Observations indicate that the anode fall is especially low for metals with low metastable levels. This is an argument in favor of stepwise ionization of atoms in the metal vapor. Table 10.1 lists some parameters of cathode spots of several metals. We have included either averaged values or their spread if the results of different authors are very divergent or a quantity is strongly dependent on measurement conditions. Among the multitude of data accumulated over decades of studies, the table selects, where possible, those measurement results that have been obtained since 1960.

Table 10.1. Characteristics of cathodes with cathode spots

Metal	Cu	Ag	Zn	Hg	Fe	W
Ionization potential [V]	7.68	7.54	9.36	10.39	7.83	7.98
Potential excited metastables [V]			4	4.7–4.9		
Cathode fall [V]	15–21	12–16	10–11	8–9.5; 19[a]	17–18	16–22
Boiling point [K]	3510	2436	1046	630	3045	5900
Thermal conductivity [W/cm K]	4.1	4.17	1.13	0.104	0.84	1.67
Threshold spot current [A]	1.6	1.2	0.3	0.07	1.5	1.6
Average current to a spot [A]	75–200	60–100	9	0.5–2	60–100	100–300
Current density [A/cm^2]	10^4–10^8		3×10^4	10^4–10^6	10^7	10^4–10^6
Specific erosion at a current of 100–200 A [g/C]	10^{-4}	1.3×10^{-4}				1.3×10^{-5}
Jet velocity [km/s]	15	9	3–5	1–4	9	13–30

[a] Two modes are observed: $V_C \approx 8$–9.5 V in one, and 19 V in the other

g) $V - i$ characteristic. $V - i$ characterisitcs of "metal" vacuum arcs are plotted in Fig. 10.8. In contrast to many other arcs, all these are rising characteristics. No explanation of this fact has been found. Details of experimental results (and attempts at interpreting them) can be found in [10.4–6], where bibliographies are also given.

h) Spot in a magnetic field. One curious phenomenon was noticed by *Stark* in 1903, who observed the behavior of cathode spots on the surface of liquid mercury cathodes: in a magnetic field tangential to the surface, the spot moves in the direction opposite to the magnetic force $[i \times H]$ acting on the current. No satisfactory explanation of this effect has been found, even at the qualitative level (despite numerous attempts).

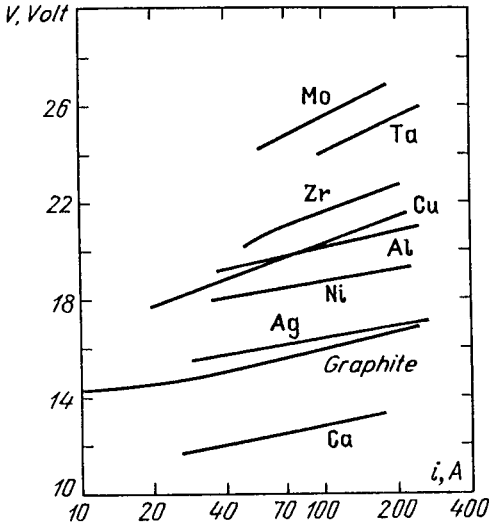

Fig. 10.8. $V - i$ curves of low-current vacuum arcs with various materials as cathodes. Electrode diameter is 1.27 cm and separation 0.5 cm [10.3]

10.6.2 The Status of the Theory of Cathode Spots

Very few phenomena in gas discharge physics have generated a comparable number of hypotheses, models, and theoretical frameworks to those devoted to cathode spots. None of them explains the totality of experimental facts. The theories offer descriptions (sometimes correct ones) of some parts of the picture but leave many a "Why?" unanswered. Why do spots split? Why do they "run"? Why do they shift in the "wrong" direction in a magnetic field? Why such tremendous current densities [about 10^8 A/cm^2, assuming these values are reliable]? And so forth. In 1968 one arc discharge researcher counted as many as 17 different – and even mutually exclusive – interpretations of cathode spot effects [10.4], and a host of new papers have been published since. This situation is definitely caused by the extreme complexity and entanglement of the picture in which solid state, surface, interfacial, plasma, electric, and thermal processes are closely intertwined.[2]

What happens in the spot area greatly resembles the picture found at a hot cathode. The spot receives the ionic current. Ions bring in the kinetic energy acquired in the cathode fall. Together with the potential energy released in neutralization, this kinetic energy goes to the heating up of the metal. This factor combines with the effect of strong field (Sect. 10.6.3) to produce emission and, on the other hand, vaporization of the metal. In a vacuum gap, vapor creates the medium that is ionized by emitted electrons accelerated in the cathode fall. This,

[2] The exceptional practical importance of cathode spot phenomena focused the attention of specialists and led to an impression that the cathode spot si a uniquely complex object. In fact, numerous complex and unexplained aspects of gas discharges are passed by simply because they seem to be of secondary importance. The situation may well change with the appearance of a practical stimulus, as happened with glow discharge instabilities (Chap. 9).

in turn, constitutes the source of ionic current. The process of evaporation from a localized heated center depends on the outflow of energy by heat conduction into adjacent metal layers, on other components of the energy balance, etc. Quite a few elements of this picture allow calculation in reasonable agreement with experiments, although theories included, until recently, a number of experimentally determined parameters.

The hydrodynamic model of a cathode spot, in which the complex of processes is reconstructed in a self-consistent form and no empirical parameters are used, has been fully developed [10.7]. It also describes cathode spots on film cathodes. Such cathodes are often used in real systems. It is not infrequent that the cathode spot which is seemingly localized on the massive cathode actually burns on the oxide coating or a coating of other containments. Inhibited heat transfer from the film to the massive cathode facilitates local heating. As the film under the spot burns out, the spot tends to jump to another area on the film, rather than to continue burning on the surface of the massive cathode. This is one of the causes of spot displacement, in addition to the jumping of the discharge from one microscopic protrusion to another after thermal destruction of the former.

10.6.3 Emission Mechanism

This is definitely a point of crucial importance. Among familiar emission mechanisms, only thermionic field emission can supply current densities $j \sim 10^6\,\mathrm{A/cm^2}$ without assuming the existence of superhigh temperatures and fields at the surface.[3] Table 4.8 shows that for $T = 3000\,\mathrm{K}$ and work function $\varphi = 4\,\mathrm{eV}$, the emission current density reaches the required order of value $10^6\,\mathrm{A/cm^2}$, even without assuming that the field near microscopic protrusions on the surface is enhanced. The survival of such tips in a well-developed spot appears to be doubtful because they would be the first to melt, splash out, and vaporize.

The spot current density j, the ionic current fraction $1 - S$, the field E at the surface, and the metal temperature T are related by a system of equations describing the emission, $j_e = Sj = F(T, E)$, the field according to (10.5), $E = C\sqrt{j_+} = C\sqrt{j(1-S)}$, and the energy balance. *Lee* [10.8] carried out in 1959 a series of computer calculations using the first two equations and fixing T, work function φ, and the constant C roughly corresponding to copper ($A = 63$, $V_C = 10\,\mathrm{V}$). These computations, which determined the possible sets of spot parameters, indicate that results not in dire contradiction with experimental data can be obtained on the basis of a thermionic field emission model together with equation (10.5) for the field. Several such sets are listed in Table 10.2. It must be remarked that the fraction of ionic current which is then required at low j and E

[3] Even before quantum mechanics had been developed, Langmuir hypothesized in 1923 that fields due to space charge may pull electrons from the cathode spot of the arc. When the quantum-mechanical field emission of electrons became known (1928; Sect. 4.6.3), McKeown further developed Langmuir's hypothesis and derived (10.4) for the field at the cathode.

Table 10.2. Parameters of arc cathode spots, consistent with current densities j_e and j_+ and with the field at the cathode E, for given T and φ [10.8]

T [K]	φ [V]	E [V/cm]	j [A/cm^2]	j_+/j
3000	4	3.3×10^7	4×10^6	0.30
3000	4	2.8×10^7	2×10^6	0.45
3000	4	0.8×10^7	1×10^5	0.83
3500	4	2.6×10^7	4×10^6	0.23
3500	4	2.3×10^7	2×10^6	0.30
3500	4	0.8×10^7	1×10^5	0.45
3000	3.5	2.5×10^7	4×10^6	0.20
3000	3.5	2.1×10^7	2×10^6	0.25
3000	3.5	0.6×10^7	1×10^5	0.45

appears to be unrealistically high. On the other hand, the cathode fall produces a strong field at the highest values of j and E (when the fraction j_+/j is realistic) only if it is concentrated in a layer of thickness $h \approx V_C/E \approx 10/3.3 \times 10^7 \approx 3 \times 10^{-7}$ cm, that is a mere of ten atomic diameters! In order to obtain 10^8 A/cm^2, we need $E \approx 1.5 \times 10^8$ V/cm, $h \approx 6 \times 10^{-8}$ cm, which is hardly imaginable (being of the order of the thickness of surface layer). On some other models and theories, see [10.4, 6]; however, the one outlined above is favored now as it seems capable of explaining $j \sim 10^6$ A/cm^2.

As shown in [10.7], this model covers copper-type materials with moderate volatility. In non-volatile materials (tungsten) or easily volatile materials (mercury), the parameters of the cathode spot in a vacuum arc cannot be explained in these terms. At 6000 K, which is required for the evaporation of tungsten (without which there would be no ions), the thermionic emission current density would be much higher than the observed values. No field is then generated at the cathode to pull electrons away. The negative space charge at the cathode cancels the strong field and limits the spot current as it does in vacuum diodes (Sect. 6.6). In contrast, thermionic emission and thermionic field emission are negligible in mercury where even the critical temperature is as low as 1753 K. Unrealistically high fields are necessary for electron field emission to be solely responsible for producing this current. As conjectured, in [10.9], no conventional cathode layer exists in a mercury arc and an *electric double layer* of thickness less than one free path length is formed close to the surface. According to this model, energy deposited in the plasma by ions accelerated in the double layer produces conditions for thermal ionization and formation of a *plasma cathode*.

10.6.4 Explosive Emission

This is a suitable place to describe this phenomenon discovered by *Mesyats* in 1966 [10.10], because it has common features with the processes in the cathode spot of vacuum arcs. Experiments demonstrated that in a pulsed breakdown of a vacuum gap with a very thin tip a sharp current rise is accompanied, after

some delay from the moment of applying the voltage, with an explosion of the tip point and an ejection of a cathode plume, that is, a blob of plasma. Similar processes take place on massive cathodes as well, but explosions occur on microscopic protrusions on the surface. These effects are studied by high-speed oscilloscopes, and by photoelectron and electron optic techniques with time resolution of 10^{-10}–10^{-9} s. On a tungsten tip with tip radius 0.2 μm and with field at the tip 1.2×10^8 V/cm, the current delay and explosion "induction" time are 1 ns. The time lag is the longer, the weaker the field and (in particular) the lower the current.

As a result of repeated application of voltage pulses about 10 ns long and with 1 ns rise time, the tip is eroded and smoothed but new microscopic tips are formed on it, with the tip field enhanced by an order of magnitude. Now the delay of breakdown and of current by 1 ns takes place at the macroscopic field of 10^7 V/cm at the tip. If the cathode is massive, the field at microscopic tips is enhanced by a hundredfold and more, so that the same effect is obtained at a macroscopic field of 10^6 V/cm. The plasma blob expands in all directions at a velocity of about 2×10^6 cm/s, consuming about $(2–3)\times10^{-3}$ g/s. The current density from a tip surrounded with plasma reaches 10^8 to 10^9 A/cm^2, the current being 10^2 to 10^3 A from an area of about 10^{-6} cm^2.

The metal explodes because a large amount of Joule heat is released at the end of the (micro) tip by the current of field emission which transforms to thermionic field emission as the tip heats up. The fact that these currents are indeed high has been established experimentally. Thus it was possible to obtain, without tip destruction (i.e., only at the expense of field emission), currents up to 4×10^9 A/cm^2 with voltage pulses 5 ns long, on a tip of 0.1 μm radius and 10° angle at the open of the cone. When electrons are ejected from the surface, they are replaced by new ones from inside the metal, so that a current this enormous density passes through the metal at the emitting surface. It is this current that heats the tip to the explosive vaporization of microscopic protrusions; the delay is the time necessary to accumulate the required energy.

It is interesting to identify the mechanism of emission at that stage after explosion during which current is usually sharply enhanced. Analysis shows that the number of electrons transported in the current pulse is grater than the number of atoms in the plasma blob by a factor of 10–10^3. Therefore, the ionization of the vaporized material is not crucial. Presumably, the processes are similar to what occurs in the cathode layer of the arc: the plasma plume is polarized, positive space charge is formed at the metal surface, the field is further enhanced, and even more intense thermionic field emission develops, as in the cathode spot of vacuum arc. The effect of explosive emission is exploited in devices for generating high-power nanosecond electric pulses and electron beams [10.10]. Equipment has already been developed in which a power of the order of 10^{13} W was achieved.

10.7 Anode Region

Processes at the anode are also complex and very diverse. As on the cathode, the arc may be anchored to the anode in two ways.

a) Diffuse anchoring. In this mode, the current is spread over a relatively large area of the anode, at a density $j \sim 10^2$ A/cm^2. Material erosion is negligible in this mode because energy flux densities at the surface are not very high.

b) Anode spots. A spot is formed when the anode is small and the growing current is forced to occupy its edges, "awkward" areas, lateral patches, etc. At a certain current the discharge is destabilized and contracts at the anode surface. Current density in the spot reaches $j \sim 10^4$–10^5 A/cm^2. As a rule, the number of spots increases with increasing arc current and pressure. Sometimes many spots are formed, arranged in symmetric regular patterns. The spots may move, also following regular trajectories such as concentric circles; anode spots are very bright and eject vapor jets.

10.7.1 Potential Fall

a) Space-charge layer. The anode fall is composed of two parts. One part reflects the formation of a negative space-charge layer at the very anode surface because the anode repels positive ions towards the cathode. This component of the anode fall arises to compensate for the absence of ionic current in the neighborhood of the anode, via an increased degree of ionization of gas (vapor) atoms or a corresponding slight increase in electronic current. Its magnitude is of the order of ionization or excitation potential for vapor or gas atoms. This value of anode fall may prove sufficient in the case of diffuse anchoring. The anode fall may then be very small or even negative, 1 to 3 V. This situation is observed when the anode surface is large, a dense highly ionized plasma is adjacent to it, and there is no need to supply additional energy for sustaining the electron current to the anode.

b) Geometric fall. If the anode surface area is small, less than the cross section of the positive column, or if the arc is strongly contracted on the anode, the current channel must undergo compression from the column to the anode. The current is carried almost entirely by electrons. The total current $i \approx n_e \mu_e E S_{ch}$, where S_{ch} is the channel cross section, can be conserved in the course of channel contraction if the electron density or the drift velocity (i.e., field), or both these quantities simultaneously, increase. Additional field, i.e., additional voltage, is needed to produce additional electrons and thus compensate for recombination enhanced by increased n_e, and to enhance drift. This is how the second component of potential fall appears in the anode region. Its origin is rather geometric, not connected with the formation of space charge at the electrode; strictly speaking, it should not have been added to the anode fall although the two components are sometimes added together in the literature (in fact, they cannot always be separated experimentally, which is the case in glow discharges).

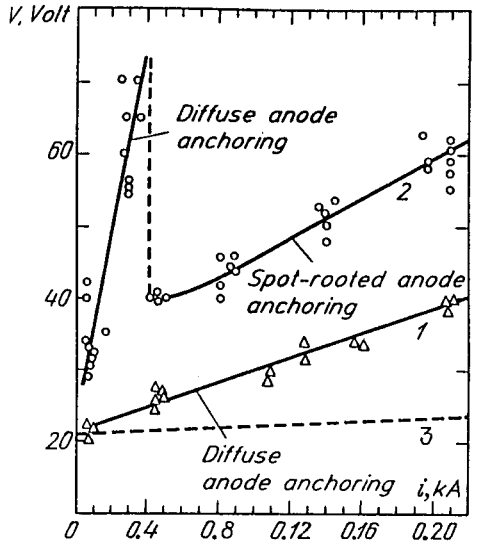

Fig. 10.9. $V - i$ characteristics of vacuum arcs with large- and small-area anode (*lower* and *upper* curves, respectively). Dashed line shows the cathode fall [10.11].

c) Effect of anchoring on $V - i$ characteristic. Figure 10.9 plots $V - i$ characteristics of vacuum arcs with large and small cathodes. A large anode results in duffise anchoring, and the anode fall is very small at low currents. The arc voltage is concentrated almost entirely in the cathode layer. In fact, subtraction of this fall (dashed line) from the total voltage gives the anode fall. As the current increases, the anode fall gradually rises. If the anode is small, the anode component of voltage grows sharply as the current increases, but then homogeneity collapses and the anode spot is formed. The transition is accompanied with an abrupt drop in voltage as a result of reduction in anode fall. Spot anchoring is more economical (in the sense of lowering the required voltage) than diffuse anchoring.

10.7.2 Carbon Arc Anode

The anchoring of carbon arc in air is diffuse up to a certain current limit ($V - i$ curve in Fig. 10.3), $j \approx 40\,\text{A/cm}^2$; the total anode fall is 36 V, of which 16 V is the "geometric" component and20 V falls in the region of negative space charge. The anode spot appears at $i \approx 15$–$20\,\text{A}$, with $j \approx 5 \times 10^4\,\text{A/cm}^2$; the arc begins to hiss (Sect. 10.3). The anode fall is then reduced by about 10 V. The spot moves at a velocity 300 m/s. As current increases further, a jet of hot vapor is ejected from the spot. The spot temperature is 4200 K. If the carbon anode contains admixture of salts or oxides of cerium or other rare earth elements, a deep very bright crater is formed at currents about 100 A, ejecting a plume of flame. The crater surface brightness corresponds to that of the Sun, emitting up to $6\,\text{kW/cm}^2$. Up to 70 % of the power from not too long arcs is emitted by the anode. This characteristic is employed in illumiination engineering (in searchlights). The anode fall at metal anodes in air reaches 1.5 to 2 times the ionization potential of the vapor atoms.

10.7.3 Energy Balance

Energy is released in that area of the anode where the current flows. It is composed of kinetic energy that electrons acquire in the anode fall and of the binding potential energy released when electrons neutralize the positive charge of metal ions. This component is equal to the work function. All in all, it comes to about 10 eV per electron of the current. Hence, the energy flux density in a spot at $j \sim 10^4$ A/cm^2 is $10^4 \times 10 = 10^5$ W/cm^2. The anode spot temperature in vacuum metal arcs is $T \approx 2700$–3300 K.

10.8 Low-Pressure Arc with Externally Heated Cathode

Discharges of this type are used in gas-filled rectifier diodes, in thyratrons etc. As a rule, oxide cathodes are employed. Gas-filled diodes are filled with argon or a mixture of Xe and Kr at a pressure of about 1 Torr (rectifier diodes with mercury vapor were also produced some time ago). The arc voltage is 10 to 20 V, the current is $\sim$ 1 A. A considerable part of the voltage is the cathode fall. The anode fall is 2–3 V. The potential across the positive column (which is not really a "column" because the discharge vessel is wide) is small.

10.8.1 The Purpose of Gas Filling

Let us compare the arc using an externally heated cathode, sustained between plane electrodes, with a similar device completely devoid of gas. This is the *vacuum diode* discussed in Sect. 6.6.1 for which the three-halves power law (6.15) is valid. Assume that the emission current of the cathode is $j_{em} = 0.1$ A/cm^2. Owing to the limiting effect of space charge, the current j of the same order of magnitude could be obtained with an interelectrode gap of 1 cm if a voltage $V = 1200$ V were applied to the electrodes.

If the diode is gas-filled, the gas breaks down and turns into plasma. In inert gases and with large transverse dimensions of the vessel, charge loss of the plasma is small and $E/p \approx 0.3$ V/cm Torr is sufficient for sustaining the electrically neutral positive column. If $p = 1$ Torr and $L = 3$ cm, the voltage across the plasma decreases by only 1 V. The anode potential, minus this and also minus a small anode fall, is carried quite well by the conducting plasma to the cathode. Most of the voltage is concentrated across the cathode layer, or rather, across its collisionless part at the metal surface, which is equal to, or shorter than, the free path length of charged particles. If we apply the same vacuum diode formula (6.15) to the "evacuated" collisionless layer $h = 0.05$ cm thick, we find that a mere 18 V are needed to carry the current $j = 0.1$ A/cm^2, instead of 1200 V.

The effect of gas filling consists in the compensation of the negative space charge of electrons in most of the diode space by ions that are copiously produced in the process of ionization of the gas by electrons. As a result, the passage of electrons emitted from the cathode on their way to the anode is facilitated.

10.8.2 Cathode Layer as a Vacuum Gap with Bipolar Current Limited by Space Charge

The function of cathode fall in a non-self-sustaining arc is very different from that in ordinary arcs. Here the cathode need not be heated up by ionic current, thereby sustaining the cathode emission. This function is served by the heating power source. What is left to the cathode layer is the acceleration of thermal electrons so that they sustain the necessary degree of ionization in the plasma. The losses in plasma being rather low, a relatively low ionization rate is sufficient. As a result, the cathode fall is of the order of the ionization or excitation potential (if ionization is stepwise), or even lower (Sect. 10.8.3; this is the so-called *low-voltage* arc). As for the thickness of the collisionless layer in the cathode fall, it grows to a value corresponding to the current dictated by the entire circuit. This current must be transported through the layer containing the space charge.

The process in the collisionless layer of a non-self-sustaining arc differs from those both in an ordinary diode and in the collisionless layer of self-sustaining arcs. In an ordinary diode, the cathode is hot but no ionic current flows. The space charge is negative; the field is practically zero at the cathode but sufficiently large at the anode (Sect. 6.6.1). In the layer of a self-sustaining arc, the ionic current from the plasma (where the field is practically absent) is weaker than the current from the cathode but not weak enough for the space charge to turn negative. The charge is positive so that the field at the cathode is very intense. This situation corresponds to the function of the layer: indeed, it is necessary to ensure strong emission and pull out all the emitted electrons. This fact is reflected in McKeown's equation (10.5).

In a *non-self-sustaining arc,* just as in a self-sustaining one, there is no field on the side of the well-conducting plasma. The plasma sends ionic current in the direction of the cathode. However, this current must not be too strong, because the cathode does not require any additional stimulation from the discharge (as long as the discharge current j is less than the emission current j_{em} produced by heating). Quite the opposite, the emission current must be limited by space charge. As a result, the space charge at the cathode is negative and the field is nearly zero, as it is in a diode with a externally heated cathode. The field thus vanishes at both ends of the layer. Hence, the magnitude of the field must reach a maximum somewhere in the middle and the space charge must reverse sign. This behavior is shown in Fig. 10.10.

The field distribution in the cathode layer is described by (10.1–3). After a single integration under the condition $E = 0$ at the plasma boundary of the layer, they yield relation (10.4) for the field at the cathode. In the case under consideration, the field is weak. Assuming $E_C = 0$ in (10.4), we find the ionic-to-electronic current ratio necessary for this:

$$j_+/j_e = (1 - S)/S = \sqrt{m/M} \approx 3 \times 10^{-3} - 10^{-2} . \qquad (10.9)$$

If the ionic current were to increase substantially in comparison with this estimate, a positive space charge would arise and a field would appear at the

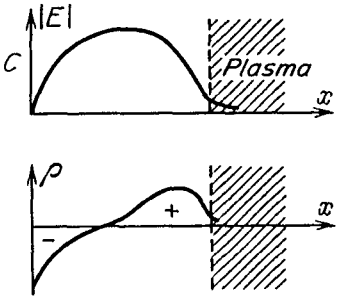

Fig. 10.10. Field (*top*) and space-charge (*bottom*) distributions in the cathode layer of an arc with auxiliary cathode heating

cathode. This indeed occurs when the discharge current exceeds the emission current and a transition to the self-sustaining arc begins. Experiments show the ionic current in a non-self-sustaining arc to be greater by a factor of 2 to 3 than that predicted by (10.9); nevertheless, its contribution to the total current is merely about one per cent.[4] At the same time, the presence of ions affects the magnitude of the space-charge-limited current to a much greater degree. Slowly moving ions considerably neutralize the negative space charge of electrons and thereby facilitate the motion of electrons from the cathode to the layer-plasma boundary.

Let us perform the appropriate calculation. We integrate (10.3) once, as we did in Sect. 10.5.3, apply the boundary condition at the cathode $E(0) = 0$, and make use of (10.9). We find

$$\frac{dV}{dx} = \left\{ 16\pi j \sqrt{\frac{m}{2e}} \left[\sqrt{V_C - V} + \sqrt{V} - \sqrt{V_C} \right] \right\}^{1/2} . \tag{10.10}$$

The integration of (10.10) reduces to a quadrature. We assign the result to the anode boundary of the layer $x = h$, where $V = V_C$, and solve the obtained relation for current:

$$j = k \frac{1}{9\pi} \sqrt{\frac{2e}{m}} \frac{V_C^{3/2}}{h^2} , \quad k = \frac{9}{16} \int_0^1 \frac{dz}{(\sqrt{1-z} + \sqrt{z} - 1)^{1/2}} = 1.86 . \tag{10.11}$$

The current, which here is *bipolar*, in contrast to the *unipolar* current in the diode (carried by charges of the same sign), is greater by a factor of 1.86 than implied by the Child-Langmuir law (6.15). This is a manifestation of the neutralizing effect of ions.

[4] The result (10.9) is illustrative in another respect as well. It gives an idea of the lower limit of the number of ionizations that an electron must perform when entering plasma from the cathode fall layer. Were it not for the ion flux to walls and other losses, each electron would have to perform only $\sqrt{m/M} \sim 10^{-2}$ acts of ion production.

10.8.3 Experiment

The voltage and layer thickness of the cathode fall were measured in experiments with arc discharges in argon at $p = 0.05$ Torr. the oxide cathode had an active surface of $2.9\,\text{cm}^2$. The voltage remained constant, $V \approx 13\,\text{V}$, in the current inteval from $i = 1\,\text{A}$ to $i = 4\,\text{A}$, and the thickness of the cathode fall layer decreased in this interval from $h = 0.031$ to $0.012\,\text{cm}$. Formula (10.11) (for $j = 0.35\text{–}1.4\,\text{A/cm}^2$) gives in this current range $h = 0.025 - 0.012\,\text{cm}$, in good agreement with experimental data [10.6]. Figure 10.11 shows $V - i$ curves of an arc in argon at a higher pressure. The current is passed between an oxidized filament cathode and a plane nickel anode. The $V - i$ curve is again horizontal in the interval $i \approx 0.5\text{–}2.5\,\text{A}$, but the voltage is 7 to 8 V lower than the argon excitation potential (low-voltage arc). It is typical for non-self-sustaining arcs that the voltage decreases as the pressure increases in a certain interval. The constancy of V points to a decrease in the layer thickness h as the current increases.

All experiments show that if the arc current is not too small, the arc voltage remains unchanged as long as the discharge current does not exceed the emissin current supplied by cathode heating. A rise of the $V - i$ curve begins when $i > i_{em}$. This rise in V is caused by the need to produce additional emission from the cathode. Therefore, the horizontal $V - i$ segment that is typically employed in gas-filled diodes stretches the further on the current axis, the stronger the cathode heating.

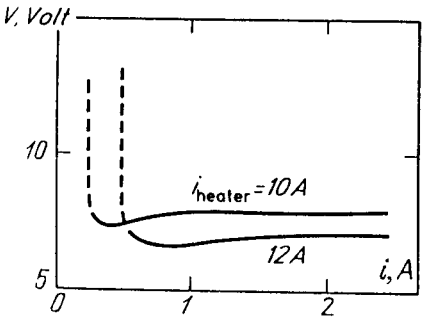

Fig. 10.11. $V - i$ characteristic of an arc with auxiliary cathode heating in a spherical vessel of 5 cm radius in argon at a presure of several Torr. Electrode spacing was 1 cm. The *upper* curve represents lower heating current and lower cathode temperature [10.12]

10.9 Positive Column of High-Pressure Arc (Experimental Data)

10.9.1 Stabilization

Considerable power is released in the arc column. For example, in air at $p = 1$ atm. and $i = 10\,\text{A}$, the field is $E = 20\,\text{V/cm}$. Hence, the power released per cm of arc length is $W = Ei = 200\,\text{W/cm}$. For the process to become steady state, this energy must be transported away from the discharge volume. The mechanism responsible for transporting the Joule heat from the current channel is heat conduction (and

radiation, at very high pressure). The subsequent fate of the heat flux depends on the arc design. If the arc is enclosed in a gas-filled tube (this is typical for research systems), the heat goes into walls that have to be cooled to prevent their destruction. Quite often (in experiments and applications) the arc column is cooled by a stream of cold gas (sometimes even liquid). A vortex flow is especially efficient because it drives the hot gas safely away from the walls. If an arc burns in a free atmosphere, its heat dissipates in the ambient atmosphere via convective flows. If the arc is short, the energy mostly goes into the electrodes which may be specially cooled. In all these approaches to realizing a steady-state burning, one speaks of an arc *stabilized* by walls, or fluid flow, or electrodes.

10.9.2 Degree of Equilibrium of Plasma

This depends on the gas, the pressure, and the current. At $p \lesssim 0.1$ atm. and $i \sim 1$ A, the plasma is invariably not in equilibrium. The plasma of air, other molecular gases, and metal vapor at $p \gtrsim 1$ atm. are in equilibrium at practically any current. The equilibration is caused by intensive energy exchange between electrons and molecules through excitation of vibrations and rotations, and by large elastic scattering cross sections of electrons in metal vapor. In Hg vapor, equilibrium sets in at $p \gtrsim 0.1$ atm. The temperature separation is greater in inert gases because the scattering cross sections of electrons by atoms are relatively small. The separation is eliminated only at high currents since the electron-ion interaction becomes strong and the degree of ionization is high. Thus in argon at $p = 1$ atm., the electron and gas temperatures are found to coincide ($T_e \approx T \approx 8000$ K) only when $i > 10$ A, so that $n_e > 3 \times 10^{15}$ cm^{-3}. If the currents are smaller, T is approximately one half of T_e (Fig. 10.12). The equilibrium in He is even more difficult to achieve: a considerable temperature

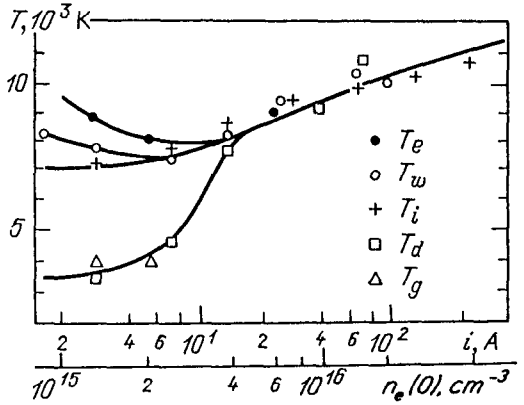

Fig. 10.12. Temperature separation in the positive arc column in argon, or Ar with an admixture of H_2 at $p = 1$ atm. as a function of current density or electron density. T_e is the electron temperature, T_w corresponds to the population of the upper levels, the ion temperature T_i is related to n_e by the Saha formula, T_g is the gas temperature, and T_d corresponds to the population of the lower levels [10.6]

gap is observed at $p = 1$ atm., from small currents up to $i \sim 100$ A ($T_e \approx 9000$–10,000 K, $T \approx 4000$–5000 K). The separation vanishes only at $i \approx 200$ A, when $n_e \approx 5 \times 10^{16}\,\mathrm{cm}^{-3}$ ($T_e \approx T \approx 10,000$ K).

10.9.3 Radial Temperature and Density Distributions of Electrons

Both of these quantities reach a maximum on the column axis and fall off towards the walls. But since equilibrium ionization is a very steep function of temperature, $n_e \propto \exp(-I/2kT)$, the electron density falls off much more quickly away from the axis than the temperature does (T falls more or less uniformly from $T_{max} \sim 10,000$ K on the axis to $T_w \sim 1000$ K at the walls if they are well cooled). The intensity of light emission behaves as n_e. As a result, the conducting, very bright arc column is a relatively thin channel on the axis. This geometry is illustrated in Figs. 10.13, 14. Note that the steepness of the falloff of $n_e(r)$ is masked by the logarithmic scale chosen for n_e in the figure.

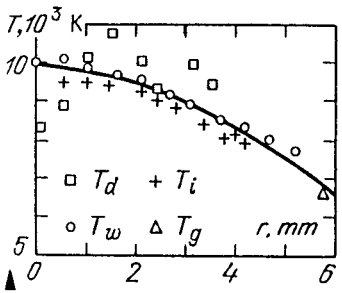

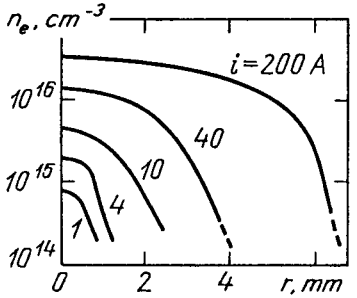

Fig. 10.13. Temperature distribution along the radius of the arc column in Ar + 5 % H_2 at $p = 1$ atm., $i = 50$ A, under nearly equilibrium conditions when all temperatures become equal. Symbols as for Fig. 10.12 [10.6]

Fig. 10.14. Radial distribution of n_e in the arc column in Ar + 5 % H_2 [10.6]

10.9.4 $V - i$ Characteristics

The field in the column is found by changing the interelectrode gap L at a constant current. If $L > 0.5$–1 cm, the voltage is a linear function of L so that $E = dV/dL \approx$ const. A long column is therefore longitudinally homogeneous. If the pressure is increased at a fixed current, the field is enhanced (Fig. 10.15). The enhancement is caused by increased radiative losses and, possibly, by a certain increase in heat transfer from plasma to the walls, dictating enhanced power per unit length, $W = Ei$. At equal currents, a stronger field is required to sustain the plasma in a tube than in an arc burning in free atmosphere, because the transfer is more intense and more power is needed (Fig. 10.16). The field is higher in hydrogen than in other gases owing to its greater thermal conductivity and to more intensive heat transfer from the column. To supplement Figs. 10.13, 14, Fig. 10.17 gives the $V - i$ characteristic of the same mixture.

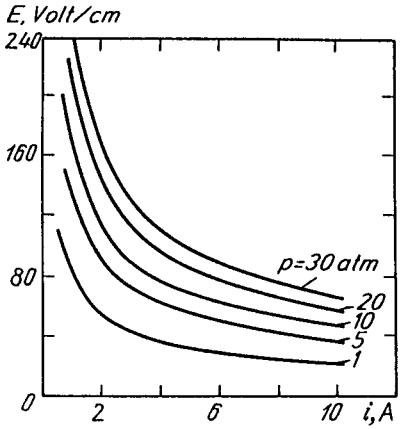

Fig. 10.15. $V - i$ characteristics of positive arc columns in air at various values of pressure [10.6]

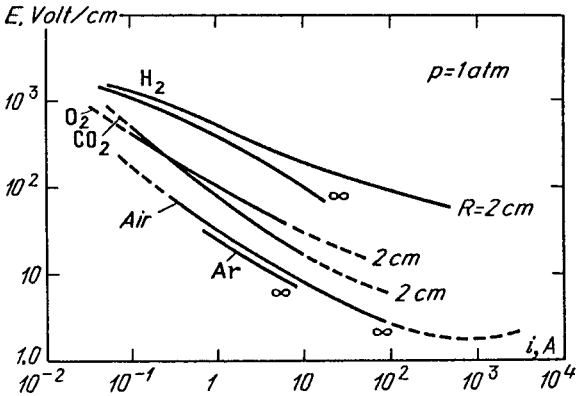

Fig. 10.16. $V - i$ characteristics of positive arc columns in various gases at atmospheric pressure in tubes of radius $R = 2$ cm, and in free gas ("$R = \infty$") [10.12]

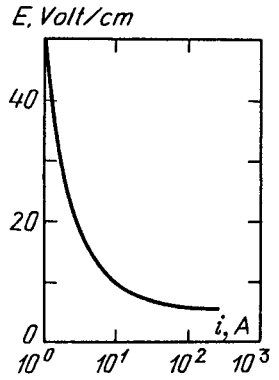

Fig. 10.17. $V - i$ curve of the positive column in Ar + 5 % H_2 [10.6]

10.9.5 Radiation of the Column

The emissivitiy and luminous flux of the column depend on the gas, its pressure, and current. To a certain approximation, they are proportional to n_e^2. In nitrogen and air at $p = 1$ atm., radiative losses make up from one to several percent of the power input. In argon at 1 atm., the losses become appreciable (greater than 15 %) at power $W > 150$ W/cm. Among a number of gases, mercury vapor has exceptionally high radiant properties. An experimental analysis of the power balance in a mercury arc in a tube of 4.1 cm internal diameter and 50 cm length at $p = 0.88$ atm., $i = 6$ A, $E = 5.8$ V/cm, has demonstrated that out of the power $W = 35$ W/cm, 10 W/cm are transported by heat conduction into walls, 18 W/cm are radiated away, and the remaining 7 W/cm appear to be transported out of the plasma in the resonance lines of Hg at $\lambda = 1850$ and 2537 Å and absorbed in the quartz walls [10.6]. In fact, the 10 W/cm transported by heat conduction from the tube filled with mercury vapor at high pressure was found to be independent of tube diameter and vapor pressure.

The radiation from the arc column is especially intense at very high pressure $p \gtrsim 10$ atm. (of course, at sufficiently high power levels), particularly in Hg, Xe, and Kr. This feature is exploited in mercury and xenon lamps. Here are empirical formulas for the radiative power of the arc column in a number of gases [10.6].

Hg: $p \gtrsim 1$ atm.,	W_{rad}[W/cm] $= 0.72\{W$[W/cm] $- 10\}$
Xe: $p = 12$ atm.,	$W_{rad} = 0.88(W - 24)$, $W > 35$
Kr: $p = 12$ atm.,	$W_{rad} = 0.72(W - 42)$, $W > 70$
Ar: $p = 1$ atm.,	$W_{rad} = 0.52(W - 95)$, $W > 150$.

10.10 Plasma Temperature and $V - i$ Characteristic of High-Pressure Arc Columns

Dense equilibrium low-temperature plasmas attract the attention of physicists and engineers probably even more than *weakly ionized inequilibrium plasma* does. They are in laboratories and exploited in experimental and industrial equipment. nowadays it is possible to generate such plasma in fields of any frequency range (Chap. 11) but the *arc plasma generation* remains the simplest, easiest, and most widespread technique. The prime characteristic of an equlibrium plasma is its *temperature*, and the problem is to understand what factors determine it, how it is related to the electrical parameters of the discharge (electric *current* and *power*), and how the $V - i$ curve of the column reflects these relations.

10.10.1 Thermal Ionization

In some respects, a description of the state of an equilibrium plasma, and of its energy balance that determines the field necessary to sustain it in a steady-state manner, is simpler than in the case of the nonequilibrium plasma of glow

discharge. There is no need to go into details of complex mechanisms and kinetics of production and removal of charges. The electric conductivity σ of the plasma is uniquely determined by its temperature and pressure (Fig. 10.18). As a rule, the pressure is known simply as an experimental parameter.

The very process of ionization differs from that which takes place in weakly ionized nonequilibrium plasmas. Molecules are ionized in the latter case by electrons that have obtained the required energy directly from the field. In thermal ionization, the effect of the field is as if "depersonalized". The field pumps energy into the electron gas as a whole. Electrons are thermalized through collisions with one another and through subsequent maxwellization of their distribution. The gas is ionized by those electrons that acquired sufficient energy not from the field but in the exchange with other particles. *Thermal ionization* proceeds quite independently of the way by which energy flows into plasma.

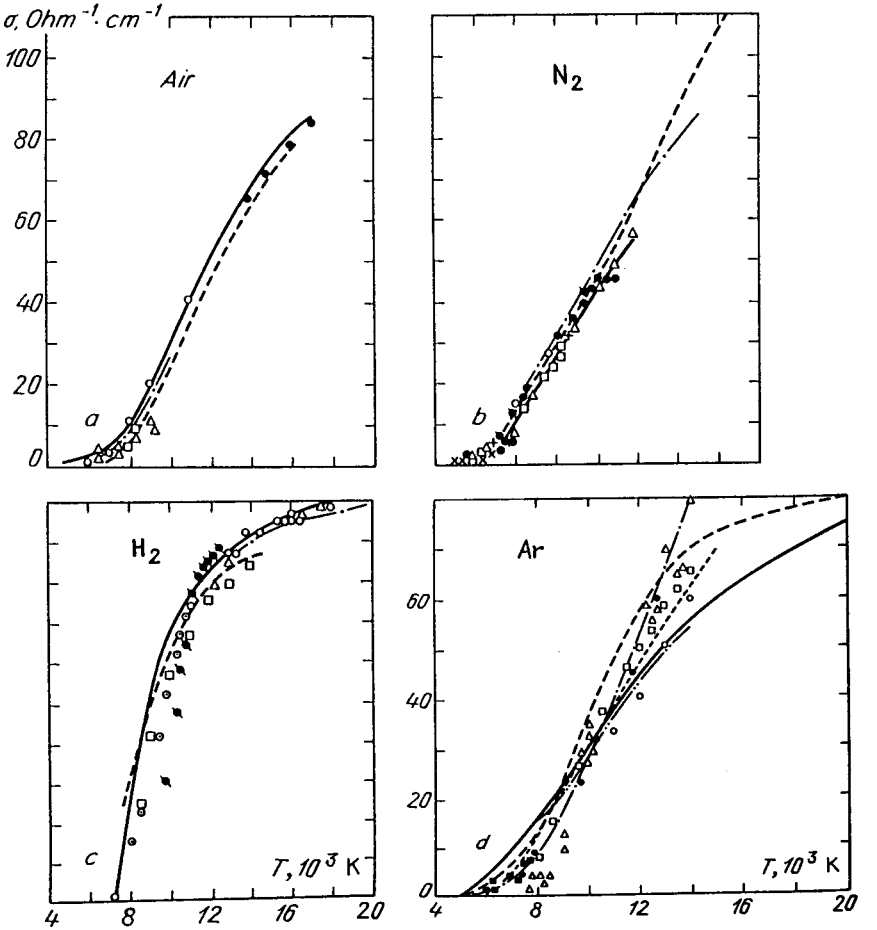

Fig. 10.18. Electrical conductivity of equilibrium plasmas in air, N_2, H_2, and Ar, at p = 1 atm.. Symbols are measurements of various authors [10.13]; solid curves: calculations of [10.14]

10.10.2 Equations of Equilibrium Plasma Columns

Consider a long cylindrical plasma column in a longitudinal field E. Let the arc burn steadily in a nonmoving gas enclosed in an externally cooled tube of radius R. Such conditions are quite frequent in discharge apparatus; actually, the model gives a good idea of the state in the conducting channel, even if the arc burns in free atmosphere or in a gas flow, because the temperature on the discharge axis is not very sensitive to external conditions. We will be interested here in moderately high pressures, say, atmospheric pressure, and moderately high currents, so that the plasma temperature does not exceed 11,000–12,000 K. In such cases the radiative losses are usually much lower than the conductive transport of heat from the column and can be neglected.

The electric field in a column which is homogeneous over its length is constant in cross section because curl $\boldsymbol{E} = 0$. The radial distributions of conductivity σ, current density $j = \sigma E$, and Joule heat sources $w = jE = \sigma E^2$ [W/cm^3] are determined only by temperature distribution, via $\sigma(T)$. The energy balance in the plasma is described by the equation

$$-\frac{1}{r}\frac{d}{dr}rJ + \sigma(T)E^2 = 0\,, \quad J = -\lambda\frac{dT}{dr}\,, \tag{10.12}$$

where λ is the thermal conductivity (Figs. 10.19, 20).

The boundary conditions to this equation are: at $r = R$, $T = T_w$, where T_w is the wall temperature; for reasons of symmetry, $dT/dr = 0$ at $r = 0$. The

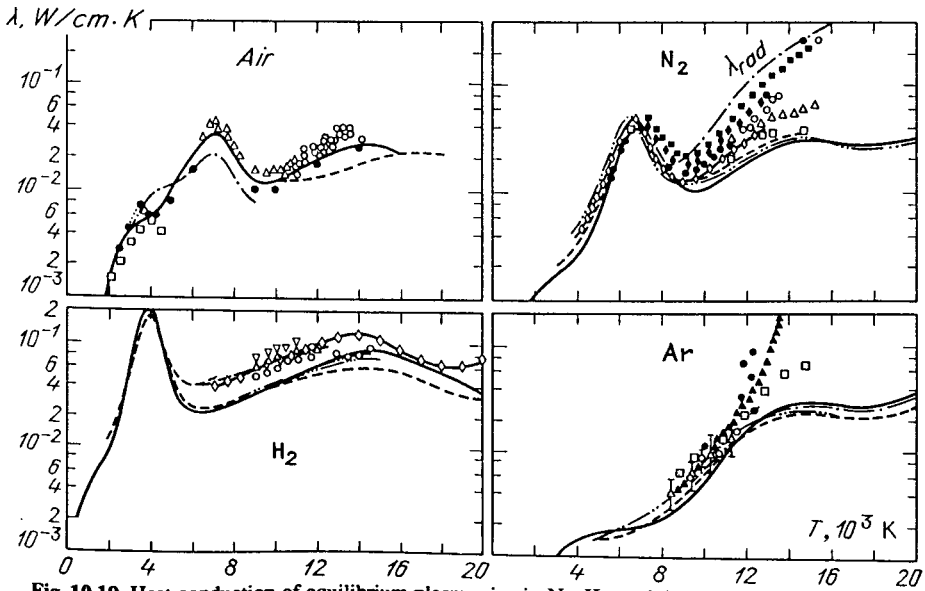

Fig. 10.19. Heat conduction of equilibrium plasmas in air, N_2, H_2, and Ar at $p = 1$ atm.. Symbols are measurements of various authors [10.13]; solid curves: calculations of [10.14]; λ_{rad} is the radiative thermal conductivity

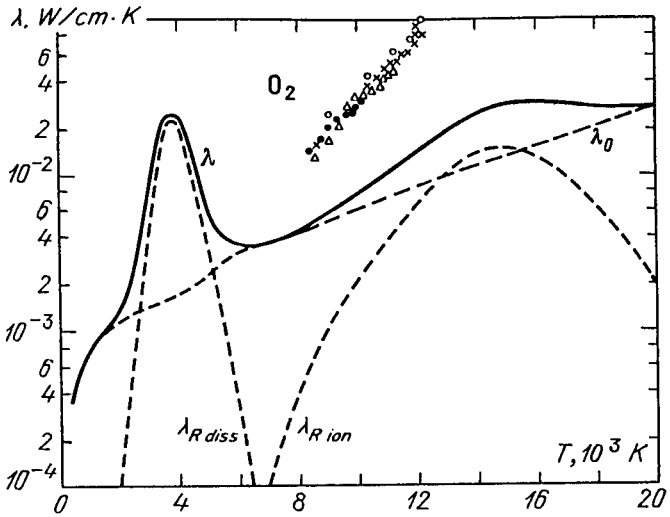

Fig. 10.20. Components of the overall thermal conductivity λ of oxygen at $p = 1$ atm.. λ_0 corresponds to ordinary transport; $\lambda_{R,dis}$ and $\lambda_{R,ion}$ are reactive components connected with the transport of dissociation and ionization energy (e.g., atoms arrive at a cold spot from a hot one and recombine, so that the potential energy of dissociation acquired in the hot spot is deposited at the cold one). Curves are from calculations of [10.14]; dots represent measurements of a number of authors [10.13]

temperature of a conducting plasma is much higher than T_w, so that we can safely assume $T_w = 0$. The discharge current is

$$i = E \int_0^R \sigma 2\pi r \, dr \, . \tag{10.13}$$

The current is controlled experimentally and thus is a prescribed parameter. The field is found by solving the problem as formulated, the problem being well defined if the material characteristics $\sigma(T)$ and $\lambda(T)$ are known. This gives us the $E(i)$ curve of the column. If we introduce the heat flux potential $\Theta = \int_0^T \lambda \, dT$ (Fig. 10.21) it becomes sufficient to work with a single material function, $\sigma(\Theta)$, instead of two. Equation (10.12) is known as the Elenbaas-Heller equation (obtained in 1934).

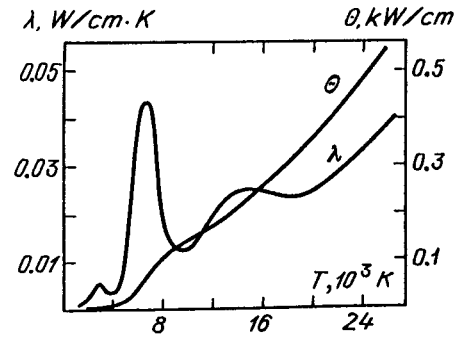

Fig. 10.21. Thermal conductivity λ and heat flux potential Θ in air at 1 atm

10.10.3 The Channel Model and the Principle of Minimum Power

The nonlinear nature of the real function $\sigma(\Theta)$ does not allow the general analytic solution of (10.12). Various formal methods based on linearizing $\sigma(\Theta)$ and on splitting the integration domain into subdomains, and various numerical methods have been developed since the 1930s when the arc column problem was first formulated [10.13]. In order to understand better the nature of the relationships, we turn to the *arc channel model* suggested by *Steenbeck* in 1932, which gives an essentially correct picture.

The conductivity is vanishingly small at not very high temperatures. At $T \approx$ 4000–6000 K it becomes appreciable and grows steeply as T increases. The heat flux makes the temperature fall off towards the walls more or less uniformly. The current, however, is vanishingly small everywhere except at the tube axis, where the temperature is sufficiently high (Fig. 10.22). The channel model is fairly obvious, in view of this picture. Let us introduce the effective radius r_0 of the conducting channel and assume approximately that $\sigma = 0$ outside the channel, at $r > r_0$, so that no current flows there. Conductivity inside the channel at $0 < r < r_0$ is high and approaches the value $\sigma_{max} \equiv \sigma(T_{max})$ that corresponds to the temperature at the axis of $T_{max} \equiv T(0)$. The channel model reduces to replacing the actual distribution $\sigma(r)$ by a stepwise curve (dashed lines in Fig. 10.22).

In this approximation, the approximate expression for the current, (10.13), transforms to

$$i = \sigma_{max} E \pi r_0^2 , \tag{10.14}$$

and equation (10.12) is readily integrated in the zero-current zone $r_0 < r < R$. We approximate the boundary conditions by $T_0 \equiv T(r_0) \approx T(0) \equiv T_{max}$ at the channel boundary and by $T_w = 0$ at the wall and find

$$\Theta_{max} = \frac{W}{2\pi} \ln \frac{R}{r_0} , \quad W = \frac{i^2}{\pi r_0^2 \sigma_{max}} , \quad \Theta_{max} = \int_0^{T_{max}} \lambda \, dT , \tag{10.15}$$

where $W = iE$ is the power released per cm of the column.

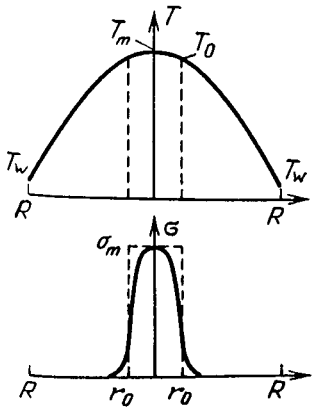

Fig. 10.22. Distribution of temperature T and conductivity σ along the arc column radius. Dashed curve replaces the $\sigma(r)$ profile with the "step" of the channel model

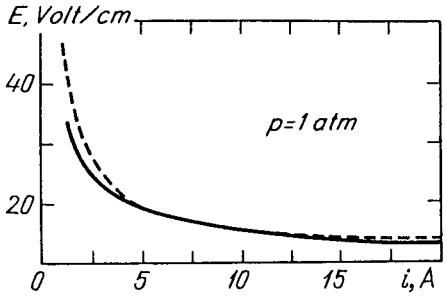

Fig. 10.23. $V - i$ characteristic of arc column in nitrogen in a tube of radius $R = 1.5$ cm. Solid curve: experiment; dashed curve: calculation employing the minimum power principle [10.1]

The equations (10.14, 15) contain three unknown variables T_{max}, r_0, E; the current i and tube radius R being externally prescribed parameters. To add a relation that is lacking, Steenbeck suggested the use of the *principle of minimum power*. For given i and R, the temperature distribution in the tube (and hence the plasma temperature T_{max} and channel radius r_0) must reach such values that the power W and field $E = W/i$ be minimum. Arc calculations based on the minimum power principle fit experimental data quite well (Fig. 10.23); this was one of the reasons why the principle enjoyed a certain popularity (see also Sect. 8.4.8).

However, the validity of this principle never ceased to be an open question for researchers; it is still being scrutinized and discussed today. A search for justification led to links with nonequilibrium thermodynamics. As for the *arc column* equations, the principle was proved to hold. Nevertheless, the possibility of its application must be verified by special analysis in each specific case. Thus an unwise application of the minimum power principle to *inductively coupled rf* and *microwave* discharge modes in the framework of models that were quite similar to the channel model led to erroneous results, the mistakes being masked by the seemingly satisfactory agreement with comon sense and with experimental data (at least in certain parameter ranges) [10.15].

10.10.4 Energy Balance in the Current Channel

We shall not be pursuing any further the matter of the minimum power principle to see what agents determine the plasma temperature. We do not need supplementary principles. Indeed, the entire information is contained in (10.12, 13). Having started the approximate solution with modeling the function $\sigma(r)$ by a rectangle, we have to complete it in a consistent manner. Integration of (10.12) in the currentless zone yielded (10.15). Now we look at the current channel. The power W released in the channel is transported through its boundary by the heat flux J_0, $W = 2\pi r_0 J_0$. Despite the assumption made in deriving (10.14, 15), the heat flux from the channel is determined by an actual, even if small, temperature difference across the conducting channel, $\Delta T = T_{max} - T_0$. To an order of magnitude, $J_0 \sim \lambda_{max} \Delta T / r_0$, where $\lambda_{max} \equiv \lambda(T_{max})$. If this estimate is improved by integrating (10.12) in the interval $0 < r < r_0$, again assuming the uniform distribution of heat sources σE^2, we obtain

$$4\pi \Delta\Theta = W \approx 4\pi \lambda_{max} \Delta T \,, \quad \Delta\Theta = \Theta_{max} - \Theta_0 \,. \tag{10.16}$$

10.10.5 Quantitative Definition of the Notion of "Channel" and Closing of the System of Channel Equations

The new relation (10.16) introduces a new unknown: ΔT or T_0. However, we have not yet given the definition of the "*channel*". A speculative introduction of its characteristics, namely radius r_0 and temperature T_{max}, is not yet a basis for calculating them. We have first to establish quantitatively how to differentiate between media regarded as conducting and nonconducting. We cannot know the radial distribution of current in the column until the problem is solved; hence, it is natural to draw the conditional boundary at that point on the current density distribution $j(r) \propto \sigma(r)$ where it decreases by a predetermined factor in comparison with the maximum value on the channel axis. If the steep slope of the function $\sigma(T)$ is taken into account, this convention corresponds to a not too large temperature drop ΔT.

For example, assume the arc current to be small, the temperature and degree of ionization of plasma to be low, and electron-atom collisions to affect the resistance more than electron-ion collisions. Then $\sigma \sim n_e$, and if ionization is thermodynamically in equilibrium,

$$\sigma(T) = C \exp(-I/2kT) , \quad C(T) \approx \text{const} . \tag{10.17}$$

To be specific, we assume that $\sigma_0 \equiv \sigma(T_0)$ is less than σ_{max} by a factor of $\bar{e}$; recalling that $I/2kT \gg 1$, we find

$$\Delta T = T_{max} - T_0 \approx (2kT_{max}/I)T_{max} . \tag{10.18}$$

For conductivity, the main role at greater currents, when ionization exceeds 1 %, is played by electron-ion collisions; the form of $\sigma(T)$ is then changed. Nevertheless, it can be approximated by the same formula (10.17) in a certain temperature range if an effective ionization potential I_{eff} is found by approximating the $\sigma(T)$ curve. Thus for air, nitrogen, and argon at $p = 1$ atm., the same interpolation formula can describe σ with accuracy sufficient for evaluations in a temperature range typical for arc discharge:

$$\begin{aligned} &\sigma \approx 0.83 \times 10^2 \exp\left(-36{,}000/T[\mathrm{K}]\right) \ \mathrm{Ohm}^{-1}\mathrm{cm}^{-1} \\ &T \approx 8000 - 14{,}000\,\mathrm{K} , \quad I_{eff} \approx 6.2\,\mathrm{eV} . \end{aligned} \tag{10.19}$$

The condition that σ change substantially in a relatively narrow temperature range $\Delta T \ll T$, for example, by a factor of two, can be written in a general differential form, without specifying the form of the function $\sigma(T)$:

$$\frac{1}{\sigma}\left(\frac{d\sigma}{dT}\right)_{T=T_{max}} \times \Delta T \approx 1 , \quad \frac{\Delta T}{T_{max}} \approx \left(\frac{d \ln \sigma}{d \ln T}\right)^{-1}_{T=T_{max}} . \tag{10.20}$$

With $\sigma(T)$ given by (10.17), (10.20) turns into (10.18). Having eliminated ΔT from (10.16, 20), we arrive at the equality

$$4\pi\lambda_{max}\sigma_{max} = W(d\sigma/dT)_{T=T_{max}} \tag{10.21}$$

that closes the system of equations of the channel arc model and defines the maximum temperature T_{max}. It is remarkable that the formal application of the principle of minimum power, $(dW/dr_0)_{i=const} = 0$, to functional relations (10.14, 15) gives exactly (10.21). Since the validity of the principle for the arc discharge had been proved (even if in a very complex manner), this result supports the validity of simple, illustrative arguments in Sects. 10.10.4, 5.[5]

Nevertheless, these arguments contain an element of arbitrariness implied by the selection of a specific ratio σ_{max}/σ_0 equal to $\bar{e}$ in (10.18) or to unity in the right-hand side of (10.20). No such uncertainty is present in the approximate integral relation

$$\int_0^{T_{max}} \sigma\lambda\, dT = W\sigma_{max}/4\pi\,, \tag{10.22}$$

which is more general than the differential formula (10.21) and corresponds, by virtue of its derivation (Sect. 11.2), to the best replacement of the current distributed in the tube cross section by the current concentrated in a channel.

10.10.6 Plasma Temperature

Any one of the approximate relations (10.18) together with (10.16), or (10.21), or (10.22) (in the order of improving accuracy) determine the maximum plasma temperature T_{max} in the arc column as a function of the power input per unit length, W. If the power is fixed, T_{max} is independent of the tube radius and, by virtue of (10.22), depends only to a small extent on the heat conduction characteristics of the gas in the electrically nonconducting peripheral region. In the crude approximation (10.21) and (10.16) with (10.18), T_{max} is completely independent of this factor.

The final temperature T_{max} is such that the temperature drop in the energy release region, closely tied to T_{max} via (10.20) and via the conductivity $\sigma(T)$, ensures the balanced heat transport to the zone *outside the current channel*. The subsequent fate of energy hardly affects the maximum temperature (if the power is fixed). We can conclude that temperature is *equally insensitive to the method of cooling the arc* and to the organization of the discharge environment (free atmosphere or a flow of cold gas). Only the power input into the plasma, which depends (quite steeply) on cooling intensity, exerts a direct effect on T_{max}. The

[5] The reader must beware of the error encountered in some theoretical papers in which $\sigma(T)$ is approximated by a stepwise function $\sigma = 0$ for $T < T_0$, $\sigma = \text{const}$ for $T > T_0$ and the step coordinate T_0 is rigidly fixed. Indeed, one is tempted to conclude from Fig. 10.18 that $T_0 = 9000$–10,000 K. In fact, the temperature of the conductivity onset T_0 increases or decreases with the maximum plasma temperature T_{max} when the current and electric power are varied. While it is admissible to ignore some fraction of current beyond the main current channel, it is a grave error if a definite absolute amount of current is left beyond this channel. An absurd situation may result if, say, $T_0 = 9000$ K and $T_{max} = 9010$ K: almost the entire current flows outside the channel; or, at the other extreme, $T_0 = 9000$ K but $T_{max} = 15,000$ K: a predominant part of the channel carries a negligible fraction of total current and thus does not constitute a channel at all.

greater the amount of heat that can be transported out of the cold gas, the greater the power that can be introduced into it without violating the steady state.

As a result of the steep dependence of conductivity on temperature, high temperatures can be achieved only by a disproportionate increase in power. This is clear from general formulas (10.21, 22) but becomes even more convincing if an explicit dependence $T_{max}(W)$ is found by prescribing the function $\sigma(T)$ (with the true ionization potential at low temperatures and the effective one at higher temperatures):

$$T_{max} = \sqrt{(I/8\pi\lambda_{max}k)W}\ . \tag{10.23}$$

On the average, the temperature increases more slowly than $W^{1/2}$ because heat conduction generally increases with increasing T. Let us make an evaluation for a carbon arc in atmospheric air at $i = 200$ A, with measurements showing that $T_{max} \approx 10,000$–$12,000$ K (Fig. 10.2). According to the $V - i$ curve of Fig. 10.16, in these conditions the field is likely to be $E \approx 2.5$ V/cm, whence $W = 500$ W/cm. Assuming $\lambda_{max} = 1.5 \times 10^{-2}$ W/cm K (Fig. 10.19) and $I_{eff} = 6.2$ eV [from (10.19)], we find from (10.23) that $T_{max} = 9800$ K, in reasonable agreement with experimental data.

When the current is relatively low ($i = 10$ A) in air at $p = 1$ atm., the $V - i$ curve of Fig. 10.15 gives $E = 20$ V/cm, $W = 200$ W/cm. Formula (10.23) gives an estimate $T_{max} \approx 7000$ K [$\lambda_{max} \approx 2 \times 10^{-2}$ W/cm K; $I_{eff} \approx 10$ eV is now higher because the degree of ionization is low: $x = 2 \times 10^{-4}$].

10.10.7 Column Characteristics

The problem is solved using the formulas given above. For a given W, we find T_{max} from (10.23) or the more general (10.21, 22), and then find r_0 from the first relation of (10.15). The second formula of (10.15) now gives i. The field is $E = W/i$. The similarity law holds: at a fixed power W the channel radius r_0 is proportional to the tube radius R, and the entire distribution $T(r)$ varies in a similar manner as R is varied. The calculation illustrated in Fig. 10.23 uses (10.21).

The parameter that is varied and measured directly in experiments is not the power, but the current; hence, the relations governing the column behavior will become clear if all its characteristics are plotted as functions of the current. Thus we can choose $\sigma(T)$ in the form (10.17). To simplify the formulas, we also take $\lambda = \text{const}$, $\Theta = \lambda T$; this does not introduce substantial distortions.[6] Making use of (10.23, 15, 17), we find

$$\sigma_{max} = \left(IC/8\pi^2\lambda k T_{max}^2\right)^{1/2}(i/R)\ , \tag{10.24}$$

$$T_{max} = \frac{I/2k}{(1/2)\ln\left(8\pi^2\lambda C k T_{max}^2/I\right) - \ln(i/R)}\ . \tag{10.25}$$

[6] Actually, anomalies due to the nonmonotonic behavior of $\lambda(T)$ may arise in molecular gases at low temperatures $T \approx 6000$–8000 K (Figs. 10.19, 20).

As the current increases, the conductivity grows almost proportionally, so that plasma passes this current. However, σ is a steep function of temperature so that T grows much more slowly. The power is related to temperature by the energy balance in the channel and thus also grows slowly with i. Correspondingly, the field $E = W/i$ decreases:

$$W = \frac{8\pi\lambda k T_{\max}^2}{I} \approx \frac{\text{const}}{[\text{const} - \ln(i/R)]^2} , \tag{10.26}$$

$$E = \frac{8\pi\lambda k T_{\max}}{I}\,\frac{1}{i} \approx \frac{\text{const}}{i[\text{const} - \ln(i/R)]^2} . \tag{10.27}$$

Formula (10.27) gives the $V - i$ characteristic of the column, i.e., the voltage decreases with increasing current. The channel radius is

$$r_0 = R(\sigma_{\max}/C)^{1/2} = R\left(I/8\pi^2\lambda k T_{\max}^2 C\right)^{1/4}(i/R)^{1/2} . \tag{10.28}$$

Roughly speaking, $r_0^2 \propto i$, so that a current increase results in a greater area, not in a greater current density $j \sim i/r_0^2 \propto T_{\max}$, which increases as slowly as temperature does. All the quantities $T_{\max}$, $\sigma_{\max}$, W, E are functions of the ratio i/R. If the tube has a smaller radius, the same power is developed at a proportionally lower current.

A new item appears in the plasma energy balance at temperatures above 11,000–12,000 K: radiative losses. To compensate for these losses in the steady state, an additional power and stronger field are needed, and the $V - i$ curve develops a positive slope.

10.10.8 How to Achieve Extreme High Temperatures

If this aim is pursued, it is necessary to ensure intensive heat removal in order to be able to inject high power into the plasma. It is difficult to achieve this effect only by increasing the current: it would have to be too high. Heat removal can be intensified by reducing the tube radius (thus increasing the temperature gradient), or by blowing a fast flow of fluid [gas or, better still, water as in the Gerdien arc (see Sect. 10.2.8)]. Very high temperatures of several tens of thousands of degrees are easier to achieve in short pulsed discharges, because a very high current pulse can be produced and the energy accumulates in the plasma before heat removal starts (nonsteady process).

In order to generate and study a high-temperature steady state arc column, the discharge is passed through stacked, cooled and insulated copper washers with hole diameters of several millimeters. Copper washers alternate with dielectric ones having the same hole diameter. The washers form a long well-cooled small-diameter tube. An axial temperature up to 15,000 K has been obtained, in this way, in nitrogen at $p = 1$ atm.

10.11 The Gap Between Electron and Gas Temperatures in "Equilibrium" Plasma

The energy exchange in electron-atom collisions in weakly ionized nonequilibrium plasmas with $T_e \gg T$ is "unilateral": energy is transferred only from the electrons to the heavy particles. The exchange in equilibrium plasmas is bilateral. In the case of ideal equality, $T_e = T$, the electrons gain from heavy particles in some collisions exactly the same amount of energy that the former pass on to the latter in other collisions. The equality $T_e = T$ is violated in the presence of an electric field. Actually, only electrons gain energy from the field to any appreciable extent. They transfer it to heavy particles that later participate in transporting the energy away from the gas (into the walls, etc.). This form at relay transport functions owing to positive temperature differences between electrons and the gas, $T_e - T$, and between the gas and the walls, $T - T_w$. In Sect. 10.10 we neglected the difference between T_e and T and worked in terms of the common temperature T. Let us try to check the validity of this assumption.

10.11.1 Energy Balance Equation of Electrons Interacting with the Field and the Heated Gas

This is a generalization of (2.12):

$$\frac{3}{2}k\frac{dT_e}{dt} = \left[\frac{e^2E^2}{m\nu_m^2} - \frac{3}{2}\delta k(T_e - T)\right]\nu_m \,. \tag{10.29}$$

As before, δ in (10.29) must be interpreted as the fraction of energy that an electron transfers, on the average, to a colliding heavy particle if the latter has negligible energy. If $T_e \gg T$, the equation transforms into (2.12). If the field is zero, stable equilibrium, $T_e = T$, is implied by this equation.

10.11.2 Criterion of Equilibrium

Applying (10.29) to steady-state conditions [electron temperature builds up quite rapidly (Table 9.1) and is practically always quasistationary] we obtain the relation between the temperature gap and the field:

$$\frac{T_e - T}{T_e} = \frac{2e^2E^2}{3\delta kT_e m\nu_m^2} = 2 \times 10^2 A\left\{\frac{E[\text{V/cm}]l}{T_e[\text{eV}]}\right\}^2 . \tag{10.30}$$

In this last transformation, we changed from collision frequency to electron path length $l = v/\nu_m$ and set $mv^2/2 = 3kT_e/2$. In addition, we assumed that $\delta = 2m/M$, where M is the atomic mass and A is the atomic weight. If the gas were molecular before heating, the presence of small number of remaining molecules slightly intensifies the exchange (δ is increased) and reduces the temperature gap. Formula (10.30) can be used to evaluate the extent of nonequilibrium caused by the difference between the electron and ion temperature.

The field necessary to sustain nearly equilibrium plasma is determined by the energy balance of the ionized gas as a whole (Sect. 10.10). Having found E and $T \approx T_e$ for a given current either by calculations or experimentally, we find from (10.30) the actual temperature gap that ensures a steady transfer of Joule heat from electrons to the gas. If the relative gap exceeds the admissible limit of, say, 50 %, the assumption of equilibrium plasma has to be dropped from calculations and one has to consider the system of equations for the energy of electrons, (10.30), and of the gas, (10.12) – but with the true conductivity, which now depends not on T, but on T_e.

The ionization equilibrium in the plasma may also be disturbed. In that case the kinetics of electron density must also be analyzed, as in Chap. 8. This is indeed the situation with processes in the contracted current filaments that are formed in glow discharges (Sect. 9.8).

The plasma of high-pressure arcs may be very highly ionized. The Coulomb scattering of electrons by ions plays an essential, and often dominant, role. In the general case, with (2.8) taken into account, we have

$$l^{-1} = N\sigma_m + 1.3 \times 10^{-13} n_e \, (T_e[\mathrm{eV}])^{-2} \ \mathrm{cm}^{-1} \ , \tag{10.31}$$

where the first term refers to neutral atoms. The Coulomb logarithm is assumed to equal $\ln \Lambda = 4.5$, which corresponds to $T_e \approx 10^4$ K, $n_e \sim 10^{16}$–$10^{17}\,\mathrm{cm}^{-3}$. Collisions with ions are dominant if the degree of ionization exceeds the level

$$n_e/N > 0.77 \times 10^{13} \sigma_m \, (T_e[\mathrm{eV}])^2 \tag{10.32}$$

of order 10^{-2}. For instance, in Ar + 5 %H_2 at $p = 1$ atm. we find that at a current $i = 50$ A, $T \approx T_e \approx 10^4$ K and $n_e \approx 2 \times 10^{16}\,\mathrm{cm}^{-3}$ (Figs. 10.13, 14); $N \approx 7.2 \times 10^{17}\,\mathrm{cm}^{-3}$, $n_e/N \approx 0.028$. According to Fig. 10.17, $E \approx 6$ V/cm. Collisions are coulombic, $l \approx 3 \times 10^{-4}$ cm, and the temperature gap is $(T_e - T)/T_e = 3.5$ %, so that in this sense the plasma is fairly well in equilibrium.

10.11.3 Why a Lower Field Is Required, Other Conditions Being Equal, to Sustain Equilibrium Plasma Rather than Nonequilibrium

As an example, the field in the positive column of an atmospheric-pressure nitrogen arc burning in a cooled tube of $R = 1.5$ cm in diameter is $E = 10$ V/cm at a current $i = 10$ A (Fig. 10.23). In this arc, $T \approx 8000$ K and the gas number density $N \approx 10^{18}\,\mathrm{cm}^{-3}$; $n_e \approx 2 \times 10^{15}\,\mathrm{cm}^{-3}$, $n_e/N \approx 2 \times 10^{-3}$, and collisions of electrons with neutral atoms are predominant. For the same densities of the gas, ($p \approx 30$ Torr) and the same radius in a glow discharge column in nitrogen, $E/p \approx 3.5$ V/cm Torr (Fig. 8.14) and the field $E \approx 100$ V/cm is stronger by an order of magnitude.

Formula (10.30) also leads to this picture if it is applied (in order to equalize conditions) to the case of negligible collisions with ions. The relative temperature gap is proportional to $(E/N)^2$. In the example given above, the arc temperature gap is less by two orders of magnitude than in a glow discharge, because the

electron temperature varies over a rather narrow interval. It cannot be lower than about 1/10 of the ionization potential I, otherwise there would be no free electrons.

The physical reason for the described difference in temperature gaps lies in the difference between the mechanisms by which electrons acquire the energy I necessary to ionize an atom.In a nonequilibrium weakly ionized plasma, electrons acquire energy directly from the field: $e^2E^2/m\nu_m^2 \sim (E/N)^2$ in each collision. In equilibrium plasma, electrons obtain energy from other particles, including heavy ones. Each electron of the ensemble gains from the field in a collision an essentially smaller portion of energy since $(E/N)^2$ is less by two orders of magnitude. Electrons feed energy to atoms, and then all particles "pool" their energy to concentrate it on colilsions into the energy of some electrons (in the "tail" of the Maxwellian distribution) which produce ionization. In short, the field in nonequilibrium plasma must bring an electron's energy up to I, and in equilibrium plasma, only to $kT_e \ll I$.

10.11.4 When Is Plasma in Equilibrium?

Each electron thus gains much less energy from the field in an equilibrium plasma than in nonequilibrium one, but the gas gets heated up to a much higher temperature, so that a greater energy release is required, $w = jE$. So much heat is released because electrons are numerous and the current (not the field) is strong. This is quite clear in the energy balance equation of the gas (10.12), if we use (10.30) to rewrite $\sigma E^2 = n_e e^2 E^2/m\nu_m^2$ in terms of the rate of energy transfer from electrons to heavy particles:

$$\sigma E^2 = \frac{3}{2}\delta(T_e - T)\nu_m n_e = -\frac{1}{r}\frac{d}{dr}r\frac{d\Theta}{dr} \sim \frac{\Theta}{R^2}\,. \tag{10.33}$$

A small gap corresponding to $T \approx T_e$ is achieved at high n_e (at high current). The same effect is achieved by increasing the collision frequency ν_m, thereby intensifying the exchange of energy. This is one of the reasons why plasma is more often in equilibrium at high pressures. The second reason, which sometimes is even more important, is the slowing down of the diffusion losses of electrons; this factor facilitates the increase in the degree of ionization to the equilibrium level corresponding to T_e.

11. Sustainment and Production of Equilibrium Plasma by Fields in Various Frequency Ranges

11.1 Introduction. Energy Balance in Plasma

Equilibrium plasma is formed in steady-state (and in sufficiently long-pulsed) *high-pressure* discharges. Fields in all four frequency ranges are currently employed to generate this plasma: dc, rf, microwave, and optical. The words "sustainment of plasma" will mean a process in which the energy of the field is continuously released in a certain mass of gas, so that the plasma state is preserved. The *generation* (*production*) of plasma is defined here as a process of continuous production of plasma, whereby fresh masses of cold gas are continuously turned into plasma. Every process of plasma sustainment by electric field can be used to generate it, by blowing cold gas through the volume where the discharge is sustained in order to obtain a continuous plasma jet. Such generators of dense low-temperature plasma – *plasmatrons* – are widely used in physics research and in industrial applications.

This chapter outlines the processes of sustainment and generation of equilibrium plasma in various fields; we will emphasize the common features and see how the main physical problem is solved: the determination of *plasma temperature* depending on the characteristics of the applied external field.

11.1.1 Energy Balance Equation

In the general case, the gas temperature obeys gas dynamics equations that must also take into account non-hydrodynamic mechanisms of energy transfer: heat conduction and radiation. However, quite a few practically important processes are such that even if the plasma is moving, its velocity is subsonic and the pressure is constant in time and space. The gas dynamics energy equation is then transformed into an equation for temperature involving specific heat at constant pressure c_p:

$$\varrho c_p dT/dt = -\mathrm{div}\, \boldsymbol{J} + \sigma\langle \boldsymbol{E}^2\rangle - \Phi\,, \quad \boldsymbol{J} = -\lambda \nabla T\,. \tag{11.1}$$

Here $\varrho = NM$ is the mass density of the gas, related to temperature by the condition of constant pressure, $p = (N+n_e)kT$, and λ is the thermal conductivity. The derivative d/dt refers to a finite mass of the gas. If this mass moves at a velocity $\boldsymbol{u}$, then

$$dT/dt = \partial T/\partial t + (\boldsymbol{u}\cdot\nabla)T\,, \tag{11.2}$$

where $\partial/\partial t$ refers to a fixed point of space. We consider, in addition to constant fields, only sinusoidal fields. In this case, σ in the expression $\langle \boldsymbol{j}\boldsymbol{E}\rangle = \sigma\langle \boldsymbol{E}^2\rangle$ for energy released in $1\,\mathrm{cm}^3$ per second stands for high-frequency conductivity (Sect. 3.4), and angle brackets $\langle\,\rangle$ denote the averaging of a quantity over one oscillation period that is assumed to be sufficiently short. The quantity Φ in (11.1) describes radiative losses. As a rule, we neglect them because their role is not significant at atmospheric pressure and at $T < 11{,}000$–$12{,}000\,\mathrm{K}$.

11.1.2 Conservation Law for Total Energy Flux in Steady-State Static Discharges

The energy balance equation can be analyzed and solved for $\boldsymbol{E}$ regarded as a constant parameter only in the case of a constant and homogeneous field, as in the arc column (Sect. 10.10). In the general case, the electric field distribution is to be determined together with the temperature distribution. The field satisfies Maxwell's equations (Sect. 3.3) which contain electrodynamic material characteristics σ and ε which are functions of temperature. The temperature and electric field are thus described by a system of interrelated equations.

Typically, the plasma temperature in the zone where the field energy is released is independent of whether the gas is moving or not. To determine it and its dependence on the applied field we can analyze *static modes*, with the discharge burning in *stationary* gas [11.1]. We will consider steady-state static discharges neglecting radiative losses. In this case (11.1) transforms to

$$-\mathrm{div}\,\boldsymbol{J} + \sigma\langle \boldsymbol{E}^2\rangle = 0\,, \quad \boldsymbol{J} = -\lambda\nabla T \tag{11.3}$$

[cf. (10.12)].

Let us turn to the equation of energy balance of the electromagnetic field, (3.21), which follows from Maxwell's equations. In stationary conditions,

$$\mathrm{div}\,\langle \boldsymbol{S}\rangle = -\sigma\langle \boldsymbol{E}^2\rangle\,, \quad \boldsymbol{S} = (c/4\pi)[\boldsymbol{E}\cdot\boldsymbol{H}]\,, \tag{11.4}$$

where $\boldsymbol{S}$ is the flux density vector of electromagnetic energy. Equation (11.4) indicates that the flux is attenuated because the energy supplied by the electromagnetic field is dissipated in the medium. Combining (11.3) and (11.4), we obtain

$$\mathrm{div}\,\big(\boldsymbol{J} + \langle \boldsymbol{S}\rangle\big) = 0\,, \tag{11.5}$$

which indicates that the total flux of thermal and electromagnetic energy has no sources. The amount of electromagnetic energy entering a volume and dissipated within it is exactly equal to the amount of heat leaving the volume.

11.1.3 Fluxes Integral

In the one-dimensional case, (11.5) is integrable, yielding the first integral of the system of the equations of field and plasma energy, known as the *"fluxes integral"*:

$$r^n \left(J + \langle S \rangle\right) = \text{const} . \tag{11.6}$$

Here $n = 0$ for flat geometry, $n = 1$ for cylindrical, and $n = 2$ for spherical. The integration constant is found from the boundary conditions.

11.2 Arc Column in a Constant Field

To demonstrate a greater generality of relations that prescribe plasma temperature in any equilibrium discharge, we return to the problem, discussed in Sect. 10.10, of determining the temperature in the arc column. We approach it from a new standpoint, using the fluxes integral (11.6). By virtue of symmetry conditions, radial fluxes (both thermal and electromagnetic) vanish at the column axis, that is,

$$J_r + S_r = 0 , \quad -\lambda dT/dr = -S_r = cE_z H_\varphi/4\pi , \tag{11.7}$$

where the flux S_r is expressed through (11.4) in terms of the electric field E_z directed along the axis and the magnetic field H_φ; if current is linear, H_φ has azimuthal orientation. Electromagnetic energy flows into the current channel from the outside across the lateral surface, is dissipated in the plasma, and is carried back to the outside by heat conduction flow. The "field" interpretation of energy transformations in terms of the electromagnetic concepts is equivalent to the concept of the release of Joule heat by the current.

We express E_z in (11.7) in terms of H_φ using Maxwell's equations (3.13):

$$E_z = \frac{c}{4\pi\sigma}\frac{1}{r}\frac{d}{dr}rH_\varphi , \quad S_r = -\frac{c^2}{16\pi^2\sigma}\frac{H_\varphi}{r}\frac{d}{dr}rH_\varphi . \tag{11.8}$$

Now we multiply (11.7) by σ so as to have all temperature-dependent quantities on one side of the equation. Integrating in r from the axis to tube walls ($r = R$), we find the relation between plasma temperature T_m on the axis and the radial distribution of magnetic field:

$$\int_{T_\text{w}}^{T_\text{m}} \sigma(T)\lambda(T)dT = \frac{c^2}{16\pi^2}\int_0^R \frac{H_\varphi}{r}\frac{d}{dr}(rH_\varphi)dr , \tag{11.9}$$

where $T_\text{w} \approx 0$ is the temperature of the inner wall of the tube surrounding the column.

The exact integral relation (11.9) can be approximated by using the *channel model* for calculating the right-hand side. Then we are able to express the known

function of the sought temperature T_m in the left-hand side in terms of the arc current i to which the magnetic field is proportional. According to (11.8), H_φ outside the channel is $H_\varphi = H_1(r_0/r)$, where $H_1 = 2i/cr_0$ is the field at the boundary of the conductor $r = r_0$; inside the channel, $H_\varphi = H_1(r/r_0)$. Substituting these expressions into (11.9) and integrating, we arrive at (10.22),

$$\int_{T_w \approx 0}^{T_m} \sigma(T)\lambda(T)dT = \frac{i^2}{4\pi^2 r_0^2} = \frac{W\sigma_m}{4\pi} , \qquad (11.10)$$

mentioned in Sect. 10.10.5. It closes the set of equations of the channel model of arc discharge without any assumptions about the form of $\sigma(T)$ and about the numerical relation between conductivities at the points $r = 0$ and $r = r_0$; besides, it makes the simplified channel model an excellent approximation to the true situation. We will see that relations of type (11.10) also give the temperature of plasma in other types of discharge.

11.3 Inductively Coupled Radio-Frequency Discharge

11.3.1 Introductory Remarks

Radio-frequency inductively coupled discharges are becoming increasingly more widespread as a method of plasma generation in laboratories and industry, although the arc generation method is still the most common method of producing dense low-temperature plasmas. The principle of inductively coupled plasma generation was outlined in Sect. 7.6. It has been used to develop *electrodeless plasmatrons,* which have important advantages in comparison with arc plasmatrons. The plasma of electrodeless systems is pure, while in arc plasmatrons the contamination of plasma by products of electrode erosion is inevitable. This characteristic is decisive for the progress of *plasma* production of high-purity compounds and high-purity granulated refractory materials, and so forth. The service life of electrodeless plasmatrons is virtually unlimited while high-power arc plasmatrons suffer from rapid erosion and failure of electrodes. Obviously, however, the operation of a high-power rf discharge is much more complicated than a dc discharge. The required power sources (high-power generators of Megahertz range) are also more complex, more expensive, and troublesome.

The magnitude and spatial distribution of plasma temperature in inductively coupled discharges have two aspects of interest. As in the case of dc arc discharges, they are important for clarifying the physical relations governing the sustainment of plasma by the field and for practical applications. Furthermore, a new problem arises, not encountered in dc discharges: the discharge (as a load) must be coupled to the rf generator, otherwise the generator cannot function efficiently. Such electrical parameters of the plasma load as its ohmic resistance, self-inductance, and mutual inductance that characterize the magnetic coupling to the inductor (all of them affect the functioning of the electric system as a

whole) are directly linked with the magnitude and distributions of temperature and currents in the discharge.

The schematic circuit of an inductively coupled discharge was shown in Fig. 7.18. *Inductor* designs vary, using from one or two to many turns in the coil. The current flowing through the inductor after the power source has been switched on is often not associated with electric fields high enough to initiate breakdown in atmospheric-pressure gas: they are sufficient to sustain an already burning discharge, but not to start it. For example, an auxiliary electrode may be introduced for a short time into the discharge tube. This electrode may be heated up by the Foucault current induced by the rf field, and it may vaporize. Heated and therefore rarefied metal vapor or gas thereby undergoes breakdown. After the discharge in the main gas has been fired, the auxiliary electrode is removed.

11.3.2 Equations of Discharge in a Long Solenoid

An analysis of the idealized one-dimensional process gives a fairly detailed idea of the energy and electrodynamic characteristics of an inductively coupled discharge, as it did in the case of the long arc column. Let a dielectric tube of radius R be inserted into a long solenoid coil (Fig. 11.1). The plasma is sustained at the expense of the Joule heat of the circular current induced by the oscillating magnetic field of the rf current in the coil. The steady state is maintained via the heat conduction transport of energy to the cooled tube walls. The radial temperature distribution in the gas within the tube, schematically shown in Fig. 11.1, is described by (11.3):

$$-\frac{1}{r}\frac{d}{dr}rJ_r + \sigma\langle E_\varphi^2\rangle = 0\ ,\quad J_r = -\lambda\frac{dT}{dr}\ . \tag{11.11}$$

In form, it coincides with (10.12) for an arc column, but now the electric field is azimuthal and the magnetic field is directed along the axis. In the MHz frequency range and at atmospheric pressure, high-frequency conductivity (3.23) does not differ from the dc plasma conductivity, the polarization and displacement currents are small in comparison with the conduction currents, and the complex dielectric permittivity is purely imaginary (Sect. 3.5.1). In cylindrical geometry, Maxwell's equations (3.13, 14) without displacement current and with E and $H \propto \exp(-i\omega t)$ take the form

$$-\frac{dH_z}{dr} = \frac{4\pi}{c}\sigma E_\varphi\ ,\quad \frac{1}{r}\frac{d}{dr}rE_\varphi = \frac{i\omega}{c}H_z\ . \tag{11.12}$$

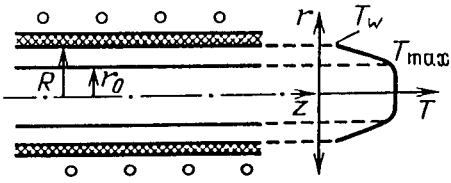

Fig. 11.1. Induction discharge in a tube of radius R placed inside a long solenoid; r_0 is the discharge radius. The radial temperature distribution is given on the *right*

The boundary conditions to the system (11.11, 12) are as follows. By virtue of symmetry, at $r = 0$ we have $J_r = 0$, $E_\varphi = 0$. At $r = R$, we have $T = T_w \approx 0$. The magnetic field in a nonconducting cold medium at the tube wall is the same as inside an empty solenoid [11.2],

$$H_z(R) \equiv H_0 = (4\pi/c)(I_0 n) , \tag{11.13}$$

where I_0 is the current in the coil and n is the number of turns per unit length. The complex amplitudes I_0 and H_0 can be assumed real. The phase shifts of the oscillating fields H_z and E_φ are counted off the phase of the field H_0 in the neighborhood of the coil.

11.3.3 Inductively Coupled Heating of Materials

This method is widely used in industry for hardening of metal parts, drying, melting, etc. For instance, a metal rod is inserted into an inductor, such as a solenoid coil. The metal is heated by induction currents. The field does not penetrate deep into the conductor because of the skin effect (Sect. 3.5.6), so that Joule heat is released only in the surface layer. Owing to the high thermal conductivity, however, the metal soon heats up as a whole. If the geometry is cylindrical (a long rod of radius r_0 and conductivity σ in a long solenoid coil), the field is described by the same equations (11.12).Since $H_z(r) = \text{const}$ in the nonconducting gap between the coil and the rod boundary, condition (11.13) is transferred directly to the surface of the conductor where $H_z(r_0) = H_0$. The equations are solved in Bessel functions of complex argument, which are tabulated for the cases of interest.

11.3.4 Model of Metallic Cylinder

This model states that the plasma conductor is similar to a metal conductor; the only difference is that now the rod "radius" r_0 and its conductivity σ_m [which is assumed to be constant, in the first approximation, and corresponding to the maximum plasma temperature T_m at the axis], are not known in advance. This model is a literal analogue of the channel model of arc discharge, being based on the same steep dependence of σ on T whereby the conductivity of the gas drops sharply where the plasma temperature falls off appreciably towards the tube walls. If the plasma temperature is sufficiently high, the skin effect forces the heat of the induction currents to be deposited in an annular layer, as in a metal. A plateau on the temperature distribution is formed in the middle of the ring as a result of conductive heating of the medium (Fig. 11.2).

The metallic cylinder model makes it possible to separate, at least partly, the solutions of the electrodynamic and thermal problems. In the former problem, σ_m and r_0 are treated as parameters. We will not write the general solution for a cylindrical conductor and only consider the case of strong skin effect when the field penetrates into the conductor to a small depth and the layer geometry is practically planar. The condition of validity of this approximation is $\delta \ll r_0$,

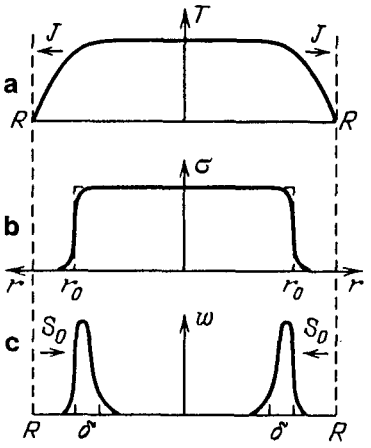

Fig. 11.2. Radial distributions of (a) temperature, (b) conductivity, and (c) Joule heat release in induction discharge. Dashed curves correspond to step function $\sigma(r)$ in the metallic cylinder model. *Arrows:* J, heat flux; S_0, electromagnetic energy flux; δ, skin layer thickness

where $\delta = c/\sqrt{2\pi\sigma\omega}$ is the skin-layer thickness (3.29); it is usually satisfied in inductively coupled discharges at frequencies in the range of the industrial value $f = 13.6\,\text{MHz}$. Measuring the x coordinate from the surface into the layer (against the radius r) and directing the axis y tangentially to the surface, we rewrite (11.12) in the form

$$\frac{dH_z}{dx} = \frac{4\pi}{c}\sigma E_y\,, \quad \frac{dE_y}{dx} = -\frac{i\omega}{c}H_z\,. \tag{11.14}$$

Now $H = H_0$ at $x = 0$ and E_y, $H_z \to 0$ as $x \to \infty$. Equations (11.14) describe a plane monochromatic electromagnetic wave in a medium with purely imaginary complex dielectric permittivity. Let us write out their solution in a complex form, as in Sect. 3.5, and then convert to the real form:

$$\begin{aligned} H_z &= H_0 \exp\left[-i(\omega t - x/\delta) - x/\delta\right] \to H_0 e^{-x/\delta}\cos(\omega t - x/\delta)\,, \\ E_y &= H_0(\omega/4\pi\sigma)^{1/2}\exp\left[-i(\omega t - x/\delta + \pi/4) - x/\delta\right] \to \\ &\to H_0(\omega/4\pi\sigma)^{1/2}e^{-x/\delta}\cos(\omega t - x/\delta + \pi/4)\,. \end{aligned} \tag{11.15}$$

The amplitudes of H_a and E_a fall off exponentially into the plasma, and $E_a \ll H_a$ at the phase shift of $\pi/4$. For instance, in air at $p = 1\,\text{atm}$. and $T = 10{,}000\,\text{K}$, $\sigma = 25\,\text{Ohm}^{-1}\text{cm}^{-1}$; at $f = 13.6\,\text{MHz}$, $\delta = 0.27\,\text{cm}$, $4\pi\sigma/\omega = 3.3 \times 10^6$ and $E_a = 5.5 \times 10^{-4} H_a$. The electromagnetic energy flux is directed into the conductor, normal to its surface, and equals

$$\langle S\rangle = S_0 e^{-2x/\delta}\,, \quad S_0 = (c/16\pi)(\omega/2\pi\sigma)^{1/2}H_0^2\,. \tag{11.16}$$

The energy coming from the inductor into the conductor is

$$S_0 = 9.94 \times 10^{-2}\frac{(I_0 n[\text{A/cm}])^2(f[\text{MHz}])^{1/2}}{(\sigma[\text{Ohm}^{-1}\text{cm}^{-1}])^{1/2}}\,\frac{\text{W}}{\text{cm}^2}\,. \tag{11.17}$$

The power released per unit length of a cylindrical conductor is $W = 2\pi r_0 S_0$. The sources of Joule heat are concentrated in the surface layer of effective thickness $\delta/2$.

11.3.5 Plasma Conductor Radius

The plasma conductor radius is readily linked to the plasma temperature T_m and power W, if we consider heat transfer across the nonconducting gap between the conductor and the tube. Integrating (11.11) with $\sigma = 0$, we find

$$\Theta_m - \Theta_w = (W/2\pi) \ln(R/r_0) \approx \Delta r S_0 . \tag{11.18}$$

As we have not specified the expression for W, (11.18) is similar to a similar equation (10.15) for arcs. The last transformation in (11.18) takes into account that in static induction discharges the cylindrical annulus in which the heat is deposited is nearly contiguous to the tube, so that the tube-plasma gap is narrow: $\Delta r = R - r_0 \ll R$. In this respect, an induction discharge subjected to skin effect behaves differently from a dc arc in which the current flows within a thin axial channel.

11.3.6 Plasma Temperature

The *metallic cylinder* model does not allow the calculation of the main factor, i.e., the *conductivity* of the plasma conductor or the *plasma temperature*. The reasons for this are clear now that we have discussed the channel model of arc discharge in Sect. 10.10. Temperature is determined by the energy balance in the energy deposition zone; hence, in order to analyze the transport of energy from this zone, one has to take into consideration the actual temperature drop in the model cylinder and draw a qualitative distinction between *conducting* and *nonconducting* media.

According to (11.11), the zone where the rf field does not penetrate and there are no heat sources is characterized by $T(r) = \text{const} = T_m$ (Fig. 11.2). The entire temperature difference cylinder, $\Delta T = T_m - T_0$, falls across the surface layer of thickness $\delta/2$, where the energy is released. The heat flux leaving the conductor is approximately $J_0 \approx 2\lambda_m \Delta T/\delta$ ($\lambda_m \equiv \lambda(T_m)$; it coincides with the electromagnetic energy flux S_0 from the inductor. This gives us the energy balance equation for the conduction plasma itself, by analogy to (10.16) for an arc discharge:

$$2\lambda_m \Delta T/\delta \approx S_0 , \quad 4\pi\lambda_m \Delta T \approx W(\delta/r_0) . \tag{11.19}$$

The function $\sigma(T)$ being the same as for the constant field in the arc, the condition specifying the temperature drop at which the conducting medium can be assumed to transform into "nonconducting" one [(10.18) or (10.20)] remains valid. Combining one of these relations with (11.19) we obtain an equation yielding the plasma temperature of the inductively coupled discharge. Thus, using (10.17) with effective ionization potential I (Sect. 10.10.5) and formulas (11.16)

for S_0, (11.13) for H_0, and (3.29) for δ, we express the plasma conductivity of a steady discharge in terms of the parameter controlled in experiments, namely, the inductor current (ampere-turns):

$$\lambda_m \left(2kT_m^2/I\right) \sigma_m = (I_0 n/2)^2 \,. \tag{11.20}$$

The function $\sigma(T)$ being steep, T_m and λ_m vary in a narrow range, so that, approximately, $\sigma_m \propto (I_0 n)^2$. As the inductor current increases, the temperature increases slowly,

$$T_m = \frac{I/2k}{\ln(4\lambda_m k T_m^2 C/I) - \ln(I_0 n)} = \frac{\text{const}}{\text{const} - \ln(I_0 n)} \,, \tag{11.21}$$

in complete analogy with (10.25) for dc arc discharges. As in the latter case, a high temperature is hard to achieve: high ampere-turns are necessary, and also high power:

$$W = 2\pi r_0 S_0 \approx 2\pi R S_0 \propto H_0^2 \sigma_m^{-1/2} \propto I_0 n \propto \sigma_m^{1/2} \,. \tag{11.22}$$

the plasma temperature is independent of the field frequency (provided the skin layer is thin).

11.3.7 Exact Formula for Temperature

It is striking that, in addition to (11.6), for an inductively coupled discharge there is a second integral of the system of plasma energy equations and Maxwell's equations. This is so because equations without displacement current, (11.12), make it possible to recast the electromagnetic energy flux in differential form,

$$\langle S_r \rangle = -\frac{c^2}{32\pi^2\sigma} \left\langle \frac{dH_z^2}{dz} \right\rangle = -\frac{c^2}{64\pi^2\sigma} \frac{dH_a^2}{dr} \,, \tag{11.23}$$

where H_a is the real amplitude of magnetic field. We now substitute (11.23) into the fluxes integral (11.6) [where the constant is zero, as in (11.7) for the arc discharge], multiply the entire equality by σ, and integrate over r from 0 to R. Taking into account (11.13) and recalling that if the skin layer is thin, $H_a \approx 0$ at $r = 0$, we obtain the expression

$$\int_{T_w \approx 0}^{T_m} \sigma(T)\lambda(T)\, dT = \frac{c^2 H_0^2}{64\pi^2} = \left(\frac{I_0 n}{2}\right)^2 \tag{11.24}$$

which determines the plasma temperature as a function of inductor current; it was first derived in [11.3]. In contrast to (11.10), it is exact. In the case of arc discharges the right-hand side of (11.9) cannot be integrated, because (11.8) implies that S_r cannot be presented in purely differential form; however, common features of (11.24) and (11.10) are obvious. If $\sigma(T)$ is given in the form of (10.17) and $I_{eff} \gg kT_m$, then (11.24) can be reduced to equality (11.20), which we obtained above in a simplified way.[1]

[1] Footnote see opposite page

11.3.8 Examples of Calculations and Measurements

Let us use the formulas to make some estimates. Let the discharge burn in air at $p = 1\,\text{atm.}$, $f = 13.6\,\text{MHz}$ and plasma temperature $T_m = 10,000\,\text{K}$; $\lambda_m = 1.4 \times 10^{-2}\,\text{W/cm K}$. We have already mentioned in Sect. 11.3.4 that under these conditions $\sigma_m = 25\,\text{Ohm}^{-1}\,\text{cm}^{-1}$ and $\delta = 0.27\,\text{cm}$. The Joule heat is deposited in the ring of effective thickness $\delta/2 = 0.14\,\text{cm}$. According to (11.19, 10.18), plasma is sustained in this plasma cylinder if the inflow of energy from the surface is $S_0 = 250\,\text{W/cm}^2$. According to (11.16, 13), this flux is obtained if $H_0 = 75\,\text{Oe}$ and $I_0 n = 60\,\text{A/cm}$. The maximum amplitude of electric field at the external plasma boundary is found from (11.15) to be $E_a \approx 12\,\text{V/cm}$. The maximum density of the circular current in plasma is $j_a \approx \sigma_m E \approx 300\,\text{A/cm}^2$. The total circular current in plasma per unit column length is $j_a\delta \approx 80\,\text{A/cm}$. It is comparable to the inductor current per unit length, $I_0 n = 60\,\text{A/cm}$. Therefore, the mutual-induction effect of the plasma current on the operation of the rf generator circuit is fairly strong.

The heat flux potential in plasma is $\Theta_m \approx 0.14\,\text{kW/cm}$. Let the discharge burn in a tube of radius $R = 3\,\text{cm}$. As follows from (11.18), the plasma-tube gap of $\Delta r = 0.56\,\text{cm}$ is relatively narrow. The power input per unit length of plasma column, given by (11.22), is $W \approx 3.8\,\text{kW/cm}$. These calculations indicate that for heating the plasma not to 10,000, but to 12,000 K the power and ampere-turns must be doubled. In fact, this high temperature was calculated with radiative losses not taken into account, so that an even higher power is required. The temperature in inductively coupled rf discharges does not normally exceed 10,000–11,000 K.

Radial distributions of temperature and electron density measured in experiments are plotted in Fig. 11.3. In xenon, the temperature is lower than in argon, since the ionization potential is lower. A small temperature drop in the central part of the discharge, about 500 K, is caused by radiative losses. The Joule heat is deposited only in the peripheral annular layer, while the radiative losses occur in the central part as well because plasma transparency turns them into bulk losses.

11.3.9 Threshold for the Existence of Equilibrium Plasma

If the current through the inductor starts to decrease from the values at which the skin layer thickness $\delta \ll r_0 \approx R$, the plasma temperature and conductivity decrease and δ increases [see (11.21,22)]. When δ reaches a value of the order of r_0 or R, the skin effect becomes insignificant and the formulae used above are invalidated. In the opposite extreme, $\delta \gg R$, the magnetic field inside the

---

[1] Integrals containing the Boltzmann function are calculated approximately by a method suggested by Frank-Kamenetsky: $1/T$ in the exponent of the exponential is expanded in the neighborhood of the upper limit T_m,

$$1/T \approx 1/T_m + (T_m - T)/T_m^2 ,$$

and all slowly varying factors with $T = T_m$ are factored out of the integral.

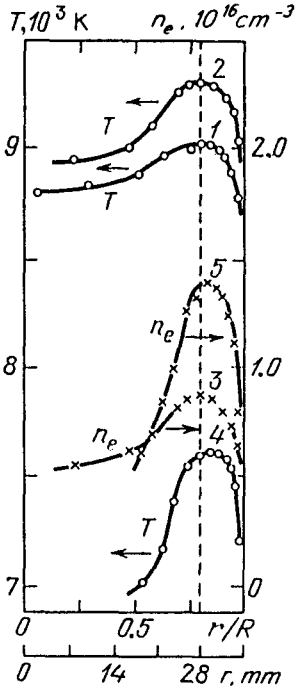

Fig. 11.3. Measured distributions of temperature (circles) and electron densities (crosses) in an induction discharge in a tube of $R = 3.5$ cm at frequency $f = 11.5$ MHz and $p = 1$ atm. [11.4]. Curve *(1)* argon, power input into plasma 4.7 kW; *(2), (3)* Ar, 7.2 kW; *(4), (5)* Xe, 6 kW

solenoid is homogeneous and equal to H_0, as it is in the absence of plasma. According to (11.12), the electric field is $E(r) = i\omega H_0 r/2c$. The power released per unit length of the plasma cylinder of radius r_0 is

$$W = \int_0^R \sigma\langle E^2\rangle 2\pi r\, dr \approx \frac{\pi\sigma_m\omega^2 H_0^2 r_0^4}{16c^2} = \frac{\pi^3\sigma_m\omega^2 r_0 (I_0 n)^2}{c^4}\,. \tag{11.25}$$

Now the temperature falls from T_m to T_0 (the effective plasma boundary) over the entire radius r_0, so that we find, in contrast to (11.19) and in similarity with (10.16), that

$$W \approx 4\pi r_0 \lambda_m \Delta T/r_0 \approx 4\pi\lambda_m \Delta T \approx 8\pi\lambda_m k T_m^2/I\,. \tag{11.26}$$

The plasma temperature cannot be allowd to drop too much since otherwise conductivity vanishes and energy is not released any more. Therefore, the power given by (11.26) is now more or less stable even if the conductivity decreases. As follows from (11.18, 24), the plasma radius decreases with decreasing temperature. We conclude that the inductor current or $I_0 n$, as implied by (11.25), depends inversely on plasma conductivity or temperature and field frequency. Over a wide range of conductivity values that covers the cases of both $\delta \ll R$ and $\delta \gg R$, $I_0 n$ and W as functions of σ_m and ω must have the forms shown in Figs. 11.4, 5 (if $\delta \ll R$, then $W \propto I_0 n \propto \sigma_m^{1/2}$).

The current $I_0 n$ as a function of σ_m or T_m passes through a minimum, which corresponds to the point of merger of the curves for the two extreme cases

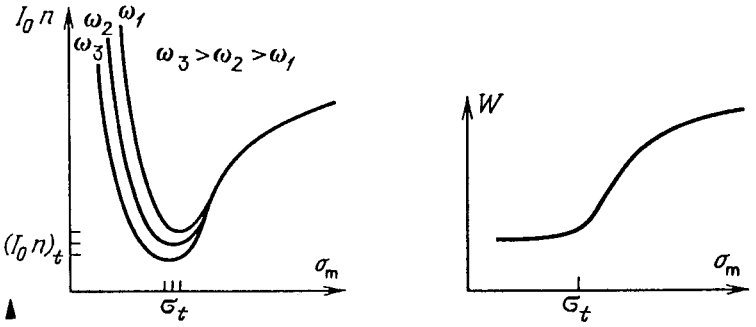

Fig. 11.4. Qualitative dependences of the number of ampere-turns per cm on the plasma conductivity. If there are these unequalities in the drawing, they may be omitted from subscription

Fig. 11.5. Qualitative dependence of power input into plasma on conductivity

discussed above, that is, to the condition $\delta \approx R$. There is a minimum (*threshold*) value of inductor current at which equilibrium plasma is still sustainable in inductively coupled discharge. It can be evaluated by extrapolating (11.20) up to the *threshold* temperature $T_m = T_t$ at which $\delta = R$:

$$(I_0 n)_t \equiv (I_0 n)_{min} \approx \left(\frac{4}{\pi} \frac{\lambda_t k T_t^2 c^2}{I \omega R^2} \right)^{1/2} . \tag{11.27}$$

For example, in air at $p = 1$ atm. and for $R = 3$ cm, $f = 13.6$ MHz, we have $(I_0 n)_t \approx 10$ A/cm. The threshold temperature $T_t \approx 7000$–8000 K.

11.3.10 Stable and Unstable States

Figure 11.4 also demonstrates another property typical of equilibrium discharges of various types. At a given inductor current $I_0 > (I_0)_t$, other conditions being equal, *two* steady states of equilibrium discharge exist. One of them corresponds to high conductivity and considerable skin effect; the other corresponds to low conductivity and no skin effect. Only the former state is realizable experimentally. The states on the left-hand branch at $T < T_t$ *are unstable*. For instance, let the temperature fluctuate upwards. A lower inductor current than the actual one would be needed for sustaining the new state. Plasma starts to heat up until a state at $T > T_t$ is reached on the right-hand branch of the curve in Fig. 11.4. Similar arguments readily confirm that it is *stable*.

11.4 Discharge in Microwave Fields

11.4.1 Discharges in Waveguides

Long-lasting discharges were obtained at high pressures in the early fifties when high-power (kilowatt) continuously operating generators became available. A number of methods of feeding microwave field energy to plasmas are possible.

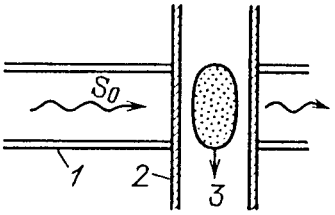

Fig. 11.6. Microwave discharge in a waveguide: *(1)* waveguide, *(2)* dielectric tube, *(3)* discharge plasma

A typical arrangement used is shown in Fig. 11.6. A dielectric tube, transparent to microwave radiation, passes through a rectangular waveguide. The plasma is maintained in the intersection region at the expense of dissipation of microwave energy. The released heat is transported away either conductively through cooled tube walls or, more frequently, by a gas blown through the tube. The latter version is a microwave plasmatron (Sect. 11.6).

Typically, the H_{01} mode of electromagnetic wave travelling in the waveguide is employed. In this mode, the electric field vector is parallel to the narrow waveguide walls (Fig. 11.7a). The field intensity in this direction is constant and it varies sinusoidally along the wider walls (Fig. 11.7b). The discharge takes place in the middle of the waveguide cross section, where the electric field has its highest value. The plasma column is elongated along the electric vector $\boldsymbol{E}$. The waveguide size is usually related to the frequency used. For $f = 2.5\,\text{GHz}$ (wavelength in vacuum $\lambda_0 = 12\,\text{cm}$), the wider wall width is 7.2 cm, the narrow wall is 3.4 cm wide. The dielectric tube is about 2 cm in diameter. The resulting plasma column is then about 1 cm in diameter.

The electric field of the incident wave induces an alternating current in the plasma column. The conduction current is not closed, or rather, it is closed by the displacement current. A rapidly varying current is in itself a source of electromagnetic radiation. The result is the scattering (and reflection) of the incident wave by the plasma conductor placed in a waveguide. The scattered wave interferes with the incident one; the resulting field sustains the plasma. A part of

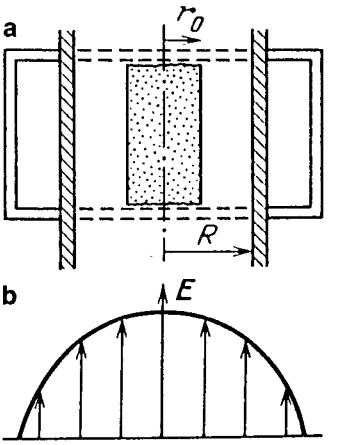

Fig. 11.7. Discharge in a waveguide maintained by an H_{01} mode: **(a)** cross section of the waveguide by the diametric plane of the tube (the plasma is shown *shaded*); **(b)** distribution of electric field along the wider wall

the incident wave is transmitted through the plasma. The power P_0 fed by the generator into the incident wave is thus divided between the reflected and the transmitted waves and is partly dissipated in the plasma. A thin well-conducting rod may dissipate half the incident power; one quarter is transmitted and one quarter is reflected.

The efficiency of the discharge device is greatly increased if the tube is followed by a reflector which returns the transmitted wave, making it pass through the plasma again. As a result, a standing wave is formed in the waveguide in the region of discharge. The reflector–discharge distance is adjusted so that the plasma column lies at the antinode of the electric field. In this way it was found possible to inject up to 80–90 % of the energy produced by the generator into the plasma [11.5].

This system, injecting 1 to 2 kW into a plasma in air at atmospheric pressure produces $T \approx 4000$ K, and up to 5000 K in nitrogen. A temperature gap arises in argon: ($T_e \approx 6500$–7000 K, $T \approx 4500$ K) because energy exchange between electrons and heavy particles in a monatomic gas is slow, especially if the temperature and electron density are not too high (cf. Sects. 10.9, 11). The temperature at a higher frequency ($\lambda_0 = 3$ cm) and in a waveguide of correspondingly smaller cross section is somewhat higher (6000 K in nitrogen). The temperature in microwave discharges is always lower than in rf discharges: the reflectivity of plasma sharply increases with increasing electron density (Sect. 11.4.4).

11.4.2 Discharge in Resonators

Major developments in this field were due to *P.L. Kapitsa* and coworkers, also in the early 1950s [11.6]. This work lead to the development of a continuously operating 175 kW generator operating at a frequency 1.6 GHz ($\lambda_0 = 19$ cm). Standing waves E_{01} were excited in a cylindrical resonator (Fig. 11.8). The electric field at the cylinder axis was directed along the axis and varied sinusoidally along the axis, with the maximum at the center of the cylinder, and the field diminishing radially. The discharge is started on the axis, in the region of maximum field. The plasma region is elongated parallel to the electric field; it forms a filament at high discharge power. The length of this filament reaches half the wavelength (about 10 cm), at a diameter of 1 cm. At high powers of plasma filament twists and floats upwards, pushed by the Archimedes force. It is stabilized by forcing the gas in the resonator to follow a helical trajectory, which prevents floating and makes the filament stable. It was thus possible to inject up to 20 kW of power

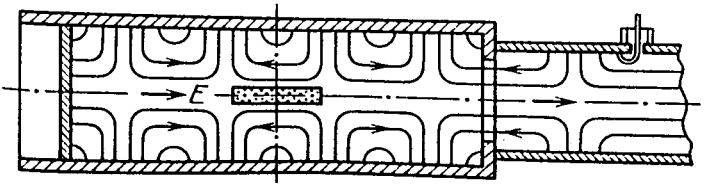

Fig. 11.8. Discharge in a resonator [11.6]. The lines of force of the electric field are shown for an E_{01} mode; the plasma filament is shown *shaded*

into a stabilized discharge in hydrogen, deuterium, and helium at pressures of one to several atmospheres, with the plasma temperature not normally exceeding 8000 K.

11.4.3 Discharges Sustained by a Plane Electromagnetic Wave

The process occurring in waveguides involves numerous details caused by complicated geometry and scattering of the wave by the plasma. These details mostly affect the quantitative rather than qualitative characteristics. To clarify the main features of equilibrium microwave discharges, consider a simple one-dimensional model. Assume that a plane electromagnetic wave passes through a plane dielectric wall transparent to microwaves and is incident on a plasma. The heat deposited in the plasma is transported conductively to the externally cooled wall, so that the steady state is maintained (Fig. 11.9).

At first glance, this model may seem extremely unrealistic; actually, it is not. In fact, we concentrate our attention on that segment of the tube and of the adjacent discharge surface which face the incident wave (Fig. 11.6). If the wave does not penetrate deeply into the plasma and the plasma temperature is quite high due to sufficiently high power (this is indeed realized), the curvature of the surface is unimportant. At any rate, this idealization preserves all the significant qualitative features, and the numerical values of the main parameters that are obtained give a good idea of the true values.

In plane geometry, the temperature deep inside the plasma tends to a constant value T_m as $x \to \infty$ and the wave damps out, that is, the constant in (11.6) is zero and

$$J + \langle S \rangle = 0 , \quad J = -\lambda \, dT/dx . \tag{11.28}$$

In the microwave range, effects of *wave* nature (reflection, interference) become important, and the field is described by the wave equation of type (3.31) but with complex dielectric permittivity. Equations for the complex amplitudes E_y, H_z of the monochromatic field are

$$\frac{d^2 E_y}{dx^2} + \left(\varepsilon + \mathrm{i} \frac{4\pi\sigma}{\omega} \right) \frac{\omega^2}{c^2} E_y = 0 , \tag{11.29}$$

where σ and ε are given by (3.23, 24). The temperature and degree of ionization in microwave discharges are never high, and electron-ion collisions play an insignificant role in (10.32). In this case,

$$\sigma \propto (1 - \varepsilon) \propto n_e \propto \exp(-I/2kT) , \tag{11.30}$$

where (in the case of a one-component gas) I is the true (not effective) ionization potential. The boundary conditions to system (11.3, 29) or (11.28, 29) with S defined by (11.4) state that deep inside the plasma ($x \to \infty$), $E = 0$ and that at the wall ($x = -x_0$), $T = T_w \approx 0$, and that the energy flux S_0 in the incident wave is given. The solution must determine the plasma temperature $T_m \equiv T(\infty)$

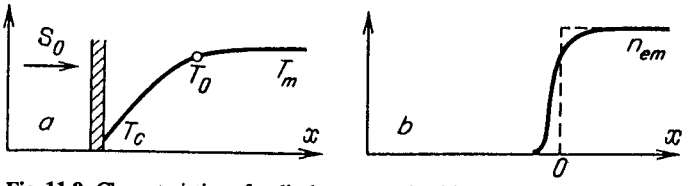

Fig. 11.9. Characteristics of a discharge sustained by electromagnetic waves: (a) Temperature distribution, transparent dielectric wall is *shaded*. (b) Corresponding electron density distribution. *Dashed line* is he approximation of $n_e(x)$ by a step

and that part of the electromagnetic energy flux S_1 which is spent on plasma maintenance [this is equivalent to finding the *reflection coefficient* of the plasma (for power of electromagnetic wave), $\varrho = (S_0 - S_1)/S_0$].

11.4.4 Approximate Solution

Following the arc channel model and the metallic cylinder model for inductively coupled discharges, we introduce the effective plasma boundary, which we place at $x = 0$ where $T = T_0$, and set $\sigma = 0$, $\varepsilon = 1$ for $T \leq T_0$ and $x \leq 0$ but $\sigma = \sigma_m$ and $\varepsilon = \varepsilon_m$ for $T_0 \leq T \leq T_m$ and $x \geq 0$; this corresponds to replacing the $n_e(x)$ distribution with a step (Fig. 11.9). The reflection coefficient for a wave that is in normal incidence from the "vacuum" onto a sharp homogeneous medium is [11.2]

$$\varrho = \frac{(n-1)^2 + \varkappa^2}{(n+1)^2 + \varkappa^2} \,. \tag{11.31}$$

The indices n and $\varkappa$ are expressed in terms of σ and ε by (3.34).

The part of the electromagnetic energy flux that penetrates the plasma is damped there, obeying (3.37):

$$d\langle S\rangle/dx = -\mu_\omega \langle S\rangle \,, \tag{11.32}$$

where the absorption coefficient μ_ω is given by (3.36) or (3.38). The energy of the wave is dissipated in the surface layer of thickness of order $l_\omega = \mu_\omega^{-1}$. Here the temperature drops from T_m to T_0. The energy balance in the layer is described by an approximate equality $S_1 = J_0 \approx \lambda_m \Delta T / l_\omega$, in complete analogy to the arc and rf discharges. The temperature T_m is found from the equation

$$S_0 [1 - \varrho(T_m)] = \lambda_m \left(2kT_m^2/I\right) \mu_\omega(T_m) \,, \tag{11.33}$$

which is similar to (11.20) for the rf discharge. The equation for heat transfer from plasma to walls across the "nonionized" gap, $\Theta_m - \Theta_w = S_1 |x_0|$, yields the gap width x_0.

Tables 11.1,2 illustrate the situation with the results of calculations of the electromagnetic characteristics of atmospheric-pressure air plasma and microwave radiation fluxes necessary to maintain various temperatures. Calculations were carried out for one of the frequencies used in experiments, $f = 10\,\text{GHz}$

Table 11.1. Electrodynamic characteristics of air plasma at $p = 1$ atm. and frequency $f = 10$ GHz

T [10^3 K]	n_e [cm^{-3}]	ν_m [10^{10} s^{-1}]	σ [10^{10} s^{-1}]	ε	$\frac{4\pi\sigma}{\omega\lvert\varepsilon\rvert}$	n	$\varkappa$	l_ω [cm]	ϱ_0
3.5	6.6×10^{11}	7.5	0.13	0.78	0.33	0.89	0.14	1.7	0.0089
4.0	4.4×10^{12}	7.1	0.88	−0.53	3.3	0.81	1.1	0.22	0.28
4.5	1.6×10^{13}	6.6	3.3	−5.1	1.3	1.3	2.6	0.091	0.57
5.0	4.8×10^{13}	6.4	9.9	−18	1.1	2.1	4.7	0.050	0.71
5.5	9.3×10^{13}	6.0	19	−39	1.1	2.8	7.3	0.032	0.83
6.0	2.1×10^{14}	5.8	41	−88	1.0	4.3	11	0.022	0.88

Table 11.2. Microwave radiation fluxes necessary to sustain air plasma at $p = 1$ atm. and $f = 10$ GHz

T [10^3 K]	λ [10^{-2} W/cm K]	Θ [10^{-2} kW/cm]	S_1 [kW/cm^2]	ϱ	S_0 [kW/cm^2]	S_1^* [kW/cm^2][a]	S_0^* [kW/cm^2][a]
4.2	0.92	1.1	–	0.2	–	0.2	0.25
4.5	0.95	1.4	0.045	0.4	0.075	0.23	0.38
5.0	1.1	1.9	0.14	0.65	0.40	0.35	1.0
5.5	1.3	2.5	0.30	0.76	1.25	0.56	2.3
6.0	1.55	3.3	0.60	0.81	3.1	1.06	5.6

[a] Taking into account heat-conduction losses from the plasma column of radius $R = 0.3$ cm.

($\lambda_0 = 3\,\text{cm}$). The reflection coefficient (11.31) is denoted by ϱ_0, and a better value of ϱ (found as an approximation that takes into account the smearing of plasma boundaries, which reduces the reflection coefficient) was used [11.1].

As the temperature decreases, the absorption length of the electromagnetic waves, $l_\omega \propto n_e^{-1} \propto \exp(I/2kT)$, sharply increases. The plane wave model becomes meaningless when l_ω is comparable with the radius R of the discharge column. Progressively greater power is needed because of the plasma's "transparency" to the wave, $l_\omega > R$. This is similar to the situation with the rf discharge (Sects. 11.3.9, 10). The minimum *threshold* temperature T_t for microwave discharges is found from the condition $l_\omega(T_t) \approx R$. In air, $T_t \approx 4200\,\text{K}$ for $R = 0.3\,\text{cm}$ and it corresponds to *threshold* fluxes in the plasma of $S_{1t} \approx 0.2\,\text{kW/cm}^2$, and to the incident wave flux $S_{0t} \approx 0.25\,\text{kW/cm}^2$. These figures agree with experimental data. The reflection of the electromagnetic wave from the plasma, increasing as temperature increases, restricts the possibility of reaching high temperatures in microwave discharges. In air, the plasma temperature does not exceed 5000–6000 K.

11.4.5 Geometrical Optics Limit

In the general case of comparable real and imaginary parts of the complex dielectric permittivity, that is, $4\pi\sigma/\omega|\varepsilon| \sim 1$, the flux $\langle S \rangle$ cannot be given in purely differential form (11.23) or (11.32). This situation is typical for microwave discharges (Table 11.1). However, in the limit $4\pi\sigma/\omega\varepsilon \ll 1$ and $\varepsilon \approx 1$ (which becomes possible at high frequencies) the equation that is exactly valid for homogeneous media, (11.32), becomes meaningful for nonhomogeneous media as well because in this case electromagnetic waves are only weakly damped over a distance of the order of one wavelength, λ_0/n ($\varkappa \approx 2\pi\sigma/\omega \ll 1$, $n \approx \sqrt{\varepsilon} \approx 1$; Sect. 3.5.5). This case corresponds to the geometrical optics approximation. If $n \approx 1$, $\varkappa \ll 1$, then (11.31) implies that reflection is low: $\varrho \ll 1$. There then exists an exact second integral of Maxwell's equations and of the equations for energy; like (11.24), this integral makes it possible to express the plasma temperature in terms of the external field parameters. Substituting $\langle S \rangle$ given by (11.32) into (11.28), multiplying the result by $\sigma = c\mu_\omega/4\pi$, and integrating the result, we find the relation

$$\int_{T_w \approx 0}^{T_m} \sigma(T)\lambda(T)dT = \frac{c}{4\pi} S_0 \,, \tag{11.34}$$

which is akin to (16.10) for constant fields and to (11.24) for rf fields.

11.4.6 Quasistationary Field Limit (RF Discharge)

The rf discharges treated in Sect. 11.3, where it was possible to neglect the displacement current in Maxwell's equation, correspond to the opposite limiting case of $4\pi\sigma/\omega|\varepsilon| \gg 1$. As follows from the arguments of Sect. 3.5.6, in this case $n \approx \varkappa \approx \sqrt{2\pi\sigma/\omega} \gg 1$, and (11.31) implies that $\varrho \approx 1$. The incident wave is reflected from the plasma almost completely and the field penetrating

into it is damped out over one skin layer thickness, $\delta = c/\sqrt{2\pi\sigma\omega}$. This does not mean, though, that only a small fraction of the energy supplied by the generator is injected into the plasma in rf discharges. First of all, it is meaningless to speak of inductively coupled rf discharges in *wave* terms, because the wavelength is much greater than the dimensions of the system. If, however, we insist on the "wave" standpoint, the effect can be interpreted to indicate that the "reflected" power is returned into the generator, which only has to replenish the small difference between the incident and reflected fluxes of electromagnetic energy. The situation with discharges in waveguides is different. For technical reasons, here we have to transport the wave reflected by the plasma away from the generator, so that reflection brings down the efficiency of utilizing the generator energy.

11.5 Continuous Optical Discharges

11.5.1 Specific Features of Optical Sustainment of Plasma

The discharge in the optical frequency range is a relatively novel phenomenon. Even the combination of these two terms – *optical discharge* – has been accepted only rather recently. Nevertheless, the term reflects the physical content of the process to the same extent that the long-familiar terms "microwave disharge" and "rf discharge" do. Dense equilibrium plasmas can be sustained in a steady state by optical radiation, just as by other constant and oscillating fields. Likewise, an optical plasma generator (*optical plasmatron*) can be obtained if cold gas is pumped through the discharge zone. The possibility of implementing these processes was given a theoretical foundation in [11.7], and a *continuously burning optical discharge* was realized in the laboratory in 1970 [11.8].

A fairly high optical power is required to sustain a plasma. If the objective is a long-term effect, as achieved in all other fields, only CO_2 laser radiation can be exploited at present, because this is the only practically available high-power cw laser. Fortunately, the wavelength of the IR radiation of CO_2 lasers is large, since the absorption coefficient of plasma for light falls off steeply with frequency. For instance, visible light is absorbed rather weakly in atmospheric-pressure plasmas (Sect. 11.5.3). Pumping the necessary power into a plasma in the visible light frequency range would require a power greater than that of CO_2 lasers by a factor of 10^2 to 10^3.

The optical method of supplying energy to plasma has a very distinctive feature. No structural elements are needed to carry the energy to plasma (electrodes, inductor, waveguide or resonator). Optical radiation can be transported by a light beam across empty space or through any gas; this is attractive and promissing for applications. In principle, an optical discharge can be initiated anywhere, far from any solid objects; the disharge can be made to travel along the beam, or it may be localized by *focusing* the radiation and thus stabilizing the discharge. The plasma can be moved through space by shifting the beam, for example, by moving the focus to which the discharge is "locked". As we have mentioned, an

optical plasmatron can be designed by blowing a cold gas through the discharge zone stabilized by focusing the beam; this plasmatron produces a continuous plasma jet with a very high temperature. Even under standard conditions, the plasma temperature of optical disharge is substantially higher than in other discharges: 15,000–20,000 K. Finally, the high temperature of optical discharge can be used for developing stable light sources of very high brightness localized, in principle, in free space.

The possibility of generating a continuously burning optical disharge by nonlaser light sources is extremely limited. The absorption coefficient in the optical frequency range being quite low, a very high degree of gas ionization (close to total single ionization of atoms) is required for appreciable energy deposition in a given volume. The plasma temperature must be correspondingly high, 15,000–20,000 K. But the source of energy sustaining the plasma must be at a temperature at least as high. Indeed, the second law of thermodynamics forbids free transfer of energy from a colder to a hotter body. It is thus impossible to sustain a temperature above the solar temperature of 6000 K by focusing rays from the sun with a mirror or lens, of even arbitrarily large diameter and concentrating arbitrarily high power. However, the absorption of light by plasma at this low temperature is so weak that even if a plasma were somehow initiated, it would immediately decay because of nonreplenished energy losses.

11.5.2 Experimental Arrangement

The beam of a CO_2 laser is focused by a lens (or a mirror) (Fig. 11.10). The lens is made of NaCl or KCl, since ordinary glass is opaque to the infrared line $\lambda = 10.6\,\mu$. To initiate the discharge, it is necessary to create the *seed plasma nucleus* (the problem of *initiation* has to be solved for all types of equilibrium discharge). This can be achieved by stimulating breakdown in the focal spot with an auxiliary system or with a tungsten wire introduced into the focal spot for a short time. The metal on the wire surface is slightly vaporized, the vapor is ionized and starts absorbing laser light. The wire is immediately removed and the discharge keeps burning in the gas. The plasma slightly shifts from the focal spot towards the laser up to the point where the intensity of the beam is just sufficient for to sustain the plasma. The size of the plasma region changes from 1 mm at a threshold power to 1 cm and more at higher power levels.

In order to be able to work with different gases and to vary their pressure, the beam is sent into a chamber through a salt window. If the laser power is

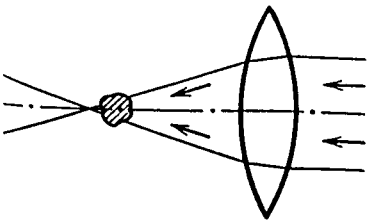

Fig. 11.10. Experiment for sustaining continuous optical discharge. Plasma (*shaded*) is shifted from the focal point towards the laser beam

high enough, a continuous optical discharge can be started in free air. Pioneer experiments [11.8] used a laser that was small by today's standards, 150 W. More powerful lasers were a rarity at the time (1970). The discharge was initiated in xenon at a pressure of several atmospheres, since theory predicted that the required laser power should be small. Now that researchers have considerably more powerful lasers, discharges are produced in different conditions, including in the open air. Actually, this last feat requires laser power that is high even by current standards, not less than 5 kW, and a high-quality beam (low-divergence beam) that allows good focusing.

11.5.3 Absorption of CO_2 Laser Radiation in Plasmas

The quanta of the CO_2 laser, $\hbar\omega = 0.117$ eV, are small in comparison with kT ($\hbar\omega/k = 1360$ K) and are thus absorbed in a strongly ionized optical-discharge plasma, by reverse bremsstrahlung mechanism, in electron-ion collisions. After doubly charged ions are taken into account, the formula for the coefficient of absorption of CO_2-laser quanta, with numerical coefficients, is [11.1]

$$\mu_{\omega(CO_2)} = \frac{2.82 \times 10^{-29} n_e (n_+ + 4n_{++})}{\{T[\mathrm{K}]\}^{3/2}} \lg \left\{ \frac{2.7 \times 10^3 T[\mathrm{K}]}{n_e^{1/3}} \right\} \mathrm{cm}^{-1} . \quad (11.35)$$

An important point for what follows is the maximum that $\mu_\omega(T)$ has at $p = \text{const}$ (Fig. 11.11). The maximum appears when the single ionization of atoms is almost complete. As the temperature increases further within a certain interval, the degree of ionization remains almost unchanged. Double ionization starts at considerably higher temperatures, while the gas density and hence $n_e \approx n_+$ at $p = \text{const}$, keep decreasing as $1/T$. Therefore, prior to the onset of double ionization, $\mu_\omega \propto n_e^2 T^{-3/2} \propto T^{-7/2}$. A new strong increase of $\mu_\omega(T)$ occurs in the course of double ionization, but such high temperatures are not achieved in discharges.

The maximum value of the coefficient $\mu_{\omega,\max}$ increases with pressure somewhat more slowly than p^2. In air at $p = 1$ atm., $\mu_{\omega,\max} \approx 0.85\ \mathrm{cm}^{-1}$ and the minimum absorption length of the laser radiation is $l_{\omega,\min} \approx 1.2$ cm. For neodymium laser light, $\lambda = 1.06\ \mu$, $\mu_{\omega,\max} \approx 6 \times 10^{-3}$ cm, and $l_{\omega,\min} \approx 170$ cm. These figures show clearly why short-wave radiation is not advantageous for sustaining a plasma: the transparency of the plasma is too great.

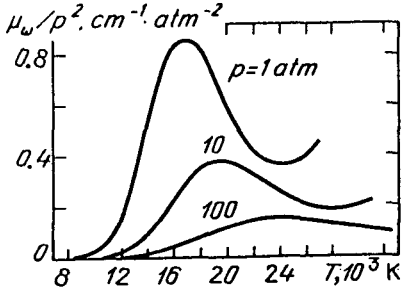

Fig. 11.11. Absorption coefficients for CO_2 laser radiation in air. The maximum absorption coefficients (from the *upper* to *lower* curve) are $\mu_{\omega,\max} = 0.85$, 38, 1600 cm^{-1}

11.5.4 Plasma Temperature and Threshold Power

Figure 11.10 shows the complex geometry of light beams supplying energy to the plasma, and of the discharge zone. As in the case of discharges in waveguides, the selection of a suitable one-dimensional model for analytical evaluations involves certain crude assumptions. Nevertheless, the main features of the process are in satisfactory agreement with the spherical model, especially if the beam is focused by short-focus optics and the beam power is not much greater than the threshold level (so that the plasma cannot shift away from the focal spot).

Consider a plasma sphere of radius r_0; high temperature is maintained in it by absorbing convergent spherically symmetric rays of total power P_0. As in all preceding cases, we assume that absorption is absent ($\mu_\omega = 0$) outside the sphere, where $T < T_0$, while inside the sphere the absorption coefficient μ_ω is constant and corresponds to the maximum temperature at the center, T_m. The possibility of approximating $\mu_\omega(T)$ by a step function is justified by the steep rise of this function to the maximum value. At the *threshold* power level, the dimensions of the plasma region are small and the plasma is transparent to the laser light. The power absorbed in the plasma is of the order of $P_1 \approx P_0 \mu_\omega r_0$. It is transported out of the energy deposition zone by the heat conduction flux J_0.

In general, the temperature in optical discharges is high, and radiative losses may be considerable, although this is mostly true for pressures above 5 atm. and powers substantially greater than the threshold level. The size of the plasma region at the limit of plasma existence is so small that heat conduction losses, proportional to $4\pi r_0^2$, are greater than the radiative losses, which are proportional to the plasma volume $4\pi r_0^3/3$ (owing to the plasma transparency). Therefore,

$$P_1 = 4\pi r_0^2 J_0 \approx 4\pi r_0^2 \Delta\Theta / r_0 = 4\pi r_0 \Delta\Theta \,. \tag{11.36}$$

where $\Delta\Theta = \Theta_m - \Theta_0$ is the drop in the heat flux potential in the plasma. Beyond the absorbing sphere of radius r_0,

$$-4\pi r^2 d\Theta/dr = P_1 \,, \quad \Theta = P_1/4\pi r \,, \quad \Theta_0 = P_1/4\pi r_0 \,. \tag{11.37}$$

This expression takes into account that the gas at "infinity" is cold. As follows from (11.36) and the last equation of (11.37), $\Delta\Theta = \Theta_0$ or $\Theta_m = 2\Theta_0$. The substitution of the absorbed power $P_1 = P_0 \mu_\omega r_0$ into the equation $P_1 = 2\pi r_0 \Theta_m$ gives the relation of the laser power to the temperature at the center of the plasma region:

$$P_0 = 2\pi\Theta(T_m)/\mu_\omega(T_m) \,. \tag{11.38}$$

As the function $\mu_\omega(T)$ has a maximum and $\Theta(T)$ is monotonic, the power P_0 passes through a minimum (Fig. 11.12). The minimum $P_{0,\min} \equiv P_t$ lies at a temperature T_t close to the point $\mu_{\omega,\max}$. This is the lowest (*threshold*) power of focused light beam that is sufficient for sustaining a steady-state plasma. The states on the left-hand branch of the curve $P_0(T_m)$, where $T < T_t$, are *unstable* and thus cannot be realized. Indeed, if the temperature increases, the actual power

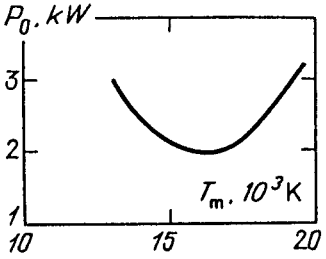

Fig. 11.12. Power of spherically convergent laser beam as a function of maximum plasma temperature of steadily sustained plasma. Air, $p = 1$ atm., CO_2 laser radiation

becomes greater than that required to maintain the new state. The plasma gets heated up until the state switches to the right-hand side. Similar arguments then readily show that these states are stable. This situation is typical for equilibrium discharges.

More detailed analysis is required to evaluate the plasma radius r_0. It cannot be found from (11.36–38). The point is that r_0 is connected with the dimensions of the light channel (in the spherical model, this is the focal spot radius ϱ_0). This radius was ignored in earlier arguments because we assumed that the rays coverge exactly at the center. The minimum plasma radius corresponding to threshold conditions equals $r_{0,\min} \equiv r_t \approx \sqrt{(4/3)\varrho_0 l_\omega}$ [11.1]. For $\varrho_0 \approx 10^{-2}$ cm, $l_\omega \approx l_{\omega\min} \approx 1$ cm, $r_t \approx 1$ mm.

11.5.5 Required Laser Power

The evaluation formula (11.38) predicts the laser power needed to sustain a continuously burning optical discharge under specific conditions. It corresponds to roughly $T_m = T_t$ and $\mu_{\omega,\max} = \mu_\omega(T_t)$. Thus the plasma temperature for the CO_2-laser radiation ($\mu_{\omega,\max} \approx 0.85\,\text{cm}^{-1}$) in atmospheric-pressure air is $T_t \approx 18,000$ K and $\Theta_t \equiv \Theta(T_t) \approx 0.3$ kW/cm; the threshold is $P_t \approx 2.2$ kW. These figures are confirmed by experimental data. As the pressure increases, the threshold power decreases rather rapidly since $\mu_{\omega,\max}$ increases; this behavior is obsrved up to a certain limit at which radiative losses become important. The threshold is lower in gases with low ionization potential and low thermal conductivity (lower T_t and Θ_t). This is why xenon at $p \approx 3$–4 atm. was chosen for the initial experiments with a low-power laser: from 100 to 200 W would be sufficient then in Xe or Ar. About 300 kW would be needed to sustain a discharge in atmospheric-pressure air at the frequency of the neodymium-glass laser.

11.5.6 Why Unusually High Temperature Is Obtained in Optical Discharges

The temperature in arc and rf discharges in atmospheric-pressure air is about 10,000 K, in microwave discharges it is about 5000 K, and in optical discharges, about 18,000 K. In argon $T \approx 20,000$ K, twice that of arc and rf discharges. The reason lies in the transparency of the plasma to optical radiation, owing to the dependence $\mu_\omega \propto \omega^{-2}$.

At not too high frequencies, the field energy is efficiently dissipated even if ionization is not too high, that is, if temperature is moderately high. Moreover,

the field does not penetrate a strongly ionized plasma (owing to skin effect or reflection), which diminishes dissipation and heating. Dissipation at optical frequencies is at its highest when the degree of ionization is very high. As the gas gets hotter, it remains transparent but absorbs more and more strongly, thereby facilitating further heating, until total single ionization is achieved. At very high pressures, however, it is very difficult to raise the temperature higher than 13,000–15,000 K, since radiative losses, going up with temperature, become considerable.

The unusually high temperature in an unenclosed gas, not shaded by walls, is a unique property of the continuous optical discharge which makes it possible to develop a light source of extremely high brightness: The optical discharge plasma emits blindingly bright white light, which cannot be viewed with the naked eye. Especialle high temperatures up to 25,000–30,000 K, are predicted for helium at $p \approx 1$–3 atm., since helium has an extremely high ionization potential [11.9]. This could be a high-power source of UV light. However, helium also manifests a high threshold, so that this source would not be inexpensive.

11.5.7 Measurement of Temperature and Thresholds

Figure 11.13 shows photographs of continuously burning optical discharge [11.10]. The temperature field is plotted in Fig. 11.14 [11.11]. The temperature was measured by recording continuum radiation in a narrow interval of wavelengths around $\lambda = 5125$ Å and the radiation in spectral lines of nitrogen atoms and ions. The center of the plasma region shifted 1.1 cm towards the beam. The temperature measured at the center at $p = 2$ atm. was 18,000 K in Ar, but 14,000 K in Xe (below the ionization potential). In H_2 at 6 atm., it was 21,000 K, and in N_2 at 2 atm. it was 22,000 K. The temperature always falls off in a monotonic manner from the center to the periphery of the plasma region. The region size is

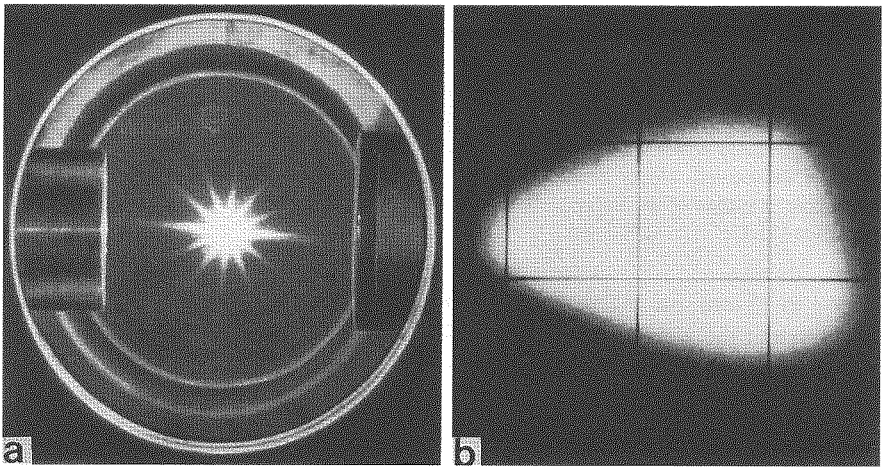

Fig. 11.13. Photograph of continuous optical discharge [11.10]. **(a)** General view through the chamber window (8 cm diameter); **(b)** enlarged image: 1 division: 1 mm, the beam travels from *right* to *left*

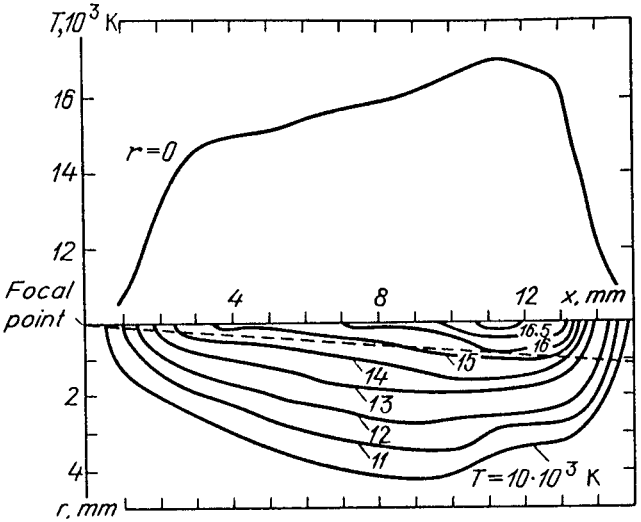

Fig. 11.14. Measured spatial temperature distribution in continuous optical discharge [11.11] in air at 1 atm.; CO_2 laser power is 6 kW and the beam travels from *right* to *left*. Effective boundary of the convergent light channel is shown by the *dashed line*. *Lower* part: isotherms, x is the optical axis, r is the radial distance from the axis. *Upper* part: distribution $T(x)$ along the beam axis

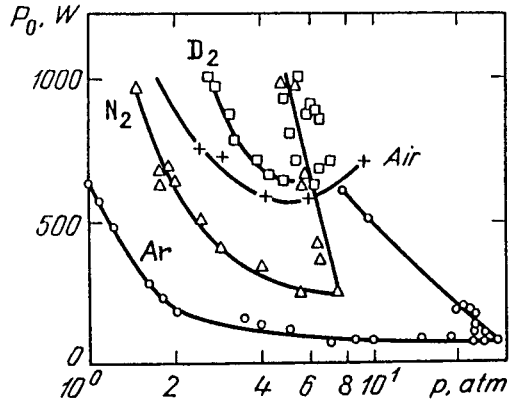

Fig. 11.15. Threshold power required to sustain continuous optical discharge in several gases (lower branches of the curves). Upper boundaries for the existence of discharge in N_2 and Ar are also shown (upper branches of the curves). The existence domain in P_0, p lies betwen the *upper* and *lower* curves [11.12]

usually 3 to 15 mm; the plasma is elongated parallel to the optical axis, following to some extent the shape of the light channel.

The threshold power as a function of pressure is plotted in Fig. 11.15 [11.12]. At $p \sim 1$ atm. the threshold power falls off steeply with p (lower curves), but the curves flatter out at $p \sim 5$ atm. This behavior is caused by a change in the energy loss mechanism. The heat radiation loses Φ [W/cm^3] at a given temperature increase with pressure very nearly as the laser light absorption coefficient μ_ω,

because both of these quantities are proportional to $n_e n_+ \approx n_e^2$. Under nearly threshold conditions, the energy release due to absorbed laser energy compensates for the radiative losses. Now $\mu_\omega S \approx \Phi$, where $S = P/\pi R^2$ is the intensity of laser radiation, and R is the radius of light channel in the region of plasma generation. If μ_ω and Φ depend on p in the same manner, the threshold power $S\pi R^2$ is a weak function of p. The thresholds in molecular gases are higher than in heavy inert gases: the transfer of the molecular dissociation energy contributing appreciably to the thermal conductivity (Figs. 10.19, 20).

When a laser beam is focused by a lens with a not very short focal length ($f \approx 8$–10 cm or more), an upper limit to both P and p may be observed in some gases (Fig. 11.15). Steady-state discharges cannot be sustained at power levels P above the upper limit, and at pressures p above the point where the upper and lower curves converge (Fig. 11.15). This is a consequence of the attenuation of the laser beam when it penetrates the absorbing plasma. The beam intensity becomes insufficient for compensating radiative losses deep in the plasma [11.12]. If the beam is focused by a short-focus mirror with $f = 1.5$–2.5 cm, the upper limits on P and p are not observed (Fig. 11.16) [11.13]. In this case, the attenuation of the beam intensity due to light absorption upon penetration into the plasma is overcome by the intensity increase due to the large beam-convergence angle. As a result, the energy source supplying the making up for radiative loss is not depleted. Note that the laser beam in experiments [11.13] is sent vertically upward, which helps stabilize the discharge. The upward convective flux of heated gas caused by the Archimedes' force shifts the plasma toward the focal spot, into the zone of increased intensity. In experiments [11.12], the beam was horizontal so that the convective flow tended to displace the plasma out of

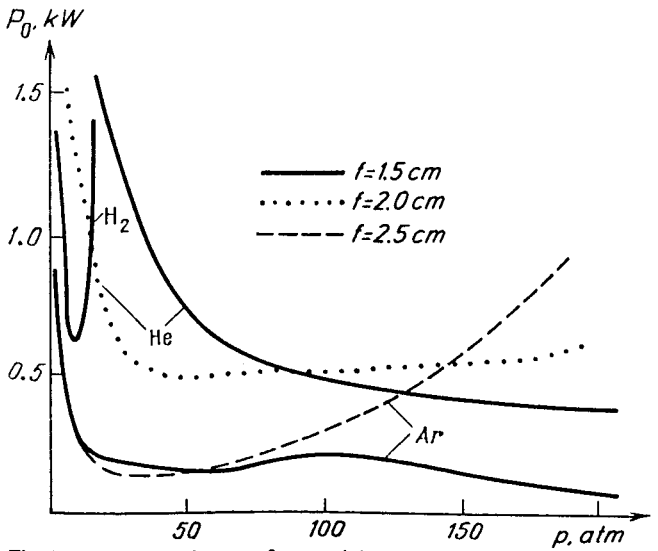

Fig. 11.16. Threshold power for sustaining continuous optical discharge at high pressures [11.13]. f is the focal distance of the focusing mirror

the light beam, thereby impeding the sustainment of discharge. Presumably, this factor may constitute a constraint on the domain of existence of the discharge.

11.5.8 Two-Dimensional Calculations and a One-Dimensional Model

The temperature field of the optical discharge is described by the balance equation for plasma energy (11.1), where it is advisable to replace $\sigma\langle E^2\rangle$ by $\mu_\omega S$. The geometry of the discharge is two-dimensional: the temperature $T(x,r)$ is a function of x along the optical axis and of radius r in the transverse direction (Figs. 11.10, 14). To simplify the problem, we assume that the laser intensity S has a constant distribution over the light beam cross section, and operates with power $P(x) = S\pi R^2$ and replace the absorption coefficient $\mu_\omega[T(x,r)]$ by its value $\mu_\omega[T(x,0)]$ on the axis. Then the energy release term is $\mu_\omega P/\pi R^2$, where P satisfies the equation $\partial P/\partial x = -\mu_\omega P$ – equivalent to (11.4, 32) for a variable cross section channel. In the heated zone, the shape of the light channel is essentially non-conical owing to the *refraction* of laser radiation in the plasma that it generates. Correspondingly, an equation is added to the system which describes the channel radius $R(x)$. An important factor is the *radiative heat transfer;* owing to this, the term Φ is not just the bulk radiation rate, but the difference between the emission and absorption of thermal radiation. To find Φ, the spectral *equation of radiative heat transfer* is used [11.14], and it is also included into the system of equations.

The solution of the above problem for the conditions corresponding to Fig. 11.14 [11.15] is in good agreement with the recorded temperature field and provides an explanation of one previously unexplained effect. The point is that usually a considerable part of the laser power passes through the plasma: 2.8 kW out of 6 kW in the present case. This would be amply sufficient for sustaining the discharge at the focal point, since only 2 kW is needed (this is the threshold for atmospheric air). Actually, two separated plasma regions are never observed, and the temperature at the point of the geometrical focus is considerably lower than at the center of the plasma region (Fig. 11.14). It was found that as a result of refraction, conically converging rays begin to diverge precisely at the point of $T \approx T_{\max}$. Now everything is clear: the hottest plasma is at the narrowest part of the light channel, where the laser radiation reaches its maximum concentration. Obviously, this segment lies closer to the lens than the geometrical focal point. The smallest radius of the distorted light channel is greater by an order of magnitude than the radius of the focal spot in the absence of plasma.

The energy balance of a discharge sustained in atmospheric air is illustrative: out of 6 kW of laser power, the plasma consumes 3.2 kW. The absorption takes place in the central zone, where $T > 10,000$ K. Almost all of the absorbed energy is radiated away apart from the UV part of the radiation, representing 1.9 kW, which is absorbed in the region where $6000 < T < 10,000$ K. Out of the energy transported to "infinity", 2 kW is lost via heat conduction and 1.2 kW via radiative losses. The radiative heat transfer is thus quite intense in high-temperature gas.

Two-dimensional calculations are complicated and time-consuming. For this reason, a simplified one-dimensional model of a continuously burning optical discharge has proved to be quite useful [11.16]; it provides a speedier way of solving a number of problems and leads to a fairly satisfactory fit to experimental data (an example is given in Sect. 11.6.5). The one-dimensional model deals with the temperature distribution along the optical x axis. Correspondingly, the radial part of the heat flux divergence in (11.1) is replaced approximately by the term of radial heat-conduction losses $A\Theta/R^2$, where $\Theta(x)$ is the heat flux potential (Sect. 10.10.2), and $A \approx 1.5$–2 is a numerical coefficient whose value reflects the specific radial temperature profile. Radiative heat transfer is treated in this model using the radiative transfer equation. On the subjects of optical discharge see [11.1, 17, 18]; these references give the necessary bibliography.

11.6 Plasmatrons: Generators of Dense Low-Temperature Plasma

In Sect. 11.1 it was mentioned that any steady discharge can be used for developing a *plasmatron* by blowing cold gas through it. Plasmatrons of three types are currently employed in practice: *arc*, *rf*, and *microwave* systems (the *optical* plasmatron has not yet progressed left beyond the experimental stage).

11.6.1 Arc Plasmatrons

This type evolved long ago to the stage of industrial units, with powers ranging from hundreds of watts to thousands of kilowatts [11.19]. The design of high-power machines involves numerous engineering problems: stabilization, cooling, increasing the electrode service life, material selection, etc. The schematic diagram of a plasmatron is shown in Fig. 11.17a. The material to be processed is often used as the anode (Fig. 11.17b). Such systems are employed for cutting, welding, and arc-plasma melting of metals.

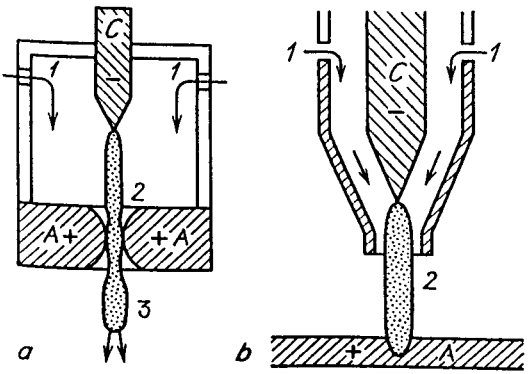

Fig. 11.17. Layout of an arc plasmatron: (a) Plasma jet *(3)* emerges from an orifice in the anode A; C is the cathode, *(1)* cold gas supply, *(2)* discharge. (b) The machined part (metal sheet to be cut) serves as the anode

11.6.2 RF Plasmatron

The basic scheme of an rf plasmatron is not very different from that of static discharge devices. The discharge burns in a tube placed inside an inductor coil. A cold gas is fed into the tube, and a plasma jet flows out of it (quite often, into the ambient atmosphere). The inductively *coupled plasma torch* in its modern form was designed by *Reed* in 1960 (Fig. 11.18). The most important design feature in it is the use of a *tangential gas inflow*. The point is that the plasma of a steady rf discharge extends nearly to the tube wall, so that the thermal load on the tube is very heavy. The situation is not greatly alleviated by simply pumping the gas axially. In the tangential inflow systems, the gas is pumped into the tube 20 to 30 cm upstream of the inductor tangentially to the cylindrical surface. The gas flow is helical. As a result of the centrifugal force, the pressure in the axial region is lowered and a vortex is formed. The longitudinal flow is weak here. The cold gas mostly flows along the tube within the peripheral cylindrical layer and squeezes the discharge away from the walls, thereby protecting them from the destructive effects of the high temperature. Gas flow rates are usually such that the average longitudinal velocity of the cold gas is about 1 m/s. The plasma jet is ejected into the atmosphere at a velocity of several tens of m/s. Inductively coupled plasmatrons whose power reaches tens and even hundreds of kilowatts are in operation today. Figure 11.19 shows a photograph of a discharge and plasma jet.

11.6.3 Microwave Plasmatrons

Typical designs of microwave plasmatrons are shown in Fig. 11.20. The one shown in Fig. 11.20a is not very different from the waveguide discharge scheme. A helical flow of gas is forced through the dielectric tube inserted through the waveguide. The discharge is squeezed away from the walls and the heat is transported out of the tube by the plasma jet. One advantage of microwave plasmatrons is their high efficiency: up to 90 %. This is achieved, among other things, by reflecting the wave transmitted through plasma back into it (Sect. 11.4.1). The plasma temperature here is not high, 4000–6000 K, less than in rf plasmatrons (9000 to 10,000 K) but this is sufficiently high for some applications. The plasma is as pure as in rf plasmatrons, in contrast to arc plasmas contaminated with products of electrode erosion. A power of several kilowatts is pumped into the plasma.

Figure 11.20b shows a different, quite promising arrangement aimed at producing high powers [11.5]. The discharge is sustained at the axis of a circular cross section waveguide of 5 cm radius and several tens of cm long. Microwaves of type E_{01} and wavelength in vacuum $\lambda_0 = 12.5$ cm are sent into the waveguide. The inner surface of the waveguide and the outer surface of the plasma column (its radius is about 1 cm) form a coaxial line for electromagnetic waves. The discharge is stabilized at the axis by a helical flow of gas pumped through the waveguide tube. The tube ends with a nozzle that lets out the plasma jet. The microwave power is almost completely absorbed by the plasma. The elec-

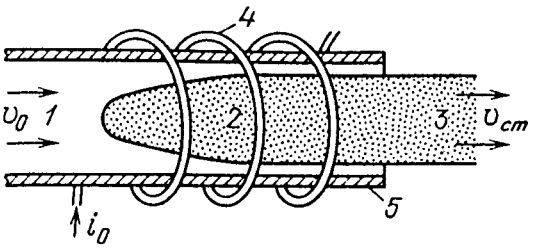

Fig. 11.18. Layout of an inductively coupled plasmatron. *(1)* cold gas inflow, *(2)* discharge, *(3)* plasma jet, *(4)* inductor coil, *(5)* dielectric tube

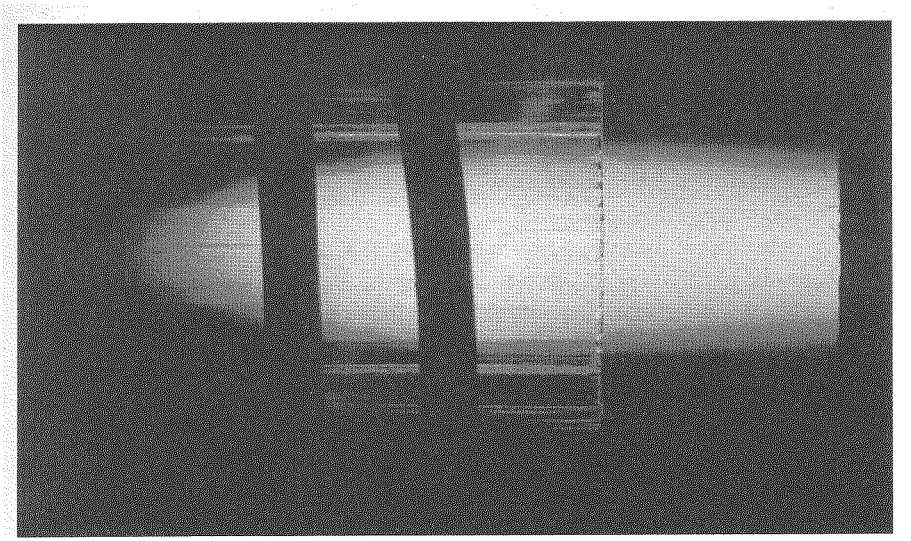

Fig. 11.19. Photograph of discharge and plasma jet. Tube diameter 6 cm; gas (air) flows from *left* to *right*; $p = 1$ atm.; flowrate 2×10^3 cm^3/s; power input into plasma 27 kW; temperature measured on the axis at the tube end 9800 K [11.20]

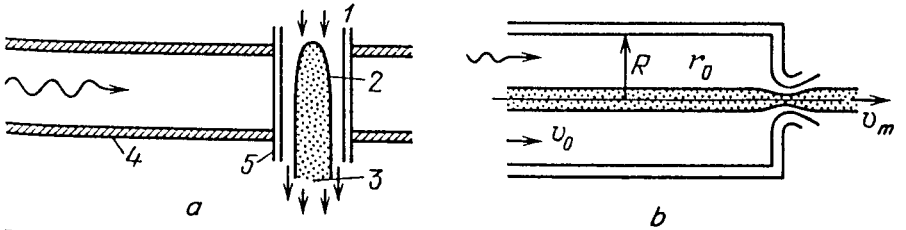

Fig. 11.20. Microwave plasmatrons. **(a)** Discharge *(2)* in dielectric tube *(5)* passing through a waveguide. *(1)* cold gas inflow, *(3)* plasma jet, *(4)* waveguide. **(b)** Coaxial design. Arrows show the gas flow and the electromagnetic wave. Discharge column and plasma jet are *shaded*

tromagnetic energy flux flows into the discharge column from the surface, along radii, just as in the inductively coupled rf discharge or in the resonator discharge; as microwaves travel along the tube, their energy is gradually dissipated. The plasma temperature is $T \approx 5000\,\mathrm{K}$.

11.6.4 Flow Around or Flow Through?

Two mutually exclusive idealized schemes can be used to begin analyzing the complex pattern of hydrodynamic flow in plasmatrons. We can assume that the discharge is burning not only in a region that is spatially defined, but also in a specified mass of gas which is, on the average, not moving and is placed in a gas flowing around it. This situation resembles the convective cooling of a solid heated from within. If the discharge ("heated body") is cylindrical, the flow around it can be illustrated with streamlines, as in Fig. 11.21. Heat conduction transfers the heat of the hotter volume to the contiguous layers of the gas flowing around it. Clearly, the temperature in the converging part of the stream just behind the heated body must be close to that of the body.

As follows from the analysis of all static discharges, the plasma temperature is mostly determined by the energy balance in the energy deposition zone. The temperature is hardly dependent on the fate of the energy once it has been transported beyond the discharge volume into the nonabsorbing, currentless zone. It can be expected, therefore, that the temperature in the discharge zone is not very sensitive to whether the heat goes through the walls cooled by a flow outside or carried away by the flow that is in direct contact with the fixed discharge volume. In other words, the discharge plasma temperature in the flow-around mode is approximately found by calculations for the appropriate static situation.

If the gs flows *through* the discharge, each mass of high-temperature gas leaving the plasmatron has resided in the discharge zone, and has had energy deposited directly in it. A qualitative representation of the flow is shown in Fig. 11.22 for the case of an inductively coupled plasmatron [11.1]. The heat is transported from the skin layer, where the energy is deposited, by the radial heat conduction flux. As a result of simultaneous longitudinal heat transport by the gas stream, the discharge surface [rather, an isotherm corresponding to the ionization temperature ("conduction onset point") $T_0 \approx 8000\,\mathrm{K}$] is tilted with respect to the axial flow. Cold-gas streamlines entering the high-temperature zone become tilted with respect to the axis and they undergo refraction in the layer where the temperature abruptly increases. This happens because of the expansion of the gas upon heating. The velocity component tangential of the isothermal surface

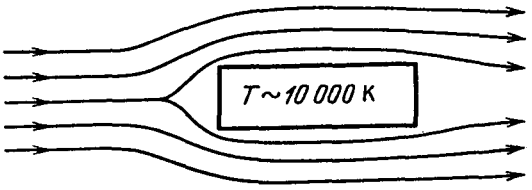

Fig. 11.21. Flow of cold gas around a static discharge burning in a specified mass of gas

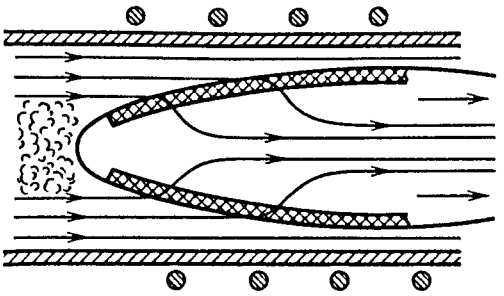

Fig. 11.22. Gas flow in an inductively coupled plasmatron if the gas is assumed to flow through the discharge region. The transitional region from the cold gas to the plasma and the layer of energy deposition are *shaded*. Gas streamlines are traced. Eddies are shown on the *left* in front of discharge

remains unchanged but the normal component greatly increases by virtue of the conservation of the mass flux density, $\varrho_0 v_n = \varrho_m u_m$. Here ϱ_0 is the density of the cold gas, v_n is the velocity at which the gas flows into the discharge zone along the normal, and ϱ_m and u_m are the density and normal component of the velocity of the hot gas emerging from the skin layer. The plasma temperature in the flow-through mode is also not very different from that in the static discharge [11.1, 18].

The actual flow pattern is intermediate between the diagrams of Figs. 11.21 and 11.22, and may sometimes be closer to one or other of the two version (Sect. 11.6.7).

11.6.5 Normal Velocity of Discharge Propagation

The crucial element in the interaction of gas flow and electrical discharge as shown in Fig. 11.22 is the process, in some segment of the shaded layer, where the field energy is dissipated and the cold gas is transformed into heated plasma. An ideal model for analyzing this process is that of a plane stationary system viewed in the reference frame fixed to a given element of the discharge front surface.

A cold gas flux $\varrho_0 v_n$ and a flux S of electromagnetic energy enter the discharge (Fig. 11.23). The dissipated energy is conductively transported counter to the gas stream, facilitating the heating of the cold gas to the "ionization" temperature T_0 at which it becomes capable of intensively absorbing the electromagnetic energy. In response to dissipation, the gas heats up from T_0 to T_m. The maximum plasma temperature T_m is not very different from that achieved in the corresponding static discharge; indeed, it is mostly determined by the energy balance in the energy deposition zone, where the temperature difference $\Delta T = T_m - T_0$ is small and the acceleration of the gas is insignificant. In a steady-state process, the gas flows into the discharge zone with a normal component of velocity v_n, related to T_m and S by the energy conservation law. If the entire field energy, released in this zone, is ultimately carried away by the flow, then $S = \varrho_0 v_n w(T_m)$, where w is the specific enthalpy of the gas (the process takes place at constant pressure).

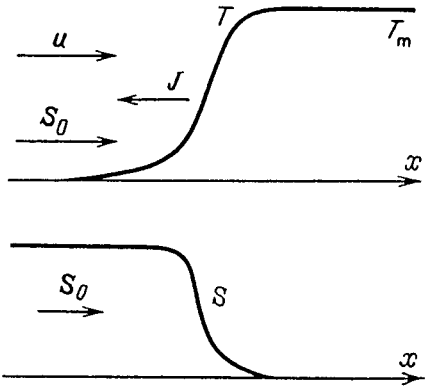

Fig. 11.23. Plane discharge mode in gas flow: temperature (T) and electromagnetic energy flux (S) distributions. *Arrows* indicate the directions of heat flux J, gas flow u, and electromagnetic energy flux S_0

The heat-conduction nature of v_n becomes evident it we resort to (11.19) which expresses the balance of the fluxes of the heat and electromagnetic energy in the dissipation zone of the latter, and to (10.18) which determines the temperature drop in this zone (its thickness is δ). We obtain

$$v_n = \frac{S}{\varrho_0 w(T_m)} = \frac{2\lambda_m \Delta T}{\delta \varrho_0 w_m} = \frac{4\lambda_m k T_m^2}{\delta \varrho_0 w_m I} \approx \frac{4\chi_m}{\delta} \frac{kT_m}{I} \frac{(c_p)_m T_m}{w_m} \frac{\varrho_m}{\varrho_0}$$

where $\chi_m = \lambda_m / \varrho_m (c_p)_m$ is the thermal diffusivity of the hot gas and $(c_p)_m$ is its specific heat at constant pressure; $w_m \equiv w(T_m)$. Normal velocities v_n are typically of the order of $v_n \sim 10 \div 100$ cm/s. For details on discharge propagation, see [11.1, 18].

11.6.6 Optical Plasmatron

Let us consider a continuously burning optical discharge in gas streams (Fig. 11.24). The one-dimensional model outlined in Sect. 11.5.8 is quite suitable for clarifying a number of characteristics of this process. Let us approximate the convergent-divergent light channel by two adjacent truncated cones. Assume the flow to be straight; then the mass conservation law is simply $\varrho u = \varrho_0 v$, where ϱ and u are the density and velocity of the gas at a point x, and ϱ_0 and v are those in the cold incoming stream. Bearing this in mind and converting to spherical polar

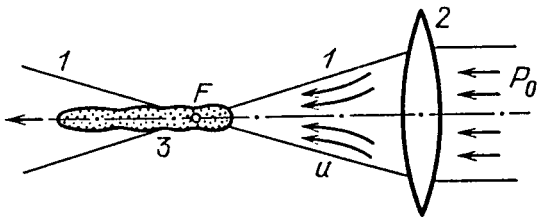

Fig. 11.24. Optical plasmatron: *(1)* light channel contour, *(2)* lens, *(3)* focal spot; *arrows* indicate the directions of laser beam P_0 and of gas flow u

coordinates, as they are more suitable for the cone geometry than cylindrical ones, we rewrite the steady-state equation for energy balance, (11.1, 2):

$$\varrho_0 v c_p \frac{dT}{dx} = \frac{1}{x^2}\frac{d}{dx}x^2\lambda\frac{dT}{dx} - \frac{A\Theta}{R^2} + \frac{P\mu_\omega(T)}{\pi R^2} - \Phi\,. \tag{11.39}$$

This equation is solved simultaneously with $dP/dx = -\mu_\omega P$ and the radiative heat transfer equations for Φ.

Figure 11.25 gives the result of calculations [11.16] for a case that has been experimentally analyzed [11.21]. The discharge plasma was photographed at for several values of v, the velocity of the cold gas stream. The luminous region is spindle-shaped. As the velocity increases, the flow "forces" the plasma into the focal spot while the hot luminous jet stretches beyond this point. At $v > 310$ cm/s, the plasma is blown out and the discharge disappears. As the flow is intensified, the maximum plasma temperature increases; this has also been confirmed by measurements.

Experiments have demonstrated that if the beam is focused by a long-focus lens with $f = 40$ cm, the discharge cannot be sustained at velocities lower than a

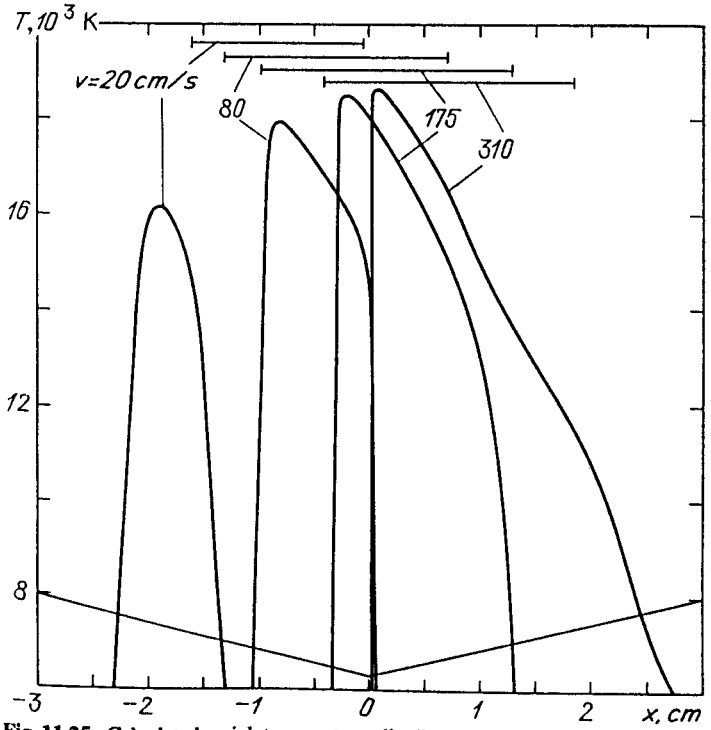

Fig. 11.25. Calculated axial temperature distributions in an optical plasmatron, based on (11.39) [11.16], and comparison with experimental data [11.21]. The beam and gas flow point from *left* to *right*, and the focus lies at $x = 0$. Argon, 1 atm. laser power $P_0 = 1.25$ kW, the focal length $f = 40$ cm, beam divergence 2 mrad. Heat-conduction loss coefficient $A = 2$. *Horizontal bars* show the length and position of the luminous region in the photographs given in [11.21]. Numbers at curves and bars indicate cold gas velocity

certain lower limit, $v \approx 5$ cm/s. If the lens has a short focus, say $f = 10$ cm, the discharge survives at any low gas velocity, and also in stationary gas. Calculations have also shown this effect, defining the domain in power P and velocity v in which the discharge is sustainable; the results fit the experimental data. We can conclude that the one-dimensional model of the phenomenon, as reflected in (11.39), is a good description (see also [11.17]).

The first two-dimensional calculations for continuous optical discharge in a gas stream, based on the system of gas-dynamics Navier-Stokes equations and energy balance equations (11.1,2), have now been performed. They take into account radiative heat exchange and the refraction of laser radiation in the plasma (Fig. 11.26). An interesting feature of the gas dynamics process was revealed by these calculations. The flow is found to be *unstable*. *Vortices* are generated downstream of the central part of the plasma; they are carried away by the flow and new ones are generated.

11.6.7 Fraction of the Flow Passing Through the Discharge

As we see in Fig. 11.26, the stream flows around the energy deposition zone, but nevertheless, some amount of gas flows through it. This was to be expected in view of the analysis presented in Sect. 11.6.4. Let us try to evaluate quantitatively the roles of the two elements in the flow pattern. Consider that part of the discharge front surface, facing the incoming flow, which is effectively the interface of the cold and hot regions. The gas density and temperature in the former are

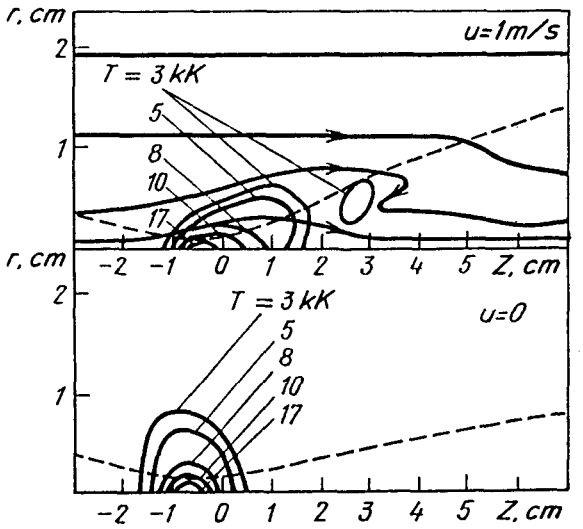

Fig. 11.26. Two-dimensional gas-dynamics calculation of gas flow in optical plasmatron [11.22]: Air, $p = 1$ atm., laser power $P_0 = 6$ kW, focal length $f = 15$ cm, velocity of uniform cold flow $u = 1$ m/s, z is the axial coordinate measured from the geometric focus point, and r is the radial coordinate. Lines of flow (with *arrows*), isotherms (marked by T [kK]), and refraction-distorted contour of the light channel (dashed curve) are traced. Below: isotherms in discharge with no flow is shown for comparison

ϱ_0, $T_{00} \approx 300\,\mathrm{K}$, and in the latter, ϱ_m, T_m; because the pressure is approximately constant $\varrho_0/\varrho_m = \mu_0 T_m/\mu_m T_{00} \sim 10^2$, where μ_0, μ_m are the molecular weights of the cold and hot (dissociated in the case of air and ionized) gases.

Any pressure drops Δp in a region of strongly subsonic flow are independent of the value of the pressure p and are determined by the dynamic pressure of the incoming flow: $\Delta p \sim \varrho_0 v^2$, where v is the velocity of unperturbed flow. The pressure at the critical point of a hot body is somewhat higher than the pressure at infinity. As a result, the velocity of the cold flow drops to a value v_n and the flow turns sideways, streaming around the hot region. The pressure decreases behind the energy deposition front, so that the gas penetrating the discharge is accelerated from v_n to u_m, as dictated by the law of mass conservation: $\varrho_0 v_n = \varrho_m u_m$. The velocity v_n at which the gas flows into the discharge front is the normal propagation velocity described in Sect. 11.6.5. The relations between the velocities v, v_n, and u_m are easily derived if we take into account that there is no scale for the dynamic pressure of hot gas except Δp or the dynamic pressure of the cold gas. This means that $\varrho_m u_m^2 \sim \varrho_0 v^2$. These two relations imply that $v/v_n \sim u_m/v \sim \sqrt{\varrho_0/\varrho_m} \sim 10$ while $u_m/v_n \sim \varrho_0/\varrho_m \sim 10^2$. In contrast to the idealized one-dimensional plane regime (Sect. 11.6.5), the cold gas impinges on the region of stationary discharge, not restricted transversely, not at the normal velocity v_n but at a velocity higher by a factor of $\sqrt{\varrho_0/\varrho_m} \sim 10$. From the total mass flux $\varrho_0 v \Sigma_0$ impinging on the section area Σ_0 of the hot region, a fraction on the order of $\varrho_0 v_n \Sigma_0$ penetrates the front surface. Therefore, the fraction of the incoming flow in the discharge is $v_n/v \sim \sqrt{\varrho_m/\varrho_0} \sim 10\,\%$; the remaining 90 % streams around the heated region as if around a solid body. This displays the effect of the two-dimensional nature of the flow. See details in [11.23].

12. Spark and Corona Discharges

12.1 General Concepts

12.1.1 Outward Features

The *spark discharge* (sparkover) occurs at voltages above the breakdown level at pressures above atmospheric (roughly) in gaps of about 1 cm and longer, that is, at $pd > 10^3$ Torr cm. The voltages required for the breakdown at such high values of pd are quite high, running to tens and hundreds of kV. The discharge is a rapid transient process, not a steady one, and is aptly described by the colloquial phrase "a spark jumps". *Lightning* is a discharge on a grandiose scale: it may be several kilometers long and is the electrical breakdown of the gap between a cloud and the ground, or between two clouds. A spark in laboratory conditions is but miniature lightning. When the breakdown voltage is reached, the interelectrode gap is pierced by a "fast as a lightning" light channel, sometimes zigzag, sometimes branching out, which immediately dies away. A spark is accompanied with a characteristic cracking sound, just as a lightning produces thunder. The sound is caused by the *shock wave*. It is generated by a sharp rise in pressure due to an intensive release of Joule heat in the spark channel when a high discharge current passes through it.

Many people will have seen – in photographs and in films – how a spark jumps across the gap between giant metal spheres supported by insulating columns (film directors are fond of this impressive performance). Such discharge devices are employed in high-voltage engineering (e.g., for voltage measurements). The discharge takes place at a certain minimum voltage that depends on the diameters of the spheres, the distance between them, and – slightly – on atmospheric conditions: pressure, temperature (rather, density), and humidity of the air. The system is calibrated and measurement parameters are standardized. If electrodes are separated by a not too thick dielectric plate of glass or cardboard, the spark may find a way through the plate, shooting a hole in it. Sparkovers occur both in the uniform field of plane gaps, being rooted at spurious points on the electrodes, and in strongly nonuniform fields: between the point and a plane, between a thin wire and a concentric cylinder, etc. In these last cases, the *corona* discharge precedes the sparkover if higher and higher voltages are considered.

A corona, that is, a weakly luminous discharge, appears in the neighborhood of a point or a thin wire, where the field is greatly enhanced. Ionization takes place only locally, and the gas there emits light. The electric current is closed by a flux of charges of a specific sign (depending on the polarity of the point) that

are produced in the self-sustaining-discharge zone at the point and are dragged by a relatively weak field to the other electrode. No radiation appears from the outer region. A corona is typically observed at nearly atmospheric pressures, in air around high-voltage transmission line conductors, around lightning rods and the masts of ships ("Saint Elmo's fire"). To ignite a corona, a certain rather high voltage is required , which depends on the specific conditions. If the voltage is still higher, the remaining part of the gap breaks down and a spark jumps between the electrodes.

A large current, about 10^4–10^5 A, flows through the developed spark channel which is a good conductor. The voltage on the electrodes sharply decreases in response to voltage drop across the external resistance or as a result of the rapid discharge of the capacitor energizing the sparkover, so that the discharge burns out. If the voltage across the electrodes builds up again after the quenching of the discharge, the sparking is repeated. If the power supply is sufficiently powerful for sustaining a large current for a considerable time, the spark current produces a *cathode spot* and the spark transforms into an *arc* (Chap. 10). In fact, the state of the plasma in the channel of even a very transient spark discharge resembles the state in the arc column, so that it is sometimes legitimate to treat the final stage of the spark discharge as a pulsed arc.

The spark discharge is a multifacetted and complicated phenomenon. Its first stage is the process of the *streamer* or *leader* breakdown, which proceeds in a much more complex way than at low pressures where dark or glow discharges are initiated. After the conducting channel has been formed (this is also a multistage and "tricky" process), the discharge occurs. The capacitor is discharged the charge being transferred by the large current which flows across the gap that closes the circuit.

In one type of sparking, the sparks *"creep" along a dielectric* (glass or ebonite). They are produced when the end face of one electrode (e.g., a rod) contacts a dielectric plate and the other electrode is a metal plate on the other side of the dielectric. Discharge channels in the gas hug approach the dielectric, branching out from the rod and running around the plate to reach the metal on the opposite side. A branched trace may be seen on the plate, caused by the deformation of the material due to elevated temperature and pressure in the spark channel. The resulting pattern is known as *Lichtenberg figures*. the type of the pattern depends on the polarity of the rod, and its size is determined by voltage; the latter fact has been used for measurements and for studying atmospheric storm discharges.

12.1.2 Inapplicability of Townsend's Breakdown Model for High Pressure, Long Gaps, and Considerable Overvoltages

The breakdown mechanism based on the *multiplication of avalanches* via *secondary cathode emission* is predominant at low pressure, approximately at $pd < 200$ Torr cm. The corresponding theory, the principles of which were formulated by Townsend early in this century, explains a great number of observations. It gives a consistent interpretation of Paschen's dependence of the breakdown

voltage V_t on pd, with its characteristic minimum (Sect. 7.2), and even gives a satisfactory quantitative fit to experimental data. With additional arguments concerning the accumulation of positive space charge in the gap in the consequent distortion of the external field by the increasing current, it is possible to trace, at least qualitatively, the initation of glow discharge from the onset of breakdown until the formation of the cathode layer. This is done by considering the transition from the dark Townsend to glow discharge, not by analyzing a sequence of steady states corresponding to progressively greater final currents, but by following the dynamics of the transition and the temporal growth of the current.

As the experimental techniques, equipment, and methods of analyzing short-lived transient processes were perfected, however, fresh facts were constantly revealed that could not be reconciled with the Townsend scheme. The study of individual avalanches and series of multiplying avalanches in the Wilson cloud chamber (*Raether* and his coworkers [12.1]), recording of visual patterns by photomultipliers and image converters, recording of oscillograms of breakdown current increasing with time, and frame-by-frame filming of the process by high-speed cameras led to considerable progress in understanding the nature of the breakdown.

At high pd and considerable overvoltages, the breakdown in plane gaps develops much faster than is predicted by the multiplication of avalanches through cathode emission. The secondary electron emission due to ion impact can be ignored because the duration of discharge is simply insufficient for ions to cross the gap. Even the photoemission mechanism is not sufficiently fast, because under these conditions the current-conducting channel is formed in the time of flight of an electron from the cathode to anode, or even faster. There is not enough time for the repetition of avalanches through cathode emission. High-speed filming made it possible to observe an ionized luminous channel that closes the gap immediately after the first powerful avalanche has passed.

The independence of the breakdown voltage on the material of the cathode, established by very accurate measurements, is evidence agains the participation of cathode processes in the breakdown mechanims. Under some conditions, the irrelevance of the cathode vis-a-vis sparking is fairly obvious, for example, in the breakdown between a point anode and a distant plane cathode. At the threshold voltage, the field at the cathode and over a considerable part of the gap on the cathode side is too low for electron multiplication to occur. It does occur only far from the cathode, in the neighborhood of the positive point, where the field is greatly enhanced. Lightning is another example. Other discrepancies between Townsend's theory and experimental data were also found. Thus there are such combinations as methylal or ester vapor and copper cathode that have extremely low secondary emission coefficients at the cathode, $\gamma_{eff} < 10^{-8}$, so that the breakdown cannot be explained by the avalanche multiplication mechanism. There were no doubt by the late thirties that Townsend's theory fails completely at high pd and high overvoltages, that is, exactly at the conditions required to produce sparking.

12.1.3 Streamer Theory

The fundamentals of the new theory of spark breakdown were developed by *Loeb, Meek* and *Raether* [12.1, 12.2, 12.3] about 1940. The theory is based on the concept of the growth of a thin ionized channel (*streamer*) between the electrodes; the streamer follows the positively charged *trail* left by the *primary* intensive avalanche. Electrons of numerous secondary avalanches are pulled into the trail by the field. These avalanches are initiated by new electrons created by *photons* close to this trail. Photons are emitted by atoms that the primary and secondary avalanches have excited. Numerous results were reported in the course of subsequent efforts, and a number of details were found that greatly modified some of the initial concepts and estimates; nevertheless, the philosophy of the theory, reflecting the observatios, withstood the test of time. The story was not without complications, as when the importance of the Townsend mechanism was neglected – on inadequate grounds – in response to the achievements of the new theory (a detailed analysis of the situation is given in the review [12.4]). The Townsend mechanism does dominate at moderate values of pd (definitely so if $pd < 200\,\text{Torr cm}$) and small overvoltages. As for the precise boundary values of pd at which the breakdown mechanisms replace each other, the information reported in the literature is very contradictory and rather poorly argued. According to [12.1], the transition in atmospheric air happens at $d \approx 5$–$6\,\text{cm}$, that is, the streamer mechanism works only if $pd > 4000\,\text{Torr cm}$. It is very likely that certain intermediate forms exist in the boundary range of $pd \approx 200$–$5000\,\text{Torr cm}$, where neither cathode multiplication nor streamers are realized and bulk reactions serve as the secondary process: excitation of atoms by resonance radiation with subsequent associative ionization [12.5].

12.1.4 Leader

The breakdown in air gaps of many meters and in lightning discharges occurs via a growth of a *leader* from one electrode to the other: a thin channel that is conducting, orders of magnitude higher than the streamer channel. The leader process is a larger-scale event: it includes streamers as its elements. We will turn to leaders after Sect. 12.8 but now consider only streamers, since the process does not often go beyond them in short discharge gaps.

12.1.5 How Do We Define "Breakdown"?

The definition of "breakdown" is not so difficult at low pressures (Sect. 7.2). As a rule, the breakdown initiates a self-stustaining discharge and there is no need to distinguish between the two events. If the pressure is high, and especially if the field is non-uniform (one or both electrodes are points, wires, etc.), a self-sustaining current does not necessarily lead to catastrophic consequences. For example, the initiation of a corona discharge (which is self-sustaining) is not yet a breakdown. The current is quite low, and nothing special happens to the voltage, even though energy leakage through the corona is an undesirable effect for high-voltage transmission lines. The breakdown which is a real danger

in high-voltage equipment is *short-circuiting*, that is, the formation of a highly conductive *spark channel;* this channel passes such a large current that the voltage across the discharge gap falls abruptly.[1]

12.2 Individual Electron Avalanche

An individual *avalanche* is a primary and inescapable element of any breakdown mechanism. Consider an avalanche in a uniform external field E_0 between plane electrodes. Let it be initiated by a single electron that leaves the cathode at the time $t = 0$. The x axis is directed from a point on the cathode to the anode. The radial distance from the x axis is denoted by r.

12.2.1 Numbers and Diffusional Spatial Distributions of Charges

Taking into account the possible formation of negative ions, we find the total numbers of electrons and ions increasing as the avalanche moves forward:

$$dN_e/dx = (\alpha - a)N_e\ ,\quad dN_+/dx = \alpha N_e\ ,\quad dN_-/dx = aN_e\ , \tag{12.1}$$

$$N_e = \exp[(\alpha - a)x]\ ,\quad N_+ = \frac{\alpha}{\alpha - a}(N_e - 1)\ ,\quad N_- = \frac{a}{\alpha - a}(N_e - 1)\ , \tag{12.2}$$

where α and a are the ionization and attachment coefficients. All the new electrons fly to the anode in a group at the drift velocity $v_d = \mu_e E_0$. However, diffusion makes the electron cloud spread around the central point $x_0 = v_d t$, $r = 0$. The electron density $n_e(x, r, t)$ in the cloud obeys the general diffusion equation (2.22, 20) in which the drift motion and electron production must both be taken into account. The solution of the equation takes the form [12.5]

$$n_e = (4\pi D_e t)^{-3/2} \exp\left[-\frac{(x - v_d t)^2 + r^2}{4D_e t} + (\alpha - a)v_d t\right]\ . \tag{12.3}$$

The density n_e decreases with distance from the moving center following a Gaussian law. The radius of the sphere on which the density is exactly $\bar{e}$ times less than that at the centre, $n_e(x_0, 0, t)$, increases with time (during the progress of the avalanche) by the characteristic diffusion law:

$$r_D = \sqrt{4D_e t} = \sqrt{4\frac{D_e}{\mu_e}\frac{x_0}{E_0}} = \sqrt{\frac{8\bar{\varepsilon}x_0}{3eE_0}}\ , \tag{12.4}$$

where $\bar{\varepsilon}$ is the mean random energy of electrons given by (2.23).

[1] In fact, voltage also drops slightly when a steady-state dark Townsend discharge is initiated: the overvoltage is removed. When a glow discharge is initiated, the voltage drops from the breakdown value to the steady burning voltage; if the positive column is short, V falls practically to the minimum breakdown voltage, which is fairly close to the cathode fall (Chap. 8).

The ions remain practically fixed during the time of flight of the avalanche to the anode. Hence, they accumulate at each point. The positive ion density is

$$n_+(x,r,t) = \int_0^t \alpha v_d n_e(x,r,t')dt' .$$

To obtain n_-, we have to replace α with a. The function n_e in the integral is given by (12.3). In the absence of attachment in the limit $t \to \infty$ and for regions not too far from the axis, an approximate calculation of the integral gives [12.5]

$$n_+(x,r) = \frac{\alpha}{\pi[r_D(x)]^2} \exp\left\{\alpha x - \frac{r^2}{[r_D(x)]^2}\right\} , \tag{12.5}$$

where $r_D(x)$ is defined by (12.4). This result has a clear physical meaning. The ion density in the trail of the avalanche increases exponentially with the distance x from the cathode, in accord with the $\exp(\alpha x)$ law of multiplication of charges. In each cross section at a given x, the density decreases from the axis by the same Gaussian law for diffusion that governs the density of electrons (which produce the ions) at the moment when the centroid of the electron cloud passes through this section.

12.2.2 Visible Outlines of the Avalanche

In addition to ionizing the gas, electrons excite molecules, which remain practically fixed, as the ions do. The spatial distribution of excited particles that can give an image of the avalanche when emitting light is similar to the distribution of ions. A glance at (12.5) may suggest that the visible shape of the avalanche reflects the characteristic radius $r_D(x)$ of the distribution, that is, the outline of the avalanche is parabolic, $r = r_D(x) \propto \sqrt{x}$, and transforms smoothly into a spherical profile in the region of the electron head of the avalanche. This conclusion is not correct. Whatever the method of experimentally fixing the boundaries of the avalanche image (Sect. 12.2.3), this boundary inevitably corresponds to a definite absolute density of active particles (emitting molecules and ions), not their relative density. In general, this level is dictated by the sensitivity of the recording equipment. The sensitivity of instruments being sufficiently high, the minimum recordable density is much lower than the number density on the axis far from the cathode, where $\alpha x \gg 1$. As a result, the low number density at the visible outline $r_m(x)$ of the avalanche corresponds to a small value of the exponent in (12.5), much lower than αx. The outlines thus correspond to an approximately vanishing exponent; this curve is not parabolic, $r_D \propto \sqrt{x}$, but wedge-shaped:

$$r_m \approx r_D\sqrt{\alpha x} = \sqrt{8\bar{\varepsilon}\alpha/eE_0}x .$$

The wedge becomes rounded in the region of the avalanche head (Fig. 12.1).

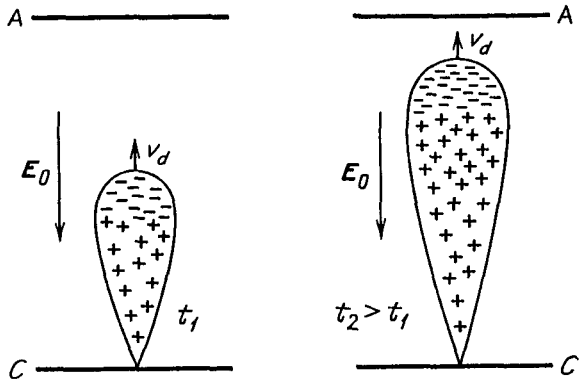

Fig. 12.1. Shape and charge distribution of an electron avalanche at two consecutive moments of time. *Arrows* indicate directions of external field E_0 and velocity of motion of the avalanche head, v_d

12.2.3 Elementary Current in a Circuit Containing the Discharge Gap

Let us calculate the current i in the circuit when only one electron moves in the gap between electrodes to which a voltage V is applied. We will then be able to find the current produced by the avalanche (Sect. 12.2.4). The external circuit is subjected to the electrostatic influence of the electron even when it is far from both electrodes. The metal of the electrodes is polarized by the field of the electron and positive *induced charges* appear on their surface (Fig. 12.2). The effect is the stronger, the smaller the charge–surface distance. Therefore, as the electron moves from the cathode to the anode, the induced positive charge on the anode surface increases and that on the cathode surface decreases (however, the sum of the induced charges on the two electrodes is e). Obviously, these changes are accompanied with a flow of charge in the connecting wires.

To find the induced charges, we make use of the *Ramo–Shockley theorem* of electrostatics published in 1938. A charge q_C on the surface of a conductor C, induced by a charge q, equals $q_C = -q(\varphi_{MC}/\varphi_C)$, where φ_{MC} is the potential at the point M where q is located; this potential arises if the conductor C is placed at a potential φ_C, while other conductors in the system, A in this particular case, have zero potential: $\varphi_A = 0$. Likewise, the charge induced on the electrode A is $q_A = -q(\varphi_{MA}/\varphi_A)$, and $\varphi_C = 0$. In the case shown in Fig. 12.2, $\varphi_{MC}/\varphi_C = (d-x)/d$, $\varphi_{MA}/\varphi_A = x/d$. Since $q = -e$, we have $q_C = e(d-x)/d$, $q_A = ex/d$, whence the *elementary* current is

$$i = \dot{q}_A = -\dot{q}_C = e\dot{x}/d = ev/d\,. \tag{12.6}$$

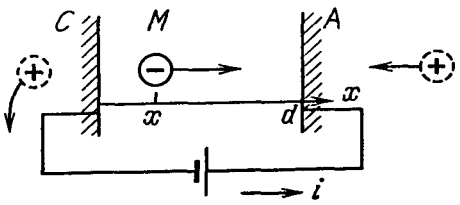

Fig. 12.2. Current flow through the circuit when a charge moves across the gap

The same result can be obtained by phenomenological arguments. An electron passing along a path $dx = v\,dt$ gains from the external field $E = V/d$ an energy $eE\,dx$. This work is done by the power supply source; it equals $iV\,dt$, whence $i = ev/d$. The derivation is elementary but in contrast to the preceding one, it does not specify the mechanism of the effect.

In the case of arbitrary-shape electrodes, that is, of nonuniform field, we obtain

$$i(t) = \dot{q}_A = -q\dot{\varphi}_{MA}/\varphi_A = -q\nabla\varphi_{MA}\dot{\boldsymbol{r}}/\varphi_A = q\boldsymbol{v}\cdot\boldsymbol{E}/V\ , \qquad (12.6')$$

where $\boldsymbol{v}(t) = \dot{\boldsymbol{r}}$ is the velocity of the charge q at a moment t, and $\boldsymbol{E}$ is the field at the point $\boldsymbol{r}$ that it passes through. The ratio $\boldsymbol{E}/V$ is a function of geometry of the field but is independent of field magnitude.

12.2.4 Experimental Studies of Avalanches

A great deal of important information has been obtained in the course of studying single avalanches, series of avalanches, multiplication of avalanches, and avalanche-streamer transformations in the Wilson cloud chamber [12.1]. This chamber makes use of the fact that ions usually serve as centers of condensation of supersaturated vapor. To make avalanches visible, a system of electrodes is placed in a chamber and an admixture of water, alcohol, etc., is added to the host gas. Synchronously with the application of the voltage and with the starting of the avalanche, the gas mixture is expanded adiabatically by 15–20 % so that the vapor becomes supersaturated. The cloud of droplets reproduces the shape of the ionic trail of the avalanche. The visual image is produced by light scattering on droplets, whose density equals (or is proportional to) the density of ions.

The main body of the avalanche has a well-pronounced wedge shape, rounded at the head. The avalanche length (the time of its motion) is controlled by fixing a prescribed length of the rectangular pulse applied to electrodes. The mean electron energy $\bar{\varepsilon}$ can be evaluated using the measured wedge angle (Sect. 12.2.2) and the known ionization coefficient α. The measured length and lifetime of the avalanche yield the drift velocity of electrons, $v_d = x/t$. Photographs of avalanches are also obtained by using the light emission due to the excitation of molecules and atoms. The luminosity being quite faint, photomultipliers and optoelectronic converters are employed for this purpose.

Another useful technique includes measuring with the very small current in external circuit and recording it with oscilloscopes. The result obtained in Sect. 12.2.3 implies that an avalanche produces a current

$$i(t) = N_e(t)ev_d/d = (ev_d/d)\,\exp\left[(\alpha - a)v_d t\right]\ .$$

Having measured $i(t)$, one can find $\alpha - a$, or α in a gas without attachment. When all the electrons have reached the anode, a much weaker current, that lasts much longer, is recorded; it is caused by the motion of ions. If avalanches multiply, consecutive pulses of electronic current with increasing mean value are observed. The time intervals between pulses indicate whether ions participate in cathode emission or not.

12.2.5 Field Distortion Due to Space Charge

Considerable *space discharge* is generated in an avalanche with high *amplification*, $\exp(\alpha x)$. Space charges produce their own field $\boldsymbol{E}'$ that adds up vectorially with the external field $\boldsymbol{E}_0$ and distort it in the vicinity of the avalanche. This effect becomes strong as charge multiplication continues and influences the subsequent process of ionization. Space charges form a sort of dipole: all the electrons are at the head of the avalanche, while most of the positive ions remain behind. The distance by which the electrons are separated from the main part of ions is determined by the *ionization length* α^{-1} that an electron covers, on the average, before it produces a pair of ions. As long as the external field is only slightly distorted, $\alpha = \alpha(E_0)$. When the amplification becomes high, both α and the spatial distribution of charges become dependent on the resulting field $\boldsymbol{E}$. The field and charge distributions (Fig. 12.3) are described by a set of simultaneous equations that are very difficult to solve.

The fields E' and E_0 in front of the avalanche head add up to give a field stronger than E_0. The fields $\boldsymbol{E}'$ and $\boldsymbol{E}_0$ in the zone between the centers of the space charges of opposite signs point in opposite directions and the resultant field is weaker than E_0. The field also develops a radial component. Assume that the charges of each sign are within a sphere of radius R. The field at its surface is $E' = eN_e/R^2$. The diffusion radius (12.4) can be taken for R, while the amplification and the number of electrons in the avalanche $N_e = \exp(\alpha x)$, are not too great. A preliminary idea of the scales of the quantities can be obtained, if we evaluate the values of r_D and N_e at which E' grows to E_0. For instance, in the field $E_0 = 31.4\,\text{kV/cm}$ that produces breakdown of the air gap of $x = 1\,\text{cm}$ at $p = 1\,\text{atm}$. and with $\bar{\varepsilon} = 3.6\,\text{eV}$, equation (12.4) gives $r_D = 1.8 \times 10^{-2}\,\text{cm}$. The equality $E' = E_0$ is met when $N_e = \exp(\alpha x) = 0.8 \times 10^8$, $\alpha x \approx 18$. In fact, R at such a high N_e is several times the diffusional value so that $E' < E_0$ (Sect. 12.2.6).

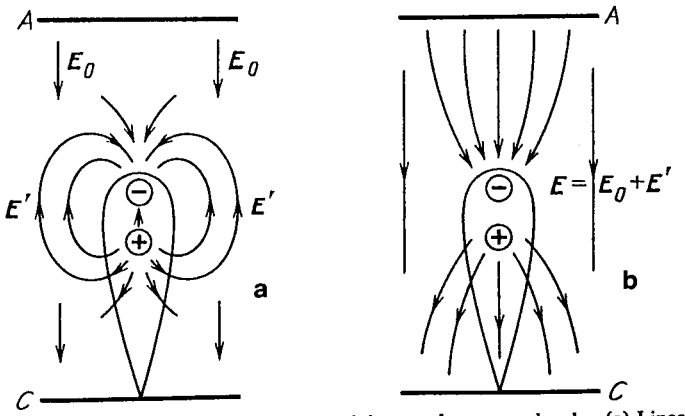

Fig. 12.3. Electric fields in a gap containing an electron avalanche. **(a)** Lines of force of the external field $\boldsymbol{E}_0$ and of the field of space charge of the avalanche, $\boldsymbol{E}'$, are shown separately. **(b)** lines of force of the resulting field $\boldsymbol{E} = \boldsymbol{E}_0 + \boldsymbol{E}'$. Circles mark the centers of space charges

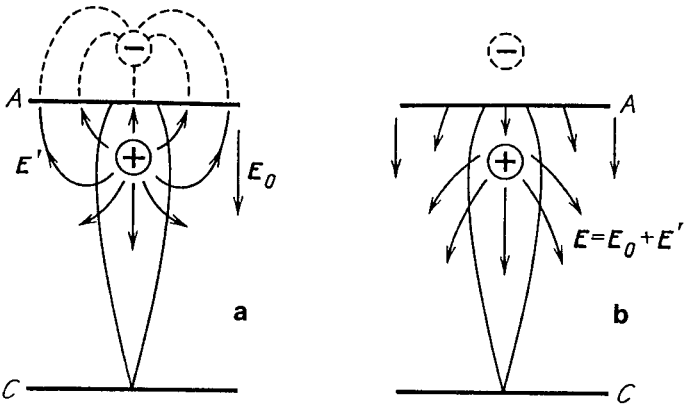

Fig. 12.4. Electric field in a gap after the avalanche has reached the anode and all electrons have sunk into the matal. (**a**) lines of force $\boldsymbol{E}'$ of the space charge of the trace left by the avalanche and of its mirror image in the anode. (**b**) lines of force of the resulting field, $\boldsymbol{E} = \boldsymbol{E}_0 + \boldsymbol{E}'$

When the avalanche reaches the anode, the electrons sink into the metal and only the positive space charge of the *ionic trail* remains in the gap (Fig. 12.4). The field is formed by the ionic charge and by its "image" in the anode. The image in the relatively distant cathode plays a rather insignificant role. The field close to the anode is less than E_0, but exceeds it farther off. The field reaches its maximum at the axial distance from the anode of the order of one ionization length α^{-1}. An approximate solution of the corresponding electrostatics problem was given in [12.5].

12.2.6 Repulsion of Electrons

When the number of charges N_e is high, the diffusional spreading of the electron cloud is replaced by their electrostatic repulsion. The rate of spreading due to the latter factor increases with increasing N_e, that is, with t and x, while the rate of diffusion decreases: $dr_D/dt \propto t^{-1/2} \propto x^{-1}$. The rate of expansion of a charged sphere due to repulsion is determined by the drift of electrons in the field of their own space charge:

$$\frac{dR}{dt} = \mu_e E' = e\mu_e R^{-2} \exp(\alpha x) \ , \quad x = \mu_e E_0 t \ .$$

Integration first gives the law of expansion $R(t)$ or $R(x)$, and then the field E' and electron density $n_e = 3N_e/4\pi R^3$:

$$R = \left(\frac{3e}{\alpha E_0}\right)^{1/3} \exp\left(\frac{\alpha x}{3}\right) = \frac{3}{\alpha}\frac{E'}{E_0} \ , \quad n_e = \frac{\alpha E_0}{4\pi e} \ . \tag{12.7}$$

The field E' is proportional to R, and the mean electron density remains unaffected by repulsion accompanied by multiplication. The evaluation shows that diffusional spreading is replaced by repulsion at $N_e = \exp(\alpha x) \sim 10^6$, $\alpha x \approx 14$. The corresponding field E' comes to 2–3 % of E_0. Photographs of

avalanches clearly show how the avalanche head broadens abruptly, beginning with a certain length x which corresponds to a certain amplification exponent $\alpha(E_0)x$; presumably, the reason is repulsion. Measurements agree with estimates of the above type [12.1].

Once the electron cloud increases to about one ionization length, $R \approx \alpha^{-1}$, the separation between electrons and ions ceases to be so well pronounced as when $R \ll \alpha^{-1}$. Now the distance between the charges of opposite signs is relatively small and the attractive force due to the positive charge restrictes further repulsive spreading of electrons. The broadening of the avalanche head slows down, or even ceases completely. The maximum transverse size of the avalanche head is thus of the order of $R_{max} \approx \alpha^{-1} \sim 0.1\,\mathrm{cm}$, because the ionization coefficient in atmospheric-pressure breakdown fields in air is typically about $\alpha(E_0) \sim 10\,\mathrm{cm}^{-1}$. According to (12.7), at the moment when the head ceases to grow we find $E'/E_0 \approx 1/3$. If $E_0 \approx 30\,\mathrm{kV/cm}$ and $\alpha \approx 10\,\mathrm{cm}^{-1}$, then $N_e \approx 7 \times 10^8$, $\alpha x = \ln N_e \approx 20$, $n_e \approx 2 \times 10^{11}\,\mathrm{cm}^{-3}$.

In breakdown fields, $d \ln \alpha/d \ln E \approx 4$. A change in E of 1 % changes α by 4 %. Therefore, the ionization rate at the outer boundary of the electron cloud (on the side of the anode), in the enhanced field $E \approx E_0 + E'$, is several times greater than $\alpha(E_0)$; it is much smaller at the inner boundary, on the side of the ionic trail. In this region we have not just $E \approx E_0 - E'$, but rather $E \approx E_0 - 2E'$, because the field E' of the ionic positive charge is also subtracted from E_0 (Fig. 12.3). Dramatic weakening of the field inside the avalanche head favours the formation there of *quasineutral plasma*, that is, of a streamer (directed to the anode).

12.3 Concept of Streamers

A streamer is a moderately, one can even say, weakly ionized thin channel formed from the primary avalanche in a sufficiently strong electrc field; it grows in one, or both, directions toward the electrodes. In the breakdown of a plane gap, the streamer grows from the anode to the cathode. A streamer, possessing a certain conductivity, can so modify the field upon reaching the electrodes that the degree of ionization and the current may be greatly increased; ultimately, this will lead to a *spark discharge* in the gap. The creation of a streamer (and the resulting gap closure) is not a necessary – but is sometimes a sufficient – condition for breakdown.

For an avalanche to transform into a streamer, it must reach sufficiently high amplification. The space-charge field must increase to a level on the order of the applied field. Otherwise there are no reasons for disturbing the normal evolution of the avalanche. If gaps are not too long and overvoltages are not too high (in comparison with the breakdown voltage), the transformation occurs when the avalanche exhausts its reserves of amplification, that is, when it reaches the anode. The streamer is now initiated at the anode surface, in the region of maximum space charge, and then propagates to the cathode. Such streamers are known as

cathode-directed or *positive*. The number of charges in the primary avalanche in wide plane gaps and (or) at high overvoltages becomes high even earlier. The avalanche transforms into a streamer before it reaches the anode. In this case the streamer grows toward both electrodes. If the streamer is formed while the avalanche has not yet gone far from the cathode, it mostly grows toward the anode; it is then said to be *anode-directed* or *negative*.

12.3.1 The Mechanism of Formation of Cathode-Directed Streamers

The situation is illustrated in Fig. 12.5. One hypothesis states that the decisive role is played by energetic *photons* that are emitted by atoms excited in the avalanche and produce *photoionization* in the vicinity of the primary avalanche. (Events of production of electrons at the cathode or far from the trail are unimportant in this context because they result in avalanches similar to the primary one.) Electrons produced by photons initiate *secondary avalanches* that are *pulled into the trail* due to the direction of the resulting field (Fig. 12.4). Secondary-avalanche electrons intermix with primary-avalanche ions and form a *quasineutral plasma*. They also excite atoms, so that new photons are emitted. Secondary-avalanche ions enhance the positive charge at the cathode end of the evolved plasma channel. This charge attracts the electrons of the next generation of secondary avalanches, etc. This is how the streamer grows. The process of ionization along the ion trail of the primary avalanche begins at the spot where the positive charge and the field are the highest, that is, at the anode, provided the *degeneration condition* $E' \approx E_0$ has been reached there. This is the situation shown in Fig. 12.5.

In this case the plasma streamer contacts the anode. A streamer is a conductor, so that electrostatically it acts as a metallic "needle" protruding from the surface of the anode (a perfectly conducting needle would be exactly at the anode potential): the field at the end of the streamer is greatly enhanced. The lines of force fan out from this end, which stimulates the attraction of secondary avalanches on all sides of the streamer and hence its growth. The mechanism that somewhat levels off the potential in the needle is the *polarization* of the conductor by the

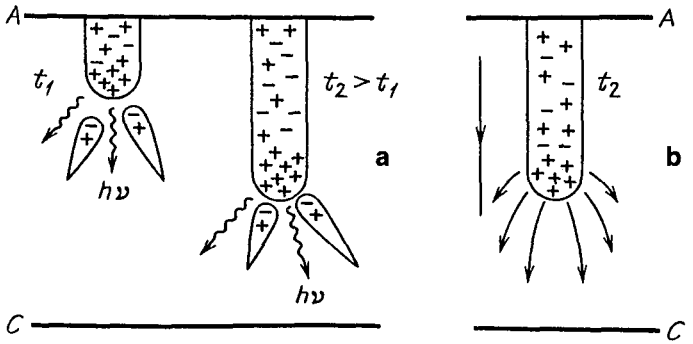

Fig. 12.5. Cathode-directed streamer. **(a)** Streamer at two consecutive moments of time, with secondary avalanches moving towards the positive head of the streamer; wavy arrows are photons that generate seed electrons for avalanches. **(b)** Lines of force of the field near the streamer head

external field. Electrons are displaced towards the anode, thus "baring" the positive ions at the cathode end. The field of the resulting dipole, being opposite to the external field, partly cancels the latter and reduces the potential difference along the conductor. In fact, this is the same effect that produces the patterns of Figs. 12.3, 4.

If the source of photons and seed electrons for secondary avalanches is sufficiently great (this seems to be the case), the rate of streamer growth is limited by the rate of neutralization of the positive space charge at the cathode side of the streamer, not by the rate of avalanche production. As for the electrons, they are pulled into this region at the drift velocity corresponding to the field within it. This field is considerably higher than the external one, and is stronger the longer the needle. (This is implied by electrostatics.) Experiments indeed prove that the velocity of propagation (*growth*) of the streamer is greater, the longer it is and the stronger the external field is. To an order of magnitude, the measured velocities are about 10^8 cm/s, while the drift velocities in the external field are about 10^7 cm/s. The streamer channel diameter is comparable with the avalanche head diameter at the stage of maximum expansion, 10^{-2}–10^{-1} cm (Sect. 12.2.6). At any rate, the charge density is not less than the maximum density in the avalanche: presumably, $10^{12}\,\mathrm{cm}^{-3}$ (an estimate of $10^{13}\,\mathrm{cm}^{-3}$ has also been made).

Photons are emitted and absorbed in a random manner; hence, situations are possible in which a new predominant direction appears for the propagation of a great number of secondary avalanches. This is a likely mechanism of generation of experimentally observed zigzag streamers and spark channels.

12.3.2 Formation Criterion

As follows from the preceding presentation, a streamer is born of an avalanche if the field of its space charge reaches a value of the order of the external field. The correspondingly approximate equality,

$$E' = eR^{-2} \exp[\alpha(E_0)x] \approx E_0 \,, \tag{12.8}$$

can be regarded as the *criterion of streamer formation*. It imposes a condition on the parameters of experiment: E_0 and the gap width $d = x$ that is minimal for the given E_0. Numerical results obtained using (12.7) are dependent on the value chosen for the avalanche head radius R. The diffusional radius $r_D(E_0)$ was taken in the earlier work of Loeb and Meek from a formula of the type (12.4). Thus we obtain the well-known Meek breakdown condition, which demands (in the simplified form) that

$$\alpha(E_0)d \approx 18 - 20 \,, \quad N_e = \exp(\alpha d) \sim 10^8 \tag{12.9}$$

(cf. the numerical example of Sect. 12.2.5).

The onset of breakdown was identified in the Loeb-Meek theory with the event of streamer formation. In fact, this is not always so. We know now that if

$d < 5\,\mathrm{cm}$, atmospheric air undergoes breakdown via the Townsend mechanism of avalanche multiplication, not the streamer one. The condition $\alpha d \approx 20$ imposed on the avalanche *enhancement coefficient* by the time the streamer is formed is insensitive to the choice of the value of R because $R \approx \alpha^{-1} \sim 10^{-1}\,\mathrm{cm}$ (Sect. 12.2.6), we find $N_e \sim 10^9$, although $\alpha d \approx 21$ is again quite close to (12.9). Note that the processing of experimental data on the breakdown of various gases at $p \sim 1\,\mathrm{atm.}$ and $d \sim 1$–$10\,\mathrm{cm}$ points to an approximate empirical relation $\alpha(E_0)d \approx 20$, which is equivalent to *Meek's criterion*. The significance of this fact should not be overestimated, because any criterion of type (12.8) implies weak logarithmic dependence of αd on other quantities in the formula.

After an analysis of experiments, Loeb supplemented condition (12.9) with the demand that the electron density in the avalanche at the moment of formation of a streamer be at least $0.7 \times 10^{12}\,\mathrm{cm}^{-3}$, assuming that this level ensures the required rate of emission of photoionization radiation. It cannot be said that the specific mechanism of photoionization of the gas, so important for the streamer process, is clearly understood. Indeed, for a photon to knock out an electron from an unexcited atom, the atom that has emitted this photon, had to be excited to energies above the ionization potential; such events are infrequent. It is assumed that oxygen molecules in the air are ionized by photons emitted by highly excited nitrogen molecules ($I_{N_2} = 15.6\,\mathrm{eV} > I_{O_2} = 12.2\,\mathrm{eV}$), although there is hardly any experimental confirmation of this. Seed electrons may be produced in a complex manner, during the diffusion of the resonance radiation and associative ionization of an excited atom as it combines with an unexcited one.

12.3.3 Anode-Directed Streamer

If the applied field E_0 is such that the condition (12.8,9) is satisfied at a distance x form the cathode, shorter than the gap width d, the avalanche transforms into a streamer "halfway to the anode". The mechanism of growth towards the cathode remains the same (Sect. 12.3.1). The characteristics of propagation towards the anode are somewhat different from those of the above process because here electrons drift in the same direction as the front of the plasma streamer, not counter to it as in the case of cathode-directed growth. As a result of radition causing photoionization, secondary avalanches are produced in front of the negatively charged streamer head facing the anode (Fig. 12.6). The front electrons of the head, moving rapidly in a strong total field $E_0 + E'$, join the ionic trails of secondary avalanches and together form the plasma. Presumably, in this case a propagation mechanims without photons is also possible. The plasma front propagates at the expense of the electrons of the front, accelerated in the strong field, while the electrons behind the front (in a weak field) do not separate from the ions, that is, the charges form a quasineutral plasma. This resembles the propagation of an ionization wave [12.5. 6]. Some models developed for the description of streamer propagation are outlined in Sect. 12.7.

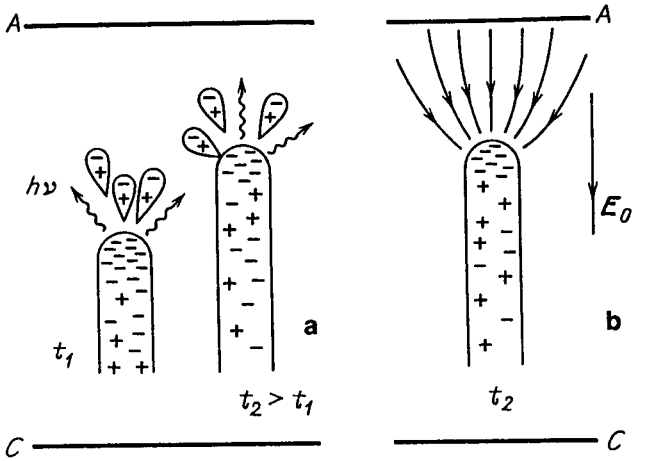

Fig. 12.6. Anode-directed streamer. **(a)** Photons and secondary avalanches in front of the streamer head at two consecutive moments of time. **(b)** Field in the vicinity of the head

12.4 Breakdown and Streamers in Electronegative Gases (Air) in Moderately Wide Gaps with a Uniform Field

Attachment of electrons slows down the ionization in avalanches and results in higher breakdown fields and the boundary values of pd at which the Townsend mechanism is replaced by the streamer one. In this respect, the analysis of experimentally obtained characteristics for atmospheric air is very illustrative. For obvious reasons, air is of exceptional interest and has been intensively investigated.

12.4.1 Breakdown Fields

Figure 12.7 gives the results of measurements of breakdown voltage in plane gaps in room air. In contrast to Fig. 7.5, where the range is limited to $d = 3\,\text{cm}$, here it is extended to $d = 30\,\text{cm}$. The asymptotic tendency of the breakdown field to a constant value of about 26 kV/cm, $E/p \approx 34\,\text{V/cm Torr}$ is evident. This fact is definitely caused by the following: at slightly lower values of E/p the attachment coefficient a is greater than the ionization coefficient α so that the multiplication of electrons is impossible (Sect. 7.2.5). The exact value of $(E/p)_1$ at which the curves of α/p and a/p as functions of E/p intersect is very difficult to determine either experimentally or numerically. One of the more recent sources gives an experimental value $(E/p)_1 = 31\,\text{V/ cm Torr} = 23.6\,\text{kV/cm atm}$. It can be regarded as the *theoretical lower limit* for air breakdown in an *ideal* plane gap. In fact, this conclusion holds only for a limited pressure range. At $p = 1\,\text{atm}$. the breakdown voltage in uniform field does tend to $V_t \approx E_1 d$ as d increases (Fig. 12.7). But beginning at a value of p around 10 atm. (the value depending on d) the breakdown voltage for a given d increases significantly less than linearly

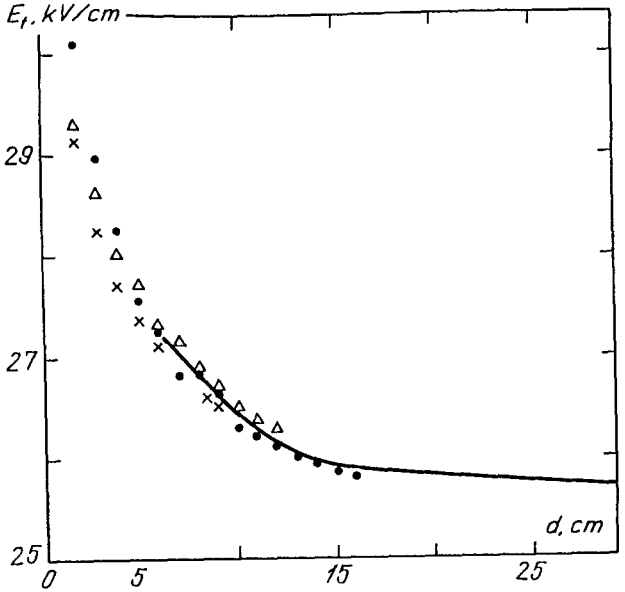

Fig. 12.7. Threshold field for the breakdown of air in a plane gap of length d [12.1]; p = 760 Torr + 10 Torr H_2O, t = 20° C. Data of a number of authors are shown. Spread in thresholds may have been caused by differences in voltage pulse durations [12.1]

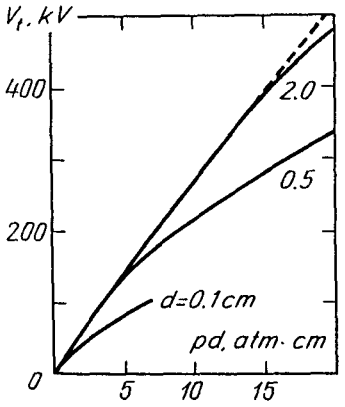

Fig. 12.8. Amplitude of breakdwon voltage (frequency 50 Hz in air in uniform field) as a function of pd, at high gas pressure. Labels to the curves give d in cm [12.7]

with p. Therefore, E_t/p decreases more and more in comparison with $(E/p)_1$ [12.7] (Fig. 12.8). The nature of the effect is not quite clear. There are indications that it is caused by enhanced fields at protrusions on the cathode surface where multiplication is initiated. If this is so, the process occurs as in a gap with a strongly nonuniform field (Sects. 12.8, 9).

12.4.2 Electronegative Gas SF_6

Owing to its high dielectric strength and other suitable properties, SF_6 is used for insulating. Its theoretical lower limit of breakdown threshold, corresponding to the equality $\alpha = a$, is very high: $(E/p)_1 = 117.5$ V/cm Torr = 89 kV/cm atm; see Fig. 12.9. The effect of a decrease in E_1/p with respect to $(E/p)_1$ is also observed (at $p \gtrsim 3$ atm.).

12.4.3 Multiplication of Avalanches or the Streamer?

Table 12.1 lists modern experimental data on the effective multiplication constant $\alpha_{\text{eff}} = \alpha - a$ of avalanches in dry air at $p = 1$ atm. in fields that produce breakdown in gaps of various width d. The table gives the numbers of electrons (enhancement factor) in avalanches initiated at the cathode by a single electron and reaching the anode. The table is limited to $d = 3$ cm because the data on α_{eff} at lower E is very unreliable in view of the closeness to the intersection point: $\alpha - a \ll \alpha, a$. We already know that a streamer is formed when the field of the space charge increases to the level of the external field; this event occurs when the critical number of electrons, $N_e \sim 10^8$–10^9, is produced in the avalanche ($\alpha_{\text{eff}} d \approx 20$). Table 12.1 shows that in air at $d < 3$ cm this event definitely cannot happen, but if $d \approx 3$ cm, the situation tends to the "critical" one, though the steeply decreasing α_{eff} shifts this point slightly further along the d axis. This conclusion fits the direct data obtained by analyzing oscilloscope traces of the breakdown current: breakdown in air goes via avalanche multiplication if $d < 5$ cm and via the streamer (or leader) mechanism if $d > 6$ cm.

An analysis of the table demonstrates why it is the *Loeb* and *Meek* seem to show conclusively in their early work [12.2, 12.3] that an air gap of $d = 1$ cm undergoes breakdown via the streamer mechanism. These calculations paid no

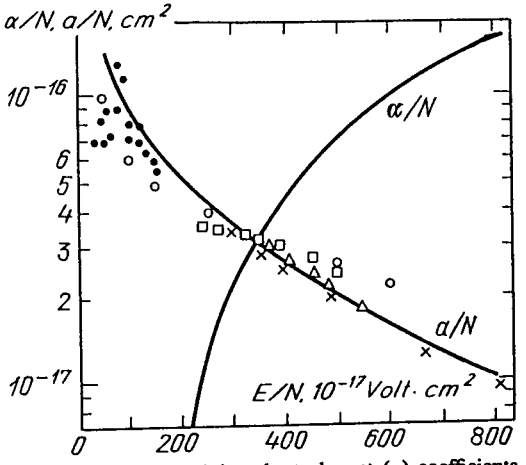

Fig. 12.9. Ionization (α) and attachment (a) coefficients in electronegative gas SF_6. Dots, circles, triangles, and squares represent experimental data. Solid curves plot the calculations using the kinetic equation [12.8]

Table 12.1. Multiplication of electrons in an avalanche at p = 1 atm. in fields E_t producing breakdown in gaps of width d [12.9]

d [cm]	pd [10^2 Torr cm]	V_t [kV]	E_t [kV/cm]	E_t/p [V/cm Torr]	$\alpha - a$ [cm^{-1}]	$(\alpha - a)/p$ [$10^{-2}\,cm^{-1}\,Torr^{-1}$]	$(\alpha - a)d$	N_e
0.1	0.76	4.54	45.4	59.7	81	10.7	8.1	3.3×10^3
0.3	2.3	11	36.7	48.4	31	4.1	9.3	1.1×10^4
0.5	3.8	17	34	44.7	20.5	2.7	10.2	2.8×10^4
1	7.6	31.4	31.4	41.4	12.4	1.63	12.4	2.4×10^5
2	15	58.5	29.3	38.6	8.0	1.05	16	8.9×10^6
3	23	85.5	28.6	37.6	6.5	0.85	19.5	2.9×10^8

attention to attachment and used for the multiplication coefficient α the results of earlier experiments which also ignored this factor. Thus it was assumed that $\alpha \approx 18\,\mathrm{cm}^{-1}$ at $E = 31.6\,\mathrm{kV/cm}$ ($d = 1\,\mathrm{cm}$). In fact, if attachment is taken into consideration, then $\alpha_{\mathrm{eff}} \approx 12.4$, and this reduces N_e by three orders of magnitude. At the same time, it is difficult to assume that the mechanism of secondary emission from the cathode acts in the interval $d \approx 0.3$–$3\,\mathrm{cm}$. This would require an extremely steep dependence of the secondary emission coefficient γ on E. Indeed, the Townsend breakdown condition (7.1) gives $\gamma \approx \exp(-\alpha_{\mathrm{eff}} d)$, and Table 12.1 indicates that this γ decreases in the corresponding interval of $E \approx$ 36.7–28.6 kV/cm by 4 orders of magnitude. The mechanism outlined at the end of Sect. 12.1.3 [12.5] may have been at work.

12.4.4 Effect of Overvoltage on Breakdown Mechanism

As a rule, the breakdown field is defined as the minimum field at which breakdown is still observable. Threshold values slightly depend on the initial current (the number of *seed* electrons) and on the *time delay* needed for the discharge to *develop*. Loeb and Meek assume that the breakdown voltage is that at which the breakdown is realized with a time delay of 30 s after the voltage has been applied, provided the initial current density of the cathode is $10^{-13}\,\mathrm{A/cm^2} \approx 1$ electron/μs cm^2. This quantity is known as the *static* breakdown voltage because this process first develops at a slow rate. Since α or α_{eff} depend steeply on E, overvoltage of, say, 10 % is sufficient for a streamer to be produced in a gap in which the breakdown at static voltage occurs by the Townsend mechanism.

Experiments on nitrogen breakdown in uniform field [12.10] are illustrative in this respect. At $p = 400\,\mathrm{Torr}$, $d = 3\,\mathrm{cm}$, and static breakdown field $E/p =$ 38.5 V/cm Torr, when $\alpha d = 9$ (nitrogen has no attachment), the breakdown current increases slowly, with a characteristic rise time of 1–2 μs. The oscilloscope trace shows peaks due to successive multiplying avalanches; photoemission occurs at the cathode. At the same p and d but at overvoltages above 17 %, a streamer is clearly formed. Thus a steep rise in current is recorded at 19 % overvoltage, when $E/p = 45.2$, only 0.2 μs after the peak of the first avalanche. There is competition between the streamer and the avalanche multiplication mechanisms, and its result can be tipped in either direction. An admixture of 2.5 % methane in the above-described experiments with nitrogen reduces to 7–8 % the overvoltage required for the streamer mechanism to dominate. The methane admixture affects α very little, while it reduces the seconary emission coefficient γ by a factor of 10^2, thereby suppressing the process of avalanche multiplication.

12.4.5 Effects of Negative Ions on Streamer Formation

Oscilloscope traces of current in the case of streamer breakdown of air ($d = 9\,\mathrm{cm}$) reveal the following characteristic effect [12.1]. After a short peak due to the first avalanche, a weak "delayed" current flows for a relatively long time, up to 10 μs (this current was proved to be carried by electrons). The trace ends with a stepwise increase in current, that is, breakdown. The lag in the formation of the

streamer and in breakdown is caused by attachment. After the first avalanche travels through the gap, the positive charge of the ionic trail is largely compensated for by negative ions. The space charge is not sufficient to produce a streamer. However, negative ions that are mostly concentrated at a short distance $\alpha_{\text{eff}}^{-1} \sim 10^{-1}$ cm from the anode are pulled toward the anode at a drift velocity of order 10^5 cm/s. The positive ionic charge is bared and the field gradually increases to a level required to form a streamer. The delayed electronic current is explained by detachment of electrons from negative ions in the increasing field of the space charge (we can only guess what the specific detachment mechanism may be; Sect. 12.6.4).

12.5 Spark Channel

The formation of the strongly ionized plasma of a well-developed spark channel is preceded by a poorly understood stage at which the degree of ionization in the zone of the initial streamer channel increases quite rapidly. This is indicated by a dramatic increase of current after the streamer closes the gap in the course of the streamer breakdown. Note that the original streamer channel is incapable of passing a high current. According to Table 2.1, the conductivity of weakly ionized plasma $\sigma \sim 10^{-16} n_e/p\,[\text{atm.}]\,\text{Ohm}^{-1}\text{cm}^{-1}$. At $p = 1$ atm. and $n_e \sim 10^{13}\,\text{cm}^{-3}$ $\sigma \sim 10^{-3}\,\text{Ohm}^{-1}\text{cm}^{-1}$. If the channel diameter $2r_c \sim 10^{-1}$ cm and the field in it $E \sim 10\,\text{kV/cm}$, then the current is negligible: $i = \sigma E \pi r_c^2 \sim 10^{-2}\,\text{A}$.

12.5.1 Back Wave of Strong Field and Ionization

This process, which seems to initiate the formation of the spark channel, is more pronounced and better understood in the case of leader breakdown in which the gap is closed by a much better conducting channel (Sect. 12.10). Nevertheless, the qualitative picture can be outlined as follows. The potential of the tip, or head, of the streamer growing from the anode to the cathode differs less from the anode potential than that of the nonperturbed field at the same point. An ideally conducting streamer contacting the anode would be entirely at the anode potential. As the tip approaches the cathode, both the fraction of the voltage applied to the electrodes which falls across the nonconducting gap between the streamer tip and cathode, and the field in the gap increase. By the time the tip touches the cathode, the field becomes so strong that electrons liberated by photons from the cathode or from atoms multiply at enormous intensity. The front then propagates from the cathode along the channel of the initial streamer towards the anode; it leaves behind a much stronger ionized plasma. The process looks like a reversed streamer at an ionization considerably higher than in the original one. The highly conducting plasma of the back "streamer" is at a potential close to that of the cathode; hence, an abrupt potential drop and a very strong field appear at the front. Electrons accelerated here are those producing the intensive ionization. The wave front is assumed to propagate to the anode at a velocity on

the order of 10^9 cm/s. This is not the velocity of motion of electrons: it is the phase velocity of the propagation of the potential jump (field wave). When this thin highly ionized channel reaches the anode and closes the gap, the foundation is laid for the formation of the "true" spark channel.

12.5.2 Expansion of Spark Channel

The high-density current in a spark channel releases highly localized heat. As a result, the plasma is greatly heated up and thermalized, and its degree of ionization may even increase thermally. The rapid surge in gas temperature, not being compensated for by similarly rapid heat removal, sharply increases the pressure in the current channel. This produces a *cylindrical shock wave,* resembling the explosion of a filament-shaped explosive charge. At the initial stages, the shock wave amplitude is so high that the temperature behind the front is sufficient for the thermal ionization of the gas. The boundary of the current channel is then almost indistinguishable from the shock wave front. Soon, however, the shock wave expanding from the axis weakens, ceases to ionize the gas, and separates from the relatively slowly expanding boundary of the highly ionized region, that is, from the *spark channel.* Now the channel expands only owing to the radial movement of the gas driven by the shock wave, and to heat conduction.

The temperature in the channel reaches 20,000 K; the electron density has been measured and found to reach $n_e \sim 10^{17}\,\mathrm{cm}^{-3}$. The electric conductivity is then determined by Coulomb collisions and is independent of n_e. As follows from (2.9), $\sigma \sim 10^2\,\mathrm{Ohm}^{-1}\mathrm{cm}^{-1}$. The current mostly increases because of the expansion of the channel and the enlarged cross section of the conductor, not because of current density changes. The channel radius grows to $r \sim 1$ cm, the maximum current is $i \sim 10^4$–10^5 A, $j \sim 10^4\,\mathrm{A/cm}^2$, the voltage at the electrodes is substantially lower than the original value, and the field in the channel $E \sim 10^2$ V/cm. A cathode spot seems to form on the cathode. If the power supply source is a capacitor (this is typical of laboratory experiments), the current decreases after the maximum is reached, and several repeated delayed oscillations occur with a half-period of about 10 μs.

This behavior has been studied in a large number of experiments. The first direct evidence of shock waves produced by spark discharges was reported in 1947 [12.11]. Streak photographs of sparks clearly show an advancing shock wave front and a not so rapidly expanding spark channel. At an early stage, 10^{-7}–10^{-6} s after the onset of breakdown, the channel expands at a velocity of about 1 km/s, and then slows down. The theory of gas-dynamics expansion of the spark channel, taking into account the shock wave and the energy release due to time-dependent discharge current, was first developed by *S.I. Drabkina* in 1951 [12.12]. A great deal of experimental data is reviewed in [12.3].

12.6 Corona Discharge

Corona discharges occur only if the field is sharply *nonuniform*. The field near one or both electrodes must be much stronger than in the rest of the gap. This situation typically arises when the characteristic size r of the electrodes is much smaller than the interelectrode distance d. For example, parallel wires of radius r manifest corona discharge in air only if $d/r > 5.85$. Otherwise the increase of voltage between the wires produces a spark between them, and not a corona discharge.

12.6.1 Field Distribution in the Simplest Cases

Exact solutions of electrostatics for simple geometry are indispensable for constructing a theory of corona and for the interpretation of experimental results. The field in the space between coaxial cylinders of radii r (internal) and R at a distance x from the axis is

$$E = V/\left[x \ln(R/r)\right] , \quad E_{\max} = V/\left[r \ln(R/r)\right] , \tag{12.10}$$

where V is the voltage between cylinders. Between concentric spheres of radii r and R we find

$$E = VrR/x^2(R-r) ; \quad E_{\max} \approx V/r \text{ if } R \gg r . \tag{12.11}$$

In the space between a sphere and a remote plane ($R/r \to \infty$), the field is $E \approx Vr/x^2$. Between a parabolic tip with curvature radius r and a plane perpendicular to it at a distance d, the field at a distance x from the tip along the axis is

$$E = \frac{2V}{(r+2x)\ln(2d/r+1)} , \quad E_{\max} \approx \frac{2V}{r \ln(2d/r)} . \tag{12.12}$$

If a voltage V is applied between parallel wires spaced by a distance d, or between a single wire and a parallel plane at a distance h, the maximum field at a wire of radius r is

$$E_{\max} = V/2r \ln(d/r) \text{ and } E_{\max} = V/r \ln(2h/r) . \tag{12.13}$$

12.6.2 Ignition Criteria

If the applied voltage V is less than the ignition voltage for corona V_c for the given conditions, a non-self-sustaining current on the order of 10^{-14} A can be detected in the circuit. This current is formed by ions produced by cosmic rays and natural radioactivity. About 10 pairs of ions are produced in air at sea level in 1 cm^3 per 1 s, and the steady-state number of ions in 1 cm^3 is about 10^3. The ignition of corona under laboratory conditions manifests itself not only by a luminous layer around the electrode (which may not be noticed at all) but also by a jump in the discharge current to about 10^{-6} A. The corona discharge belongs to the group of *self-sustained* discharges; the conditions under which it appears

reflect the physical mechanism of reproduction of electrons in that region of the enhanced field where ionization occurs. The mechanism of multiplication of electrons is esentially dependent on the *polarity* of the electrode surrounded by the corona.

If this electrode is the cathode (the corona is then said to be *negative*), then *avalanche multiplication* takes place. The secondary process is the emission from the cathode and, possibly, photoionization in the bulk of the gas. In principle, the ignition of a negative corona does not differ from the *Townsend breakdown* and from the ignition of the *dark Townsend discharge* (Sect. 8.3). The *ignition criterion* is an equality of type (7.1), generalized to include nonuniform fields. With attachment effects taken into consideration, we have

$$\int_0^{x_1} [\alpha(x) - a(x)]\, dx = \ln(1 + \gamma^{-1})\,, \tag{12.14}$$

where γ is the effective coefficient of secondary emission. The integration region in (12.14) stretches from the cathode surface to that point x_1 where $\alpha = a$ and the multiplication of electrons stops. In gases without attachment, the integral is formally extended up to the anode, but in practice it is sufficient to extend it only to the not very remote point x_1 where the field is considerably weakened and $\alpha[E(x_1)] \approx 0$, because $\alpha(E)$ decreases very steeply as we move away from the wire or tip. Molecules are also excited by electrons in the multiplication region. There are practically no electrons beyond this region in an electronegative gas: they form negative ions after having traveled a very short path; in electropositive gases, the field is in any case too weak, electrons are slow, so that the gas is not luminous outside the corona.

If the wire (or tip) is the anode (*positive corona*), the remote large cathode does not participate in multipliation, on account of the weak field in its vicinity. The reproduction of electrons is ensured by *secondary photoprocesses* in the gas around the tip. In contrast to the homogeneous glow of a negative corona, a positive corona displays luminous filaments running away from the tip (Fig. 12.12). These are thought to be streamers. The condition of streamer formation (12.9), also generalized to nonuniform fields, can be chosen as a *criterion of ignition of a positive corona*:

$$\int_0^{x_1} (\alpha - a)dx \approx 18 - 20\,. \tag{12.15}$$

Despite a possible difference of a factor of 2 to 3 in the enhancement coefficient, that is, in the values of integrals (12.14, 15), this coefficients affects rather insignificantly the value of the critical field at the electrode. The reason is the sharp dependence of α or $\alpha - a$ on E, so that even a small change in $E(x)$ strongly affects the integral. Indeed, experiments show that the ignition voltages of positive and negative coronas differ only a little in a number of gases, including air (V_c of negative corona is lower: presumably in (12.14), $\ln \gamma^{-1} < 20$ because $\gamma \gg 10^{-8}$).

12.6.3 Thresholds in Air

It is clear from the form of criteria (12.14, 15) that they impose constraints mostly on the maximum field at the corona-carrying electrode, which must be above a certain lower limit E_c. The threshold voltage V_c for the ignition of corona is related to E_c by the electrostatic laws of field distribution in the gap, (12.10–13). In 1929 Peek found the following empirical formula for the critical field of corona ignition in air between coaxial cylinders:

$$E_c = 31\delta(1 + 0.308/\sqrt{\delta r})\,\mathrm{kV/cm}\ . \tag{12.16}$$

Here δ is the ratio of air density to the normal density corresponding to $p = 760\,\mathrm{Torr}$, $t = 25°\,\mathrm{C}$; r is the radius of the internal electrode in cm. The formula describes experiments with a smoothly polished inner electrode, in the ranges $r \sim 10^{-2}$–1 cm, $p \sim 10^{-1}$–10 atm., including experiments in oscillating fields of frequency up to 1 kHz (in this case, E_c stands for field amplitude). Roughness of the electrode surface may lower the threshold value of E_c by 10–20 % because the field is additionally enhanced at the tiniest protrusions. The formula in the generalized form (with different numerical coefficients) is applicable to a number of gases. It can also be used for the wire-plane gap. The ignition voltage V_c is related to $E_c = E_{max}$ by (12.10, 13).

Peek's empirical formula bears the imprint of physical criteria, such as (12.14, 15). This is seen from the calculation of E_c in [12.13] on the basis of the criteria (12.14, 15) with $E(x)$ given by (12.10) and α_{eff} approximated for air at $E/p < 150\,\mathrm{V/cm\,Torr} = 110\,\mathrm{kV/cm\,atm.}$ by the formula (employed by electrical engineers):

$$\alpha = 0.14\delta\left\{\left(E\,[\mathrm{kV/cm}]/31\delta\right)^2 - 1\right\}\ \mathrm{cm}^{-1}\ . \tag{12.17}$$

As an exmaple, consider an air gap between a wire of $r = 0.1\,\mathrm{cm}$ and a coaxial cylinder of $R = 10\,\mathrm{cm}$; $p = 1\,\mathrm{atm.}$, $\delta = 1$. Using Peek's formula, $E_c = 61\,\mathrm{kV/cm}$. According to (12.10), $V_c = 28\,\mathrm{kV}$, and the field at the outer electrode is $E(R) = 0.61\,\mathrm{kV/cm}$. By discharge standards, this field is extremely weak: $E/p = 0.8\,\mathrm{V/cm\,Torr}$. Multiplication ends at a radius $x_1 = rE_c/E_1 = 0.25\,\mathrm{cm}$ ($E_1 \approx 24\,\mathrm{kV/cm}$), that is, the thickness of the layer around the wire where multiplication at the avalanche stage occurs is $x_1 - r \approx 0.15\,\mathrm{cm}$.

12.6.4 Ignition Lag

The time lag between the moment of application of voltage and the onset of steep rise in current consists of the statistical time of *waiting for a seed electron* at the tip, and the time of *avalanche multiplication* or *streamer formation*. Experiments point to a large, difficult to interpret spread of data for negative coronas; large and not readily controllable effects due to the state of the cathode surface may be responsible for this. In the case of positive coronas, the streamer formation time of 10^{-8} s is evidently too short in comparison with the reported time lags of 10^{-8}–10^{-6} s – which must be assigned to be the waiting time for seed electrons.

They are obviously not produced at the cathode because the lag is typically shorter than the time of drifting from the cathode to the positive tip. Occasional electrons in air convert very rapidly into negative ions. It is assumed that a strong field *liberates electrons* from O_2^- ions colliding with molecules; the efficiency of this process is a maximum at $E/p = 90$ V/cm Torr= 68.5 kV/cm atm. Moist air hydrates ions, forming clusters with water molecules. Ions in clusters are destroyed less efficiently.

12.6.5 Charge Transfer Beyond the Region of Multiplication, and $V - i$ Characteristics

Charge carriers are produced only in the direct vicinity of the corona-carrying electrode surrounded by a strong field. In the remaining part of the gap (*outer region*), the current is carried by charges that are pulled out by the weak field present there. The carriers are positive ions in positive coronas and negative ions in negative coronas (or electrons if the gas is devoid of electronegative components). The current in the outer region of the corona discharge is *non-self-sustaining*, the gas there is not ionized (i.e., suffered no breakdown).

The corona current depends on the applied voltage, or rather, on its excess over the ignition potential V_c. The current is limited by the *space charge* of the charge carriers in the outer region. The region of self-sustained discharge at the corona-carrying electrode is capable of generating a high current and a large number of carriers, but some of them are turned back by the space charge of the same sign and cease moving towards the electrode of the opposite sign. The situation is very similar to the limitation of current by space charge in a vacuum diode (Sect. 6.6); the difference is that here charges drift rather than move freely. These arguments lead to an approximative curve for the $V - i$ characteristic of steady-state corona discharge derived by Townsend, in 1914.

Consider the gap between coaxial cylinders. The current per unit cylinder length across a surface of arbitrary radius x outside the narrow zone of multiplication is $i = 2\pi x e n \mu E = \text{const}$, where n is the charge carrier density and μ is their mobility. Assume that the current, charge density, and distortion of the external field by the space charge are not too large. Then (12.10), corresponding to zero current but also to the actual voltage V, can be retained as a first approximation for the distribution $E(x)$. In this approximation,

$$n = i/2\pi e \mu E x = i \ln(R/r)/2\pi e \mu V = \text{const} .$$

Substituting this n into Poisson's equation $x^{-1} d(xE)/dx = 4\pi e n$ and integrating, we arrive at the next approximation to the field distribution. The constant of integration will be so chosen that the product xE in the limit $i \to 0$ be given by (12.10) in terms of the ignition potential V_c:

$$E = \frac{2i \ln(R/r)}{\mu V} \frac{x^2 - r^2}{2x} + \frac{V_c \ln(R/r)}{x} , \quad \int_r^R E \, dx = V .$$

Integrating E with respect to x, recalling that $x^2 \gg r^2$ in the predominant part of the gap, and solving the resulting equation for i, we find the $V - i$ characteristic of the corona:

$$i = \frac{2\mu V(V - V_c)}{R^2 \ln(R/r)} . \tag{12.18}$$

Formula (12.18) is confirmed by experimental data: the inverse resistance i/V is plotted as a function of V (the curve is known as reduced characteristic), the linearity of the curve giving the confirmation. The extrapolation of the curve to $i/V = 0$ determines the ignition potential V_c in a simpler and more accurate manner than the search for the corona inception point. The mobilities of positive and negative ions being more or less identical, the currents of *positive* and *negative* coronas in an *electronegative* gas at a given V are also *nearly equal*. In a gas *without attachment*, the *negative* corona current, being transported by electrons, is substantially *greater*. An admixture of an electronegative component immediately reduces this current.

Let us make some evaluations for the example considered at the end of Sect. 12.6.3: air at 1 atm., $r = 0.1$ cm, $R = 10$ cm, $V_c = 28$ kV. We set $\mu = 2\,\mathrm{cm^2/V\,s}$. The mobilities of O_2^-, O_4^-, O_2^+, O_4^+ in O_2, N_2^+, N_4^+ in N_2 at 1 atm. cluster around this value. Let $V = 40$ kV. We have $i = 4.6\,\mu$A/cm ($1\,\mathrm{A} = 9 \cdot 10^{11}\,\mathrm{V\,cm/s}$). The ion density is $n = 2.6 \times 10^8\,\mathrm{cm^{-3}}$. Experiments show that the $i(V)$ dependence of type (12.8) also holds for other geometries. Thus the current in atmospheric air between a needle cathode with tip radius $r \approx 3 \times 10^{-3}$–$3.5 \times 10^{-2}$ mm, and a plane anode perpendicular to the neelde axis at a distance $d \approx 4$–16 mm from the needle tip, is

$$i \approx (52/d^2)V(V - V_c)\,\mu\mathrm{A}\ ,\quad V[\mathrm{kV}]\ ,\quad d[\mathrm{mm}]\ , \tag{12.19}$$

with $V_c \approx 2.3$ kV being independent of d [12.13].

12.6.6 Corona Losses in High-Voltage Power Lines

This is a problem important in the transmission of electrical energy. The losses due to the corona discharge may be comparable to the Joule heat released in power line conductors. When both electrodes produce a corona discharge, as is the case for two parallel wires of opposite polarity, the current in the outer region separating them is carried by ions of opposite signs moving in opposite directions. The current and energy losses in such *bipolar* corona are much greater than in a *unipolar* corona (with a single corona-producing electrode). As a rule, the total recombination of ions is not achieved, while the mutual *neutralization of space charge* reduces the degree of limitation imposed by the space charge. Furthermore, negative ions arriving at the positive conductor decay in its strong field. This process is an additional source of electrons, somewhat facilitating the ignition of the corona. Using Peek's formula for two parallel wires,

$$E_c = 29.8\delta\left(1 + 0.301/\sqrt{\delta r}\right)\ \mathrm{kV/cm}\ ,\quad r < 1\,\mathrm{cm}\ , \tag{12.20}$$

which is somewhat less than implied by (12.16) for a single wire. A different empirical formula is used nowadays in electrical engineering: for smooth conductors,

$$E_c = 24.5\delta\left[1 + 0.65(\delta r)^{-0.38}\right] \text{ kV/cm} . \tag{12.21}$$

In the absence of discharges, the field distribution between two parallel wires with a voltage V between them is equivalent to the field distribution between a wire and a plane midway between the two wires, provided the voltage between the plane and a wire is $V/2$. Nevertheless, a corona is easier to start in the former case: one half of V_c in the wire-wire geometry is about 10 % lower than V_c in the wire-plane geometry.

$V - i$ characteristics of type (12.18) imply that the power released in a corona discharge is $P = iV \approx \text{const}\, V^2(V - V_c)$. Figure 12.10 shows losses per km of a high-voltage power line with conductors 2.5 cm in diameter. The ignition voltage diminishes considerably in rainy weather and in winter because water droplets and ice crystals deposited on conductors form additional sources of field enhancement. The current and losses sharply increase at the same voltage V.

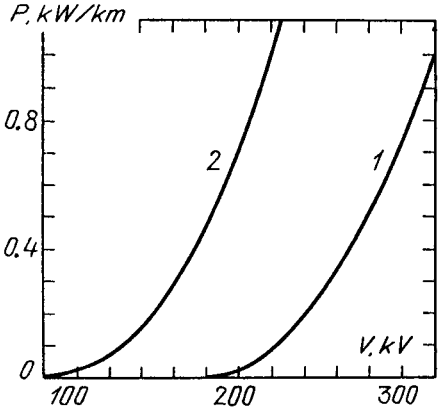

Fig. 12.10. Corona losses from a conductor 2.5 cm in diameter as a function of voltage. *(1)* fine sunny weather, *(2)* slight rain [12.7]

12.6.7 Intermittent Corona Discharge

Under certain conditions, the corona burns in the form of *periodic current pulses*, despite the constancy of voltage; the pulse repetition rate reaches 10^4 Hz if the corona is on the anode, and 10^6 Hz if it is on the cathode. Intermittence was discovered in Loeb's laboratory by Trichel and Kip in 1938. (Loeb and his school greatly contributed to the study of spark and corona discharges.) Periodic phenomena may also prove to be of practical interest. Their frequencies lie in the rf range, so that a corona in a power transmission line may be a source of radio noise. The most convenient source for laboratory study is the corona from a point to a plane electrode in room air.

Positive point. With a point of radius $r = 0.17\,\text{mm}$ at a distance $d = 3.1\,\text{cm}$ from a plane cathode, the corona appears at $V_c \approx 5\,\text{kV}$ and stays intermittent up to $V_1 \approx 9.3\,\text{kV}$ [12.13]. The repetition rate is low at the ends of the interval V_c–V_1, and reaches 6.5 kHz in the middle. The mean current increases to $1\,\mu\text{A}$ at V_1. Such pulses are known as *flashing corona.* Pulses are absent in the interval from V_1 to $V_2 \approx 16\,\text{kV}$; the current becoming steady. At V_2, the current increases to $10\,\mu\text{A}$. In the interval from V_2 until the *spark breakdown* of the entire gap at $V_t \approx 29\,\text{kV}$, the discharge again becomes pulsed, the pulse repetition rate increasing from a low value of 4.5 kHz. The mean current increases with V and reaches $100\,\mu\text{A}$ in the pre-breakdown stage.

If V is only slightly greater than V_c, the flashing corona is associated with so-called *pre-inception streamers.* Electrons produced by ionization flow into the point anode, while a space charge of positive ions accumulates outside the narrow zone where ionization processes take place and streamers appear. The positive layer surrounding the point creates a field that is directed against the external one on the inside of the layer, that is, it reduces the field around the point, thus screening it. The criterion of self-sustainment, (12.5), is thereby violated. New streamers are not formed and the current decreases. As the ions are pulled to the cathode, the strong field at the tip is restored (the point becomes "bare" again). Streamers appear, a new surge of ionization follows, then of current, and the cycle begins anew. Something similar takes place on the second pulsed interval V_2–V_t, but now *pre-breakdown streamers* are involved. In the interval V_1–V_2, the condition of self-sustainment is strictly satisfied and a dc current flows. The current between the pulses of the flashing corona does not drop to zero: a constant component is observed.

Negative point. The current is intermittent in a certain interval of mean currents and voltages, beginning with the ignition point V_c. The pulse repetition rate is greater than in positive coronas, $10^5\,\text{Hz}$ at $20\,\mu\text{A}$, while the pulses are shorter ($10^{-7}\,\text{s}$) and higher: the peak current reaches 10 mA. The pulses follow in a very regular manner. They are known as *Trichel pulses.* As the voltage is increased, the pulses disappear and a steady-state corona is sustained until the spark breakdown of the discharge gap.

In principle, the factors causing the nonsteady behavior here are the same as in the case of positive coronas, although some differences are observed. When an avalanche grows from the cathode point, the positive space charge lies close to the point, while the negative charge is at a somewhat greater distance. If this charge is formed by electrons, they are rapidly pulled away to the anode, so that the negative charge density is very low, i.e., it produces no screening of the field of the point. The presence of positive ions in the immediate vicinity of the tip only enhances the field there. As a result, Trichel pulses are *not observed* in the *electropositive* gases N_2 and Ar. Air is different: once an electron is far from the point, it finds itself in a weaker field and becomes attached to a molecule. The space charge of negative ions weakens the field of the point, the multiplication of avalanches is suppressed, and the current decays. As the negative ions are

pulled towards the anode and positive ions move to the point, the external field is restored and favorable conditions for a new pulse build up.

The corona discharge is not necessarily harmful, as it is in power transmission lines. It is usefully employed in electric filters and separators, and is fundamental for Geiger-Müller counters, developed in 1929 to detect nuclear particles. A recent good review is available on the physics of corona discharges [12.13].

12.7 Models of Streamer Propagation

Is the Head of a Cathode-Directed Streamer Insulated from the Anode? The insulation degree of and the extent to which the anode potential is transferred by the streamer channel to its positive tip constitute one of the *main questions of the theory,* because the answer determines whether the streamer channel will be transformed into a spark channel after the gap is closed (Sect. 12.5), that is, whether the streamer breakdown may be realized. Until recently, two models of the streamer process, based on *extreme* assumptions, were considered: *absolute insulation* of the positive streamer head from the anode[2] and *ideal conduction* of the streamer channel.

12.7.1 Model of Self-Sustaining Streamers

This model was developed by *Dawson* and *Winn* in 1965 [12.14]. The head of a cathode-directed streamer is a sphere of radius r_0, containing N_+ positive ions. As it moves, it leaves behind a quasineutral ionized channel; however, it is assumed that its conductivity is negligibly low and the head is not connected to the anode. The problem then is to find the conditions under which the head is absolutely *autonomous,* that is, moves regardless of the external field, producing and absorbing avalanches by its own field.

Let a photoelectron that initiates the avalanche be liberated at a distance x_1 from the center of the positive sphere, in the direction of motion (Fig. 12.11). An electron avalanche develops at this point in the field $E = eN_+/x^2$ and moves towards the head. The number of electrons produced in it at a point x_2 is $N_e = \exp \int_{x_1}^{x_2} \alpha \, dx$. Let the avalanche radius r_D increase by the diffusion law

$$dr_D^2/dt \approx 4D_e \,, \quad r_D(x_2) = \left\{ \int_{x_1}^{x_2} 4 \frac{D_e/\mu_e}{E(x)} dx \right\}^{1/2} .$$

When the "spherical" electron head of the avalanche enters the ionic head of the streamer, quasineutral plasma is formed at this point, and the ionic trail of the avalanche transforms into the newly-advanced streamer head. For this process to be continuous and steady, it is necessary that at the moment when the head of the

[2] A slight refinement must be added here: what is meant is that insulation sets in after the very first electrons sink into the anode at the moment of formation of the streamer.

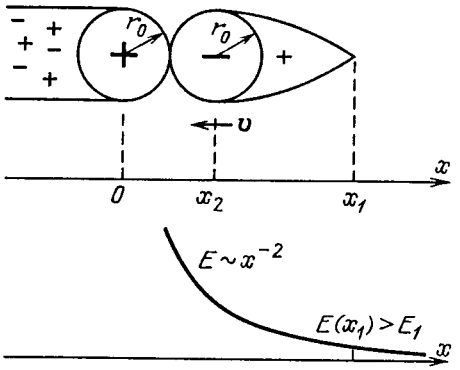

Fig. 12.11. Model of self-sustaining streamer

avalanche touches the head of the streamer, that is, at $x_2 = r_0 + r_D$, the numbers of charges in the two heads and their radii be equal: $N_e = N_+ \equiv N_0$, $r_D = r_0$. The point of avalanche inception, x_1, has been fixed artificially, to correspond to the free path length of photons, but so as to meet the condition that the field $E(x_1)$ in air be sufficient for ionization: $E(x_1) \gtrsim 30\,\text{kV/cm}$.

The self-sustained process air is possible with the following values of parameters: photon "path length" $x_1 \approx 2 \times 10^{-2}\,\text{cm}$, number of ions in the streamer head $N_+ \equiv N_0 \approx 10^8$, head radius $r_0 \approx 2.7 \times 10^{-3}\,\text{cm}$. The streamer propagation rate is $v = x_2/t$, where t is the time in which the avalanche progresses from x_1 to x_2; $v \approx 10^7\,\text{cm/s}$. These figures do not go beyond reasonable limits, but they do not in fact seem to be realistic. The streamer radius r_0 is too small, and the charge density in it is correspondingly too high: $n_e = n_+ \approx 3N_0/4\pi r_0^3 \approx 2.6 \times 10^{15}\,\text{cm}^{-3}$. The neglected repulsion of electrons in the avalanche increases its radiuss, the field $E \approx eN_0/r_0^2$ decreases, ionization slows down significantly, that is, the process may become "disbalanced".

12.7.2 Is Strictly Steady Propagation of Streamers Possible in the Absence of External Fields?

The answer to this question is "it is not", because energy is needed for the ionization of the new volume of gas absorbed by the streamer channel, and this energy can be drawn only from outside. Actually, the process in question is not steady but merely quasi-steady, in the sense that the parameters change by only a little during one steep of propagation of the head, over a distance about equal to the size of the head. Estimates show [12.14] that the initial amount of energy in the head (electrostatic energy $e^2N_0^2/2r_0 \approx 2.7 \times 10^{11}\,\text{eV}$), taking into account the expenditure on ionization and excitation, is sufficient for moving the streamer by about 3 cm. This result fits remarkably well the experiment of the inventors of the model, who measured the distance covered by the streamer after the external voltage was switched off (finite-length pulses with abrupt rise and fall edges were applied to the electrodes).

12.7.3 Positive Streamer Insulated from the Anode in a Nonuniform Field (Streamer Corona)

The Dawson-Winn model was considerably improved by *Gallimberti* in 1972 [12.15], who was taken into account consistently the energy balance of processes involving the external field. Gallimberti also introduced an approximate description of photoionization, so as to eliminate the arbitrariness in prescribing the distance x_1 at which the avalanche is initiated. As in [12.14], it was assumed that only one "equivalent" avalanche is started. The positive sphere was again assumed insulated from the anode. The parameters of the streamer (N_0, r_0) change as it propagates in the nonuniform field. The energy balance equation expresses the fact that the work done by the external field on electrons compensates for the energy spent by electrons on ionization, excitation, attachment, on transfer to molecules, and also on the change in the potential electrostatic energy of the positive charge of the streamer head (both intrinsic and in the external field).

The fairly complicated equations were solved numerically for the specific conditions of corona in air. Figure 12.12 demonstrates excellent agreement with experimental results. The length of the streamer is about 11 cm, which the head covers in 10^{-7} s. The streamer moves over the first 5 cm (the region of especially strong field of 15 to 5 kV/cm) at a velocity of about 2×10^8 cm/s. The streamer stops where the field drops to 2 kV/cm. The number of positive charges in the head reaches the maximum $N_0 \approx 1.6 \times 10^9$ ($eN_0 \approx 2.5 \times 10^{-10}$ C).

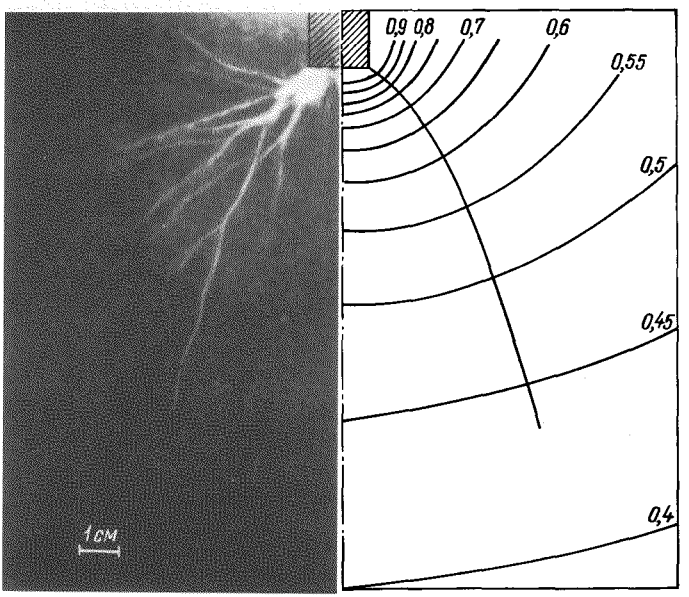

Fig. 12.12. Streamer moving from a positive rod 2 cm in diameter to a plane at a distance of 150 cm [12.15]. Constant voltage, 125 kV. *Right:* results of calculations; equipotential surfaces are shown; numbers on the curves give the fraction of applied voltage measured from the plane electrode. *Left:* photograph of streamers under the conditions of calculations

A numerical Monte Carlo procedure was developed for the approximation of two equivalent avalanches that are randomly initiated at different points of the angle sector near the streamer head [12.16]. This computer simulation produced a branching zigzag pattern of streamers under the same conditions; it resembled the photograph even more.

12.7.4 External Field Necessary for the Propagation of a Streamer

It is clear from the arguments above that the growing streamer must be supplied with energy; this function is fulfilled by the applied field, which does work on the electrons. This can be interpreted macroscopically as the energy released by the *streamer current*. The streamer current in the approximation of a concentrated charged head moving at a velocity v is given by formulas (12.6′, 6). If $N_0 \sim 10^9$, $v \sim 10^8$ cm/s in a long discharge gap of $d \sim 1$ m, then the average current is $i \sim 10^{-4}$ A, and if the gap is narrow, $d \sim 10$ cm, then $i \sim 10^{-3}$ A. The power $iV = eN_0vE$ is spent on ionization, on electron and vibrational excitation of molecules, and an attachment compensation. If the average energy spent on producing one electron is w, then $eN_0vE = n\pi r_0^2 vw$, where the charge density is $n \approx 3N_0/4\pi r_0^3$. The external field required to supply the energy to sustain the streamer is $E_s \approx w/er_0$, which satisfies the obvious condition $eE_s r_0 \approx w$.

The radius r_0 of the charged head and of the streamer channel is found from the condition of self-sustainment of the head in the strong field it creates and depends very little on the external field. If in air $w \approx 50$ eV and $r_0 \approx 10^{-2}$ cm, we obtain an estimate $E_s \approx 5$ kV/cm. A detailed calculation [12.15] for the case of a homogeneous field yielded $E_s = 7$ kV/cm.

These figures are in reasonable agreement with experimental data. According to [12.17], in dry atmospheric-pressure air we find $E_s \approx 4$ kV/cm. As reported in [12.18], the average external field that was necessary to sustain the steady growth of a streamer in air in the experiment was $E_s \approx 4.7$ kV/cm, almost independently of gap width and field nonuniformity. In technical grade nitrogen (up to 2 % O_2), $E_s \approx 1.5$ kV/cm; in Ar, $E_s \approx 0.4$ kV/cm (all at 1 atm.). The value of E_s is very sensitive to attachment, which removes electrons from the process. To multiply electrons up to the required level N_0, high energy expenditure is necessary.[3] Thus an admixture of O_2 to Ar increases E_s from 0.4 to 2.3 kV/cm at an O_2 content of 10 %. On the other hand, if air is heated to 1000 K, electrons are liberated from negative ions and E_s falls from 4.7 to 0.7 kV/cm [12.18]. The necessary field also increases as the humidity is raised. At a water vapour content of 2×10^{-5} g/cm^3, E_s is greater by a factor of 1.5 than in dry air [12.17].

[3] This may reflect the reduction of conductivity in the streamer channel (see Sect. 12.7.7), although this certainly has no place in the theory of the self-sustaining streamer heads.

12.7.5 Model of an Ideally Conducting Streamer Channel

This assumption was first suggested by Loeb in early work on the streamer theory, and was incorported into the constructed one-dimensional theory of the ionization wave (modeling the streamer) in the field [12.19]. The two-dimensional model was developed in [12.5] for the process of streamer growth from the midpoint of a plane gap towards both electrodes. The surface of the ideally conducting body of the streamer is equipotential. Surface charges induced by the external field are distributed over this surface (the plus sign on the side facing the cathode, the minus sign towards the anode). It was assumed that the streamer body forms an ellipsoid of revolution elongated parallel to the field, the velocity of motion of the surface at each point being directed along the outward normal and equal in magnitude to the electron drift velocity in the appropriate field (Sect. 12.3). The calculated velocities of the anode and cathode ends of the streamer coincided with the results of measurements in neon at $p = 1$ atm. in external fields of $E = 10$–15 kV/cm. The velocities increase as E and the streamer length l increase; for $l \approx 0.5$ cm, $v \sim 10^8$ cm/s.

Let us note a useful formula for estimating the enhanced field E_m at a rounded tip of radius r at the end of a conducting rod of length l placed along the external field E_0:

$$E_m/E_0 = 3 + 0.56(l/r)^{0.92}\ ,\quad 10 < l/r < 2000\ .$$

This formula was obtained by approximating the calculated fields [12.18].

If the ideally conducting channel begins at the anode, it is as a whole at that potential, $\varphi = V$ (at the cathode, $\varphi = 0$). There is no longitudinal field in the channel. We denote the potenital at a point x of the channel that is produced by the applied voltage in the absence of the streamer by $\varphi_0(x)$. The coordinate x is measured along the channel from the anode. The additional potential $\varphi_1(x) = V - \varphi_0(x)$ is mostly produced by the positive charge concentrated on the channel surface. The charge per cm of its length is $q(x) = C\varphi_1(x)$, where C is the conductor capacitance per unit length. It can be evaluated by the formula $C = [2\ln(R/r_0)]^{-1}$, valid for a conductor of radius r_0 in a grounded coaxial cylinder. For its radius R, can take the distance X to grounded cathode (if X is less than the streamer length l or l if $X > l$. If $r_0 = 10^{-2}$ cm, $R = 30$ cm, $C = 0.062 = 0.07$ pF/cm.[4] Far from the anode, $\varphi_1 \sim V$. If, for example, $\varphi_1 = 50$ kV, then $q = 3.5 \times 10^{-9}$ C/cm. The current of an ideally conducting streamer of length $x = l$ is created by the continuous sinking of electrons into the anode and by the formation of a new region of positive charge at the end of the conductor: $i = q(l)v$. If $q = 3.5 \times 10^{-9}$ C/cm and $v = 10^8$ cm/s, then $i = 0.35$ A. This value is significantly greater than in an insulated streamer head.

[4] The measurements [12.20] best agree with calculations for $C = 0.05$ pF/cm.

12.7.6 Compensation Zone

Actually, the concept of a charged sphere with a moderate-conductivity electroneutral channel stretching out behind it (as in the Dawson-Winn model) contains a contradiction.

The contradiction was pointed out by *Griffiths* and *Phelphs*.[5] Let the entire positive charge eN_0 be concentrated in a sphere of radius r_0. The potential φ_1 created by this charge falls off away from the sphere, including the direction along the channel toward the anode; the maximum of φ_1 equals $\varphi_s = eN_0/r_0$ (for $N_0 = 10^9$, $r_0 = 10^{-2}$, $\varphi_s = 14\,\text{kV}$). A very strong additional field, $E_1 \sim eN_0/r_0^2 \sim 10^3\,\text{kV/cm}$, will draw electrons from the immediate neighborhood of the channel to the head.

The positive charge thus gets distributed not within the sphere but over a certain length L at the end of a "nonconducting" channel so as to level off the potential $\varphi(x)$ at about $\varphi_0(l-L)$. Beyond the right end of the region $l-L < x < l$ (the "compensation zone"), the potential drops sharply to the level of the external potential, $\varphi_0(l)$. If the potential jump at the end of the streamer is $\varphi_1 \approx \varphi_0(l-L) - \varphi_0(l) \approx E_0(l)L \sim 10\,\text{kV}$, and the external field is $E_0 \sim 10\,\text{kV/cm}$, then $L \sim 1\,\text{cm}$. For $C \sim 10^{-13}\,\text{F/cm}$, $q(l) \sim 10^{-9}\,\text{C/cm}$ and the total charge of the extended tip of the streamer $Q \approx q(l)L/2 \sim 10^{-9}\,\text{C}$ is somewhat greater than in the case of the spherical head.

12.7.7 Which Model Is Closer to the Truth?

In fact, this question opened Sect. 12.7. The answer can be obtained experimentally or found in the theory which takes into account the finite conductivity of the streamer channel. Even in very simplified physical formulations, the streamer process is described by equations so complicated that hopes of a solution may be associated only with numerical methods, and such publications are now appearing. Some experimental results have also been obtained. In experiments [12.18], the charge transfer to the cathode in the process of the propagation of a single streamer from the anode was recorded using an oscilloscope; the streamer current was then calculated. The current in technical-grade nitrogen at $p = 1$ atm. in a gap of $d = 1\,\text{m}$, between the positive rod and a plane during the streamer propagation time $t \sim 10^{-5}\,\text{s}$, is $i \sim 10^{-3}\,\text{A}$. The current transfers the charge $Q \sim 10^{-8}\,\text{C}$. This is much greater than that found in the spherical head theory. If we assume that what is measured is the conduction current through the streamer channel, the conductance for unit length is found from Ohm's law $i = \gamma E$, for the external field, E to be $\gamma = \pi r_0^2 \sigma \sim 10^{-7}$–$10^{-6}\,\text{cm/Ohm}$.

Unfortunately, the channel radius is unknown. If $r_0 = 10^{-2}\,\text{cm}$, then $\gamma = 10^{-6}$ leads to $\sigma = 3 \times 10^{-3}\,(\text{Ohm·cm})^{-1}$, which corresponds to the plasma density in the channel $n_e \approx 4 \times 10^{13}\,\text{cm}^{-3}$. If $r_0 \approx 3 \times 10^{-3}\,\text{cm}$, then $n_e \approx 4 \times 10^{14}$; this is apparently an upper bound. The measured values of i and Q are too high for the insulated sphere model but too low for the model of an ideally conducting

[5] Their arguments are presented in a detailed review [12.21] on the spark breakdown of long gaps.

channel. Under the conditions of the experiment, $V \sim 10^2$ kV, the charge on the tip of an ideally conducting streamer that has traveled half the gap length is $q \approx CV \sim 10^{-8}$ C/cm, so that at $v \sim 10^7$–10^8 cm/s the current is $i = qv \sim 0.1$–1 A. The real situation is intermediate between the two models; and presumably, it corresponds to a considerable insulation of the streamer tip from the anode and to a compensation zone in that region.

These conclusions are supported by numerical calculations. Numerical results do not point to the nonmonotonic potential $\varphi(x)$ implied by the sphere model, or to the vanishing of the field in the channel, as in the case of ideal conduction. A two-dimensional problem was treated in [12.22], on the propagation of the plasma channel in nitrogen at 1 atm. in a plane gap of $d = 0.5$ cm at $V = 30$ kV, $E_0 = 60$ kV/cm. Self-sustainment via initiation of secondary avalanches due to photoionization was not discussed. Instead, an initial electron background was postulated, $n_e = 10^8$ cm^{-3}. An initial plasma source was defined at the anode with $n_e \sim 10^{14}$ cm^{-3}. The plasma channel with $n_e \sim 10^{14}$ cm^{-3} grows from it toward the cathode at a veloctiy $v \approx 2 \times 10^8$ cm/s. The field at its end reaches 150 kV/cm, but the field inside the channel is reduced by a mere 20 to 30 % in comparison with the external field. The initial channel radius, arbitrarily fixed in the calculation (about 10^{-2} cm), was preserved in the course of channel growth; the streamer radius thus could not be obtained from the equations (neither was it possible to measure it experimentally).

This is a weak spot in the calculations [12.23] for air, as well, although in other respects this work is more comprehensive: the process in the channel and around the streamer head has been analyzed with photoionization taken into account. The calculation was quasi-one-dimensional, the radius was imposed artificially: $r_0 = 10^{-2}$ cm. Such parameters of the streamer as velocity and density of plasma at the tip and the field at the tip on the side of the channel, are determined by the increase of potential $\varphi_1(l)$ at the head over the initial level. The quantity $\varphi_1(l)$ is a function of external conditions and conductivity in the channel, which is determined by electronic kinetics. For example, if $\varphi_1(l) = 9$ kV, we obtain $v = 1.4 \times 10^8$ cm/s, $E = 4$ kV/cm, and $n_e \approx 10^{15}$ cm^{-3}.

The unit-length conduction of the streamer channel in air far from the tip does not exceed 10^{-10} cm/Ohm owing to attachment. This is seen from the negligibly low current, less than 10^{-6} A, that flows after the streamer touches the cathode and "closes" the gap [12.18]. Attachment is unimportant only in short streamers, and at early stages of the propagation of long ones. In air at $p = 1$ atm., the attachment frequency is $\nu_a \approx 10^7$ s^{-1} so that at $v \sim 10^8$ cm/s the concentration n_e in the channel decreases considerably at a distance $x \sim v/\nu_a \sim 10$ cm. According to the calculation [12.23], the concentrations in the streamer channel of $l \approx 8$ cm are $n_e \approx 2 \times 10^{14}$ cm^{-3} and $n_- \sim 1.5 \times 10^{13}$ cm^{-3}.

A relatively high conductivity of the streamer channel has been recorded in argon cleaned of electronegative impurities [12.18]: $\gamma > 10^{-5}$ cm/Ohm, $i \sim 10^{-2}$ A. The streamer channel was observed to transform into a spark channel after the cathode was reached. Generally, streamer (not leader; see Sects. 12.8, 9)

breakdown has been observed only in inert gases. It seems that if the model of the ideally conducting streamer remains meaningful at all, it may hold only for inert gases.

12.7.8 Plasma Decay and the Radius of a Streamer Channel

The conductivity of the channel in air decreases rapidly as we move away from the streamer head. Actually, the plasma in the channel decays even in nitrogen (where attachment does not occur) if the external field is not much greater than the limiting field for the streamer propagation. $E_s \approx 1.5\,\text{kV/cm}$ at $p = 1\,\text{atm}$. The field behind the head does not exceed the external field and the corresponding $E/p = 2\,\text{V/cm Torr}$ is too low for the ionization of the cold nitrogen (Sect. 8.7.7). Over the period $t \sim 10^{-5}\,\text{s}$ during which a streamer passes across a meter-wide gap, electrons recombine to a density $n_e \sim (\beta t)^{-1} \sim 10^{12}\,\text{cm}^{-3}$ from an arbitrarily higher initial value. A decrease in the conductivity of the channel (the more important, the longer the channel and the more uniform the external field) prevents the streamer breakdown of long uniform gaps.

Despite a certain similarity, a streamer channel with weakly ionized nonequilibrium plasma cannot be likened to the positive column of a glow discharge. Ionization processes in the discharge column balance out the loss of charge and the plasma in the column is self-sustained. The streamer channel is rather a "passive" plasma trace left behind the advancing self-sustained streamer head. The trace radius (channel radius) r is presumably determined by ambipolar diffusional expansion of the plasma from its initial size, that is, from the streamer head radius $r_0 \approx 3 \times 10^{-3}$–$10^{-2}\,\text{cm}$ (Sect. 12.7.1). The seemingly unchanging "thinness" of a long channel creates the false impression of an inherent channel radius. In reality, the trace simply has not had enough time to expand significantly: at $D_a \approx 2\,\text{cm}^2/\text{s}$, the increase of the radius over a time $t \sim 10^{-5}\,\text{s}$ is $r - r_0 \approx \sqrt{D_a t} \approx 4 \times 10^{-3}\,\text{cm} \approx r_0$.

The preservation of the radius of the initial perturbation of the growing plasma channel in the calculation [12.22] (mentioned in Sect. 12.7.7) is caused by the field build-up in the neighborhood of the channel; the spreading due to diffusion is negligible. The authors choose such a high value of the external field, $E \approx 40E_s$, that the ionization in the channel greatly exceeds the recombination.

12.8 Breakdown in Long Air Gaps with Strongly Nonuniform Fields (Experimental Data)

12.8.1 Effect of Field Nonuniformity on Breakdown Voltage

Field nonuniformity reduces the breakdown voltage for a given distance between the electrodes. This is illustrated in Fig. 12.13, where the measurements were conducted at the industrial frequency of 50 Hz. The nonsteady nature of the field makes practically no difference, because the half-period of $10^{-2}\,\text{s}$ is long in com-

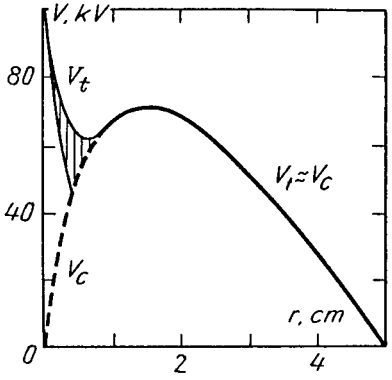

Fig. 12.13. Voltages of corona ignition V_c and of breakdown V_t in an air gap between concentric cylinders as functions of radius of the inner electrode; outer electrode radius $R = 5$ cm. (Amplitude of 50 Hz ac voltage is plotted.) The region of enhanced sprad in breakdown voltages is shaded [12.9]

parison with the time scale of breakdown.[6] Since the polarity of electrodes is alternating, the breakdown occurs at the polarity that facilitates it (see below). The tangent to the curve $V_t(r)$ at $r = R$, with the slope of 32 kV/cm, roughly corresponds to the breakdown of plane gaps of the same size $d = R - r$ in uniform field. As r decreases, that is, as the degree of nonuniformity is enhanced, the threshold curve $V_t(r)$ deviates more and more downwards from the tangent. The mean breakdown field $E_{av} = V_t/(R - r)$ diminishes monotonically in comparison with the level 32 kV/cm. The reason for this effect of nonuniformity is that any breakdown criterion includes the coefficient of enhancement of primary avalanches, $\int \alpha\, dx$, which is very sensitive to the distribution $E(x)$ owing to the steeply climbing curve $\alpha(E)$. The distribution of the field in comparison with the uniform picture increases the enhancement at preserved $\int E\, dx$, or decreases the potential difference at constant enhancement. We have already encountered this effect several times (Chap. 8).

Figure 12.13 is illustrative in another aspect, as well. The range of voltages $V_c < V < V_t$ over which a corona burns contracts as r increases, and the degree of field nonuniformity decreases. If the field is not too nonuniform, $r/R \gtrsim 0.1$, no corona develops: increasing the voltage on the electrodes leads straight to the breakdown of the gap. If, however, the radius of the electrode carrying the corona is very small (very high nonuniformity), the difference between the corona initiation and breakdown potentials, $V_t - V_c$, becomes large.

The effect of the degree of field nonuniformity on breakdown voltage is also revealed by the fact that it is easier to produce breakdown between a rod and a plane than between two rods, at the same separation d. The corresponding threshold voltages (also at 50 Hz) are plotted in Fig. 12.14 for gaps of d up to 10–12 m. The rod was a rectangular metal bar of square cross section, of $1/2''$ sides. For the same d, the capacitance of the rod-plane gap is greater than that of the rod-rod gap, because the volume occupied by the field is greater. Therefore,

[6] In order to eliminate the effect of the rate of voltage build-up during the "switch-on" period in measurements of dielectric strength of a gap for dc or for time-dependent (not pulsed) fields, the electrode voltage (or the amplitude of the 50-Hz voltage) is raised gradually, over a time of up to several minutes (Sect. 12.8.4).

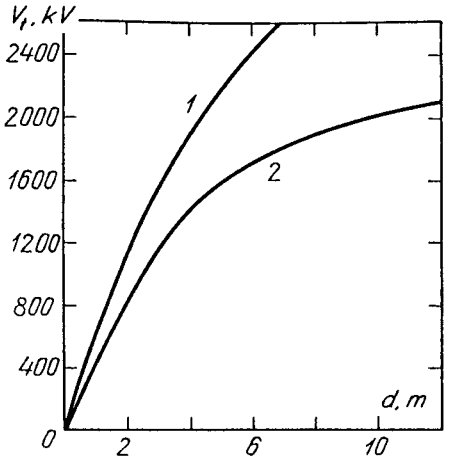

Fig. 12.14. Amplitude of breakdown voltage at $f = 50$ Hz in an air gap of length d. *(1)* rod–rod, *(2)* rod–plane gap [12.7]

the electric charge on the rod is greater at the same voltage in the former case; furthermore, the field at the tip and in most of the gap is higher.

From the standpoint of field distribution, the rod-rod gap of d at V is equivalent to a rod-plane gap of $d/2$ at $V/2$. This factor affects the values of the respective breakdown parameters in the conditions of complete symmetry produced by the oscillating field. Thus the rod-rod gap of $d = 6$ m has $V_t = 2400$ kV, while the rod-plane gap of $d = 3$ m has $V_t = 1200$ kV. At smaller separations this equivalence rule does not hold as strictly: $V_t = 1850$ kV in the rod-rod gap of $d = 4$ m, and $V_t = 850$ kV in the rod-plane gap of $d = 2$ m. Nevertheless, the deviation is not large.

12.8.2 Effect of Polarity

The breakdown threshold in a constant field depends very strongly on the polarity of the "active" electrode (Fig. 12.15; the same rod geometry). In the case of a negative rod, the breakdown voltage is roughly twice that of the positive one. This is a result of the difference between the conditions for the development of avalanches and streamers at the active electrode. The avalanches at the *rod anode* travel to it from the outside; as they come nearer, they enter the region of

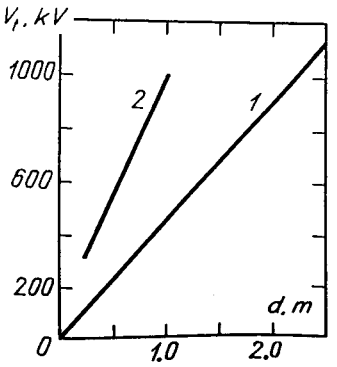

Fig. 12.15. Threshold voltages in air gaps of length d between a rod and a plane. *(1)* positive rod (anode), *(2)* negative rod [12.9]

progressively stronger field. This factor *facilitates* the multiplication of electrons and *stimulates the avalanche-streamer transition.* In the case of the *rod cathode,* multiplying avalanches move farther from the electrode into the region of progressively weaker field. The multiplication process is therefore *slowed down* and the *avalanche-streamer transition is inhibited.* Moreover, in the case of the positive rod electrons sink into the metal, leaving behind a noncompensated positive space charge, which enhances the field at the electrode. In the case of the negative rod, however, the field of the corresponding negative space charge is somewhat compensated for by the field of positive ions, all of which stay in the gas.

The data presented above are typical of that reported laboratories doing research into high-voltage equipment. This information is used in designing power transmission lines and other high-voltage structures.

12.8.3 Mean Breakdown Field Is Low: Important Implications

Although the voltages required for the breakdown of long gaps in air are enormous (millions of volts if $d \gtrsim 10\,\text{m}$), the *mean* electric field in the gap, $E_{\text{av}} = V_{\text{t}}/d$, is puzzlingly *low.* If $d \approx 1$–$2\,\text{m}$, then $E_{\text{av}} \approx 10\,\text{kV/cm}$ for negative and $4.5\,\text{kV/cm}$ for positive points (Fig. 12.15); at $d \approx 10\,\text{m}$ and industrial frequency, the mean amplitude is $E_{\text{av}} \approx 2\,\text{kV/cm}$ (Fig. 12.14); if $d \approx 30\,\text{m}$, it is $1\,\text{kV/cm}$. This is the level of field in the predominant part of the gap; the minimum values (at the plane) are even lower. We know, however, that the ionization of air by electron impact requires at least $E_{\text{l}} \approx 24\,\text{kV/cm}$. The conclusion is unambiguous: once the ionized channel or leader in a long air gap has been created at the electrode at which the field is concentrated, it breaks through to the other electrode with no ionizing assistance from the external field.

The role played in this case by the applied voltage is not directly to sustain an intensive multiplication of electrons in any region within the gap. This would be required for the breakdown in an ideal plane gap at vanishingly small overvoltage. The important factor here is the ionization at each point in the path of the avalanche. Its every segment must contribute to enhancement so as to make it sufficient for the reproduction of secondary avalanches (involving cathode emission), or for the avalanche–streamer transition. If, however, the potential difference is nonuniformly distributed in space, it only has to create a field sufficient for intensive multiplication in the neighborhood of a single electrode. Once a *plasma channel* is initiated, it *grows,* energizing the required ionization in the gas mostly by its *own field,* or rather, by the *field of its charged tip.*

12.8.4 Effect of the Rate of Voltage Build-up

The description above *does not imply* that the voltage is determined by the field required only to *generate* the leader. As the channel grows longer, it is more and more difficult to sustain this growth, so that it is desirable to *constantly increase* the voltage in order to sustain the advancement of the leader over long distances and to make it reach the opposite electrode. Obviously, breakdown can

be achieved at a constant voltage $V_{t,const}$ but this voltage needs to be higher than the final voltage at the closing of the gap by the channel in the case of a gradual increase of V. For each length d, there is an *optimal rate of voltage growth*, dV/dt. At this rate, the final (i.e. the breakdown) voltage has a minimum value. $V_{t,min}$. Breakdown is obstructed both by too slow and by too rapid a voltage increase. The optimal time of voltage build-up rate on a rod electrode above the grounded plane is found from an empirical formula $\tau_{opt} \approx 50d\,[\mathrm{m}]\ \mu\mathrm{s}$; it has been experimentally verified up to $d \approx 30\,\mathrm{m}$.

Since the regime in which the leader channel grows under gradually increasing voltage is the most favorable for breakdown, it is natural to interpret the experimental value τ_{opt} as the time scale for the leader bridging the gap. This gives us the velocity of motion of leader tip, $v_l \approx d/\tau_{opt} \approx 2 \times 10^6\,\mathrm{cm/s}$. Direct measurements give similar values (Sect. 12.9.4). For values of $d \approx 10\,\mathrm{m}$, the quantities $V_{t,min}$ are found to be 30 % lower than $V_{t,const}$. Breakdown also occurs after pulses shorter than τ_{opt}. As an example, consider the so-called "standard storm pulse" of 50 μs duration and front rise time of 1.2 μs. This calls for higher voltages than $V_{t,min}$. For example, for $d = 4\,\mathrm{m}$, the voltage must be twice $V_{t,min}$ ($V_{t,min} \approx 1.1\,\mathrm{MV}$); the latter corresponds to $\tau_{opt} \approx 200\,\mu\mathrm{s}$. Roughly speaking, in this case it is necessary to have the leader traverse the gap at four times the speed.

12.9 Leader Mechanism of Breakdown of Long Gaps

12.9.1 Insufficiency of the Streamer Process for the Realization of Breakdown

In Sect. 12.5 we discussed the simplest scheme of *streamer breakdown*, such as appeared realistic in the early days of spark theory. A lone streamer grows from the anode; having reached the cathode, it triggers the propagation of a return wave of intense ionization; the result is the formation of the spark channel. Gradually it became clear that something of this sort *is* realized; but only if the gap is *not too long*, the *degree of nonuniformity of the field is not too high*, and *attachment is absent* (Sect. 12.7.7). The point is that the conductivity in the streamer channel is not high enough effectively to transfer the anode potential towards the cathode, in order that a strong field and the subsequent return wave of intense ionization can be generated. Moreover, as the streamer advances, its head enters the region of progressively weaker fields, thereby setting the limit to further advance. These processes become much more severe in electronegative gases (Sect. 12.7).

In a strongly nonuniform air gap (in fact, it is virtually unrealistic to hope to create uniform field in very long gaps), where the conditions for streamer growth are unfavourable, the streamers *stop without reaching the opposite electrode*. This is clearly seen in the photographs of streamer corona at a point (Fig. 12.12) but the same occurs in breakdown. The streamer length depends on the applied voltage and on a number of other conditions. It may be 10–100 cm; streamers in electropositive gases are longer, up to 1 m.

We know that streamers become longer as the voltage increases; hence, we would hypothesize that the breakdown of the entire gap occurs when the field $E_{av} = V_t/d$ grows to reach E_s, so that the streamer is given the possibility to reach the electrode it was traveling towards. In fact, long gaps undergo breakdown at much lower voltages and mean fields: if d = 10–30 m, E_{av} = 2–1 kV/cm (Sect. 12.8.3), while E_s = 4.7 kV/cm (Sect. 12.7.4). Nature prefers a *different way out;* it is seen in high-speed photographs of long laboratory sparks and lightning (historically, the work began with lightning).

12.9.2 Growth of Leader Channel

A thin, highly ionized, highly conductive channel grows from the active electrode (from the strong field region) along the path prepared by the preceding streamers; this channel transfers the electrode potential to its tip to a much greater extend than streamers do. This channel is known as a *leader*. The leader channel "extends" the tip of the electrode and carries it, at a high potential relative to the opposite electrode, toward this electrode. The leader head, like a metallic tip, is a source of exceptionally strong field and thus sends out streamers that fan out and prepare the initial (far from low) electron density. Electrons ionize the gas intensively in the strong field of the leader head, thereby creating a "new" head and thus supporting the advance of the strongly ionized channel (Fig. 12.16). When the channel closes the gap, the return wave starts from the second electrode (the plane), which triggers the transformation of the leader channel into the spark.

Here we more or less repeat the description given in Sects. 12.3, 12.5 of the streamer breakdown mechanism. Indeed, the differences between the streamer and leader is not so much qualitative as quantitative, i.e., in the degree of ionization and in the strength of the field produced. A streamer absorbs avalanches, a leader absorbs streamers, parallelling Peter Brueghel's famous drawing "Large fishes gobbling up smaller ones". One more link is added to the already described chain of processes that precede the spark breakdown: *avalanches-streamer-return wave* is replaced by *avalanches-streamer-leader-return wave.*

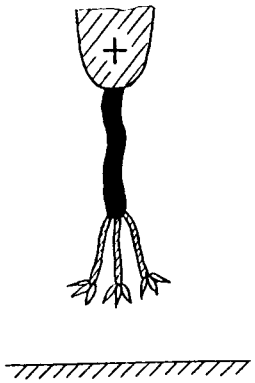

Fig. 12.16. A leader grows from a positive tip along the path prepared by streamers which, in their turn, absorb avalanches

12.9.3 On the Mechanism of Leader Formation

The foremost condition of leader formation in air is an increase in gas temperature, at least to the extent necessary to suppress a decrease in conductivity owing to electron attachment. When streamers start at a positively charged tip (*streamer corona*), they normally branch off a single *stem*. It has been suggested that the total electron current of all the streamers converging at this channel deposits enough Joule heat to raise the temperature of the gas to a level sufficient for thermal ionization [12.24]. The gas is thereby strongly ionized, electrons sink into the anode, and a large positive charge is left behind in the channel; this charge producing a strong field. The cycle is then repeated, with the streamer corona starting now not at the anode, but at the head of the new segment of the ionized channel. Thus starts the growth of the leader. However, evaluations made to support this hypothesis [12.9] indicate that the streamer current heats the air in the channel only to 3000 K. This is certainly insufficient for the onset of thermal ionization of air: about 8000 K would be needed. Spectroscopic data also indicate that the temperature in the stem of the streamer head is not high enough.

A mechanism of low-temperature transition from streamers to leader in air was suggested in [12.25]. This model also postulated the Joule heating of air in the stem of the streamer corona, but the mechanism of conductivity growth is the intense liberation of electrons from earlier-formed negative ions. To destroy O_2^- ions in dry air, a temperature $T \approx 1500\,\mathrm{K}$ is sufficient; detachment takes about 10^{-7} s. A slightly higher temperature, up to 2000 K, is required for appreciable detachment in humid air.

In moist air, hydrated ions $O_2^-\,[H_2O]_n$ ($n = 1, 2, 3$) are formed. In these ions, the electron binding energy I_n^- increases with n while the bonding energy of the H_2O molecule, $E_{n\,H_2O}$ decreases. For example, $I_3^- = 2.65\,\mathrm{eV}$, while for O_2^-, $I_0^- = 0.44\,\mathrm{eV}$; $E_{3\,H_2O} = 0.23\,\mathrm{eV}$. Hydrated ions are progressively decomposed by successive separation of H_2O by successive molecular impacts, after which the electron is lost. The time required for detachment is 10^{-6}–10^{-5} s at $T \approx 1500$–$2000\,\mathrm{K}$, and is much greater at lower temperatures. We may recall in this connection the observations described in Sect. 12.7.4 concerning the experimentally observed sharp rise in conductivity of the streamer channel in response to "artificial" heating of the air. The rate of temperature increase with current also increases. At low temperatures, Joule heat is stored in molecular vibration; as T increases, the energy passes more and more rapidly to translational (and rotational) degrees of freedom. Thus the vibrational relaxation time at nearly normal air humidity of $0.8 \cdot 10^{-5}\,\mathrm{g/cm^3}$ and $T = 300\,\mathrm{K}$ is $\tau_{VT} \approx 60 \times 10^{-5}$ s; at 1000 K, it is 8×10^{-5} s, and at 2300 K, it is 10^{-5} s.

An increase in the conductivity due to an increase in temperature will result in the narrowing of current flow to a thin channel, that is, in something like the contraction of Sect. 9.11.

12.9.4 Experimental Data on Leader Parameters

Information on the leader can be extracted by deciphering the data obtained from high-speed photography using optoelectronic equipment, concurrent electrical measurements in the external circuit (current and voltage), by measuring the field in the channel using auxiliary electrodes or by other methods, performing spectroscopic measurements, and so forth [12.21, 12.26].

The following figures give an idea of leader parameters [12.21]. The mean velocity of leader propagation in an air gap of $d = 10\,\text{m}$ between a conical anode and a plane cathode, with voltage rising to $V = 1.6\,\text{MV}$ during $t \approx 2 \cdot 10^{-4}\,\text{s}$, is $v_\text{l} \approx 2 \times 10^6\,\text{cm/s}$. During the first $10^{-4}\,\text{s}$, the leader channel expands at a radial velocity of $v_r \approx 10^4\,\text{cm/s}$; by $t \approx 10^{-4}\,\text{s}$, the expansion slows down considerably to $v_r \approx 2 \times 10^2\,\text{cm/s}$ and the channel radius is $r \approx 0.2\,\text{cm}$. The current during the passage of the leader across the gap is $i_\text{l} \approx 1\,\text{A}$ (for $t \approx 5 \times 10^{-4}\,\text{s}$), and the power released is $P \approx 1\,\text{MW}$. The mean field in the channel falls as the leader propagates; when half of the gap has been crossed, it levels off (by estimate) at about $E \approx 1\,\text{kV/cm}$. These figures imply that the channel conductivity is $\sigma \approx 10^{-2}\,(\text{Ohm cm})^{-1}$. Calculations show the vibrational relaxation to take $10^{-4}\,\text{s}$ and a temperature $T \approx 5000\,\text{K}$ to be established in the gas; at the same time, $T_\text{e} \approx 2 \times 10^4\,\text{K}$. The density of electrons, estimated from σ and the gas density at this temperature and $p = 1\,\text{atm.}$, is $n_\text{e} \approx 10^{13}\,\text{cm}^{-3}$.

This estimate of n_e is comparable with the results of calculations and of measurement data analysis for attachment in the streamer channel close to its head, where not all the electrons have yet been removed. Using the above data, we can estimate the linear charge of the leader channel at the tip, $q = i/v_\text{l} \approx 5 \times 10^{-7}\,\text{C/cm}$. In a channel of length $l \approx d/2$, the voltage drop is $El \approx 500\,\text{kV}$; at $V = 1.6\,\text{MV}$, the potential of the leader head is $\varphi \approx 1\,\text{MV}$. Hence, the linear capacitance is $C \approx q/\varphi \approx 0.5\,\text{pF/cm}$. Other measurements give $C \approx 0.25\,\text{pF/cm}$ [12.27]. The linear capacitance of a leader is about five times that of a single streamer. This finds an explanation in the relatively thick "sheath" surrounding the high-conductivity thin leader channel; the sheath is formed of weakly conducting plasma and the space charge injected into it by streamers.

Numerous streamers fan out forwards from the leader tip. The streamer corona in front of the leader head (Fig. 12.16) in a gap of $d = 10\,\text{m}$ extends to a distance about 1 m. When these streamers reach the cathode plane, the advance of the leader is accelerated. This stage is called the *final jump*. At this stage the leader current increases jumpwise to $i \sim 100\,\text{A}$, the ionization in the channel increases considerably, and the field drops to $E \sim 100\,\text{V/cm}$. The transition to the final jump, which may start very early in not too long gaps, reliably leads to breakdown. Before the final jump the breakdown may be prevented by lowering the external voltage. Sometimes, as the leader head approaches the electrode, the greatly enhanced field between them starts a counterleader from the electrode.

12.9.5 What Contributes to the Leader Current

A leader fuses the currents of numerous streamers that start from the tip, into a single channel. Only the *joint efforts* of streamers can heat the gas to the required temperature. Short, newborn streamers which still retain ahigh conductivity contribute via their conduction current, and long streamers which have lost electrical contact with the leader owing to attachment contribute via displacement current (as described in Sect. 12.2.3). The long streamers are much more numerous because of their longer lifetimes. Before the final jump, their heads travel at the streamer velocity $v_s \gg v_l$ over a distance $l \sim 1$ m to a spot where the field of the leader tip falls below the level $E_s \approx 4.7$ kV/cm (Sect. 7.4). There the streamers slow down and for some time travel at the leader velocity. This is because the leader carries forward the point where $E = E_s$ at the velocity v_l.

If a long streamer carries a charge Q_s (independent measurements give $Q_s \approx 5 \times 10^{-10}$ C in air), the entire leader current $i_l \approx 1$ A can be generated solely at the expense of the displacement current only if streamers appear at a frequency $\nu_b \approx i_l/Q_s \approx 2 \times 10^9\ s^{-1}$ [12.27]. If the deceleration time over a length $l \sim 1$ m is $\tau_{dec} \sim l/v_s \sim 10^{-5}$ s, the number of long streamers in the corona in front of the leader tip is $N_s \sim \nu_b/\tau_{dec} \sim 2 \times 10^4$. The loss of conductivity in a streamer is, say, 20-fold over a time $\tau_{cond} \sim 3\nu_a^{-1} \sim 3 \times 10^{-7}$ s, that is, the number of short (still conducting) streamers is $N_{s,cond} \sim \nu_b \tau_{cond} \sim 10^3$. If the current due to conducting streamers produces a predominant contribution to i_l, then the frequency ν_b needs redefinition; nevertheless, independent experiments [12.18] support the estimate given above.

The behavior during the final jump is different, a fact used in [12.28] to explain the observed rise in current. Roughly speaking, now each longer streamer hits the cathode without slowing down, at a velocity v_s, and brings a charge Q_s. While the leader current i_l before the final jump is proportional to v_l, during the final jump $i_l' \sim v_s$. Hence, $i_l'/i_l \approx v_s/v_l \approx 10^2$. For details, see [12.28].

12.9.6 Why Voltage Has to Be Raised During Leader Progress in Order to Facilitate Its Advance

As in the case of a streamer, the leader velocity and current are determined by the potential φ_l of its tip. A rough empirical formula is known: $v_l = 1.2 \times 10^6 \times (\varphi_l\ [\text{MV}])^{1/2}$ cm/s [12.27]; if $\varphi_l < 200$–300 kV, no leader can form in a long gap: $i_l = C\varphi_l v_l$, where the linear capacitance of a channel C is a quantity less dependent on parameters (Sects. 12.9.4, 12.7.5). If V is the instantaneous voltage between the electrodes and E_l is the average field in the leader channel of length l, then $V = \varphi_l + E_l l$. If the potential φ_l is insufficient, the current is very low and the field E_l is high as a result of poor conductivity; hence an exceedingly high voltage V is needed to sustain the progress of a leader. If φ_l is too high, an excessively high voltage is again required despite the smallness of the drop $E_l l$. For each length l, there is an optimal potential φ_l at which V is minimal. This is a fairly stable quantity, approximately equal to 1 MV. It is to sustain the optimal regime at a moderate advance velocity $v_l \sim 1.5 \times 10^6$ cm/s and current $i_l \approx 1$ A

(before a final jump) that the voltage needs to be continuously increased as the leader increases in length.

12.9.7 What Is the Main Difference Between a Leader and a Streamer? Why Does an Intermediate Streamer Stage Appear in the Leader Process?

These are questions of principal importance and we will complete the discussion of the streamer and leader mechanisms by trying to give as clear answers to these questions as possible. The leader and the streamer are formations *of the same type*. Both are plasma channels which grow in a self-sustaining manner in an external field which is too low for ionization. The electron density and radius of the channel heads are comparable, differing by one to two orders of magnitude at the most. The principal difference lies in the *tendencies* of the plasma. The streamer plasma tends to lose conductivity because of attachment, especially in air, while the leader plasma does not. A streamer is thus insufficient for the breakdown in a long gap. The difference in tendencies is connected with the gas temperature at the channel head, and this temperature depends on the current i and is determined by the power released per unit length, $W = iE$ (compare with formulas (10.15), (10.33)). The elevated temperature in the leader head suppresses the attachment in air. This opens the way to a further increase in temperature and ionization (as in the contraction of the glow discharge).

When the current is sufficiently high to heat the gas, avalanches cannot directly be transformed into a leader channel, since this process is preceded by the streamer-avalanche transition. Once the number of electrons reaches a certain, not extremely high, level and the avalanche radius reaches a very low value $r_0 \sim 10^{-2}$ cm, the avalanche immediately transforms into a weak-current streamer of this radius, with low power per unit length. Additional growth of the avalanche is needed for the "avalanche-leader" transition; it is prevented since the avalanche-streamer transitions *stops the growth*. As a result, a sufficiently high-current leader channel can be formed only by the merging of streamers.

We also mention an unusual theory of leader propagation [12.29] in which the ionization of the gas around the leader head is assumed to originate in the heating of the gas by a shock wave. The latter is produced by the release of the Joule heat in the leader head. This mechanism is similar to that of light detonation, supported by high intensity laser beam (see [12.6]). In spite of the attractiveness of the theory [12.29] its quantitative arguments do not seem quite convincing. On *negative* leaders, see Sect. 12.12.

12.10 Return Wave (Return Stroke)

When the leader head reaches the electrode, its charge is immediately neutralized and the channel head acquires the potential of the electrode. If this is the cathode, electrons are knocked out of it by photons or the strong field and a cathode spot

is formed; if it is the anode, the electrons of the leader head sink into the metal. A *return wave* is then sent through the leader channel towards the point, this is a wave of decay of potential and of neutralization of the linear charge of the leader channel and of its surroundings (the sheath); the neutralization is not necessarily complete. The physical mechanism of the return stroke is best understood in terms of discharging a charged long line connected to ground. This interpretation has been used in numerical calculations [12.26].

Let an electric charge, q per cm, be distributed over a long wire. The capacitance, inductance, and ohmic resistance per cm are denoted below by C, L, and R. The potential U (with respect to "ground") and current i, treated as functions of time t and coordinate x along the wire, are described by the equations (in absolute system of units)

$$-\frac{\partial U}{\partial x} = \frac{L}{c^2}\frac{\partial i}{\partial t} + Ri\,, \quad -\frac{\partial i}{\partial x} = C\frac{\partial U}{\partial t}\,, \tag{12.22}$$

which have a fairly lucid physical meaning (see any textbook on electricity). If the conductor is ideal ($R = 0$), (12.22) reduces to the wave equation

$$\partial^2 U/\partial t^2 - v^2 \partial^2 U/\partial x^2 = 0\,, \tag{12.23}$$

where the wave velocity is $v = c/\sqrt{LC}$.

If a uniformly charged line with $q_0 = CU_0 = \text{const}$ and $i_0 = 0$ is connected at the initial instant $t = 0$ to ground at $U = 0$, a wave of potential decay and line discharge travels from the ground contact at a velocity v (Fig. 12.17). The current behind the wave is $i = -U_0/\varrho = -q_0 v$, where $\varrho = c^{-1}\sqrt{L/C}$ is the so-called wave resistance (characteristic impedance). In this idealized scheme, the potential at the wave front changes abruptly from U_0 to 0, and the field is "infinite". For a wire of radius r in vacuum, surrounded at a large distance H by a grounded cylinder, $L = C^{-1} = 2\ln(H/r)$ in absolute values and v equals the speed of light c.

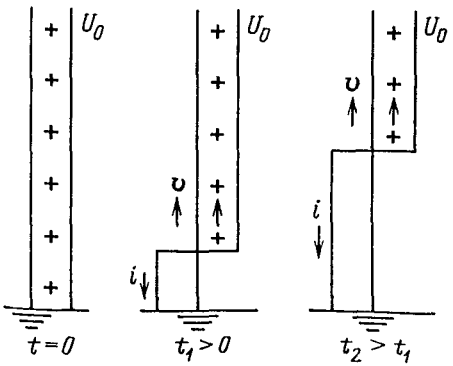

Fig. 12.17. Discharge of an ideally conducting charged line to ground; the diagram models the return wave after a positive leader arrives at the cathode. $t = 0$, the moment the line connects to ground; t_1 and t_2, two stages of wave propagation; diagrams of current i and potential V are shown

In reality, when a conductor possesses active resistance and a charge in a sheath around the leader channel, the wave front has a finite width, the field in it is finite, and the velocity $v \sim 0.1c$ (this follows from experiments and evaluations [12.26]). It is this field at the potential "jump" that imparts high energy to the electrons. In macroscopic terms, a large amount of Joule heat $W = iE$ W/cm is released at the wave front, where both the current and the field are high. It is this *wave of high energy release* rushing through the channel that results in the formation of the *spark channel,* as described in Sect. 12.5. Some quantitative characteristics will be given later with regard to the lightning discharge (Sect. 12.11.5).

12.11 Lightning

12.11.1 Thunderclouds

The cause of electric discharges in the atmosphere is the formation and spatial separation of positive and negative charges, resulting in an electric field. If the field reaches the value sufficient for the breakdown of air, the discharge occurs. In almost 90% of cases, the negative charge is found at the bottom part of the cloud and the main positive charge is at the top. For the cloud shown in Fig. 12.18, the potential difference V between the centers of the positive and negative charges q, and between the lower part of the cloud and the ground, is on the order of $V \sim q/L \sim 10^8$ V ($q = 40$ C $= 3.6 \times 10^{13}$ V/cm, $L \approx 2.5$ km), the mean electric fields being on the order of $E_{av} \sim V/L \sim 300$ V/cm. Fields of this order of magnitude are also measured on the ground under heavy clouds, and inside clouds (on aircraft).

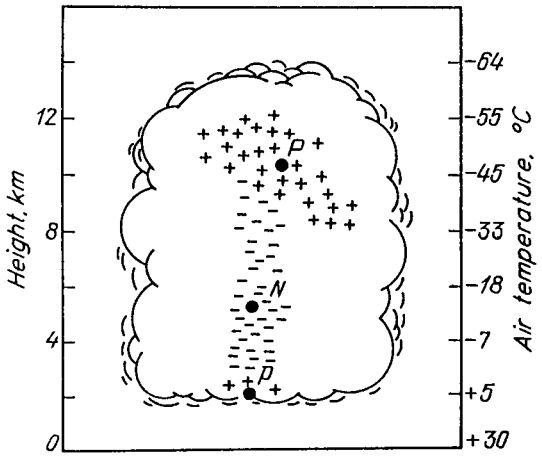

Fig. 12.18. Probable charge distribution of a thundercloud. Black dots mark centroids of charge clouds. According to measurements of electric fields around clouds, $P = +40$ C above, $p = +10$ C below, and $N = -40$ C. [12.30]

The current concepts of the origin of atmospheric electricity were largely developed in 1940s by *Ya.I. Frenkel* [12.31]. Charges appear in the atmosphere as a result of ionization of molecules and the knocking out of electrons from macroscopic particles by cosmic rays. Electrification of water droplets when they break into fragments during their fall is also possible, the separating fine droplets carrying away mostly negative charge. Negative ions generated by the ionization of air tend to stick to water droplets. Polar molecules of water in the surface layer of a droplet become aligned with their positive ends oriented inwards and negative ends pointing outwards, thus forming an electrical double layer. The field formed inside the layer points outwards, towards the air. There is no field beyond the layer. Hence, the potential jump $\Delta\varphi$ takes place within the layer, the value of φ inside the droplet being higher than in the surrounding medium; measurements give $\Delta\varphi = 0.26$ V. A droplet absorbs negative ions until the potential difference between liquid and air vanishes. The number of absorbed charges, N, is given by the equality $eN/r = \Delta\varphi$, where r is the droplet radius. If $r = 10^{-3}$ cm, $N \approx 2 \times 10^3$. The separation of charges on the scale of a cloud is caused by the downward drift of negatively charged droplets due to gravity; most positively charged particles retain molecular form and do not move downwards.

In general, lightning discharges inside clouds are more frequent than discharges between the lower part of clouds and the ground. For obvious reasons, however, experimental study has concentrated on the latter species, the one to be discussed in the sections below.

12.11.2 Experimental Techniques

A camera for high-speed filming of lightning was constructed by C.V. Boys in 1900. The film was placed under a disk with two objective lenses installed on the disk diameter on two sides of the center. The disk revolved, producing two photoscans of the process. In 1929 Boys designed a camera in which fixed objective lenses projected an image onto a moving film via prisms. The film was clamped to the inner surface of a revolving drum.[7] The first photoscans of lightning (sometimes called *Boys' patterns*) were successfully obtained only in 1928. Current notions of the evolution of the lightning discharge are based on the research of B.F.J. Schonland (1935–1940), who worked with redesigned Boys' cameras.

Photography is supplemented with measurements of the discharge current. This is best accomplished using a "lightning receiver," that is, by recroding the oscillogram of current on the spot receiving the lightning stroke. Simultaneously obtained, synchronized lightning photoscans and current oscillograms are especially valuable. Electric and magnetic perturbations due to the discharge are picked up by antennae on other devices, although it is far from easy to extract information on lightning current from these data. At the early stages of light-

[7] In a typical modern high-speed photorecorder, the objective lens and the film are fixed, and the beam moves along the film, being reflected from a rotating mirror.

ning research, *klydonographs* were widely used, that is, instruments which form Lichtenberg figures (Sect. 12.1.1). In the USSR, I.S. Stekolnikov and co-workers carried out much work on lightning discharges (from the 1930s). Their success mostly stemmed from the careful combination of lightning studies and the analysis of long sparks produced in the laboratory [12.26]. On methods and equipment, see also [12.32].

12.11.3 Sequence of Events

On the average, a lightning flash lasts for 200 ms. It consists of several *pulses* each of some 10 ms separated by about 40 ms. Each pulse begins with the growth of a *leader channel* from the cloud to the ground (Fig. 12.19). With the exception of its head, the channel is rather dark. The leader transports negative charge (from the negatively charged cloud); the current at this stage is about 100 A. As the leader approaches ground, its channel begins to branch out, the branches developing in a zig-zag manner. When the main leader reaches the ground, or collides with the counter-leader (Sect. 12.9.4), a highly luminous channel (return wave) starts to travel on its path towards the cloud at an enormous velocity, 0.1–0.3 of the speed of light. This phenomenon is called the *return stroke* or the *main stage* of the lightning discharge. The lightning current then reaches its maximum of about 100 kA. The most dangerous effects of the lightning stroke are connected with this peak current (e.g., overvoltage surges in transmission lines). Then the negative charge of the cloud is drained to the ground through the spark channel within 40 ms, by a low current (about 200 A). The outflow of electric charge from the large volume of a cloud about 1 km in size is possible only because electrons are released from negatively charged macroscopic particles and ions by strong electric fields.

In response to heat release in the channel, the pressure rises, sending out a *shock wave*. The acoustic wave to which the shock wave decays at a large distance is perceived as *thunder*. The energy released in one lightning discharge is $qV/2 \sim 10^9$–10^{10} J, corresponding to the explosion of about a tonne of explosive.

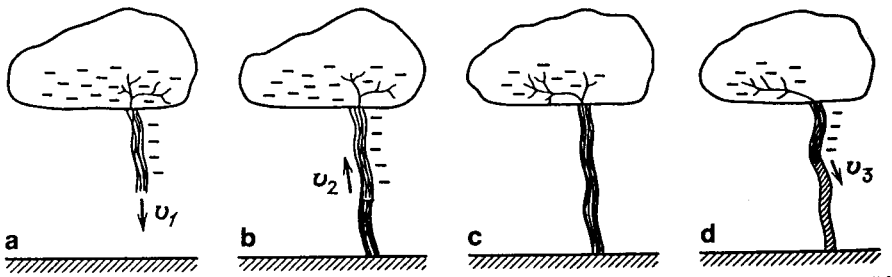

Fig. 12.19. Lightning discharge: (a) primary (step) leader travels to the ground at a velocity v_1; (b) return stroke wave travels upward at a velocity v_2; (c) intracloud breakdown occurs from the return stroke channel to the left-hand part of the cloud. The charge of the right-hand part has been drained through the spark channel; (d) secondary leader (dart leader) travels at a velocity v_3 through the partly decayed plasma of the spark channel, and so forth

According to spectroscopic data, the temperature in the spark channel is about 25,000 K and the electron density is $(1-5) \times 10^{17}\,\mathrm{cm}^{-3}$ [12.32], which on the whole corresponds to total single ionization of atoms.

One lightning pulse transfers to the ground only a fraction of the cloud charge contained in the neighborhood of the location reached by the tip of the return stroke channel. The supply of charges from distant locations to this region takes time, so that discharge to the ground quietens down for a while. Charges from the farther parts of the cloud arrive to the channel tip by way of *intracloud* breakdowns; once the paths to the distant regions have been traced, the next lightning pulse is triggered. The conductivity of the first-stroke spark channel has decreased by this time, so that a new leader propagates through the residual channel from the cloud to the ground: it increases ionization in the old channel. The second (and subsequent) leaders do not branch. When the second leader reaches the ground, the second return stroke occurs, and the process is repeated several more until the entire negative charge of more and more distant cloud regions is transferred to the ground. The positive charge located very far away (very high in the cloud) seems to remain there, since the available voltage is too low for the breakdown across such a large distance.

12.11.4 Dissimilarity of the First and Subsequent Leaders

Boy's patterns show (Fig. 12.20) that the motion of the first negative leader towards the ground is *intermittent*. A bright streak (step) lights up on the photograph, corresponding to a length of 50 m; this is repeated regularly. The impression is that the leader moves forward by violent dashes separated by pauses. This leader is known as a *stepped leader*. The average velocity of advancement of the leader's front towards the ground, calculated from the slope of the envelope of bright streaks on photoscans is $(1-2) \times 10^7$ cm/s. Judging by photographs, the leader radius is definitely much greater than that of the truly highly conduc-

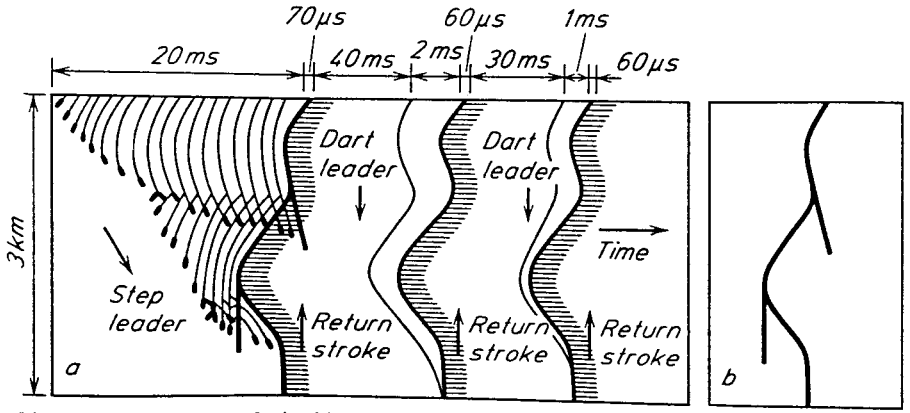

Fig. 12.20. Boys' pattern obtained by photographing a lightning flash on moving film. Time proceeds from left to right; for the sake of convenience, the time scale is nonlinear. (a) time scan, (b) the same flash, photographed without scanning [12.32, 33]

Table 12.2. Main parameters of lightning from a negatively charged cloud to the ground[a]

	Lowest	Typical	Highest
1. *Flash*			
Duration [s]	0.01	0.2	2
Number of pulses	1	3–4	26
Interval between pulses [ms]	3	40	100
total charge transferred [C]	3	25	90
2. *Step leader*			
Step length [m]	3	50	200
Pause between steps [μs]	30	50	125
Average velocity [cm/s]	1×10^7	1.5×10^7	2.6×10^8
Charge transferred [C]	3	5	20
3. *Dart leader*			
Velocity [cm/s]	1×10^8	2×10^8	2.1×10^9
Charge transferred [C]	0.2	1	6
4. *Return stroke*			
Channel length [km]	2	5	14
Velocity [cm/s]	2×10^9	5×10^9	1.4×10^{10}
Peak current [kA]		10–20	110
Peak duration at half height [μs]	10	40	250
Charge transferred, except of continuous current [C]	0.2	2.5	20

[a] Presented systematically in [12.32] using the data of numerous measurements

tive zone. The second – and subsequent – stroke leaders propagate continuously, without steps and at a much higher velocity , 10^8–10^9 cm/s. Certain similarities of the image on Boy's patterns with darts led to the term *dart leader*.

Time intervals between subsequent stages of discharge can be estimated from Fig. 12.20, and their characteristic parameters can be found in Table 12.2. The leader current is $i \sim q_l v/d$ [see (12.6)], where q_l is the charge transferred, v is its propagation velocity and d is the length on the order of cloud height. If $q_l = 5$ C, $d = 3$ km, $v = 1.5 \times 10^7$ cm/s, then $i \approx 250$ A. The leader charge per unit length is $q_l = q_l/d \sim 10^{-5}$ C/cm; $i \sim q_l v$. It appears that the field in the leader channel is of the order of 100 V/cm.

12.11.5 Return Stroke

This process was discussed in Sect. 12.10. The wave propagating upwards from the ground is followed by a high current that carries to the ground the charge from the leader channel and its surroundings. The potential behind the wave front approaches that of the ground. The potential in front of the wave stays close to the leader potential, and hence to cloud potential, at practically zero current because the leader current vanishes, together with the termination of leader advancement. Judging by photoscans, the return wave of the lightning discharge rushes upward at a velocity $v \approx (0.1\text{–}0.3)c \approx 3 \times 10^4$–$10^5$ km/s, that is, it lasts for about 10^2 μs.

The transitional wave front region in which the potential drop occurs and the field is strong, and which is correspondingly highly luminous, is shown by the scan to be $l \approx 25$–$110\,\text{m}$ long. Hence, the field there is $E \sim V/l \sim 10\,\text{kV/cm}$. This is a very high field for a strongly ionized plasma: the field in arc channels in air is $E \sim 10\,\text{V/cm}$. If the return stroke current is $i = 20\,\text{kA}$, the energy released in the front region is $W = iE = 2 \times 10^8\,\text{W/cm}$ (that in the arc is $W \sim 10^3\,\text{W/cm}$). Clearly, the plasma channel containing this tremendous heat release rapidly expands and forms a well-developed spark channel. Energy is spent mostly on heating, dissociation, and thermal ionization of the surrounding layers of air, not on any significant rise in temperature or ionization of the very zone of heat release where the gas has already been totally single ionized.

12.12 Negative Stepped Leader

A careful look at a Boys' pattern shows that bright lines (steps) do not just follow one another on the way to the ground, but overlap: each begins with a "recoil," starting from the midpoint of the preceding one. This behavior is at odds with a simple interpretation of the intermittent picture: a rapidly moving luminous object which draws a streak on the film but then stops for while. The question about the meaning carried by the term "stepped" is tacitly avoided in the monographs [12.2, 12.3, 12.5, 12.32]. Beginning with Schonland, various hypotheses were proposed concerning the step mechanism, but all arguments and estimates were extremely "fuzzy" and vague; it is highly unlikely, therefore, that it is by accident that their description of these contributions in a very solid and detailed monograph by *M.A. Uman* in [12.32] appears to be devoid of any physical meaning.[8]

Another difficulty seems to be the fact that the experimental analysis of such a remote, random, and unwieldy object as lightning does not provide adequate information for the profound understanding of the details of the extremely complex spark discharge phenomena. Indeed, although laboratory studies of several-meter-long sparks emitted from negative points (in which leaders also reveal 3–5 steps of $d = 6\,\text{m}$ [12.26]) have not yet resulted in clear physical interpretations, their better resolution yielded at least a much more detailed sequence of processes to be modelled.

The following picture emerges from the analysis of electro-optical scans and simultaneous oscillograms of the leader current (both obtained with very high resolution) [12.26], see Fig. 12.21. In the case of a positive point, or of its "extension," that is, a positive leader (both attract avalanches), streamers are formed most easily at the tips; in contrast, the avalanche–streamer transition in the case of a negative point (repulsing the avalanches) can take place only at some distance from the head of a point or leader. A brightly luminous plasma "blob" of about

[8] Uman, speaking about lightning theory, emphasized the meaninglessness of using the terms "pilot leader" and "streamer," which only replace the physical interpretation of phenomena.

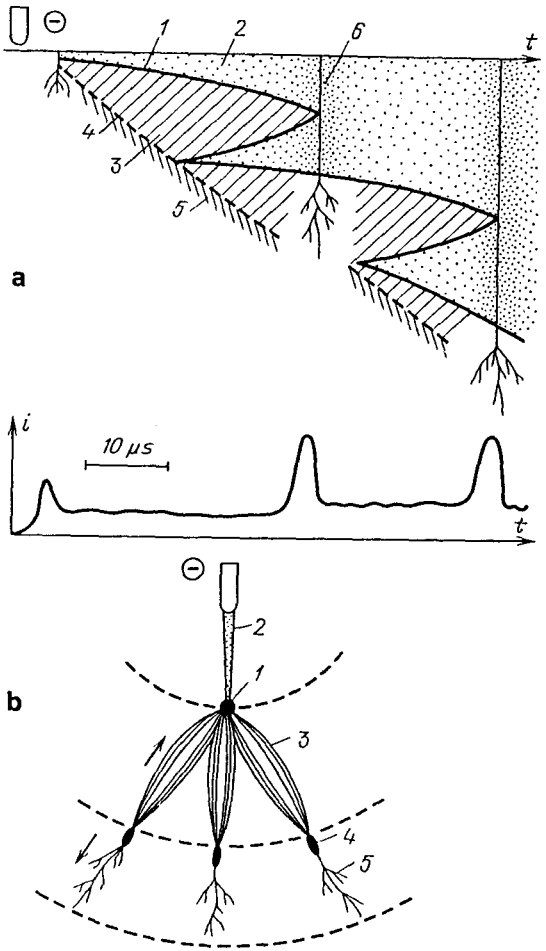

Fig. 12.21. Evolution of a negative step leader constructed using by interpretation of the photoscan of the process. The scan (**a**) is compared to the leader current trace (**b**); shown below is a spatial diagram giving a kind of "instantaneous photograph" of the process at some moment of time. Numbers on the diagram mark the same elements that they mark on photoscan (**a**). *(1)* head of the leader channel, *(2)* leader channel, *(3)* cathode-directed streamers starting from a plasma blob (hypothetical leader propagating in both directions), *(4)* plasma "blob", *(5)* anode-directed streamers, *(6)* a step of the leader [12.26]

$1\,cm^3$ in volume appears at some distance from the tip of the negative leader. It sends out streamers (cathode-directed to the leader tip and anode-directed to the plane electrode). It can be hypothesized that a secondary positive leader propagates from the plasma towards the main negative leader, as a result of the polarization of the plasma blob by the external field and owing to the enhancement of the field between the positive charge of the dipole and the leader tip. When the leaders collide, the entire path from the point to the opposite end of the secondary leader becomes highly conducting; this leads to the tip potential

building up in the channel and in a current surge which heats up the channel and produces the flash (Fig. 12.21). The head of the main leader jumps to the former plasma blob, thus producing a step. The model is certainly not quite conclusive, especially because the origin of the plasma blob remains unclear. There can be no doubt, though, that understanding will come only through such carefully designed laboratory experiments.

The understanding of the physics of long sparks, which is one of the most complicated fields in gas discharges, does more than just satisfy our inquisitiveness. It helps to solve practical problems in high-voltage equipment and lightning protection. It is no accident that an international European association of scientists, Les Renardieres Group, was created to conduct research in this field (a report on its recent work appears in [12.34]).

13. Capacitively Coupled Radio-Frequency Discharge

13.1 Drift Oscillations of Electron Gas

13.1.1 Introductory Remarks

In a capacitively coupled rf (ccrf) discharge, an rf voltage is applied to (typically) plane-parallel electrodes (Fig. 7.20). The electrodes may be in contact with the discharge, or they may be insulated from it by solid dielectrics. In this sense, we refer to discharges as *electrode* or *electrodeless*, respectively. Our presentation will mostly presume the "industrial" frequency $f \approx 13.6\,\mathrm{MHz}$[1] and medium pressures 10–100 Torr that are currently of considerable interest, partly in view of the application of ccrf discharges to high-power lasers (Chap. 14). As a rule, the plasma of such discharges is weakly ionized, nonequilibrium, and resembles the glow discharge plasma. In order to understand better the results of observations and measurements (Sect. 13.4), it is desirable to have a clear picture of some general features of ccrf discharge processes. They are given in a qualitative scheme (Sect. 13.1.2) and in a simplified *electrical-engineering-type* theory (Sect. 13.2).

The electron collision frequency ν_m at a pressure $p \sim 10\,\mathrm{Torr}$ exceeds the value $\omega = 2\pi f = 0.85 \times 10^8\,\mathrm{s}^{-1}$ by a factor of about 10^3, so that electrons in an oscillating field $E = E_a \sin \omega t$ perform *drift oscillations* (Sect. 3.1.3) with velocity and displacement amplitudes

$$v_{da} = \mu_e E_a\,, \quad A = \frac{v_{da}}{\omega} = \frac{\mu_e E_a}{\omega} = \frac{\mu_e p}{\omega}\,\frac{E_a}{p}\,. \tag{13.1}$$

For $E_a/p \sim 10\,\mathrm{V/cm\,Torr}$, which is typical of a nonequilibrium weakly ionized plasma of molecular gases, and for the value of ω given above, the oscillation amplitude is $A \approx 0.1\,\mathrm{cm}$. It is small in comparison with discharge gap lengths L typical in experiments, $L \sim 1$–$10\,\mathrm{cm}$. Drift velocities and oscillation amplitudes of ions are less by a factor of $\mu_e/\mu_+ \sim 10^2$, so that in many cases the oscillatory motion of the ions can be ignored. Even for a very low density of electrons, $n_e = 10^8\,\mathrm{cm}^{-3}$, and for the electron temperature $T = 1\,\mathrm{eV}$ characteristic of a collisional plasma, the Debye radius $d_D = 0.05\,\mathrm{cm} \ll L$. Therefore, the plasma

[1] The corresponding wavelength $\lambda = 22\,\mathrm{m}$ lies in the short-wave range. High-power rf units generate noise, interfering with radio and communications. To avoid this, several narrow frequency intervals were assigned to this work by international agreements (including the above frequency).

is *electrically neutral* over most of the discharge gap. However, the electron gas at the boundaries of the plane gap "swings" with respect to the relatively "fixed" ions and thus periodically bares the positive charges, just like receding surf leaves behind bare sand. This behavior is the reason for the appearance of *space-charge layers at the electrodes*. The same term will be applied below to the layers formed at *dielectrics* that insulate electrodes from the plasma.

13.1.2 Distribution of Space Charge, Field, and Potential in Plane Gaps

Assume the electrodes to be bare. Thus, electrons whose equilibrium positions were spaced from the electrode by a distance less than the oscillation amplitude sink into the metal "for good" [13.1]. Layers of noncompensated ionic charge remain on both sides in the equilibrium state. On the whole, the gas is *positively charged.*[2] During subsequent swings, the electron gas merely "touches" the electrodes (we neglect the slow diffusion process). Figure 13.1 shows schematically the pattern of *swings* of the electron gas under the assumption that ions are absolutely unmoving and are uniformly distributed over the gap length, while electrons perform no diffusional motion. Actually diffusion does blur the boundary between plasma and ionic layers. Figure 13.2 plots field and potential distributions corresponding to Fig. 13.1, for the same times, each quarter of the period. The field E in the uniform electroneutral part of the gap is constant over its length. To be more specific, we measure the potential from the left-hand electrode. We can assume it to be grounded, with the oscillating voltage being applied to the right-hand electrode. It can be assumed that the magnitude and direction of electric current are described by the vector $\boldsymbol{E}$, because the *conduction current* in the plasma itself is usually greater than the *displacement current.*

Various experiments have demonstrated that electrons incident on the surface of dielectrics (glass, etc.) get *attached* to the surface. The dielectric then becomes charged more and more negatively until the field produced by this charge

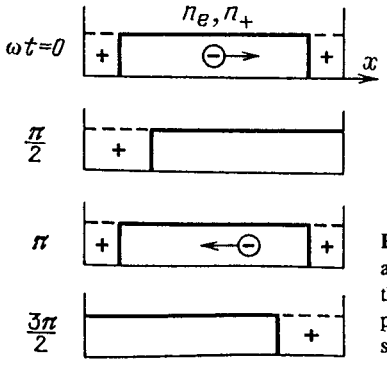

Fig. 13.1. Swings of the electron gas. The gas of ions is assumed to be fixed and uniform. Time is measured from the moment when electrons pass through the equilibrium position when moving to the right. Distributions $n_e(x)$ are shown for every quarter of the period

[2] Note that the gas in ordinary glow discharges is also charged positively as a whole, owing to the existence of the cathode layer (the negative charge of the anode layer is much smaller).

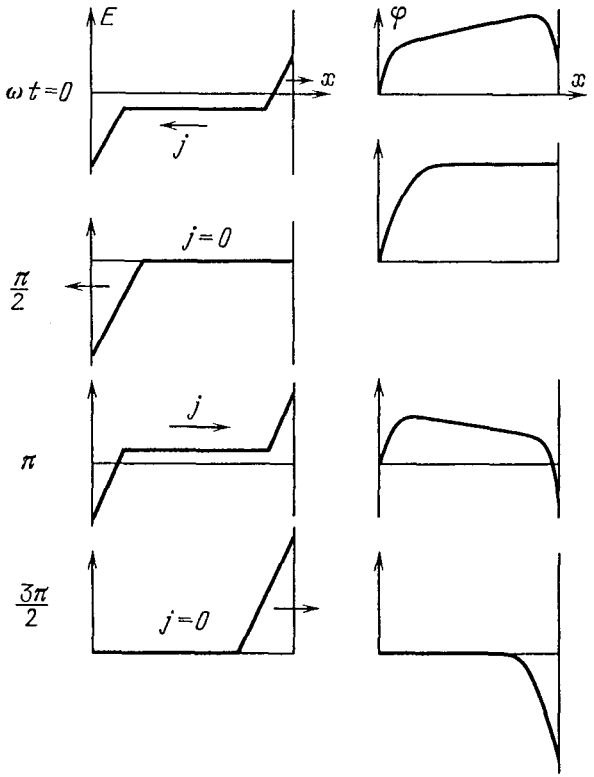

Fig. 13.2. Field and potential distributions in the gap corresponding to Fig. 13.1

repels all new electrons (Sect. 8.1.7). This also takes place in ccrf discharges with insulated electrodes, the surface of the insulator being capable of accepting all the electrons that would be contained in the electrode layer. In other words, Fig. 13.1, 2 holds equally well for ccrf discharges with insulated electrodes. Although this effect has not been directly observed, some indirect experimental confirmation is known (Sect. 13.6.4). In fact, experiments do not show appreciable differences between electrode and electrodeless ccrf discharges.[3]

[3] If a constant (d.c.) breakdown voltage is applied to such a system with insulated electrodes, breakdown occurs in the gas. After this, electrons from the gap attach to the dielectric that covers the positive electrode. The field of this charge is directed in the gap toward the applied field and thus partly cancels the latter. The field in the gap decreases to a level insufficient for sustaining the discharge, or even drops to zero, so that the process stops. Experiments show that after this the *dielectric cell* can withstand the above-breakdown voltage without repeated breakdowns and without sustaining an appreciable current.

13.2 Idealized Model of the Passage of High-Frequency Current Through a Long Plane Gap at Elevated Pressures

13.2.1 Equations of the Electrical Process in the Electrodeless Case

Consider a plane discharge gap of sufficiently large length L between solid surfaces (dielectric or metallic). Assume that the process is one-dimensional, that is, is independent of the transverse coordinates. It will soon be clear why we make the qualifications of long gap and elevated pressure. Let the electrodes be insulated from the plasma by dielectric plates, with dielectric constant ε and thickness l (Fig. 13.3a). For the plasma we assume $\varepsilon = 1$. The continuity equation for the space charge density ϱ, the equation of electrostatics, and Ohm's law for the conduction current in a plasma, j_1,

$$\frac{\partial \varrho}{\partial t} + \frac{\partial j_1}{\partial x} = 0 , \quad \frac{\partial E}{\partial x} = 4\pi\varrho , \quad j_1 = \sigma E . \tag{13.2}$$

imply that the sum of the conduction and displacement currents (Sect. 3.3.2),

$$j_1 + \frac{1}{4\pi}\frac{\partial E}{\partial t} = j_1 + j_{\text{dis}} = j(t) , \tag{13.3}$$

is independent of the coordinate x at each moment of time.

We assume the plasma to be electrically neutral throughout the entire gap, except in the thin layers at the boundaries where charges due to polarization are concentrated. The charges are regarded as *surface charges*. This is equivalent to assuming the homogeneity of plasma in space. Indeed, (13.2,3) imply that if $\varrho = 0$, then E, j_1, σ are independent of x. Conversely, once we assume the homogeneity of the gap, we conclude that the plasma in it is electrically neutral. We denote by q_1 and q the surface charge density in the plasma and on the electrodes, respectively. The latter charges are "collected" by the applied e.m.f. from the external circuit. The dielectric layers do not let them through

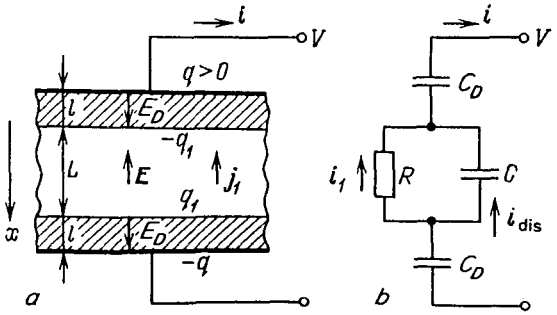

Fig. 13.3. Electrodeless ccrf discharge. **(a)** Section of discharge chamber. Signs of surface charges and the directions of field and current correspond to the phase in which the charge of the upper electrode is positive and decreasing in magnitude. **(b)** Equivalent electric circuit of the discharge device

into the plasma (see also Sect. 13.2.2). We assign directions to the field E_D in the dielectrics, and signs to the charges q and q_1 at a certain time, in accord with the instantaneous situation shown in Fig. 13.3a. In subsequent calculations, the equations automatically control the signs of the terms denoting the fields, charges, and currents.

Applying general electrostatics equations (3.16, 17) to the electrode-insulator and insulator-plasma interfaces and taking into account that the field in the metal is negligible owing to its very high conductivity, we find

$$\varepsilon E_D = 4\pi q \ , \quad E - \varepsilon E_D = -4\pi q_1 \ . \tag{13.4}$$

Applying the continuity equation to the same boundaries, we obtain

$$\dot{q}_1 \equiv dq_1/dt = j_1 \ , \quad \dot{q} = i/S \ , \tag{13.5}$$

where i is the current in the external circuit and S is the area of the electrodes. A combination of (13.4,5) implies that the current $i(t)$ in the external circuit coincides with the total current in each dielectric and in the gap, jS [by virtue of (13.3)]; this gives the *law of conservation* of the total current of conduction and displacement along the entire electric circuit.

Potential drops across layers do not exist within the framework of the assumption of the surface nature of charges at the plasma boundaries, that is, of "zero" thickness of these space-charge layers. For the time being we put off the discussion of real layers and potential drops; note only that neglecting any phenomenon at the electrodes (and the corresponding potential differences) can be justifiable to a certain extent if these differences are small in comparison with the voltage $V_1 = EL = (E/p)(pL)$ across the homogeneous plasma, and the length of this plasma is the greater part of the total gap length. Actual potential drops averaged over one period do not exceed 200 V at medium pressures, and the thickness of nonuniform electrode layers is of the order of 1 cm (Sect. 13.4). Therefore, the analysis is not meaningless if pL is sufficiently high (recall the stipulation made at the beginning of this chapter). It fits the glow discharge theory for high pL quite well. In this case, attention can be focused on the positive column, which has its analogue in the homogeneous plasma of this section. Hereafter we refer to this plasma as "positive column."

Under the assumptions made above, the instantaneous voltage across the electrodes is

$$V = 2E_D l + EL \ . \tag{13.6}$$

Eliminating the fields from (13.6) and (13.4) and from the equation $j_1 = \sigma E$, we arrive at the system of equations

$$V = \frac{8\pi l}{\varepsilon} q + \frac{j_1 L}{\sigma} \ , \quad j_1 = 4\pi\sigma(q - q_1) \ , \quad \dot{q}_1 = j_1 \ , \quad \dot{q} = j \ , \tag{13.7}$$

which determines the current. It must be supplemented by the equation of the external circuit, that is, an analogue of (8.1) that relates V to i.[4] System (13.7) can be given an "electrical engineering" form by introducing currents $i = jS$ and $i_1 = j_1 S$ instead of densities, charges $Q = qS$, $Q_1 = q_1 S$, ohmic resistance of discharge $R = L/\sigma S$, capacitance of dielectrics $C_D = \varepsilon S/4\pi l$, and that of the plasma space $C = S/4\pi L$. We obtain

$$V = \frac{2Q}{C_D} + i_1 R\,, \quad i_1 R = \frac{Q - Q_1}{C}\,, \quad \dot{Q}_1 = i_1\,, \quad \dot{Q} = i\,. \tag{13.8}$$

The equivalent electric circuit to these equations is shown in Fig. 13.3b. The conduction current passes through the active resistance and the displacement current passes through the plasma capacitance, with $i_1 + i_{dis} = i$.

13.2.2 Equations in the Case of Bare Electrodes

If the insulating plates are absent, the capacitances C_D in Fig. 13.3b must be removed (Fig. 13.4). This gives

$$V = i_1 R\,, \quad i_1 R = \frac{Q - Q_1}{C}\,, \quad \dot{Q}_1 = i_1\,, \quad \dot{Q} = i\,. \tag{13.9}$$

The problem of current closing at the interface of the plasma and metal conductors is not considered in this approximation. The conduction currents on the different sides of the interface are unequal, $i \neq i_1$, and there is surface charge on the interface, $Q - Q_1 \neq 0$, owing to the difference between the conductivities of the plasma, σ, and the metal ($'\sigma = \infty'$).

Equations (13.8, 9) describe not only rf but also all non-steady-state discharges, such as pulsed ones, provided that the formulated assumptions are not violated over their characteristic durations. For instance, the displacement of the electrons must be small in comparison with L.

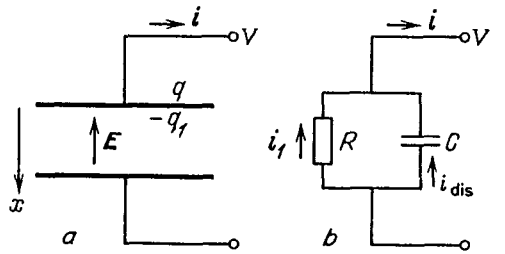

Fig. 13.4. (a) Electric circuit of the device, and (b) equivalent circuit of electrode ccrf discharge, similar to that of Fig. 13.3

[4] It depends on the method of connecting the rf oscillator to the circuit; here these details are ignored.

13.2.3 Solution for the Case of Insulated Electrodes

The plasma in the discharge gap is sustained by the field; since the field oscillates, the periods of predominant production of electrons alternate with the periods of their predominant removal. Assume that a sine voltage $V = V_a \sin \omega t$ is applied to the electrodes. Let the plasma decay to only a small extent in one half-period of oscillation. This condition holds at the postulated frequency $f \sim 10^7\,\mathrm{s}^{-1}$: the characteristic frequencies of the removal of electrons in glow discharge plasmas do not exceed $10^5\,\mathrm{s}^{-1}$. Then the *depth of modulation* of n_e, σ, and R (at a frequency $2f$) is negligible and $R(t) \approx$ const. Equations (13.8) can be integrated, regarding the plasma resistance as a constant parameter (though this is not yet known; Sect. 13.3). The results of this simple calculation will now be given. The voltage across the plasma V_1, the field in the plasma E and the conduction current i_1 are proportional to one another and are given by the formulae

$$V_1 = EL = i_1 R = \frac{V_a}{1+2C/C_D}\,\frac{\omega\tau}{\sqrt{1+\omega^2\tau^2}}\sin(\omega t+\varphi)\,,$$
$$\tau = R(C_D/2 + C)\,,\quad \varphi = \arctan(\omega\tau)\,. \tag{13.10}$$

The current in the external circuit (the discharge current) is

$$i = \frac{V_a}{R(1+2C/C_D)}\,\frac{\omega\tau\sqrt{1+\omega^2\tau_\sigma^2}}{\sqrt{1+\omega^2\tau^2}}\sin(\omega t+\varphi+\Delta\varphi)\,,$$
$$\tau_\sigma = RC = 1/4\pi\sigma\,,\quad \Delta\varphi = \arctan(\omega\tau_\sigma)\,. \tag{13.11}$$

The amplitude of the voltage across the plasma, V_1, is the lower in comparison with the applied voltage V, the smaller the capacitance of the insulators (the lower $\omega\tau$). The insulators then carry the correspondingly greater part of the voltage. The voltage V_1 is shifted in phase with respect to V because only the displacement current passes through the dielectric layers. For this same reason, and owing to the displacement current in the plasma, the discharge current i is phase-shifted relative to V. The time τ characterizes the *inertial behavior* of the entire capacitor device in Fig. 13.3. If it is charged and then its electrodes are shorted to discharge the system, the charge relaxes, obeying the law $Q = Q(0)\exp(-t/\tau)$, provided the plasma has not yet decayed (R = const).

The time τ_σ characterizes the rate of *dispersal of space charges* in the plasma itself (Sect. 9.2.2). The quantity $\omega\tau_\sigma = \omega/4\pi\sigma$ that we already know from Sect. 3.5.6 determines the ratio of amplitudes of the displacement and conduction currents in the plasma:

$$i_{\mathrm{dis,a}} = \frac{i_a\omega\tau_\sigma}{\sqrt{1+\omega^2\tau_\sigma^2}}\,,\quad i_{1a} = \frac{i_a}{\sqrt{1+\omega^2\tau_\sigma^2}}\,,\quad \frac{i_{\mathrm{dis,a}}}{i_{1a}} = \omega\tau_\sigma\,. \tag{13.12}$$

These currents are shifted in phase by $\pi/2$, so that not the amplitudes but their squares are added: $i_a^2 = i_{1a} + i_{\mathrm{dis,a}}^2$.

13.2.4 The Version with Bare Electrodes

By analogy with the above analysis, we find from (13.9) that

$$V_1 = EL = i_1 R = V = V_a \sin \omega t \,, \tag{13.13}$$

$$i = (V_a/R)\sqrt{1+\omega^2\tau_\sigma^2}\,\sin(\omega t + \Delta\varphi) \,. \tag{13.14}$$

The phase shift $\Delta\varphi$ between the discharge current i and the field E in the plasma (or the conduction current i_1 in it) is the same as with insulated electrodes; it is given by (13.11). Formulas (13.12) remain valid. However, now there is no difference between the voltage on plasma V_1 and that across the electrodes V. Indeed, we have neglected the possible insulation of electrodes by the electrode layers which were assumed to have zero thickness.

13.3 $V - i$ Characteristic of Homogeneous Positive Columns

The solution of Sect. 13.2 demonstrates the field and current arising in a homogeneous extended plasma with a specified conductivity if rf voltage is applied to the electrodes. Another side of the question is what value of conductivity is produced in the discharge gap in a given field or what field is required to sustain a given electron density. The answers depend on the electronic processes in the plasma, and the resulting relation between n_e and E, or j and E, is the $V - i$ characteristic of the positive discharge column. If other conditions are known, this characteristic can be transformed into the $V - i$ curve of the discharge device as a whole. The conditions for the sustainment of nonequilibrium homogeneous plasma in an rf discharge do not differ, in principle, from those for the positive column of the glow discharge (Sect. 8.6): ionization must compensate for the loss of electrons.

13.3.1 Frequency of Ionization by an RF Field

The ionization frequency is determined by the electron energy spectrum. The spectrum depends on the field frequency. The rate of its buildup is characterized by the electron energy loss frequency $\nu_u = \nu_m\delta$ (Sect. 2.3.7). If $\omega \gg \nu_m\delta$, the spectrum responds too slowly to oscillations of the rf field. As we have explained in Sect. 5.5.2, the frequency of ionization in the rf field, $\nu_{i,rf}$ does not differ from the ionization frequency $\nu_i(E)$ in a constant field E whose magnitude equals the effective value E_{eff} of the oscillating field. Formula (5.33) gives E_{eff} in terms of E_a, ω, and ν_m. In the frequency range where $\nu_m \gg \omega \gg \nu_m\delta$, E_{eff} is equal to the root-mean-square field $E_a/\sqrt{2}$.

In the opposite limit of $\omega \ll \nu_m\delta$, the spectrum "follows" the field oscillations, constantly adjusting itself to the instantaneous value of $E(t)$, while the instantaneous frequency of lionization is equal to the ionization frequency $\nu_i(E)$ in a constant field of the same magnitude. hence, we simply have to average $\nu_i[E(t)]$ in time:

$$\nu_{i,rf} = \frac{\omega}{2\pi}\int_0^{2\pi/\omega} \nu_i\left(E_a|\sin\omega t|\right)dt = \frac{2}{\pi}\int_0^{\pi/2} \nu_i(E_a\sin\varphi)d\varphi\,. \qquad (13.15)$$

Since $\nu_i(E)$ is a very steep function, ionization occurs by short surges when the field reaches its maximum value. For the rest of the period, electron losses predominate. The situation in molecular gases (N_2, air, $CO_2 + N_2 + He$ laser mixture) at $p \gtrsim 30$ Torr is close to the second limiting case. The electron losses are characterized by the effective recombination coefficient β_{eff} (Sect. 8.8). If the ionization coefficient $\alpha(E)$ is given in the Townsend form (4.5), the expansion of $1/\sin\varphi$ in the neighborhood of $\varphi = \pi/2$ yields a formula useful for calculations:

$$\nu_{i,rf} = (2E_a/\pi Bp)^{1/2}\nu_i(E_a)\,,\quad \nu_i(E) \propto \exp(-Bp/E)\,; \qquad (13.15')$$

it expresses $\nu_{i,rf}$ in terms of the ionization frequency in a constant field equal to the amplitude of the rf field. The coefficient multiplying $\nu_i(E)$ characterizes the effective fraction of time during which ionization occurs. Formula (13.15′) is more accurate, the smaller this fraction.

13.3.2 Example of Calculation of the $V - i$ Characteristic

Consider the positive column of a discharge at the frequency $f = 13.6$ MHz in the laser mixture $CO_2 : N_2 : He = 1 : 6 : 12$ at $p = 30$ Torr, which corresponds to conditions in high-power CO_2-lasers [13.2, 13.3] (Sects. 14.4, 5). In this plasma, $\beta_{eff} \approx 4 \times 10^{-6}\,cm^3/s$. To maintain the electron density n_e, the ionization frequency required is $\nu_{i,rf} = \beta_{eff} n_e$; for instance, $\nu_{i,rf} = 4 \times 10^4\,s^{-1}$ for $n_e = 10^{10}\,cm^3$. This quantity, characterizing also the rate of plasma decay, is so small in comparison with f that the oscillations of n_e around the mean value are negligible. In the mixture specified here, $\delta \approx 0.8 \times 10^{-2}$ and the rate of build-up of the electron spectrum, $\nu_m\delta \approx 6.4 \times 10^8\,s^{-1}$, is almost an order of magnitude greater than $\omega = 0.85 \times 10^8\,s^{-1}$. We can, therefore, consider the spectrum to oscillate with the field, and $\nu_{i,rf}$ to be given by (13.15). Figure 13.5 shows the dependence of E_a/p on n_e, that is, a sort of "$V - i$ characteristic" of the positive column. For comparison, the dashed curve plots the same dependence found under the

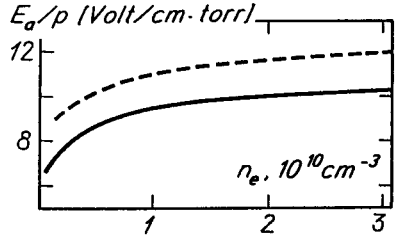

Fig. 13.5. Calculated dependence of field amplitude on electron density in the positive-column plasma of ccrf discharge (equivalent of the $V - i$ curve of the column) with laser gas mixture $CO_2 : N_2 : He = 1 : 6 : 12$, $p = 30$ Torr, $\beta_{eff} = 4 \times 10^{-6}\,cm^3/s$. *Solid curve*, electron spectrum tracks field oscillations (the low-frequency limit). *Dashed curve*, the spectrum is too slow to oscillate; it corresponds to a constant field equal to the rms value. The true dependence is close to the solid curve at the frequency 13.6 MHz [13.4]

assumption that the electron spectrum undergoes no oscillations and corresponds to the constant field $E = E_a/\sqrt{2}$, as we saw in the case of $\nu_m \gg \omega \gg \nu_m\delta$. If the inequality $\nu_m^2 \gg \omega^2$ is definitely satisfied, the true curve lies between those in Fig. 13.5, but closer to the solid curve, in accord with the estimate $\omega \ll \nu_m\delta$. As we see, the interval between the limiting versions is not great. This is natural because the ionizing field is $E_a/\sqrt{2} = 0.7E_a$ in one limit, and slightly less than E_a in the other.

13.3.3 Example of Calculations of the Electric Parameters of an Electrodeless Discharge

To illustrate the "electrical engineering" model of Sect. 13.2, we perform the calculation for the same gas at the same p and f as in Sect. 13.3.2, for the geometric parameters of the setup of [13.3], (see Sect. 14.4.5): $L = 5.5\,\text{cm}$, $l = 1\,\text{cm}$, $\varepsilon = 5$. Let us concentrate on the case of $n_e = 10^{10}\,\text{cm}^{-3}$. If $\nu_m = 0.8 \times 10^{11}\,\text{s}^{-1}$, then the conductivity is $\sigma = 3.5 \times 10^{-5}\,\text{Ohm}^{-1}\text{cm}^{-1}$. The curves of Fig. 13.5 show that plasma with this conductivity is sustained by $E_a/p = 9.4\,\text{V/cm Torr}$. The plasma parameter $\omega\tau_\sigma = 0.23$, $j_{1a}/j_{\text{dis},a} = 4.3$ and $j_{1a} = 0.95j_a$. The plasma is therefore dominated by the conduction current; its current density amplitude is $j_a \approx \sigma E_a \approx 10\,\text{mA/cm}^2$. The energy input into the plasma is $\sigma E_a^2/2 = 1.4\,\text{W/cm}^3$.

The voltage across the column is $V_1 = 1.55\,\text{kV}$. The ratio of the capacitances is $C_D/2C = 14$ and the parameter $\omega\tau = 3.6$. The amplitude V_{1a} of the voltage across the plasma is 0.9 of the applied voltage amplitude V_a, so that $V_a \approx 1.75\,\text{kV}$. The phase shift φ between E, V_1, and V is $\varphi = 74.5°$, and that between the current in the external circuit and the voltage (i and V) is $\varphi + \Delta\varphi = 87.5°$.

The above calculation is based on the assumption that the positive column (homogeneous plasma free of the influence of electrode effects) is the main element of plasma as far as the voltage drop and the extension along the field are concerned. This is true for large values of pL. Experimenters frequently work with moderately long discharges and moderate pressures; the potential drops at the electrodes are then substantial, and the positive column does not occupy the predominant part of the entire gap length. On some calculations concerning cases of this sort, see Sect. 13.8.

13.4 Two Forms of CCRF Discharge Realization and Constant Positive Potential of Space: Experiment

It has been experimentally established that ccrf discharges are possible in *two greatly different forms*. The visual differences lie in the glow distribution along the gap, the essential difference consists in the processes in the electrodes. S.M. Levitsky was the first to point this out in 1957. His papers [13.1, 13.5] were important in the evolution of the current concepts and understanding of the nature of ccrf discharge at moderate pressures.

13.4.1 Jumps on Ignition Potential Curves

Experiments [13.5] were devoted to discharges in hydrogen and argon in a glass vessel with parallel bare disk electrodes 4.2 cm in diameter placed in the vessel. The interelectrode spacing L was varied up to 10 cm; the frequency of the 100 W rf oscillator was $f \approx 1$–70 MHz, and the pressure was $p \sim 10^{-2}$–10^{1} Torr. Discharge ignition potentials V_i were measured at different f, p, L, most attention being paid to the near-jump region of the ignition curves $V_i(p)$ at given ω and L.

The jumps that had already been discovered in the experiments of the 1930s (Sect. 7.7.2) appear at combinations of parameters at which the range of the electrons' oscillations at the moment of breakdown [$2A = (\mu_e p)V_{ia}/\omega pL$] becomes equal to the interelectrode distance. If ω and L are fixed, then at higher pressures $2A < L$, so that electrons oscillating from the mid-plane of the gap do not reach the electrodes. Their losses are therefore lower (only diffusional) and V_i decreases with respect to the case of lower p at which $2A > L$ and drifting electrons strike the electrodes. This effect is well pronounced in H_2 but smeared in Ar, presumably owing to stronger diffusion. Figure 13.6 plots the ignition characteristic (lower solid curve) which clearly shows the jump.

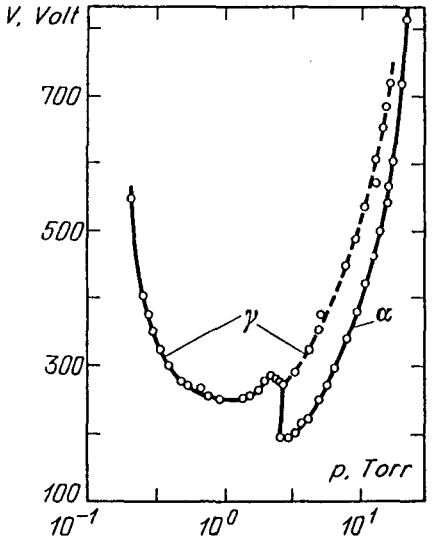

Fig. 13.6. Ignition potential of an electrode ccrf discharge as a function of pressure with hydrogen, $f = 3$ MHz, $L = 2.64$ cm. Left-hand branch up to the jump is the γ discharge; the right-hand branch (*solid curve*) is the α discharge. *Dashed curve* plots the secondary ignition potential (transition of the α to γ mode) [13.5]

13.4.2 α and γ Discharges

Observations have shown that discharges ignited at pressures to the "left" and "right" of the jump are not identical. If the discharge is on the right, a diffuse glow appears in the middle of the gap, while the gas at the electrodes is dark. The voltage on the electrodes changes very little upon ignition, indicating weak conductivity of the ionized gas and a low discharge current. In discharges to the left of the jump, an intensive glow is localized at the electrodes and consists

of alternating layers whose color and sequence resembles those of the layers in the cathode region of a dc glow discharges. The electrode voltage appreciably decreases after ignition, indicating a considerable current is the discharge.

Levitsky gave the following interpretation to these features: the current in the neighborhood of the electrodes in the weak-conductivity discharge is mostly capacitively coupled and remains as *displacement current,* as before the ignition. Hence, the ignition of the discharge does not affect the behavior of electrodes that continue neuther to emit nor to absorb charges. In high-conductivity discharges, to the left of the jump, an ionic current flows into the electrode that is negative at a given moment, *secondary emission* takes place, and a *cathode layer* is formed at the "cathode" for some time, as in glow discharge, until the polarity is reversed. Now the circuit from the middle of the gap to the electrodes (which are alternating as cathodes) is closed by *conduction currents*. Levitsky referred to discharges with nonconducting layers as "α" and to discharges with conducting layers as "γ" discharges, γ symbolizing the role of secondary emision (γ processes). When the voltage applied to a burning α discharge is increased, it suddenly transforms to the γ form, like a *secondary ignition.* The $V - i$ curve of secondary ignition extends that of the γ discharge to the left of the jump. It is shown by the dotted curve in Fig. 13.6.

13.4.3 Constant Spatial Potential in CCRF Low-Pressure Discharge

It was noticed as early as the 1930s that a low-pressure ccrf discharge leads to the *sputtering* of electrodes, so that a layer of metal is deposited on the walls of a glass tube. The only explanation was the existence of a *constant field,* directed from the midpoint to the two electrodes and accelerating positive ions to high energies. These ions strike the electrodes and cause the effect known in dc glow discharge as *cathode sputtering*. Alternating fields, even of high amplitudes, are inefficient in this respect, because the energies of the oscillatory motion of ions are too low. Probe methods detected a *constant potential positive* with respect to the electrodes in the middle of the discharge gap. Figure 13.7 shows the results of the probe measurements in the setup already described in Sect. 13.4.1. The

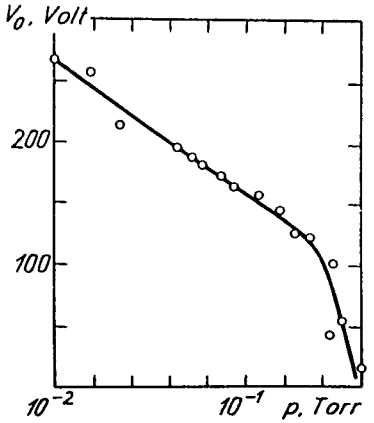

Fig. 13.7. Probe measurement results of constant plasma potential as a function of pressure. Hydrogen, f = 68 MHz, L = 10 cm [13.1]

constant potential V_0 for $f = 68\,\text{MHz}$, $L = 10\,\text{cm}$, $p = 3.8 \times 10^{-2}\,\text{Torr}$ increases almost linearly with increasing electrode voltage and is less than its amplitude V_a by a factor of about 2. Measured energy spectra revealed that the mean energy of ions is comparable with V_0, and the maximum energy, with V_a.

Levitsky's idea was that constant positive potential in a ccrf discharge is produced by the buildup of an excess of ions in the gap as a result of the absorption of electrons by the electrodes (Sect. 13.1). Using the model of oscillations of the electron gas illustrated in Fig. 13.1, he was able to evaluate the constant potential V_0 (Sect. 13.6.2). On the whole, these arguments correctly identified some key points. Each of the factors taken into consideration (the removal of a part of electrons from the gap, and the oscillations of the electron gas) may in itself generate a constant positive potential of the plasma. The first mechanism is obvious. If a body as a whole is charged positively, it possesses a positive potential. But *even if the gas is electrically neutral* (as it would be if the electrons did not attach to insulators in the electrodeless discharge), it is nevertheless at a positive potenital with respect to the boundaries in the sense of a time average (Sect. 13.6.4). Indeed, the positive charge layer is essentially thicker than the layer of the equal negative charge, because electrons are forced by the field to "huddle up" to the insulator, and the voltage drop in the negative layer is smaller.

The presented model is clearly valid only for the α discharge. If a cathode layer, just like that in ordinary glow discharge, is formed in the neighborhood of the temporary cathode in the γ discharge, then the positive potential with respect to the cathode at the layer-plasma interface must be of the order of the normal cathode fall V_n. Since no anode fall accompanies it, or this fall is small, V_0 averaged over one period must be of the order of V_n; this is indeed observed at higher pressures (Sect. 13.4.4).

Figures 13.8,9 give the results of recent measurements, carried out by the probe method in glass tube 5 to 8 cm in diameter, with disk electrodes. The potential V_0 decreases with increasing pressure, other conditions being equal. The paper does not specify the form of the discharge (α or γ), but it is worthy of note that a certain dependence of V_0 on electrode material and gas species was observed. Namely, V_0 was greater for those combinations of metal and gas

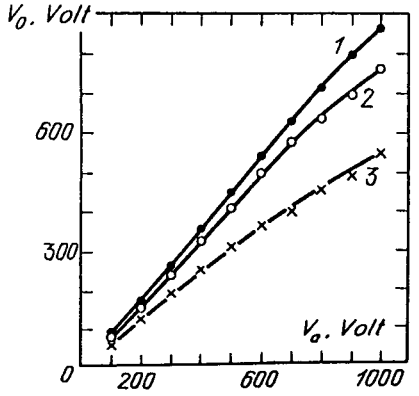

Fig. 13.8. Constant plasma potential as a function of amplitude of electrodes voltage. Discharge in neon, with titanium electrodes: $f = 6\,\text{MHz}$, *(1)* $p = 0.3\,\text{Torr}$, *(2)* $p = 0.5\,\text{Torr}$, *(3)* $p = 1.1\,\text{Torr}$ [13.6]

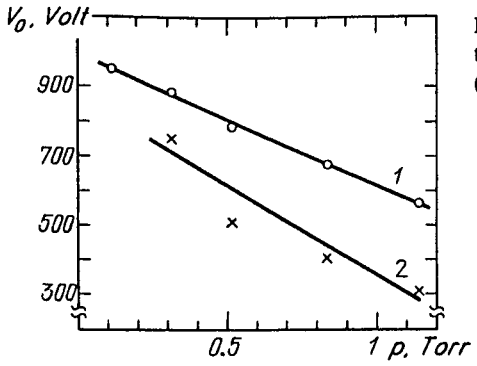

Fig. 13.9. Constant plasma potential as a function of pressure: Neon-titanium, V_a = 1000 V; *(1)* f = 6 MHz, *(2)* 1.5 MHz [13.6]

for which the normal cathode fall was higher, although V_0 was still far from V_n. The paper reported a certain, mostly increasing, dependence of V_0 on frequency (in the range from 1 to 12 MHz).

The positive potential does accelerate ions towards the electrodes but it also accelerates electrons towards the plasma. Indeed, beams of fast electrons with energies of 100 eV were recorded in experiments with helium at p = 0.66 Torr, $f \approx$ 1–15 MHz, $V_a \approx$ 390 V [13.7]. This was discovered in the course of measuring the electron distribution function by probe techniques. The energy of the beam electrons was close to V_0.

13.4.4 Weak-Current and High-Current (α and γ) Medium-Pressure CCRF Discharges

The fact that two forms of ccrf discharges exist, the properties of these forms, and the characteristics of transition of one form into the other have been thoroughly studied since 1978 by N.A. Yatsenko, who succeeded in greatly clarifying the nature of these phenomena. His chief interest was focused on the medium pressure range of $p \sim$ 10–100 Torr (it was largely ignored before). One of the important results obtained by Yatsenko was: a direct experimental proof of the fact that α and γ discharges differ in current density by more than an order of magnitude; and that the electrode layers of the γ discharge possess high conductivity. For these reasons, Yatsenko referred to the γ discharge as the high-current, and to the α discharge as the weak-current modes. The measurements [13.8] were made in a vessel of large volume (60 liters) with a pair of water-cooled disk-shaped brass electrodes, 10 cm in diameter. The gap between them could be increased up to 10 cm. Sometimes electrodes were insulated from the plasma by 1 to 3 mm thick layers of glass, Teflon, etc. The discharge was ignited by a 3 kW generator, mostly at f = 13.6 MHz.

Figure 13.10 gives static $V - i$ characteristics of discharge: i.e., the rf voltage V on the electrodes as a function of the rf current i in the steady-state regime (rms values). In the range of the lowest voltages and currents, V remains almost constant as the current increases. Under these conditions, the discharge does not cover the entire surface area of the electrodes. Its diameter in the interelectrode

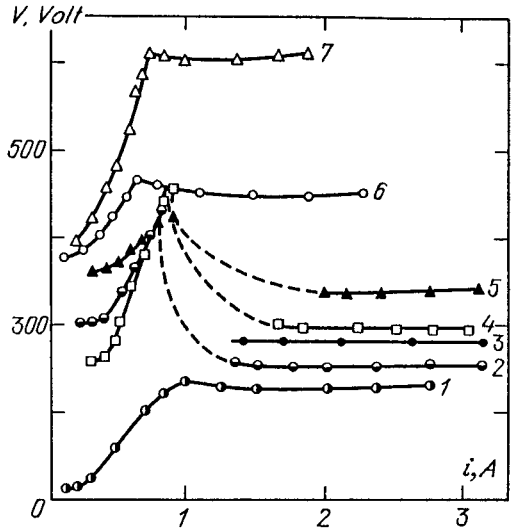

Fig. 13.10. $V - i$ characteristic of ccrf discharge at the frequency 13.6 MHz (rms values) : *(1)* helium, p = 30 Torr, L = 0.9 cm; *(2)* air, 30 Torr, 0.9 cm; *(3)* air, 30 Torr, 3 cm; *(4)* CO_2, 30 Torr, 0.9 cm; *(5)* CO_2, 15 Torr, 3 cm; *(6)* air, 7.5 Torr, 1 cm, electrodes are insulated with glass; *(7)* air, 7.5 Torr, electrodes are insulated with teflon [13.8]

gap is close to the diameter of the spot on the electrodes. The glow is concentrated at the middle of the gap, fading away at the electrodes (in space-charge layers) (Fig. 13.11, curve *a*). This is a typical weak-current (α) discharge with nonconducting electrode layers. Coating the electrodes with a dielectric does not change the picture.[5] When the current increases at this stage, the discharge broadens transversely and fills the electrode surface. The current density at the electrode remains constant, that is, the phenomenon of a *normal current density* exists in a weak-current discharge when it covers the electrode only partially. The current density depends on the gas species, on pressure, and – surprisingly – on the interelectrode spacing L (Fig. 13.12, Sect. 13.9.1).

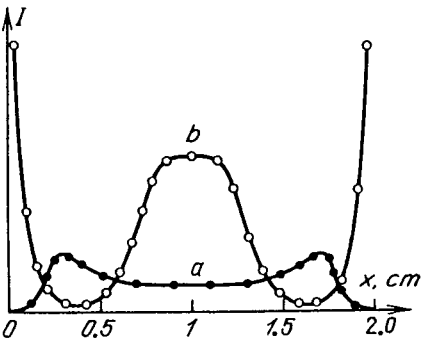

Fig. 13.11. Glow intensity distribution across the gap (in the apparatus of [13.8]): 10 Torr air, brass electrodes, L = 2 cm, (a) weak-current mode, (b) high-current mode. Rms voltage on the electrodes is close to 300 V in both cases

[5] The electrodes can be completely removed from the discharge tube: such experiments have been carried out on a number of occasions.

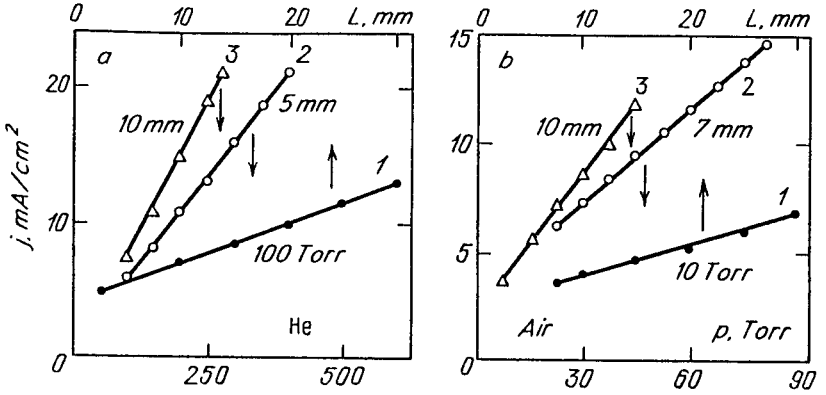

Fig. 13.12. Normal current density at the electrodes in the weak-current mode as a function of pressure and interelectrode spacing. (**a**) Helium, (**b**) air; $f = 13.6$ MHz: *(1)* $j(L)$ at $p = 100$ Torr in He and at 10 Torr in air; *(2)* $j(p)$ at $L = 0.5$ cm in He and at $L = 0.7$ cm in air; *(3)* $j(p)$ at $L = 1$ cm [13.9]

When the electrode surface is totally covered by the current and the discharge diameter increases to the electrode diameter, further increase in current requires higher voltage (as it does in an abnormal glow discharge), although the layers here remain dark and nonconducting. Their thickness in the normal regime is $d \approx 0.2$–0.6 cm. To the accuracy of a low-ionic saturation current (as in the case of a negative probe), the current is coupled to the electrode by the displacement current. The low conductivity of the discharge was checked by passing through it a dc current or (which is the same) a 50 Hz ac current.

When a sufficiently high electrode voltage is reached, the α discharge is sharply transformed into the high-current γ type. This is the secondary ignition observed in [13.5] (Sect. 13.4.2) and is indicated by jump or bend in the $V - i$ characteristic. The glow in the gap undergoes redistribution; layers resembling the *layers of a glow discharge* are formed at each electrode. The *negative glow* and the *Faraday dark space*, and also the *positive column* in the middle, are clearly pronounced. The distribution of luminance is plotted in Fig. 13.11 by the curve *b*. The total thickness of "near-cathode" regions up to the positive column in air at $p = 15$ Torr is 1.2 cm. The current density at the electrode increases sharply: at $p = 30$ Torr in air, by a factor of 20 from 1.2×10^{-2} to 0.24 A/cm^2 (the transition results in a transversal contraction of the discharge). The conductivity sharply increases. The resistance to dc or low-frequency current drops by 2 orders of magnitude. The constant potential V_0 across the discharge space in the high-current regime is 100 to 200 V; it is practically independent of pressure and roughly corresponds to the normal cathode fall of the glow discharge.[6] The thickness of the space-charge layer at the electrodes, d, becomes much smaller: in air at $p = 15$ Torr, $d \approx 0.4$ cm in the weak-current mode and $d \approx 0.03$ cm in the high-current mode. These figures are obtained by probe measurements of the

[6] It is not clear, therefore, why the potential V_0 dropped abruptly in [13.5] to a negligible value of several volts at $p \sim 1$ Torr.

distribution of constant potential $V_0(x)$ as a function of the distance x from the electrode. The layer thickness in the high-current mode is comparable with that of the cathode layer of ordinary glow discharges.

The high-current mode is also characterized by a *normal current density*; here it is similar to the effect observed in the ordinary glow discharge, but the current density in the rf discharge may be substantially larger, owing to the contribution of the *displacement current* in the "cathode" layer, where the field is very strong. As the current is increased, the electrodes fill up with the glow, and the diameter of the current spot on the electrodes and that of the plasma column (these are not very different) both grow. This stage corresponds to the last constant-voltage segment on the $V-i$ characteristic of Fig. 13.10, which corresponds to the *normal* mode of the glow discharge.

Recent measurements [13.10] make it possible to evaluate the frequency dependence of the collapse parameters of the α-discharge and its transformation into the γ-form (V_{tr}, i_{tr}). The measurements were carried out in nitrogen between two bare aluminum electrodes in the ranges of $f = 15$–55 MHz, $p \approx 10$–50 Torr, $L \approx 0.6$–1.2 cm. The $V-i$ characteristics are similar to those shown in Fig. 13.10. As the frequency increases at constant pressure, V_{tr} decreases while i_{tr} increases. Thus if $L = 0.6$ cm and $p = 35$ Torr, we have

$$\begin{aligned}
&\text{for } f = 15.4 \text{ MHz} : \quad V_{tr} = 440 \text{ V (rms)} \quad i_{tr} = 45 \text{ mA (rms)} \\
&\text{for } f = 20.4 \text{ MHz} : \quad V_{tr} = 405 \text{ V} \qquad\quad i_{tr} = 60 \text{ mA} \\
&\text{for } f = 29.25 \text{ MHz} : \quad V_{tr} = 305 \text{ V} \qquad\quad i_{tr} = 100 \text{ mA} .
\end{aligned}$$

As the pressure increases at constant frequency, V_{tr} increases and i_{tr} decreases. If $L = 0.6$ cm and $f = 29.25$ MHz, we have

$$\begin{aligned}
&\text{for } p = 25 \text{ Torr} : \quad V_{tr} = 270 \text{ V} \quad i_{tr} = 134 \text{ mA} \\
&\text{for } p = 55 \text{ Torr} : \quad V_{tr} = 320 \text{ V} \quad i_{tr} = 95 \text{ mA} .
\end{aligned}$$

In the latter case, the α-discharge occupied a whole area $1.5\,\text{cm}^2$ of the electrode, which corresponds to $j_{tr} \approx 60\,\text{mA/cm}^2$; in the γ-mode of discharge, $j \approx 1000\,\text{mA/cm}^2$.

13.4.5 The Domain of Weak-Current Discharge

Experiments demonstrate that the weak-current discharge can burn only at values of pL smaller than a certain critical value $(pL)_{cr}$ (Fig. 13.13). This value depends on the electrode material and the gas species. If $pL \approx (pL)_{cr}$, the weak-current discharge becomes unstable and either transforms into the high-current form or dies out. If $pL > (pL)_{cr}$, the former mode cannot be ignited at all, so that only the high-current discharge can be realized. Both regimes are possible if $pL < (pL)_{cr}$. Critical values in molecular gases are not large; in air, $(pL)_{cr} \approx 40$ Torr·cm. Typically, the high-current form is realized in molecular lasing mixtures CO_2 + N_2 + He at medium pressures and gap length of several centimetre. The weak-

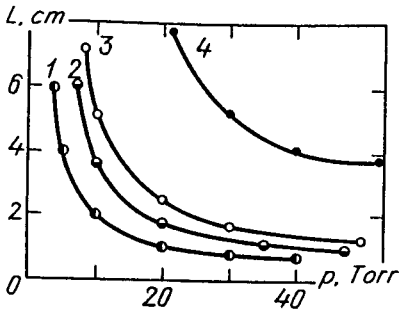

Fig. 13.13. Boundaries of domains of weak-current discharge. Only high-current mode is possible *above* and to the *right* of the curve (brass electrodes, f = 13.6 MHz): *(1)* nitrogen; *(2)* air; *(3)* CO_2; *(4)* helium [13.8]

current form transforms into the high-current form by way of the *breakdown* of the space-charge layer [13.8]. It appears that the dependence of the weak-current domain size and $(pL)_{cr}$ on frequency has never been studied experimentally.

13.4.6 Electrodeless Electrode Discharge and Electrode Electrodeless Discharges

Although this sounds like wordplay, it reflects the essentials of the process: a discharge with bare electrodes in the weak-current mode does not differ at all from a discharge with inusulated electrodes, so that it is electrodeless in the sense that the electrodes do not make their presence felt. As in the case of dielectrics, the current through the space-charge layers closes the circuit only via the displacement current. However, the "electrodeless" discharge with insulated electrodes is found to be sustainable in the high-current mode, with all the attributes of *secondary emission* and *multiplication of electrons* in the *cathode layer* (negative glow, dark Faraday space) found in the ordinary glow and high-current rf discharge with bare electrodes. This discharge does not differ from the latter one either in visual appearance or in current density. The same is indicated by Fig. 13.10 which also shows the $V-i$ characteristics of insulated-electrode cases. The voltage amplitude on the electrodes is then naturally higher than the ordinary value, because part of the voltage is developed across the dielectric layers.

When the ionic current of the dc glow discharge flows from the cathode layer into the metal, some electrons are ejected from the letter; most of them neutralize the ions at the surface, while the others create the emission electron current. The loss of electrons from the surface layer of the cathode is balanced out by their inflow from the inside, at the expense of those entering the anode. The cathode layer is charged positively; hence, the cathode of a constant-current discharge carries a constant excess electron charge. Bare electrodes of ccrf discharges also carry an excess negative charge (Sect. 13.1.2), but it changes as the cathode and anode phases alternate. When the electrodeless discharge is ignited, the electrons of the gas attach to the surface of the dielectrics, no inflow of charges occurring from the inside of the body. In the cathode phase of the high-current mode, the attached electrons neutralize the incident ions and are partly liberated by them, while in the anode phase their store is replenished.

If a capacitance equivalent to that of the dielectric insulating the plasma is introduced into the external circuit of the discharge with bare electrodes, the discharges with bare and insulated electrodes must behave equivalently provided the surfaces of the metal and of the dielectric are identical vis-a-vis *electron emission* and *neutralization of ions*. This is conclusively demonstrated by the results of numerical modeling of the structure of ccrf discharges (Sect. 13.8).

13.5 Electrical Processes in a Nonconducting Electrode Layer and the Mechanism of Closing the Circuit Current

In the approximate solution of Sect. 13.2, *space-charge layers* at the boundaries of the discharge gap were regarded as *discontinuity surfaces* on which surface charges were concentrated and the field changed abruptly. Let us look now at the nonconducting layer in the weak-current discharge as a *finite-thickness* element with a space charge and continuous field, and go into details of how the current closes the circuit between the plasma and the electrodes. From the arguments given above it is fairly clear that the closing in the α-discharge is made by the displacement current, so that it is useful to pause and consider on the physical content of this concept.

13.5.1 What Is the Displacement Current?

In trying to formulate a system of equations to describe electromagnetic phenomena (Sect. 3.3), Maxwell met with the following difficulty (this happened in the 1860s): if the fields are not constant, the equations of the magnetic field valid for dc currents and the equation of continuity for charges are incompatible. To remove the contradiction, Maxwell postulated, without any experimental justification, that the magnetic field is generated not only by the motion of charges, but also by changes in the electric field, just like the electric field is generated when the magnetic field is varied. The quantity $(1/4\pi)\partial \boldsymbol{D}/\partial t$, which Maxwell added to the conduction current, he called the *displacement current*. The phenomenon of electromagnetic induction was supplemented with a magnetoelectric analogue, while equations (3.13, 14) acquired a spectacular symmetry. Thus one of the most fundamental laws of nature, implying the existence of electromagnetic waves, was discovered in a purely speculative manner.

In fact, a connection with magnetic phenomena is not necessary for the quantity known as displacement current to appear in the theory of electricity. The purely electrical equations

$$\partial \varrho/\partial t + \operatorname{div} \boldsymbol{j} = 0 \,, \quad \operatorname{div} \boldsymbol{D} = 4\pi\varrho \tag{13.16}$$

imply that

$$\operatorname{div}\left(\boldsymbol{j} + \frac{1}{4\pi}\frac{\partial \boldsymbol{D}}{\partial t}\right) = 0 \,. \tag{13.17}$$

The vector under the divergence symbol in (13.17) has all the properties characterizing the dc current density which obeys the equation div $j = 0$. The vector has no sources, its lines of current are closed even if the electric circuit contains nonconducting segments (a line of current may also go to infinity, closing the circuit as if via infinity); the product of the magnitude of the vector and the cross-sectional area of the tube of current at any moment in time is identical along the entire circuit. The vector can therefore be interpreted as the *total* current density (conduction plus displacement). But this interpretation is to a great extent a matter of convention, because of the *two* components of displacement current (Sect. 3.3.2), the quantity $(1/4\pi)\partial \boldsymbol{E}/\partial t$ is not a current in the literal sense of the word, in contrast to the polarization current $\partial \boldsymbol{P}/\partial t$.

If we forget about the truly physical meaning of the quantity $(1/4\pi)\partial \boldsymbol{E}/\partial t$ as the source of *vortices of magnetic field,* it does not reflect any other physical reality, has no other physical content. However, when ac current is considered in a *quasipotential* electric field generated predominantly by charges,[7] we completely ignore the existence of a magnetic field. When dealing with gaseous conductors, that is, discharges, we can often neglect the tiny polarization current because $\varepsilon \approx 1$. Does this mean that by dealing with pure displacement current $(1/4\pi)\partial \boldsymbol{E}/\partial t$, we work with a concept devoid of physical content?

It evidently does. The mechanism of ac current in a quasipotential field is *exhaustively* interpreted in terms of the *motion of charges* and *electrostatics* using equations of type (13.16) (with Ohm's law) without resorting to a symbolic displacement current. Its extremely useful role arises because the interpretation of the integral of (13.16) or (13.17) as the *law of conservation of the total current* greatly simplifies the calculations and allows the representation of all results in concise, convenient, and elegant form. If, however, we wish to comprehend the real process, it is necessary to discern actual physical processes using phrases like "the displacement current flows through the capacitor." One has to build up a picture of how the e.m.f. of the power supply displaces the electrons of the external circuit towards one plate of this capacitor, where they stop, not being allowed any further by the poor-conductivity medium; how the departed electrons bare a layer of positive charge on the opposite side of the capacitor; how an electric field arises between charges of the opposite signs; how this field changes with time while charges are accumulated (or dispersed); how a strong current passes through "wires" at almost zero field, while there is no current in the poor-conductivity medium and at the same time the field is strong and

[7] A time-dependent electric field is never strictly potential: it inevitably contains an element of vortex field. If, however, the characteristic size L of the system is small compared with the wavelength λ, the field is approximately potential. Indeed, (3.14) implies $E_{\text{vort}} \sim \omega H L/c$; (3.13) implies $H \sim 4\pi j L/c$, whence $E_{\text{vort}} \sim 4\pi\omega L^2 j/c^2$. On the other hand, (3.16) implies $E_{\text{pot}} \sim 4\pi\varrho L$ and $\omega\varrho \sim j/L$, whence $E_{\text{pot}} \sim 4\pi j/\omega$. Therefore

$$E_{\text{vort}}/E_{\text{pot}} \sim (\omega L/c)^2 = (2\pi L/\lambda)^2 = (L/\lambda\!\!\!^{-})^2 .$$

For example, we find for ccrf discharge at $L \sim 10$ cm and $\lambda\!\!\!^{-} = 22$ m that $E_{\text{vort}}/E_{\text{pot}} \sim 10^{-3}$.

changing; both the chain of arguments and the electric circuit are closed. The example is clearly trivial. But such a detailed picture must be worked out for every situation that we wish to analyze thoroughly.

13.5.2 Field Within Layers

Let us examine quantitatively the situation shown in Figs. 13.1,2. As a first approximation, we make use of solution (13.13, 14) of Sect. 13.2. We only have to remember that the phase is shifted in the figures relative to (13.13, 14) so that the field E in the plasma and the discharge current i are equal now to

$$E = -E_a \cos \omega t \ , \quad i = -i_a \cos (\omega t + \Delta\varphi) \tag{13.18}$$

for the same amplitude values and $\Delta\varphi$ implied by (13.11). If we neglect the diffusional spreading of the plasma-ionic layer interface,[8] the field in the layer obeys the equation $\partial E_l/\partial x = 4\pi e n_+$. For simplification, we assume, as in Fig. 13.1, that $n_+(x) = \text{const}$. In the left-hand layer, on which we fix our attention,

$$E_l(x,t) = E(t) - 4\pi e n_+ [d(t) - x] \ , \tag{13.19}$$

where $d(t)$ is the coordinate of the interface or the layer thickness. At the electrode surface,

$$E_0(t) \equiv E_l(0,t) = E(t) - 4\pi e n_+ d(t) \ . \tag{13.20}$$

The plasma interface is formed by "edge" electrons that oscillate in the field E at the drift velocity $\dot{d} = -\mu_e E$. Taking into account that $d(0) = A$, we have

$$d(t) = A(1 + \sin \omega t) \ , \quad A = \mu_e E_a/\omega \ . \tag{13.21}$$

Substituting (13.18,21) into (13.20) and recalling that n_+ is equal to n_e in the plasma and that the conductivity of the plasma is $\sigma = e n_e \mu_e$, we find the field at the electrode:

$$E_0 = -\frac{E_a}{\omega\tau_\sigma}\sqrt{1+\omega^2\tau_\sigma^2}\,\sin(\omega t + \Delta\varphi) - \frac{E_a}{\omega\tau_\sigma} \ . \tag{13.22}$$

If the plasma conductivity is high, $\omega\tau_\sigma \ll 1$, the field at the electrode is almost always large in comparison with the field at the plasma boundary of the layer. Both its constant component and the amplitude of the variable component equal $E_{0a} = E_a/\omega\tau_\sigma$, the phase shift of the ac components of E_0 with respect to E being equal to $\pi/2$.

[8] Diffusion effects were evaluated in [13.4].

13.5.3 Charges and Currents

The field E_0 is created by the surface charge q on the electrode, $E_0 = 4\pi q$. Its variable component is caused by the discharge current $i = S\dot{q}$ in the external circuit, and the constant component, by the charge of those electrons that went into the solid from the gas. Indeed, the constant component of charge density on the electrode is equal in magnitude to the layer charge at the moment when the electrons pass through the midpoint or, which is the same, to the time-averaged charge

$$q_0 = -E_a/4\pi\omega\tau_\sigma = -en_+A\,, \quad E_{0,\text{const}} = -4\pi en_+A\,.$$

The discharge current calculated using (13.22),

$$i = -S\sigma E_a\sqrt{1+\omega^2\tau_\sigma^2}\cos(\omega t + \Delta\varphi)\,, \quad S\sigma E_a = V_a/R\,, \tag{13.23}$$

coincides with solution (13.18, 14) found in the first approximation. If $\omega\tau_\sigma \ll 1$, the plasma conduction current $i_1 = S\sigma E$ is not very different from the discharge current i. As we see from (13.22), the positive charge on the electrode ($E > 0$) appears for a shorter part of the period, the lower the value of $\omega\tau_\sigma$.

13.5.4 Reality and Symbols

The picture described in Sect. 13.2 by the discontinuity approximation thus has not been destroyed by replacing the discontinuity with an insulating space charge layer between the plasma and electrode. At the same time, the mechanism of closing the circuit at the plasma-electrode interface, qualitatively clarified in Fig. 13.1, now becomes quantitatively understandable. For example, at the stage when the negative charge accumulates at the left-hand electrode (the current flows leftward), the charge repels the electrons of the plasma progressively more strongly. The plasma boundary defined by the edge electrons shifts away from the electrode, while locally noncompensated ionic charge remains in the layer. The total positive charge of the layer also piles up, not because of enhanced concentration but owing to new positively charged regions joining the layer. The positive charge is supplied to the layer by the conduction current from the plasma (electrons leave it): $\dot{q}_1 = en_+\dot{d} = -en_e\mu_e E = i_1/S$. Of course, no current flows within the layer, but the symbolic quantity – the displacement current – coincides with the discharge current. As follows from (13.19–23),

$$\frac{1}{4\pi}\frac{\partial E_1}{\partial t} = \frac{\dot{E}_0}{4\pi} = -\sigma E_a\sqrt{1+\omega^2\tau_\sigma^2}\cos(\omega t + \Delta\varphi) = \frac{i}{S}\,.$$

The plasma conductivity being constant, the varying negative charge q of an electrode is not given enough time to be completely neutralized by the positive charge of the layer. The noncompensated charge in the region of contact of the plasma and metal conductors, $q - q_1 = E/4\pi$, is the source of field E inside the plasma, while the difference between the accumulation rates of q and q_1,

$\dot{q} - \dot{q}_1 = \dot{E}/4\pi$, that generates the variable field component in the plasma is symbolically interpreted as the displacement current i_{dis} in the plasma itself:

$$\dot{i} - \dot{i}_1 = S\dot{E}/4\pi = i_{dis}\ ,\quad i_1 + i_{dis} = i\ .$$

13.5.5 Insulated Electrodes

Figures 13.1,2 and all relations obtained above remain valid in this case also. The constant charge q_0 now attaches to the dielectric surface facing the gas. The field in the gas at the insulator surface is $E_0 = 4\pi(q + q_0)$. Its constant (time-averaged) component $4\pi q_0$ is determined by the deposited charge, and the variable $4\pi q$ is related to the variable charge q on the electrode. According to (13.22), $|q_0| = \sigma E_a/\omega \approx j_a/\omega$. In the weak-current mode at $f \sim 10\,\mathrm{MHz}$, we have $j_a \sim 10\,\mathrm{mA/cm^2}$, whence $|q_0| \sim 10^{-10}\,\mathrm{C/cm^2}$. About 10^9 electrons attach to $1\,\mathrm{cm^2}$ of the dielectric surface. This is not much in comparison with about $10^{16}\,\mathrm{atoms/cm^2}$ on the surface, so that the surface is not very densely covered with the deposited electrons.

13.6 Constant Positive Potential of the Weak-Current Discharge Plasma

13.6.1 Definition

If a sinusoidal voltage is applied to the electrodes, the time-averaged potential difference between them is zero. The time-averaged potential difference between any point in the plasma and the electrode would also vanish if the field were everywhere harmonic. The field is indeed nearly sinusoidal in the electroneutral plasma and in the insulators but it is not harmonic in the electrode layer, so that the plasma acquires a constant potential V_0, with respect to the electrode, equal to the potential difference, averaged over a period, between an arbitrary point in the plasma and the electrode. The averages of potential differences over regions of harmonic field (plasma, insulators) vanish. As a result, the constant potential V_0 of the plasma with respect to the electrode, which is measured in experiments, is equal to the time-averaged voltage V_C across the near electrode layer. In the case of a symmetric (plane) gap, both electrodes are equivalent, on the average. We will now calculate the constant potential $V_0 = \langle V_C(t)\rangle$ in several situations.

13.6.2 Electrons Perform Drift Oscillations; the Gas Is Charged

This second condition signifies that electrons from boundary layers were absorbed into the metal or attached to the dielectric. The potential of the plasma boundary of the layer with respect to the electrode is

$$V_C = -\int_0^d E_1 dx = -\frac{E_0 + E}{2}d \approx -\frac{E_0 d}{2} = \frac{E_{0a}A}{2}(1 + \sin\omega t)^2\ .$$

We have used here (13.18–22). The neglect of E in comparison with E_1 in this expression corresponds to the case of a highly-conducting plasma, $\omega\tau_\sigma \ll 1$. In this case the potential is positive nearly all the time. The constant potential calculated by averaging V_C at an arbitrary $\omega\tau_\sigma$ is

$$V_0 = \frac{3}{4}\frac{E_a}{\omega\tau_\sigma}A = 3\pi e n_e A^2 = \frac{3\pi e(\mu_e p)^2 n_e}{\omega^2}\left(\frac{E_a}{p}\right)^2 . \tag{13.24}$$

A formula of type (13.24) was first derived by *Levitsky* [13.1], where, presumably by mistake, the value of V_0 was twice as great. On the whole, (13.24) gives the correct order of magnitude for V_0. For instance, if $n_e = 10^{10}\,\mathrm{cm}^{-3}$ and $A = 0.1\,\mathrm{cm}$, then $V_0 = 140\,\mathrm{V}$. A more detailed comparison with experiments is not easy owing to the scarcity of experimental data for the conditions relevant for (13.24). Nevertheless, the calculation of V_0 using (13.24) is definitely useful for better understanding the physics of the processes and for further elaboration of the theory.

13.6.3 Effect of Inhomogeneity in Ionic Distribution

The approximation $n_+(x) = \mathrm{const}$ is quite crude. True, it does permit the successful completion of all the calculations in a simple and clear analytic form. This in fact means a lot, because a better way of uncovering the essentials of a process does not exist. Certainly, we cannot expect the obtained formulas to be highly accurate. Actually, n_+ in weak-current layers decreases in a monotonic fashion from the plasma to the electrode or dielectric boundary, undergoing a severalfold reduction. The layers are thicker than in the $n_+ = \mathrm{const}$ approximation, the field at the boundaries is weaker, but the voltage across the layers and the constant plasma potential are almost twice as large (Sect. 13.8.2).

13.6.4 Drift Oscillations; the Gas Is Neutral

Let us turn to the approximation $n_+(x) = \mathrm{const}$ and assume that electrons do not attach to insulators. At the moments of equilibrium (if $E = -E_a\cos(\omega t)$, these are $\omega t = 0, \pi$) the layers are absent, and at the moments $\omega t = \pi/2, 3\pi/2$ electrons are forced by the field towards the surface (exactly to the surface if diffusion is absent). Formulas (13.18) for the field in the plasma, and also (13.19,20), describing the left-hand layer in the cathode half-period when the layer is positively charged, still hold. But since now $d(0) = 0$, we have $d = A\sin\omega t$ instead of (13.21). The field at the insulator surface is determined by (13.22) without the second term because now the field E_0 has no constant component. The thickness of the negative charge layer is small during the anode half-period even though the field E_0 has the same magnitude. Consequently, the integral over the anode half-period can be neglected when the potential difference in the layer is time-averaged. As a result,

$$V_0 = \left\langle -\frac{E_0 + E}{2}d\right\rangle = \frac{V_{C,\max}}{4} = \frac{\pi}{2}e n_e A^2 . \tag{13.25}$$

The potential V_0 in an electrically neutral gap is less by a factor of 6 than in a charged gap. Experiments do not point to large differences in V_0 for discharges with insulated and bare electrodes. This can be regarded as an indirect proof of the attachment of electrons to insulators.

13.6.5 Low Pressures

In this case the amplitude of electron oscillations (not necessarily drift oscillations) may be comparable with the interelectrode spacing, so that any extended positive column is out of the question. The layer of positive space charge may fill nearly the entire gap in the course of electron swings. A very simple estimate of V_0 is then possible. When electrons shift to the right, a poorly conducting region occupied by ions is formed between the left-hand electrode and the electrons: almost the entire applied voltage $V(t)$ falls across this region. The approximate instantaneous potential of the plasma driven to the right-hand electrode (with respect to the left-hand one) is equal precisely to this fall. The potential difference between the plasma squeezed at the left-hand electrode and this electrode becomes small in the next half-period. Hence,

$$V_0 \approx \frac{1}{2\pi}\int_0^{\pi} V_a \sin \omega t \, d(\omega t) = \frac{V_a}{\pi} . \tag{13.26}$$

The constant positive potential of the plasma is approximately one-third of the amplitude of the applied voltage. This result follows as a limiting case from a more detailed theory of the collisionless rf discharge constructed in [13.11].[9] it is compared with experimental data in Fig. 13.14.

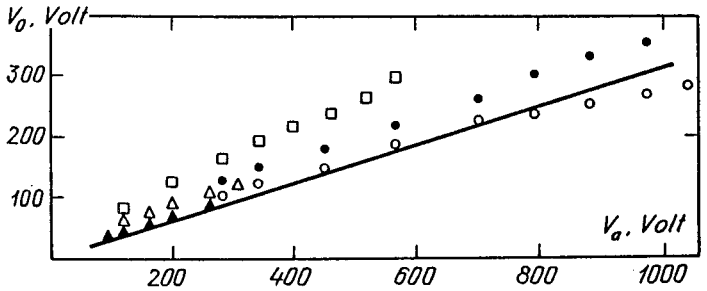

Fig. 13.14. Constant positive plasma potential as a function of voltage amplitude on electrodes at low pressure. *Solid curve:* $V_0 = V_a/\pi$. *Dots* represent experimental data for He and H_2 at low pressures [13.11]

[9] The notion of constant positive potential resulting from the rectification of rf voltage by nonlinear conduction of the layers is developed in [13.11] and in some other papers. In fact, this radioelectronics analogy must not upstage the real cause of the effect, namely, the oscillation of the electron gas with respect to the ionic residue and a positive charge of the gas volume.

13.7 High-Current Mode

13.7.1 Common Features with Weak-Current Modes

Electrode layers of positive space charge are formed in ccrf discharges of both forms. The reason is the oscillation of the electron gas over a range much greater than that of the ionic oscillations, and the resulting absorption of electrons by the electrodes. In any case, if plasma conductivity is sufficiently high, the field moves the ions towards the electrodes for the larger part of the period. An ion reaching the electrode may cause secondary emission; an emitted electron then produces numerous electron-ion pairs in the strong field of the layer. Some electrons manage to cross a considerable voltage difference without collisions and thus reach high energy. We conclude that despite the reversal of sign of the applied voltage every half-period, the electrode behaves in both regimes mostly as the cathode.[10]

Whatever the form of discharge, the field in the layers has a variable component and displacement currents are present. As for the region far removed from the electrodes, where the electrodes phenomena are not felt (the positive column if there is enough space for it), the processes of production and transfer of charges in it are of similarly local nature. The localization is caused by the smallness of the electron displacements: $A \ll L$. Possible quantitative differences in columns of different modes arise because of the differences in electron and current densities.

13.7.2 Essential Aspects of the Differences

All the best-pronounced features of the two forms of burning of ccrf discharges are determined by whether the process of multiplication of electrons due to secondary emission on the electrode is self-sustained, whether the Townsend-type condition (7.1) of reproduction of charged particles is satisfied in the layer, in fact, whether the gas in the layer suffers *breakdown*. Breakdown does occur in the high-current mode, but not in the weak-current mode. The self-sustained conduction current grows in the former case to a comparatively high value, nearly the same as in the normal glow discharge. In the latter case, the ionic current to the electrode is low and is mostly related to the thermal motion (diffusion) of ions. These small losses of ions are balanced out, most likely, at the expense of the ionization of atoms by electrons during that part of the period when electrons of the plasma approach the electrode, and partly at the expense of the flux of ions from the positive column.

We repeat this as it is an essential point. It may be said that in the high-current mode each electron emitted from the electrode (or from the dielectric)

[10] Obviously, only if $A = \mu_e E_a/\omega \ll L$. If $A \gg L$ the discharge within each half-period resembles the constant-current discharge, and the electrode serves alternatingly as cathode and then as anode. Such low-frequency discharges (known as ac-current discharges) are now employed in laser technology (Sect. 14.4.6).

and each ion absorbed into it are *reproduced* by avalanche multiplication *directly in the electrode layer*. In the weak-current mode, the *entire discharge* participates in the balance of production and removal of charges, and the multiplication in the layer due to secondary emission *is not balanced*. We will additionally clarify at the end of Sect. 13.7.4 why the current is "high" in the high-current mode and"weak" in the weak-current mode.

The available experimental data indicate that layers very similar to the *cathode layer of the normal glow discharge* are formed in the *high*-current mode at both electrodes. The experimentally measured layer thickness d and constant potential V_0, equal to the average voltage across the layer, are found to be close to the normal values d_n and V_n. As we find for d_n and V_n, $d \propto p^{-1}$ and is independent of frequency, and V_0 is independent of p and ω. The normal current density is also satisfactorily explained (Sect. 13.7.4). Typical regions of *negative glow* and *Faraday dark space* also appear. In the *weak*-current discharge, there can be no self-sustained conduction current in the layer because the layer thickness is greater than d_n by an order of magnitude and is so high that the measured voltage is too low to satisfy the Townsend condition at the actual values of pd. The layer thickness d is proportional to the electron drift velocity in the plasma, while d_n is independent of it. Furthermore, $d \propto \omega^{-1}$ and is almost independent of pressure. All this indicates that the scale that determines d is the amplitude $A = \mu_e E_a/\omega$, as we assumed in the above model that required no ionic current.

13.7.3 Secondary Ignition

The transition from the weak- to high-current mode is a result of the Townsend breakdown of the electrode layers in which the electrodes act as cathodes and the plasma column serves as an anode (i.e., it receive electrons). The transition is realized when the voltage across the layer (obviously, it is intermediate between the maximum voltage $V_{C,max}$ and the average V_0) reaches the value approximately equal to the Paschen breakdown threshold $V_i(pd)$. The value of pd in a weak-current discharge in molecular gases at medium pressures is much higher than the value corresponding to the minimum of the Paschen curve, which is close to pd_n. The breakdown voltage is appreciably higher than V_n.[11] After the breakdown, the initially thick ionic layer forms a normal cathode layer as in the initiation of a glow discharge, that is, the zone of positive space charge and the voltage across it contract to values that are optimal for the self-sustainment of the values d_n, V_n, while the remaining part of the former layer is converted into electrically neutral plasma.

This approximate condition of secondary ignition, $V_0 \approx V_i(pd)$, implies a restriction on the maximum possible current density in the weak-current mode [13.12]:

[11] If $pL < 10^{-1}$ cm Torr, the discharge gap belongs to that part of the left-hand branch of the Paschen curve where the breakdown voltage is high, regardless of the gas species. Possibly, this is why no sign of the high-current mode (conduction current) has been observed in experiments with very low pressures ($p \sim 10^{-2}$ Torr).

$$j \sim \omega V_0/4\pi d < \omega V_i(pd)/4\pi d\,, \tag{13.27}$$

which is generally supported by experimental data. The higher the frequency, the higher the limiting current density and the plasma density $n \equiv n_e$ at which the weak-current discharge is still sustainable. A more detailed calculation of breakdown in a layer [13.13] gives the following approximate formula for evaluating the critical plasma density corresponding to the transition from the weak-current mode in nitrogen at $p = 15\,\text{Torr}$ to the high-current mode:

$$n_{cr} \approx 1.7 \times 10^8 (f[\text{MHz}])^{3/2}\,\text{cm}^{-3}\,,\quad f \sim 1 - 30\,\text{MHz}\,.$$

Only the high-current mode is realized at a given frequency if $n > n_{cr}$, or a given n and $f < f_{cr}$. Thus the weak-current mode is practically unfeasible in ac discharges at $f = 10\,\text{kHz}$.

13.7.4 Current Density

The normal cathode current density in a glow discharge is $j_n = C_1 p^2$, where C_1 is a constant, specific for each gas-metal pair (Sect. 8.4). Measurements have demonstrated [13.14] that the high-current ccrf discharge also involves the *phenomenon of normal current density* in which a change in discharge current produces a proportional change in the area occupied by the discharge on the electrodes (including insulated ones). It was found, however, that the current density may considerably exceed j_n, because of the inevitable displacement current added to the conduction current at the electrodes. The conduction current must be nearly equal to j_n because the thickness d and voltage V of the space-charge layer are close to the normal values d_n, V_n. The displacement current in the layer is $j_{dis} \approx \omega V/4\pi d$. If we take into consideration that $d \approx d_n = C_2 p^{-1}$, where C_2 is also a constant for a given pair of materials and $V \approx V_n$ is independent of pressure, then $j_{dis} \approx (\omega V/4\pi C_2)p \propto p$. Since the conduction current j_n and displacement current j_{dis} are different functions of p, their relative contributios to the total current j change with p. As j_n and j_{dis} are shifted in phase by $\pi/2$, the rms value of j is

$$j = \sqrt{j_n^2 + j_{dis}^2} = C_1 p^2 \sqrt{1 + (\omega V/4\pi C_1 C_2 p)^2}\,. \tag{13.28}$$

Calculations using this formula are compared with experimental data in Fig. 13.15 taken from [13.14]. For the brass-air combination used for the measurements (obtained with the setup described in Sect. 13.4.4), $C_1 = 2 \times 10^{-4}\,\text{A/cm}^2\text{Torr}$, $C_2 = 0.23\,\text{cm Torr}$. The frequency was $f = 13\,\text{MHz}$. For the voltage V on the layer, the value 320 V was used, which is the rms rf-voltage at the electrodes when they have been brought together so closely that the positive column is practically absent ($L \approx 1$–$2\,\text{cm}$, filled with layers and parts of Faraday spaces). A large fraction of the applied voltage is developed across the layers. The experimental rms values of j fit the calculated curve 2 quite well. The curve as a whole corresponds only to the high-current mode. Note that j_{dis} at relatively

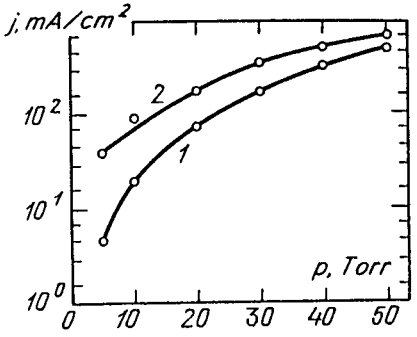

Fig. 13.15. Electrode normal current density in high-current mode as a function of pressure (air, brass electrodes, f = 13 MHz). *(1)* j_n for normal dc glow discharge in air, with brass cathode. *(2)* Calculations using (13.28), taking into account displacement current. *Dots* represent measured values [13.14]

low pressures ($p \approx 5$ Torr) is greater than j_n by an order of magnitude, while these quantities are almost equal to $p \approx 50$ Torr. The high current of the *high-current mode* at *low pressure* thus also closes the circuit via the *displacement current*. But the very possibility of letting through a high current – indicating a fairly high degree of ionization in the gas – rests on the multiplication of electrons in layers after breakdown, where optimal conditions, corresponding to a normal cathode layer, are created.

Let us emphasize again that the *difference* between the high-current and weak-current modes is *not in the ratio* of conduction and displacement currents on the electrodes. We did see that the latter is again much greater than the former in the low-pressure high-current mode. The main result of the breakdown of electrode layers is not the build-up of a high ionic current, but an abrupt *drop in layer thickness*. If the voltage remains within the same order of magnitude, the field at the electrode sharply increases, so that high-density displacement current can flow. A thick weak-field layer of the weak-current discharge cannot let through a high (displacement) current, while a thin high-field layer of high-current discharge can. This is the reason for the "high-current" behavior.

13.7.5 The Simplest Model for the Functioning of "Cathode" Layers

Assume that the ion density n_+ in the layer is constant, even though it differs from that in the positive column. Let the plasma boundary oscillate, touching the boundary for only a short time. The plasma conductivity is high, and the field amplitude in the plasma is much less than at the electrode. Finally, we assume that the ionic current to the electrode exists but is much lower than the displacement current. Then the field E_0 at the left-hand electrode, the layer thickness d, and the voltage V_C on the layer, $V_C = E_0 d/2$, are described by the same formulas as in Sect. 13.5.2. In terms of the amplitude of the discharge current density, $j = \dot{E}_0/4\pi = -j_a \cos \omega t$, we can write E_0, d, and V_C in the form

$$E_0 = -(4\pi j_a/\omega)(1 + \sin \omega t)\,,$$
$$d = (j_a/e\omega n_+)(1 + \sin \omega t)\,,\quad V_C = (2\pi j_a^2/e\omega^2 n_+)(1 + \sin \omega t)^2\,. \tag{13.29}$$

If the voltage drop across the plasma is low, in contrast to Sect. 13.2, the potential difference at the electrodes is $V = (8\pi j_a^2/e\omega^2 n_+) \sin \omega t$.

The flux of ions to the electrode, $n_+\mu_+E_0$, is balanced out by their production in the layer. In avalanche multiplication by secondary emission, charges are mostly produced far from the cathode, and if the characteristic displacement amplitude of ions $A_+ = \mu_+E_{0a}/\omega \ll d_a$, an ion needs a considerable number of periods to cover the distance from the point of production to the electrode (E_{0a}, d_a, V_{Ca} denote the maximum (amplitude) values). The correlation of the phases of production of an ion and of its arrival at the electrode thereby vanishes. Let us ignore the effect of delay in the arrival of ions and write a condition, equivalent to (8.9), *of self-stustaiment of the current of charges* in the layer [13.15]:

$$\langle n_+\mu_+E_0(t)\rangle = \left\langle \gamma n_+\mu_+E_0(t)\left\{\exp\left(\int_0^{d(t)}\alpha[E_1(x,t)]dx\right)-1\right\}\right\rangle . \quad (13.30)$$

The averaging here is carried out over one period. The field $E_1 = E_0(1 - x/d)$ is substituted into the ionization coefficient; γ is the secondary emission coefficient. The main contribution to the multplication integral is made by the short time interval around the time moment $\omega t = \pi/2$ when $|E_0|$ and d are maximal.

Equation (13.30) relates V_{Ca} and d_a or V_{Ca} and j_a because $E_{0a} = 8\pi j_a/\omega$. The "$V - i$ characteristic" of the layer, $V_{Ca}(j_a)$, has a minimum. By analogy to the theory of von Engel and Steenbeck (Sect. 8.4), it is natural to assume that precisely this "normal state" is realized. One would expect that calculations using (13.30, 29) should give *normal* values of V_{Ca} and d_a that are quite close to those obtained from (8.9) at the same A and B in (4.5) for α, and the same γ. In the example calculated in [13.15] (air, $A = 8.6$, $B = 254$, $\gamma = 0.1$, $\mu_+p = 1.4 \times 10^3$), we find that at $f = 13.6\,\text{MHz}$ and $p = 30\,\text{Torr}$, the normal amplitude of the cathode fall is $(V_{Ca})_n \approx 280\,\text{V}$, the mean layer thickness is $d_n \approx 0.02\,\text{cm}$, and the normal current density is $j_{an} \approx 50\,\text{mA/cm}^2$. The ion density is defined as $n_+ = E_{0a}/4\pi ed_a$. The ionic current amplitude $j_{ia} = en_+\mu_+E_{0a}$, calculated in the next approximation, comes to within 15 % of j_{an}.

Similarity laws hold for normal parameters: $(V_{Ca})_n$ is independent of pressurie, $(d_a)_n \propto p^{-1}$, $(E_{0a})_n \propto p$, the current is approximately equal to the displacement current, $j_{an} \propto p$, and the ionic current is $j_{in} \propto p^2$. Hence, the ionic current at sufficiently low pressures is indeed a small fraction of the total. But if we extrapolate $j_{dis} \propto p$ and $j_i \propto p^2$ to high pressures, j_i can be expected to exceed j_{dis}. According to the concepts of [13.15], the condition $j_i \geq j_{dis}$ corresponds to the weak-to-high current ($\alpha - \gamma$) transition, and the entire theory relevant to the case of $j_i \ll j_{dis}$ describes the weak-current discharge.

This conclusion is wrong and at variance with experiment. The theory is correct but holds fo the *high-current*, not the *weak-current* mode. This is indicated by using the Townsend condition of self-sustainment of conduction current in the layer, (13.30), and by choosing the normal parameters at the minimum of the $V - i$ curve of the cathode layer. The experimental curve in Fig. 13.15, showing $j_i \ll j_{dis}$ at low pressurs, belongs entirely to the high-current mode by layer thickness, glow distribution, and current-density magnitude. The transition

is always accompanied by jumps of an order of magnitude jumps in d and j. The small layer thickness calculated above, $d \approx 0.02\,\mathrm{cm}$, is typical of the high-current discharge. In the weak-current discharge at the same ambient conditions (air, $p = 30\,\mathrm{Torr}$), $d \approx 0.3\,\mathrm{cm}$, $j_a \approx 7\,\mathrm{mA/cm^2}$ [13.8, 13.12].

The ionic current at lower pressures is small compared with the displacement current because an ion needs considerable time (many periods) to cross the d_{an}-thick layer from the point of most copious production to the electrode. A kind of pause develops between the relatively fast removal of ions into the electrode from the contiguous region, $A_+ \approx \mu_+ E_{0a}/\omega$, and the arrival of new ones to replace them, after which a deficiency of ions appears at the electrode. The ionic current becomes weak, and is compensated for by the displacement current. Indeed, the ratio of currents to the electrode is characterized by the ratio of the lengths indicated:

$$\frac{j_{ia}}{j_{disp,a}} \approx \frac{en_+\mu_+ E_{0a}}{\omega E_{0a}/4\pi} = \frac{4\pi e n_+}{E_{0a}} \cdot \frac{\mu_+ E_{0a}}{\omega} = \frac{A_+}{d_a} .$$

At sufficiently high pressurs, when $d_{an} \propto p^{-1}$ decreases to the displacement amplitude A_+ which is independent of p, the removal of ions is immediately balanced out by the arrival of ions produced in the same period, and the conduction current becomes predominant. Experiments do *not* reveal *any jumps and transitions* in this situation.

13.8 The Structure of a Medium-Pressure Discharge: Results of Numerical Modeling

13.8.1 Equations

The charge density and field distributions in the discharge gap and their evolution in time are described in the one-dimensional approximation, with diffusion neglected and attachment absent, by the following system of equations:

$$\begin{aligned}
&\frac{\partial n_e}{\partial t} + \frac{\partial \Gamma_e}{\partial x} = \alpha|\Gamma_e| - \beta n_e n_+ , \quad \Gamma_e = -n_e \mu_e E , \\
&\frac{\partial n_+}{\partial t} + \frac{\partial \Gamma_+}{\partial x} = \alpha|\Gamma_e| - \beta n_e n_+ , \quad \Gamma_+ = n_+ \mu_+ E , \\
&\frac{\partial E}{\partial x} = 4\pi e(n_+ - n_e) .
\end{aligned} \tag{13.31}$$

The boundary conditions on electrodes or insulting surfaces indicate that when the field points towards the surface, secondary emission is produced, $\Gamma_e = -\gamma\Gamma_+$; when the field points away from the surface, the ionic current vanishes: $\Gamma_+ = 0$.

An rf voltage V is applied to the electrodes.[12] If the electrodes are insulated, V is divided between the gas-filled gap and the insulators. At the beginning of the discharge, the initial electron density must be specified.

The solution of this problem shows that at $L \gg d$ a homogeneous positive column is formed after some time in the greater part of the gap of length L, where the *ionization-recombination equilibrium* is maintained *on average over a period.* To study the structure of electrode layers, it is sufficient to specify the plasma density far from the solid surface, $n = n_e = n_+$, and the field E in it, $E = E_a \cos \omega t$. Its amplitude E_a is related to n by the condition $\langle \alpha \mu_e E \rangle = \beta n$ (Sect. 13.3.2 and Fig. 13.5). This is equivalent to fixing not electrode voltages, but the *discharge current* whose amplitude j_a is expressed in terms of n and $E_a(n)$. Thus $j_a \approx en\mu_e E_a$ when the displacement current in the plasma is low.

The calculations in [13.13] were carried out with the following set of data:

$$\alpha = 12p \exp(-342p/E)\,\mathrm{cm}^{-1} \quad \text{for} \quad E/p > 100\,\mathrm{V/cm\,Torr}\,,$$

$$\alpha = 2.4p \exp(-155p/E)\,\mathrm{cm}^{-1} \quad \text{for} \quad E/p < 100\,\mathrm{V/cm\,Torr}\,,$$

$$\mu_e = 4.4 \times 10^5/p\,, \quad \mu_i = 10^3/p\,\mathrm{cm^2/Vs} \quad (p \text{ in Torr})\,,$$

$$\beta = 2 \times 10^{-7}\,\mathrm{cm^3/s}\,, \quad \gamma = 0.01\,,$$

which is often used in modeling discharges in nitrogen; $f = 13.6\,\mathrm{MHz}$, $p = 15\,\mathrm{Torr}$. Calculations were continued until a strictly periodic solution was obtained; this needed about 10^2–10^3 periods.

13.8.2 Results

Depending on the specified V for a gap of given length L, or on the specified n (or j_a) in the positive column, the distributions typical of the weak- or high-current modes set in *automatically.* A *change in structure* occurs at $n_{cr} \approx 8.72 \times 10^9\,\mathrm{cm}^{-3}$, $j_{a,cr} \approx 9.2\,\mathrm{mA/cm^2}$.[13] Experimentally the transition was observed in air at 30 Torr at $j_{a,cr} \approx 17\,\mathrm{mA/cm^2}$ [13.8], but [13.12] predicts j at $p = 15\,\mathrm{Torr}$ (the pressure used in the calculation) to be less by a factor of 1.5; the agreement with measurements is thus quite good.

Figure 13.16 shows calculated density distributions of ions and electrons at the left-hand electrode (cf. Fig. 13.1) for a typical weak-current mode: $j_a = 4\,\mathrm{mA/cm^2}$, $n = 3.7 \times 10^9\,\mathrm{cm}^{-3}$ (in the positive column), $E_a/p = 14\,\mathrm{V/cm\,Torr}$ (in fact, the value of E_a/p was definitely overestimated considerably since gas heating was neglected). The discharge current is closed at the electrode almost

[12] Equations of this type were used in [13.16] to model non-self-sustaining rf discharges with external ionization (in the weak-current mode), and in [13.17], to model ac discharges (Sect. 14.4.6).

[13] The corresponding quantity $(E_a/p)_{cr} = 15\,\mathrm{V/cm\,Torr}$ is less indicative since the actual $V - i$ curve of the column may greatly differ from the postulated one owing to gas heating, stepwise ionization, etc. The typically measured critical voltage V_{cr} across the electrodes (Sect. 13.4.4) is even less indicative. It depends on discharge gap width L, on the lengths of the dielectrics (if the electrodes are insulated), and, of course, on E_a/p and on the method of cooling the gas.

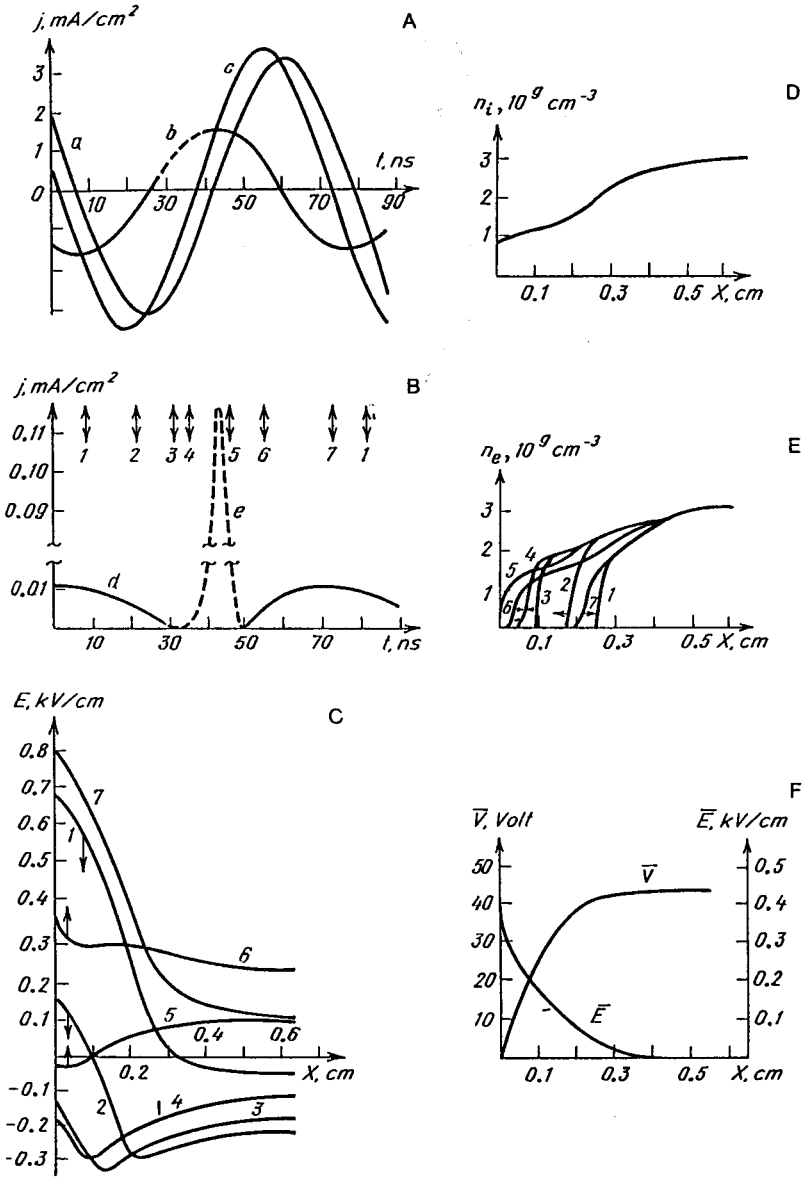

Fig. 13.16. Calculated results for the weak-current mode (N_2, $p = 15$ Torr, $f = 13.6$ MHz, discharge current amplitude $j_a = 4$ mA/cm^2). **(A), (B)** evolution of components of currents during one period. The position of the time origin is arbitrary. *Curve a* conduction current in plasma, *curve b* displacement current in plasma, *curve c* displacement current of the left-hand electrode, *curve d* ionic current and *curve e* electronic current at the left-hand electrode. In **(B)** *arrows* with numbers indicate times at which instantaneous distributions of n_e and E at the left-hand electrode are given in parts **(E)** and **(C)**. *Arrows* at n_e curves indicate the direction of motion of the plasma boundary. Fields $E > 0$ directed towards the electrode, $E < 0$ away. *Arrows* at $E(x)$ curves indicate that the field increases (↑) or decreases (↓). **(D)** density of ions, n_i. **(F)** constant field $\bar{E}(x)$ and constant potential $\bar{V}(x)$ with respect to the electrode [13.13]

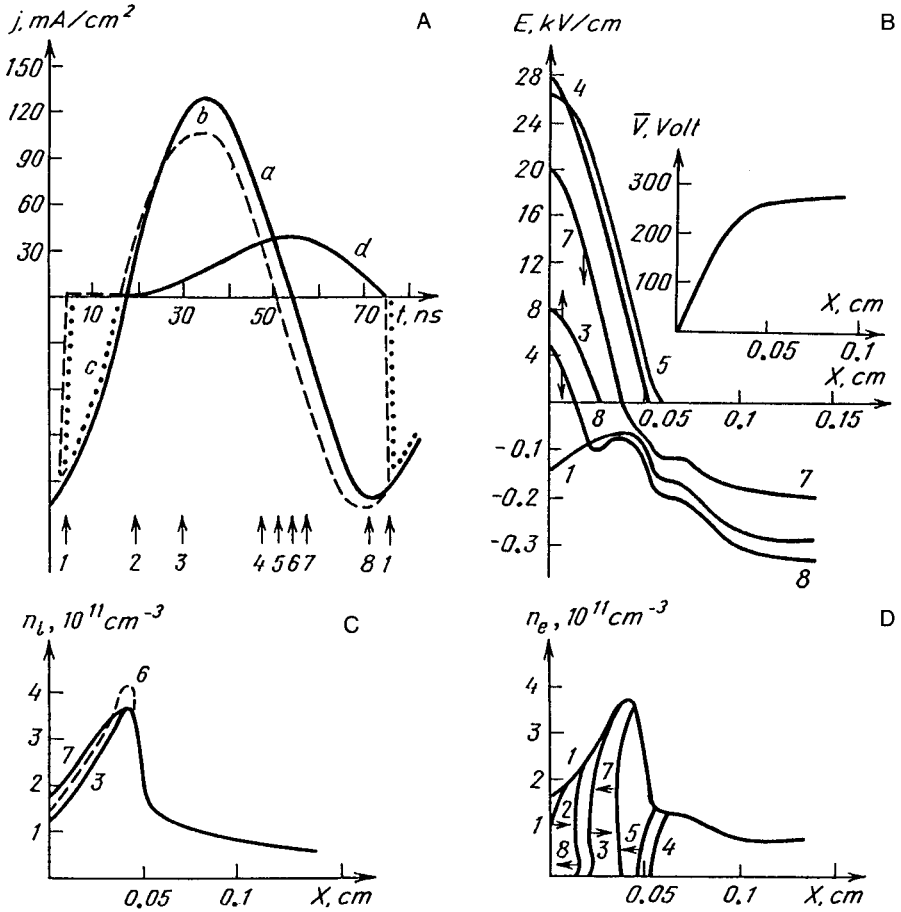

Fig. 13.17. Calculated results for high-current mode (N_2, p = 15 Torr, f = 13.6 MHz, j_a = 0.12 A/cm^2). **(A)** evolution of various components of currents during one period. The position of the origin time is arbitrary. *Curve a* conduction current in plasma, *curve b* displacement current of the left-hand electrode, *curve c* electronic current and *curve d* ionic current at the left-hand electrode; the displacement current in the plasma is to low to be shown on this figure. *Arrows* with numbers indicate times at which instantaneous distributions of n_i, n_e, and E at the left-hand electrode are given in parts **(B)**, **(C)**, **(D)**. **(B)** fields $E > 0$ (directed towards the electrode) and $E < 0$ (away from the electrode). *Scales* above and below the abscissa are different. *Arrows* at $E(x)$ curves indicate that the field increases (↑) or decreases (↓). $\bar{V}(x)$ is constant potential with respect to the electrode. **(C)**, **(D)** density of ions, n_i, and electrons, n_e. *Arrows* at n_e curves indicate the direction of motion of plasma boundary [13.13]

exclusively by the displacement current. The maximum value of ion current at the electrode is less by a factor of 400: 10^{-2} mA/cm^2. The "anode" phase, at which electrons are squeezed by the field to the electrode, lasts for only one tenth of a period. The maximum value of the electron current to the electrode is correspondingly 10 times greater than the ionic current, 10^{-1} mA/cm^2, because equal amounts of positive and negative charges are deposited on an electrode

during a period. The discharge structure is qualitatively the same as in Fig. 13.1, 13.2. The differences are connected only with the fact that in the electrode layer $n_+(x) \neq$ const but decreases from the positive column towards the electrode (as a result of removal of a certain number of ions to the electrode). The density of ions fluctuates so little in time that a figure drawn to this scale cannot show these varitions. The constant plasma potential $V_0 = 45$ V is greater by a factor of 1.7 than that given by (13.24). The maximum layer thickness of 0.3 cm fits quite well the value measured in air, 0.35 cm [13.12], and is twice that given by the model of Fig. 13.1: $2A = 2\mu_e E_a/\omega \approx 0.14$ cm.

Plots of $E(x,t)$ and other quantities for the version under consideration here can be found in [13.13] .

Figure 13.17 shows similar results for the high-current mode. In contrast to Fig. 13.16, we give here the complete picture of the process because it is not as trivial as in the case of weak-current mode. The calculations refer to $j_a = 0.12$ A/cm^2 ($n = 9 \times 10^{10}$ cm^{-3}, $E_a/p = 18.6$ V/cm Torr; as in the preceding case, the value of E/p has been greatly overestimated but this is unimportant for the structure of the electrode layer).

Similar current densities were measured in air at 15 Torr: 0.16 A/cm^2 in [13.12], 0.11 A/cm^2 in [13.14]. The ionic current to the electrode is considerable even though it is lower than the displacement component. The entire current becomes electronic at the "anode" stage. According to [13.12], the measured conduction current in the layer is one-third of the total, which agrees with the calculations. The layer is considerably thinner than in the weak-current mode; its maximum value is 0.05 cm, and n_+ has a maximum inside the layer. As the "cathode" layer is being formed, the first oscillations are followed by the formation and propagation of the ionization wave from the plasma to the electrode; the wave leaves the plasma behind and squeezes the space-charge layer to the electrode. This also happens when a d.c. glow discharge is formed after breakdown.

13.8.3 Nonlocal Effects

These effects are ignored in (13.31) (see Sect. 8.4.10), so that the calculation gives only a model behavior of the transition zone between the space-charge layer and the positive column (Sect. 8.5). In fact, experiments in the high-current mode definitely reveal a Faraday dark space, which is contiguous to the zone of negative glow (see Fig. 13.11). Figure 13.11 implies that the maximum of light emission in the weak-current mode lies at the boundary separating the electrode layer and the positive column. Note that this fact is supported by calculations based on equations (13.31). The maximum of ionization rate $\langle \alpha | \Gamma_e | \rangle$, and hence, of excitation rate of atoms, falls within the transition region between the layer and the column.

13.9 Normal Current Density in Weak-Current Mode and Limits on the Existence of this Mode

13.9.1 Physical Explanation

Yatsenko, who discovered these effects [13.8] (Sect. 13.4.4), gave them the following qualitative interpretation. The measured $V-i$ characteristic of the positive column is falling. It can be given the symbolic form $V_{col} = CpLj^{-m}$, where C and m are positive constants. The $V-i$ curve of the electrode layer, where the displacement current flows, is rising, $V_C = 4\pi dj/\omega$, because the layer thickness d is independent of current. In view of the phase shift between V_c and V_{col}, the voltage on the electrodes is $V = (V_{col}^2 + V_C^2)^{1/2}$. The current-voltage characteristic $V(j)$ of the discharge has a minimum at $j = j_n = (\omega CpL\sqrt{m}/4\pi d)^{1/(m+1)}$. One is inclined to assume that the minimum voltage V_{min} and normal current density j_n are realized, as in a dc discharge, when the electrodes are not totally covered by the discharge. The normal current density is the higher, the greater pL (as in Fig. 13.12). But as pL increases, j_n and V_C grow to critical values at which layer breakdown occurs and the high-current mode sets in. This gives the upper limit (in pL) of the existence of the weak-current mode.

13.9.2 On the Extension of the Domain of the Weak-Current Mode

This extension would be very desirable, because such a regime would be favorable for use in high-power lasers (Sect. 14.4.7). No power loss occurs in nonconducting layers, nor do they constitute sources of perturbation for the development of instability.

For the layers to remain nonconducting, the discharge current density j must not exceed the critical value j_{cr} of the transition. As follows from the arguments of Sect. 13.9.1, this is possible only if $pL < (pL)_{cr}$. However, the reason for the rising curve $j(pL)$ is the falling $V-i$ characteristic of the positive volumn, which in all likelihood results from the heating of the gas (Sect. 8.7). If the heating is partially suppressed by intensely pumping the gas through the discharge region, the constraint on pL becomes less severe. The weak-current mode will then survive at higher values of pL than those reported in [13.8]. Indeed, calculation of the $V-i$ characteristic taking into consideration the convective heat transfer [13.18] does support this expectation though, of course, the decisive proof will be given by experiment. Calculations predict the weak-current discharge domain to extend slightly at higher frequencies.

Note that the calculation of the parameters of the $\alpha-\gamma$-transition in the framework of the layer breakdown model [13.13], for the current-voltage characteristic of the positive column and of the entire discharge with gas heating taken into account as in [13.18], gave satisfactory agreement with the experimental results [13.10] concluding Sect. 13.4.4. The phenomenon of normal current density in the α-mode may vanish depending on the frequency and the role of heating in a specific experiment; on other words, the α-discharge may be anomalous. All

these remarks point to the importance of detailed calculation taking into account the heating of the gas in high-frequency electrical discharges.

13.9.3 Remark on Low-Pressure Discharges

Interest in this field was recently revived in connection with etching and deposition applications in the manufacturing of semiconductor materials for the microelectronics industry. Industrial reactors often employ plane-parallel electrodes separated by distances $L \sim 10\,\text{cm}$. The operation is conducted in the frequency range from 50 kHz to 50 MHz at pressures from 10^{-2} to 1 Torr; $V \lesssim 1000\,\text{V}$, $j \sim 1\,\text{mA/cm}^2$. Low pressures are characterized by a very low voltage drop across the positive column plasma, much lower than the ionization potential of gases [13.19]. Consequently, the production of electrons is ascribed entirely to the electrode layers, on which practically the entire voltage falls. However, the analysis of this picture in [13.19] does not reveal the mechanism of the process. A special issue of IEEE Transactions [13.20] was devoted to ccrf discharges and their applications to plasma-chemistry technologies (see also [13.21] and the recent review [13.22]).

A detailed and exhaustive consideration of the capacitive rf discharges is presented in a recently published book (see Further Reading [1]). The experimental data, physics, theory, computer simulation, experimental methods and measurement technique, applications for CO_2 lasers and plasma processing are given. There are chapters on rf discharges and technology in the new book (see Further Reading [2]).

14. Discharges in High-Power CW CO_2 Lasers

14.1 Principles of Operation of Electric-Discharge CO_2 Lasers

Electric discharge CO_2 lasers have the highest power among all existing types of cw lasers and are technologically the most advanced and best adjusted to cutting, metal welding, thermal hardening of parts, and to a number of other technological operations. Their cw power has increased in the two decades since the development of the first one by Patel in 1964 from a milliwatt to many kilowatts, and industrial lasers of up to several kW of power are now commercially available [14.1]. Systems with powers above 10 kW also exist. It can be said that no other applications-oriented problem has stimulated so much progress in gas discharge science as the problem of developing high-power cw CO_2 lasers.

14.1.1 Laser Transition in the CO_2 Molecule

CO_2 lasers employ the transition between two vibrational (rather, vibrational-rotational) levels of the electronic ground state of the CO_2 molecule. The lasing wavelength $\lambda = 10.6\,\mu m$ ($\hbar\omega = 0.117\,eV$) lies in the far infrared. The linear CO_2 molecule undegoes vibrations of three types (called vibration *modes*; see Fig. 14.1). The frequency ν_1 corresponds to symmetric vibrations, ν_2 to deformation vibrations, and ν_3 to asymmetric vibrations. A photon of lasing energy is emitted in the transition from the state 001 to 100; the numbers indicate the vibrational quantum numbers in the modes ν_1, ν_2, ν_3, respectively. The transition $001 \rightarrow 020$, $\lambda = 9.4\,\mu m$ is also possible, but it is normally much weaker.

The energy level of a molecule is determined by the state of not only the vibrational but the rotational motion as well. Thermodynamic equilibrium among rotational states sets in rapidly. Hence, while the rotational state from which the laser transition occurs is depleted, new molecules from other rotational states transfer into it, so that all rotational states form a sort of common energy pool. If necessary, a specific vibrational-rotational line can be singled out. The photon energy is 41 % of the energy of the upper level 001. This is the *principal limit* for the efficiency of a CO_2 laser. If the entire energy consumed to create the lasing medium went only to excite the 001 level of CO_2 molecules and each excitation event was followed by the emission of a photon, the energy of the laser emission would equal 41 % of the absorbed energy. The actual efficiency is typically several times lower.

14.1.2 Mechanism of Creating Population Inversion

In electric-discharge CO_2 lasers the upper laser level is pumped by *electron-impact excitation of vibrations* in the positive-column plasma of a glow discharge. The emission power is greatly increased by an admixture of *nitrogen* to CO_2. The energy of the first vibrational level of the N_2 molecule, which is efficiently excited by electron impact in the glow discharge and then slowly relaxes, is quite close to the energy of the upper 001 level of CO_2 (Fig. 14.1). Hence, fast resonance transfer of vibrational energy from N_2 molecules to CO_2, directly populating the necessary level, becomes feasible. For the N_2, frequency of the transfer of vibrational to translational energy (the rate of VT relaxation) is low even in collisions with water molecules (which are exceptionally active in this respect), namely $\nu_{VT} = 175 p_{H_2O}\ s^{-1}$,[1] while the frequency of energy transfer with CO_2 molecules is $\nu_{tr} = 1.8 \times 10^4 p_{CO_2}\ s^{-1}$. Molecules in the upper laser level 001 either emit photons (on the average, if the lower laser level has a lower population) or undergo the VT relaxation at a frequency $\nu_{VT} = 365 p_{CO_2} + 110 p_{N_2} + 85 p_{He}\ s^{-1}$ (in a mixture with helium).

High population inversion is a result not only of intense *pumping* to the upper level, but also a sufficiently fast *depletion* of the lower 100 level, which is constantly being populated by molecules that have emitted a photon of laser energy. Molecules must rapidly "leave" the 100 level for other states in order to "clear" the level and maintain a considerable difference between populations, $N_{001} - N_{100}$ (the inversion, which determines the amplification and radiation power). The lower 100 state of CO_2 is depleted by resonance transfer of vibrational energy of the ν_1 mode into that of the ν_2 mode (the 100 → 020 transition) followed by VT deactivation of vibrations (020 → 010 → 000), and by the two-step VT deactivation (100 → 010 → 000).

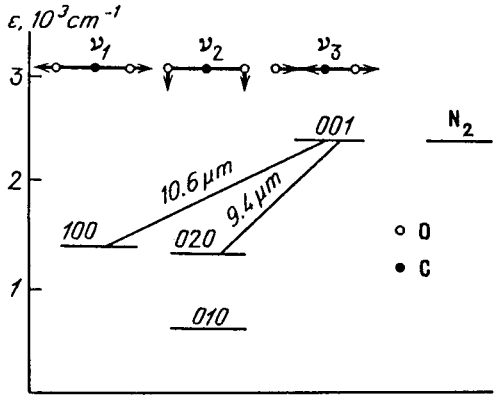

Fig. 14.1. Lower vibrational levels of the CO_2 and N_2 molecules. *Above:* directions of atomic motions of the CO_2 molecule in different types of vibrations

[1] At room temperature. In collisions of N_2^* with N_2 and O_2, $\nu_{VT} = 0.035 p_{N_2} + 0.28 p_{O_2}\ s^{-1}$; p [Torr].

14.1.3 Unacceptability of Considerable Heating

Simultaneously with deactivating collisions, reverse processes are present which excite the lower laser level 100. As a result of direct and reverse processes, its population is not very different from the equilibrium value corresponding to the translational gas temperature T. Therefore, T must be sufficiently low to maintain high population inversion and heating the gas to more than 150–200° C is undesirable. If $T > 450$–$500\,\mathrm{K}$, the inversion and output power are greatly reduced, and at $T > 600$–$650\,\mathrm{K}$ laser action becomes impossible. Sufficiently fast heat removal is the necessary condition for the operation of the laser. Indeed, if the efficiency is 10–20 %, then 80–90 % of the electric power input goes into heating the gas.

A number of factors reduce the efficiency in comparison with the ideal of 41 %. Not all of the energy acquired by electrons from the field is spent on exciting the vibrations, although about 80 % of the electrocal power is converted into vibrations of N_2 and 001 CO_2 at the optimal gas composition and optimal E/p [about several V/cm Torr]. Some 001 CO_2 molecules undergo relaxation instead of emitting a photon. Energy is also partly lost in reflections at mirrors, and so on. It appears that an efficiency higher than 24 % has never been achieved; a realistic figure is 10–15 %.

14.1.4 Laser Mixture

Experiments demonstrated that an admixture of *helium* is very useful in CO_2 lasers. Being light and possessing high thermal conductivity, helium enhances the heat removal from the discharge and improves the quality of the discharge itself. Presumably, helium atoms increase the rate of deactivation of the lower laser level of CO_2. The laser mixture is usually composed of three ingredients: CO_2, N_2, and He. Various compositions are used to optimize the gas for a given design, for instance, $CO_2 : N_2 : He = 1 : 1 : 8$ or $1 : 6 : 12$ (the ratios are in numbers of molecules), etc. However, helium is an expensive gas, while its consumption is high, because the mixture has to be constantly renewed. The cost factor being important for industrial equipment, the tendency is to reduce the helium content. Some systems are free of helium, as a result of multiparameter optimization.

14.2 Two Methods of Heat Removal from Lasers

14.2.1 Diffusion-Cooled Lasers

These are systems in which the heat is carried out of the discharge zone by heat conduction. All early designs, and modern ones for powers $P \lesssim 1\,\mathrm{kW}$, nearly always employ the classical scheme of a glow discharge in a tube (Fig. 14.2). Annular electrodes (so as not to interfere with the light beam) are placed in a long glass tube of radius $R \approx 1$–$3\,\mathrm{cm}$. For example, a mixture of $CO_2 : N_2 :$

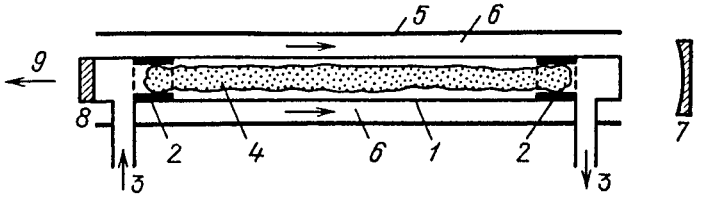

Fig. 14.2. Low-power diffusion-cooled CO_2 laser: *(1)* discharge tube, *(2)* ring electrodes, *(3)* slow pumping of laser mixture, *(4)* discharge plasma, *(5)* outer tube, *(6)* flow of water collant, *(7)* opaque mirror, *(8)* semitransparent output mirror, *(9)* output radiation

He = 1 : 1 : 8 can be employed at $p \approx 20$ Torr. In order to continuously refresh the mixture, the gas is slowly pumped through the tube: the discharge causes some molecules to dissociate, and undesirable by-products are formed. The heat flux from the discharge transfers heat to the tubes cooled by water flow. One of the mirrors (metallic) is placed outside the tube, the radiation reaching it through a salt window. The second mirror (semi-transparent) forms the window at the opposite end; it allows the exit of the beam and is made of NaCl, ZnSe, or GaAs [14.2].

To reduce the laser length at high power levels, when the tube length reaches tens of meters, the tube is broken into elbow-jointed sections with reflectors at the elbow points (Fig. 14.3a). Electric power is fed into the individual, not too long (meter-long) sections, otherwise voltage would have to be too high. Discharge parameters are typical of a noncontracted, *diffuse* positive columns: $n_e \approx 10^{10}\,\mathrm{cm}^{-3}$, $E/p \approx 2$–$4\,\mathrm{V/cm\,Torr}$, $j \approx 10\,\mathrm{mA/cm}^2$, $w \approx 0.5\,\mathrm{W/cm}^3$. Lasers of this type are reliable, robust, easy to operate, and are produced by industry in various versions of tens and hundreds of watts, up to a kilowatt (sometimes even higher).

Unfortunately the power output of this design can be increased only by increasing the tube length, to avoid the *unacceptable heating of the gas* by more than, say, $\Delta T \approx 200°$ C. The equality of energy release and heat removal rates, (8.24), gives

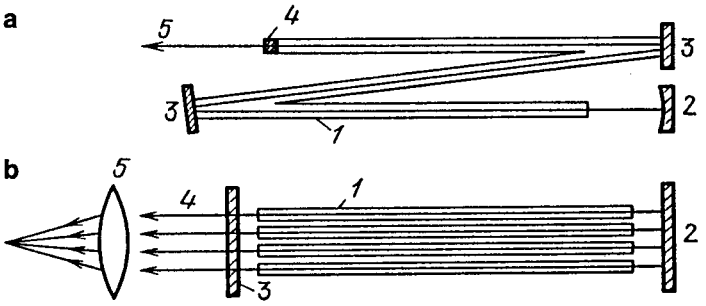

Fig. 14.3. Multiple-section laser tubes for powers of 1 kW and higher. (a) Series connection of tubes: *(1)* discharge tubes, *(2)* opaque mirror, *(3)* elbow mirrors, *(4)* semitransparent output mirror, *(5)* output beam. (b) Parallel connection of tubes in the optical resonator: *(1)* discharge tubes, *(2)* opaque mirror, *(3)* semitransparent output mirror, *(4)* output beams, *(5)* focusing lens

$$jE = Nc_{p1}\Delta T/\tau\ ,\quad \tau \approx \Lambda^2/\chi = Nc_{p1}\Lambda^2/\lambda\ , \tag{14.1}$$

where τ is, in this case, the heat-condution time for heat removal from the discharge region and $\Lambda_T \approx R/2.8$ (Sect. 8.7.1). Hence,

$$j\pi R^2 E = iE = (2.8)^2\pi\lambda\Delta T\ , \tag{14.2}$$

that is, a given ΔT is produced by a given power input per unit length of the tube, which is independent of both pressure [thermal conductivity $\lambda(p) \approx$ const] and tube radius R. It is thus impossible to increase the current arbitrarily by, for example, increasing R or to increase the voltage by increasing p : the result is overheating and the termination of lasing. One cannot input more than approximately 1 kW of electric energy per meter of tube, corresponding to an output of 70–100 W of radiation from the same length.

The principle of *diffusional cooling* found the another realization also [14.3]. A large number of small-diameter tubes are arranged into a compact bundle and "organized" into a resonator, not in series, but in parallel (Fig. 14.3b). The system consists of a large number of independent lasers, each with its own power supply but with common resonator and common cooling. The bundle of parallel light beams (in 37 [14.3])each carrying about 100 W of power can be focused by one large-diameter lens into a single focal spot, where the total power is concentrated. An industrial laser was designed on the basis of this model.

14.2.2 High-Flowrate Lasers with Convective Cooling

The time τ of heat removal from the discharge volume is effectively reduced by *intense pumping* of the gas through the discharge; this increases the density of energy release [see (14.1)] and hence increases the density of the radiative output of energy. Considerable success was achieved in this way in laser design, and *multi-kilowatt* lasers were developed with moderate size active regions. If the length of the discharge zone along the gas flow is L and the flow velocity is u, then $\tau \approx L/u$. For example, if $L = 30$ cm and $u = 100$ m/s, $\tau = 3 \times 10^{-3}$ s, while the diffusional heat removal at $p = 20$ Torr and $R = 3$ cm gives $\tau \approx 5 \times 10^{-2}$ s ($\chi \approx 30\,\text{cm}^2/\text{s}$).

The energy released per second in 1 g of a gas of density ϱ pumped through the discharge zone is jE/ϱ. In accordance with the first formula of (14.1), the temperature of the output gas increases in a time τ by ΔT. The temperature constraint imposes a limitation on the admissible *specific energy input* into the discharge, that is, on the amount of energy that can be deposited in 1 g of the gas, $q = P_E/Q$ J/g, where P_E (in W) is the power input into the discharge, $Q = \varrho u S$ g/s is the mass flowrate of the gas, and S is the cross-sectional area of the flow. The inequality $\Delta T < \Delta T_{\max}$ imposes limitations on the parameters of the system:

$$q = \frac{P_E}{Q} = \frac{jESL}{\varrho u S} = \frac{jE\tau}{\varrho} < \frac{c_p \Delta T_{\max}}{1-\eta} = q_{\max}\ . \tag{14.3}$$

Here we have introduced the efficiency $\eta = P/P_E$, because the radiated power P does not participate in the heating of the gas.

If $\eta \approx 15\,\%$, then $q_{max} \approx 700$–$800\,\mathrm{J/g}$. For instance, if we aim at a radiative output $P = 10\,\mathrm{kW}$, this requires the input $P_E = P/\eta \approx 70\,\mathrm{kW}$, demanding the flowrate $Q > P_E/q_{max} \approx 100\,\mathrm{g/s}$; a more realistic estimate is twice as high. One hour of work would need nearly a tonne of the laser mixture! Such high flowrates in high-power lasers designed for long-term operation make *closed cycling* unavoidable. The laser mixture circulates through the system, passing through the discharge chamber many times (Fig. 14.4). The gas is pumped through by compressors, pumps, and the like [14.1]. The system always includes a *heat exchanger,* in which the heat acquired in the discharge is removed from the gas. As with laser tubes, the mixture has to be gradually renewed.

The discharge chamber is often a *wide plane channel.* The field and current are either perpendicular to the flow (transverse discharge) or point along it (longitudinal discharge), as shown schematically in Fig. 8.1. A beam in a resonator is sent along the larger width of the channel at right angles to the gas flow and current. In order to collect energy from the maximum possible volume of the active medium and to make the resonator longer, the resonator is often made multi-pass (Fig. 14.5). The two end mirors form the resonator, while the intermediate (metal) mirrors send the beam back into the discharge zone. The

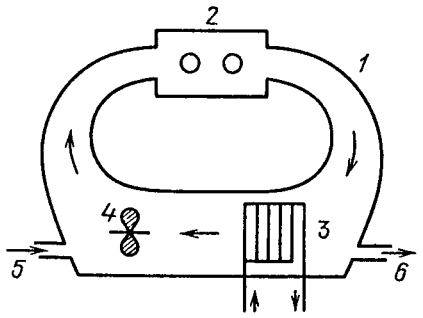

Fig. 14.4. High-flowrate, closed-cycle laser. *(1)* gas contour, *(2)* discharge chamber with resonator, *(3)* heat exchangeer, *(4)* ventilator, *(5)* fresh mixture inlet, *(6)* outlet for removing the used mixture

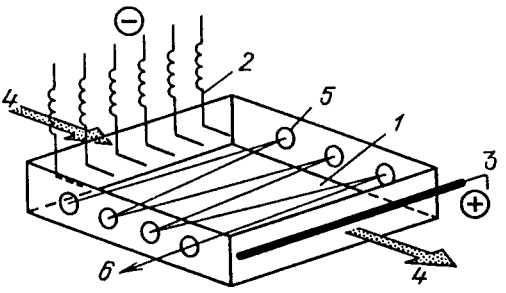

Fig. 14.5. Discharge chamber of a high-flowrate laser with longitudinal discharge pumping in which the multi-pass resonator is employed. *(1)* discharge channel, *(2)* cathode rods, connected to voltage source through individual ballast resistors (Sect. 14.3.2), *(3)* tube anode, *(4)* gas flow, *(5)* mirrors; one end mirror is semitransparent for output of laser beam *(6)* [14.4]

beam emerges either through a semitransparent mirror or through an annular window surrounding a metal mirror. Tube lasers with high-flowrate longitudinal gas pumping have become quite popular in recent years.

14.3 Methods of Suppressing Instabilities

14.3.1 The Problem of Reaching the Theoretical Limit of Energy Input

The problem of the energy input limit reaching is an acute one for high-flowrate lasers. The constraint (14.3) may be said to set a *theoretical limit* to the maximum current and electric power at a given pressure and mass flowrate of the gas. This limitation cannot be circumvented since the temperature of the gas cannot be appreciably increased. For a given time of flight $\tau = L/u$, the limiting energy input corresponds to pressure-independent maximum admissible electron and current densities. Indeed,

$$q \approx jE\tau/\varrho \propto n_e(E/p)^2\tau\ ,\quad j \propto n_e(E/p)\ , \tag{14.4}$$

and E/p is only weakly dependent on p. Numerically, for typical laser mixtures (say, 1 : 6 : 12) and for $\tau \approx 3 \times 10^{-3}$ s and $E/p \approx 8$ V cm Torr, the estimates are $n_{e,max} \approx 3 \times 10^{10}\,\mathrm{cm}^{-3}$, $j_{max} \approx 20\,\mathrm{mA/cm}^2$, and $w_{max} \approx 0.16p\,\mathrm{W/cm}^3$.

These values do not at first appear to be excessive: they are achieved in laboratory experiments time and again in discharges in tubes (generally in small volumes and at low pressures). However, the problem of reaching these levels in large volumes (channels about 100 cm wide 20–40 cm long in the flow direction, 5–10 cm high) at pressures of tens or even a hundred Torr, was found to be very difficult, and complex. As the current and power (j and w) are increased, the discharge becomes unstable long before the temperature limit (14.3) is reached, and develops inhomogeneities (Chap. 9). As a rule, *contraction* occurs (filamentation; see Fig. 14.6), which results in the complete termination of lasing. The *suppression of discharge instabilities* is the principal problem in developing high-power lasers. The buildup of instabilities is greatly stimulated by restricting the gas to a closed circuit, where instability-triggering products accumulate, and by the natural tendency to increase pressure.

Indeed, increasing the gas density is the obvious way to generate high power output and at the same time retain moderate overall dimensions of the unit. This is clear from (14.3) if we ask the question how can the flowrate $Q = \varrho uS$ be increased? Increasing the velocity above 200-250 m/s leads to considerable technical obstacles, and the cross section S is scaled up, all the dimensions increase. We are left with only one attractive approach: increase the density (pressure) and thereby make better use of the volume. The higher the pressure, however, the more easily the homogeneous discharge breaks down. Therefore, we will now discuss some methods of stabilizing the discharge and thus increasing the limiting current and power above which the discharge becomes unstable.

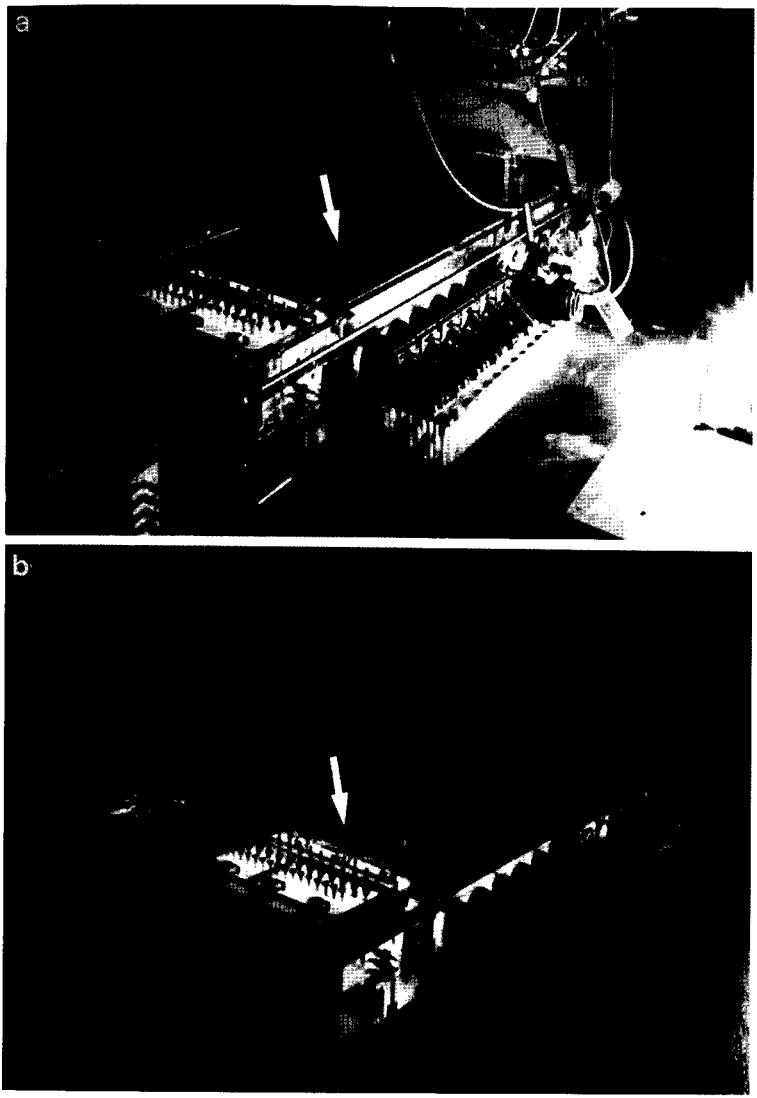

Fig. 14.6. Discharge in a large, high-flowrate closed-cycle laser (see Sect. 14.4.5). The upper plate covering the discharge channel is made of glass, allowing a good view of the discharge (shown by arrow). *Upper* photograph shows a discharge burning uniformly on the whole volume. *Lower* was taken at the moment of formation of current filaments (shown by arrow). Both the gas and the current flow in the direction of the bright columns [14.5]

14.3.2 Segmentation of the Cathode

When a current-conducting filament is formed between two points on large electrodes, the current jumps up, the voltage between the electrodes drops sharply [see (8.1)], and the field at other points becomes too low to sustain a steady discharge. This process can be partially prevented (and the discharge can there-

fore be somewhat stabilized) by segmenting the electrodes (in the particular cathode). The voltage is then applied to each segment independently through an individual ballast resistor. The resistors themseles have a stabilizing effect on the discharge, by suppressing the fluctuations of current. As a result, when a filament with enhanced current is formed on one of the cathodes, this does not lead to a catastrophic drop of voltage on other discharge paths leading to different cathode segments.

Segmented cathodes are employed in a number of systems. Another important point is that the normal current density at the cathode, j_n, is 10 to 100 times greater at elevated pressures than the admissible current density in the positive column. If the density in the column, according to the estimate of Sect. 14.3.1, is on the order of $10\,\mathrm{mA/cm^2}$, then at, say, $p = 40\,\mathrm{Torr}$, we have $j_n \approx 2 \times 10^{-4} p^2\,\mathrm{A/cm^2} \approx 300\,\mathrm{mA/cm^2}$. It is best to exploit cathodes in the regime on the border between the normal and abnormal, i.e., with complete coverage of the electrode area. This regime helps to stabilize the discharge owing to the rising $V - i$ characteristic of the abnormal cathode layer. Consequently, the cathode area has to be made much smaller than the current cross-sectional area in the main part of the discharge chamber. Hence to distribute the cathode surface more uniformly over the larger current cross section of the chamber, the cathode segments are often widely spread out.

In transverse discharges, the cathode segments are spread uniformly over the dielectric plate, "flush" to the surface, in order not to disturb the flow (Fig. 8.1a). In longitudinal discharges, a number of cathode rods are arranged at the entrance to the discharge channel (Fig. 8.1b). Their shapes and numbers are adjusted empirically. As a rule, segmented cathodes are placed at the inlet, upstream of the flow, since the most troublesome instabilities are those generated at the inlet, not those at the outlet, the latter being more rapidly carried away from the discharge zone.

14.3.3 Flow Control

Stabilization of the discharge is facilitated by making the velocity field, uniform especially in systems with a longitudinal discharge. The important point is the minimization of possible nonuniformities from which instability may later develop. An increase in velocity, that is, the reduction of the time of residence of a gas particle in the discharge zone, is generally a measure suppressing the evolution of instabilities, although an excessive flow velocity may result in the reverse [14.1, 2]. The creation of intensive *small-scale turbulence* has a favorable effect because it produces, as do diffusion and heat conduction, a damping of the incipient perturbations. The required turbulence scale and the design of turbulence-producers (rows of rods, grids, etc.) are empirically adjusted.

It must be said that when one attempts to stabilize the discharge and improve its characteristics, much is done on the basis of purely intuitive experimental study, not via a theoretically justified program. In this area experiment is clearly ahead of the theory, and the implementation of many ideas depends on the

experience, physical intuition, and skill of the experimenter, which in the most outstanding cases border on art. This is in fact typical of much work with gas discharges, which reveal a host of elusive and subtle properties.

14.3.4 Applications of Non-Self-Sustaining Discharges

Both the methods outlined above and some other techniques (typically used in combination) have given very positive results. An example is a 5 kW laser with a self-sustained transverse discharge (Sect. 14.4.1). A power output of 20 kW was achieved in a laser with a self-sustained longitudinal discharge by segmenting the electrode and using complex aerodynamic devices [14.6]. But the most revolutionary step was the application of a *non-self-sustaining discharge* for laser pumping, with a *beam of fast electrons* as an external ionizing agent (UV light can also be used for this purpose). This was first realized (1970) in pulsed CO_2 lasers and is now widespread in pulsed laser systems. In addition, considerable experience has already been gained in using electron beams in cw lasers [14.7, 8].

A non-self-sustained discharge has an advantage over a self-sustained discharge in that it allows us to break the chain of evolution of instability, (9.8), in the only link which permits such a termination. If the ionization is sustained by an external source which is immune (or nearly immune) to plasma processes, a change in ionization rate by "intrinsic" electrons due to a change in E/N becomes relatively unimportant. Indeed, the ionization by electrons accelerated in the field E is of minor importance. The most "dangerous" (namely, *thermal*) *instability* is thereby paralyzed.

When ionization is produced by an external source, n_e and the conductivity are determined by its intensity and are independent of the applied voltage. At a given intensity of the source and a given pressure, the current and energy deposition rate can be increased only by increasing the voltage applied to electrodes, that is, E/N. Once E/N gets close to the value corresponding to a self-sustaining discharge, the rate of ionization by discharge-produced electrons becomes comparable to that due to the external source and all factors leading to instability undergo a revival. The method thus has its limitations.

A non-self-sustaining discharge is also attractive because it separates the functions of sustaining ionization and of imparting to electrons the energy necessary for the efficient excitation of N_2 and 001-CO_2 vibrations. In self-sustaining discharges, both functions are served by the same applied field. In a non-self-sustaining discharge, the field serves only the latter function. Hence, the value of E/N can be optimized for laser pumping, while the power density $jE \propto n_e N(E/N)^2$ can be raised not by increasing voltage and E/N, but by increasing $p \propto N$. The limitation (14.3, 4) on heating and n_e still remains in force.

14.4 Organization of Large-Volume Discharges Involving Gas Pumping

14.4.1 Transverse Self-Sustaining Discharge

The most usual circuit for a transverse discharge is shown in Fig. 8.1a. A number of specially designed cathode segments (it may run into hundreds of elements) are connected to individual ballast resistors and installed above a common anode plate. The resultant ballast resistance must come to 20–30 % of the discharge resistance. Unfortunately, this fraction of electric power is then lost irretrievably. An expanding current stream starts at each cathode; all streams overlap at a distance of 1–2 cm, and the common plasma stretches to the anode.

Analysis demonstrates, however [14.1, 14.2, 14.9], that this common plasma of positive column is still not uniform, and that this is typical of electronegative gases under the conditions of short residence time of a particle in the discharge zone. Not enough active molecules accumulate in the plasma to detach electrons from negative ions. As a result, the balance of attachment and detachment is not set up. Electrons are lost on the way to the anode by attachment, and these losses are not compensated for either by ionization or by detachment. The conductivity decreases towards the anode, and the field increases correspondingly (since the current is constant). The situation in the anode region is reversed: the ionization rate in the enhanced field exceeds the rate of charge removal in the bulk, and an excess of positive ions is introduced into the plasma. In contrast to the classical model of the positive column, therefore, we find here no local balance of production and removal of electrons, so that the plasma column is not self-sustaining. The same is found for short longitudinal discharges, though the effect is absent in electropositive molecular gases, where the local balance is realized. Inhomogeneity transverse to the current (i.e. inhomogeneity along the flow) also exists: the temperature increases along the flow, the density decreases, and the field is reduced by a factor up to 1.5–2. The $V - i$ characteristic of this discharge is almost horizontal or slightly rising (in contrast to the falling one of the discharge in a tube without gas flow).

The discharge described above was thoroughly investigated, including the aspects of stability, formation of domains, and contraction, in [14.9]. This led to the development of the first series of closed-cycle high-flowrate commercial lasers manufactured in the USSR, which are now operating in a number of plants [14.10]. Some specifications of this laser model (using a three-pass resonator) are: power $P \approx 5$ kW, discharge length along the flow $L = 20$ cm, width $a = 90$ cm, channel height (the interelectrode spacing) $h = 4$ cm, $p \approx 50$ Torr, $u \approx 80$ m/s, the gas mixture ratio $CO_2 : N_2 : He = 1 : 20 : 20$, $w \approx 5.5$ W/cm^3, $q \approx 320$ J/q. The same principle was implemented in a 10 kW laser [14.1, 14.11] and newer, improved models are being developed.

14.4.2 Longitudinal Self-Sustained Discharge

The construction of such a laser is shown in Fig. 8.1b and also in Fig. 14.5, referred to earlier, which illustrates a multipass resonator [14.4]. High-flowrate pumping with a closed cycle is also used in tube designs similar to that of Fig. 14.3a. In a certain sense, this discharge can also be regarded as a longitudinal one. The same concept is utilized in the Soviet commercial 1.5 kW *Karat* laser [14.1, 14.12]. Industrial lasers manufactured by Spectra Physics employ a discharge arranged in an unusual way; these lasers have power of 1.2, 2.5, or 5 kW. The cathode is a tube at the entrance to a plane channel (like the anode in Fig. 14.5) and the anode lies on the bottom plane of the channel (as in Fig. 8.1a), being segmented into strips along the flow. The current is thus "curved," "transverse" at the anode and "longitudinal" at the cathode.

14.4.3 Non-Self-Sustained Discharge with Ionization by an Electron Beam

In this type of laser, a beam of electrons emitted by a hot metal surface and accelerated in a vacuum by a high voltage, $V_1 \sim 100\,\text{kV}$, is sent into the discharge chamber. The chamber is separated from the accelerator by a thin membrane (Fig. 14.7). Having traversed a grid electrode, the beam penetrates the gas. The voltage V_1 is so adjusted that the free path length of electrons at the pressure of the laser mixture is comparable with the distance to the other electrode. Then the electron energy eV_1 is used almost completely and the volume is ionized more uniformly. A dc current is passed through the electrodes and the ionized gas; the energy released by it providing the laser pumping. Fast electrons ionize the gas not so much in a direct way, but rather via secondary, slower electrons. If the excitation of electron states is taken into account, the average energy spent on forming one pair of ions is $\varepsilon_i \approx 50\,\text{eV}$.

Let us estimate the source of fast electrons needed to sustain the electron density n_e in a volume Ω of the active medium. Let S_1 electrons be produced per second in $1\,\text{cm}^3$; they are lost as a result of attachment and bulk recombination, with effective coefficient β_{eff} (Sect. 8.8). Under steady-state conditions, $S_1 = \beta_{\text{eff}} n_e^2$; if we ignore losses, the required source power is $p_e = \varepsilon_i S_1 \Omega = i_1 V_1$, where i_1 is the beam current. For example, if $n_e = 10^{11}\,\text{cm}^{-3}$, $\Omega = 10^3\,\text{cm}^3 = 1\,\text{liter}$, and $\beta_{\text{eff}} = 10^{-6}\,\text{cm}^3/\text{s}$, we find $S_1 = 10^{16}\,\text{cm}^{-3}\text{s}^{-1}$, $P_e \approx 80\,\text{W}$; if $V_1 = 100\,\text{kV}$, $i_1 = 0.8\,\text{mA}$.

The most important advantage of electron-beam ionization lasers lies in that the stability of the discharge permits their operation at about atmospheric pressures (pulsed lasers work at even higher pressures). The dimensions of the active zone are thus dramatically reduced. The power expenditure on maintaining ionization is negligible in comparison with the dc power P_E that can be injected into the volume for pumping. Thus for $p = 300\,\text{Torr}$ and the voltage producing the value of E/p favorable for pumping [$\approx 5\,\text{V/cm Torr}$], we have $P_E = \sigma E^2 \Omega \approx 75\,\text{kW}$ ($\sigma \approx 10^{-13} n_e/p\,\text{Ohm}^{-1}\text{cm}^{-1}$). Ten-kilowatt cw lasers have been developed and operated successfully with a closed cycle [14.7, 14.8]. Nevertheless, such systems have not become widespread, in contrast to pulsed

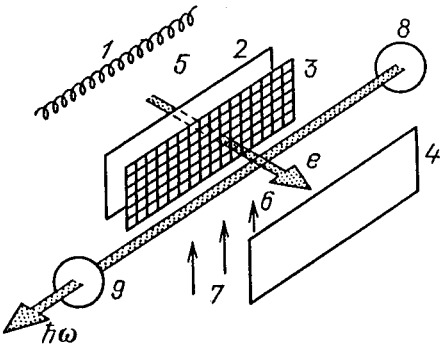

Fig. 14.7. Laser using ionizing electron beam: *(1)* emitter of electrons, *(2)* membrane separating the high-vacuum part *(5)* of the accelerator from the discharge chamber *(6)*, *(3)* grid electrode for non-self-sustained discharge, *(4)* second electrode, *(7)* direction of gas flow, *(8)* opaque mirror, *(9)* output mirror

lasers. The limitation stems from technical factors: constant use destroys the membranes, personnel have to be shielded from the laser because of the dangerous x-ray radiation, and so forth. There is, therefore, a stimulus for the continued search for alternative, more suitable methods of arranging a non-self-sustaining (or nearly so) type of discharge.

14.4.4 Combined Discharge with DC and RF Fields

A cw radiative power of 27 kW due to the input of 160 kW of electric power has been achieved in a large closed-cycle laser with a dc longitudinal discharge using a system employing an auxiliary capacitively coupled rf (ccrf) discharge [14.13]. The research preceding the development of this laser [14.14] and its successful outcome greatly stimulated the studies of ccrf discharge physics (Chap. 13). We shall now describe some parameters of this unity, whose basic form is shown in Fig. 14.8: $L = 53\,\text{cm}$, $a = 244\,\text{cm}$, $h = 6.3\,\text{cm}$, $u = 140\,\text{m/s}$; the gas ratio (CO_2 : N_2 : He) was 1 : 6.4 : 12.6 at $p = 30\,\text{Torr}$. Without the rf field only 60 kW (0.74 W/cm^3) could be supplied to the dc discharge. With the injection of 60 kW of rf power, the dc power could be raised to 100 kW, giving a total power of 160 kW (2 W/cm^3). Regarding this discharge as non-self-sustaining would be wrong: the rf and dc powers are comparable so that both fields (rather, their vector sum) serve both functions simultaneously (they ionize the gas and impart energy to electrons). However, no additional information on further developments in this field (or on the 20 kW laser [14.6]) has appeared in the literature. The system may have proved to be too complicated for general use.

14.4.5 Non-Self-Sustaining Discharge with Gas Ionization by Repeated Capacitively Coupled Pulses

This truly non-self-sustaining discharge was realized in a large closed-cycle laser [14.5]. The arrangement of the discharge device resembles that of Fig. 14.8. The essenital element is that the electrodes of the capacitor are installed within the discharge chamber; they are insulated from the plasma by thin heat-resistant glass (Fig. 14.9). This greatly increases the capacitance of the insulators and reduces the voltage across them, so that the ionizing field in the plasma is enhanced

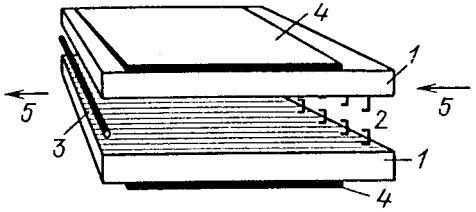

Fig. 14.8. High-flowrate laser with longitudinal dc discharge and auxiliary transverse ccrf discharge; *(1)* dielectric plates forming the discharge channel, *(2)* rows of cathode segments (360 of them), *(3)* anode (4 parallel tubes), *(4)* electrode plates for rf voltage, *(5)* direction of gas flow. Mirrors for multipass resonator, placed as indicated in Fig. 14.5, are not shown [14.13]

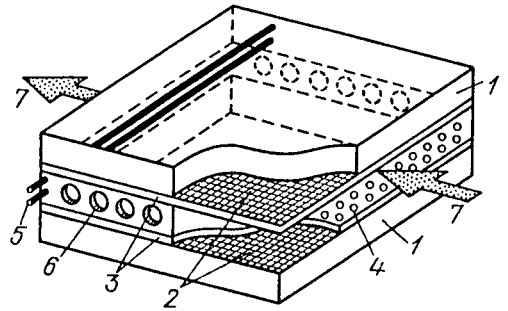

Fig. 14.9. High-flowrate laser of Fig. 14.6: *(1)* thick transparent glasses forming the channel, *(2)* metal grids to which high-voltage ionizing pulses are fed, *(3)* thin heat-resistant insulating glasses, *(4)* cathode segments (50 of them), *(5)* two anode tubes, *(6)* cavities for installing the mirrors of the multipass resonator. *Arrows* show the direction of gas flow [14.5]

(Sect. 13.2; Fig. 13.3). The discharge chamber volume is 27 liters: $L = 63\,\text{cm}$, $a = 76\,\text{cm}$, $h = 5.5\,\text{cm}$, the flow velocity $u \leq 230\,\text{m/s}$. Pulses of about $10^{-7}\,\text{s}$ duration at a voltage of about 15 kV are fed to the capacitor plates at frequencies up to 100 kHz. They sustain an extremely uniform plasma in the volume at $n_e \approx 10^{10}\,\text{cm}^{-3}$. The pulse duty factor is sufficiently low for the average power not to be high, about 1 kW. At the same time, the plasma hardly decays during the $10^{-5}\,\text{s}$ between pulses. This cc-type electrodeless discharge is in itself completely *self-sustained*, and its electrical processes have common features with ccrf discharge [14.5, 14.15].

The high power consumed for laser pumping is introduced by the longitudinal dc field, and the $V - i$ curve of dc current is almost linear (Fig. 14.10) because n_e and the plasma resistance are determined by an external ionizer and are almost independent of the dc voltage.[2] This picture holds as long as the current is much lower than the self-sustaining value. On approach to self-sustainment, the discharge undergoes filamentation. The photographs of Fig. 14.6 were taken in

[2] Cf Fig. 8.22 for the characteristics of a self-sustaining discharge in the same setup. The $V - i$ characteristic is horizontal and independent of velocity.

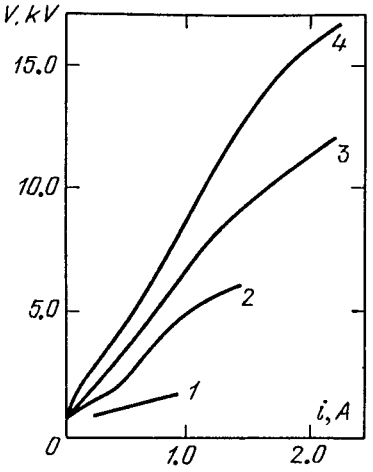

Fig. 14.10. $V - i$ characteristic of non-self-sustaining dc discharge in the apparatus of Fig. 14.9, with ionizing pulse frequency 100 kHz; laser mixture CO_2 :N_2 :He= 1 : 7 : 12; p = 30 Torr. *(1)* zero flow velocity, *(2)* u = 60 m/s, *(3)* 130 m/s, *(4)* 220 m/s [14.5]

the apparatus described above. The realization of an external ionizer producing repeated pulses made it possible to scale up the dc power by more than an order of magnitude, raising it to $P_E \approx 70$ kW (2.6 W/cm^3) at p = 50 Torr in the 1 : 6 : 12 mixture and achieving the output P = 6 kW of beam power (reaching as high as 10 kW in the improved model of this laser). A compact combined-ionization industrial laser has been developed utilizing the arrangement outlined above [14.16]. It can operate both in the cw and in the pulsed regimes, generating light pulses at a frequency up to 250 Hz. This last regime is useful for welding, and makes it possible to punch numerous small holes, etc.[3]

Note that high-voltage pulses separated by relatively long gaps sustain the same inization under the same conditions at much lower average power than the rf field ($n_e \approx 10^{10}$ cm^{-3} at 0.05 W/cm^3 and 1.4 W/cm^3, respectively). Owing to the steep dependence of ionization frequency on field, it is sufficient to raise the field by a factor of 2–3 in order to reduce the time of its application and the power required tens of times without reducing the number of electrons produced. As a result, pulses at a well-chosen frequency and duty factor ionize the gas much more efficiently than the nearly non-stop sinusoidal field in which the ionization occurs only within short intervals around the maximum value of the field. Obviously, the high rf power is not lost in the laser, being spent on laser pumping, just as dc energy is. But it is more difficult to inject nearly a hundred kilowatts of rf power into the discharge than the same wattage of dc power. This is the advantage of combining a high-power, non-self-sustaining dc discharge current with low-power ionizing pulses, instead of using a comparable high-power, self-sustaining ccrf discharge, if the latter is arranged. On the mechanism of discharge stabilization by pulses and rf fields, see Sect. 9.4.4 and [14.7].

[3] One need to say that in the latest laser structures with longitudinal discharge the stability is reached in the other way avoiding cathode segmentation which introduces some technical complications.

14.4.6 AC Discharge

By ac discharge we mean the electrode or electrodeless capacitively coupled discharge at a frequency $f \leq 10\,\text{kHz}$. Low frequencies up to 10 kHz have an important advantage in comparison with rf: they are produced by generator systems which are simpler, cheaper, and more reliable than high-power rf oscillators. Compared with dc power, low frequencies have the same important advantage that rf has: the discharge can be stabilized using reactive (capacitive) ballast elements in which Joule heat is not released and power is not lost. An ac discharge possesses the stabilization qualities of a non-self-sustaining discharge but at the same time requires no auxiliary ionization source. The same power source serves both ionization and laser pumping, but these two functions are separated in time. Electrons are produced in short bursts at the moments when the ionizing field nears its amplitude values, while the rest of the time energy is pumped into the plasma at the recombination stage when it is not subject any more to thermal instability.

The advisability of utilizing the ac discharge in CO_2 lasers was first pointed out in [14.18], which started a detailed analysis of this process. It occupies an intermediate position between dc and rf discharges. Regardless of whether the electrodes are bare or insulated, breakdown must take place at each of them in the appropriate half-period, and the cathode layer must be formed. A low-frequency, and hence weak, displacement current is too small to close the circuit at the electrode. In this respect the discharge resembles the *high-current* (i.e. γ) ccrf discharge mode. The ac discharge can also be employed in high-flowrate lasers and in diffusion-cooled tube lasers. The latter version being better investigated has received more attention, a multi-channel ac laser has been developed [14.1, 14.2] whose design resembles that of Fig. 14.3b, but the electrodes are placed outside the tubes: the resulting simplification is considerable, allowing the use of very narrow tubes (only 5 mm in diameter). A meter-long laser of overall diameter 7.5 cm encloses 61 tubes and has an output of 1.2 kW of radiative power. The ballast elements are the capacitances of the glass areas under the electrodes. An industrial laser has been developed, based on this model.

14.4.7 Self-Sustaining CCRF Discharge

The ccrf discharge has a number of advantages over both dc and ac discharges: It is more stable than the dc discharge, and allows a greater energy input. Ballast resistances, which always produce a favorable effect on discharge stability, can be replaced by reactive (capacitive) elements; this eliminates energy losses which come to about 30 % of electrical power in ordinary ballast resistors. Obviously, rf discharges are not better than low-frequency discharges in this respect, since capacitive ballast is utilized in both cases. One of the essential advantages of the ccrf discharge is the possibility of *eliminating cathode layers*, which are inherent in both dc and ac discharge currents: Firstly, some electrical energy is lost in the cathode layers, and secondly, this is the place where perturbations – the seeds of instability – are born. In this respect the *weak-current* (i.e. α) *mode* of the

ccrf discharge, in which the plasma current is coupled to the electrodes only by displacement currents (Chap. 13), corresponding to the absence of cathode layers, is more favorable for lasers. This is a drawback because it implies a limitation on current density and, in fact, on gap length and pressure (Sects. 13.4, 9).

Another advantage of ccrf discharges (actually, it also characterizes capacitively coupled low-frequency discharges) is the practical convenience of working with long tubes. Discharges with high-flowrate and axial pumping of gas have high stability and homogeneity. The latter factor is very important for the quality of radiation. As in tube lasers, a constant longitudinal field calls for voltages of tens of kV. If, however, a dielectric tube is placed between two strip electrodes (so-called strip-line design), very moderate rf voltages of about 1 kV (or even less) become sufficient. The intensity of radiation is easily modulated by modulating the applied rf voltage.

A ccrf discharge has been successfully utilized in low-power lasers.[4] it is especially convenient in small waveguide systems. Electrodes are placed above and below a tube of square cross-section (about $2 \times 2\,\text{mm}^2$ [14.21]). A considerable number of publications have appeared in recent years on CO_2 lasers utilizing ccrf discharges: Some ccrf CO_2 lasers of 1 kW (and higher) power have been reported [14.22, 14.23], and several systems of this type were mentioned in [14.24–26]. It has been claimed that a new generation of industrial CO_2 lasers (ccrf systems) that are more compact, light, simple in design, and more convenient than the preceding generation of dc lasers, has been developed recently [14.27]. At any rate, several firms already manufacture ccrf CO_2 lasers of power 1 kW and higher. A compact waveguide slit CO_2 laser of medium power of 100 to 200 W [14.28] is also very efficient; the rf discharge is excited in it not in a tube but in a zigzag extended slit. Considerable expectations are associated with the rf approach in laser design.

The detailed consideration of the CO_2 lasers with rf pumping (physical principles, slit and other devices, principles of the parameter choice and optimization) are presented in the new book (see Further Reading [1]).

[4] For information on one of the first ccrf CO_2 lasers, see [14.20].

Appendix

Selected formulas, constants, and relations between units that are frequently encountered and often used in gas discharge physics.

Fundamental Constants

Velocity of light	$c = 2.998 \cdot 10^{10}$ cm/s
Planck's constant	$h = 6.625 \cdot 10^{-27}$ erg·s
	$\hbar = h/2\pi = 1.054 \cdot 10^{-27}$ erg·s
Electron charge	$e = 4.802 \cdot 10^{-10}\,\mathrm{g}^{1/2} \cdot \mathrm{cm}^{3/2}/\mathrm{s}$
Electron mass	$m = 9.109 \cdot 10^{-28}$ g
Proton mass	$M_p = 1.672 \cdot 10^{-24}$ g
Atomic mass unit	$M_0 = 1.660 \cdot 10^{-24}$ g
Boltzmann's constant	$k = 1.380 \cdot 10^{-16}$ erg/K
Universal gas constant	$R = 8.314 \cdot 10^{7}$ erg/K·mole $= 1.986$ cal/K·mole
Avogadro's number	$N = 6.023 \cdot 10^{23}$ 1/mole

Atomic Constants

Bohr radius $a_0 = h^2/4\pi^2 me^2 = \hbar^2/me^2 = 0.529 \cdot 10^{-8}$ cm

Ionization potential of the hydrogen atom

$$I_H = e^2/2a_0 = 2\pi^2 e^4 m/h^2 = e^4 m/2\hbar^2 = 13.60\,\mathrm{eV}$$

Rydberg constant

$$\mathrm{Ry} = I_H/h = 2\pi^2 e^4 m/h^3 = 3.290 \cdot 10^{15}\,\mathrm{s}^{-1}$$

Electron velocity in the first Bohr orbit

$$v_0 = 2\pi e^2/h = e^2/\hbar = 2.187 \cdot 10^{8}\,\mathrm{cm/s}$$

Classical electron radius $r_0 = e^2/mc^2 = 2.818 \cdot 10^{-13}$ cm

Compton wavelength $\lambda_0 = h/mc = 2.426 \cdot 10^{-10}$ cm

$\lambda\!\!\!^{-}_0 = \lambda/2\pi = \hbar/mc = 3.862 \cdot 10^{-11}$ cm

Electron rest energy	$mc^2 = 511\,\text{keV} = 8.185 \cdot 10^{-7}\,\text{erg}$
Fine structure constant	$\hbar c/e^2 = 137.0$
Thomson cross section	$\Phi = 8\pi r_0^2/3 = 6.65 \cdot 10^{-25}\,\text{cm}^2$
Ratio of proton to electron masses	$M_\text{p}/m = 1836$
Electric field due to the nucleus at the first Bohr orbit	$e/a_0^2 = 5.14 \cdot 10^9\,\text{V/cm}$
Area of spectral line with unit oscillator strength	$\pi e^2/mc = 2.65 \cdot 10^{-2}\,\text{cm}^2\text{s}^{-1}$
Atomic unit of cross section (area of first Bohr orbit)	$\pi a_0^2 = 0.880 \cdot 10^{-16}\,\text{cm}^2$

Formulas

Radiation flux from a blackbody surface at temperature T

$$S = \sigma T^4 = 5.67 \cdot 10^{-5}\{T[\text{K}]\}^4 = 1.03 \cdot 10^{12}\{T[\text{eV}]\}^4\,\text{erg/cm}^2\text{s}\,.$$

Spectral intensity of equilibrium radiation

$$I_{\nu,\text{eq}}d\nu = cU_{\nu,\text{eq}}d\nu/4\pi = 2h\nu^3c^{-2}\left[\exp(h\nu/kT) - 1\right]^{-1}d\nu$$

$$\text{erg/(cm}^2\text{s} \cdot \text{sr)}\ \ (\text{maximum at } h\nu = 2.822kT)\,.$$

Saha's formula relating equilibrium densities of electrons, n_e, ions, n_+, and neutral atoms, N

$$\frac{n_\text{e}n_+}{N} = A\frac{g_+}{g_\text{a}}T^{3/2}\exp(-I/kT)\,,$$

$$A = 2\left(\frac{2\pi mk}{h}\right)^{3/2} = 4.85 \cdot 10^{15}\,\text{cm}^{-3}\text{K}^{-3/2} = 6.06 \cdot 10^{21}\,\text{cm}^{-3}\text{eV}^{-3/2}\,,$$

n is in cm^{-3}, g_+ and g_a are statistical weights.

Maxwell distribution function normalized to unity

$$f(v_x, v_y, v_z)dv_xdv_ydv_z = \left(\frac{m}{2\pi kT}\right)^{3/2}\exp\left[-\frac{m(v_x^2 + v_y^2 + v_z^2)}{2kT}\right]dv_xdv_ydv_z$$

$$\varphi(v)\,dv = 4\pi\left(\frac{m}{2\pi kT}\right)^{3/2}\exp(-mv^2/2kT)v^2dv$$

$$n(\varepsilon)\,d\varepsilon = \frac{2}{\sqrt{\pi}}\frac{\sqrt{\varepsilon}}{(kT)^{3/2}}\exp(-\varepsilon/kT)\,d\varepsilon$$

Velocity of an electron with energy ε : $v_e = 5.93 \cdot 10^7 \sqrt{\varepsilon\,[\mathrm{eV}]}$ cm/s.

Velocity of a particle with relative atomic mass A

$$v = 1.38 \cdot 10^6 \sqrt{\varepsilon[\mathrm{eV}]/A}\,\mathrm{cm/s}$$

Mean thermal velocity of an electron

$$\bar{v}_e = (8kT/\pi m)^{1/2} = 6.21 \cdot 10^5 \sqrt{T\,[\mathrm{K}]} = 6.71 \cdot 10^7 \sqrt{T\,[\mathrm{eV}]}\,\mathrm{cm/s}$$

Mean thermal velocity of a particle with relative atomic mass A

$$\bar{v} = 1.45 \cdot 10^4 \sqrt{T\,[\mathrm{K}]/A} = 1.56 \cdot 10^6 \sqrt{T\,[\mathrm{eV}]/A}\,\mathrm{cm/s}$$

Effective cross section σ in terms of the mean number of collisions P per 1 cm path at 1 mm Hg and 0° C

$$\sigma = 2.83 \cdot 10^{-17}\, P\,\mathrm{cm}^2\,, \quad P = 3.53 \cdot 10^{16} \sigma\,\mathrm{cm}^{-1}\mathrm{Torr}^{-1}$$

Debye radius

$$d = \left(\frac{kT_e}{4\pi e^2 n_e}\right)^{1/2} = 6.88 \left\{\frac{T_e[\mathrm{K}]}{n_e}\right\}^{1/2} = 742 \left\{\frac{T_e[\mathrm{eV}]}{n_e}\right\}^{1/2} \mathrm{cm}$$

Plasma frequency

$$\omega_p = \left(\frac{4\pi e^2 n_e}{m}\right)^{1/2} = 5.65 \cdot 10^4 \sqrt{n_e}\,\mathrm{s}^{-1}$$

Critical electron density for electromagnetic wave of frequency $\omega = 2\pi f$ (λ is wavelength)

$$n_{cr} = m\omega^2/4\pi e^2 = 1.24 \cdot 10^4 \{f[\mathrm{MHz}]\}^2\ \mathrm{cm}^{-3} = 1.11 \cdot 10^{13} \{\lambda[\mathrm{cm}]\}^{-2}\ \mathrm{cm}^{-3}$$

The factor in the electrostatics equation $\mathrm{div}\, \boldsymbol{E} = 4\pi e(n_+ - n_e)$:

$$4\pi e = 1.81 \cdot 10^{-6}\,\mathrm{V \cdot cm}\,, \quad e = 1.44 \cdot 10^{-7}\,\mathrm{V \cdot cm}$$

Electronic conductivity of an ionized gas for a current of frequency ω (ν_m is the collision frequency of electrons for momentum transfer)

$$\sigma = \frac{e^2 n_e \nu_m}{m(\omega^2 + \nu_m^2)} = 2.53 \cdot 10^8 n_e \frac{\nu_m}{\omega^2 + \nu_m^2}\,\mathrm{s}^{-1} = 2.82 \cdot 10^{-4} n_e \frac{\nu_m}{\omega^2 + \nu_m^2}$$

$$\mathrm{Ohm}^{-1}\mathrm{cm}^{-1}\,, \quad \nu_m[\mathrm{s}^{-1}]\,, \quad \omega[\mathrm{s}^{-1}]$$

Dielectric permittivity of an ionized gas

$$\varepsilon = 1 - \frac{4\pi e^2 n_e}{m(\omega^2 + \nu_m^2)} = 1 - \frac{\omega_p}{\omega^2 + \nu_m^2}$$

Electromagnetic wave absorption coefficient in an ionized gas

$$\mu_\omega = \frac{4\pi e^2 n_e \nu_m}{mc(\omega^2 + \nu_m^2)} = \frac{4\pi\sigma}{c} = 0.106 n_e \frac{\nu_m}{\omega^2 + \nu_m^2}\ \text{cm}^{-1}$$

The rate of electron energy increase in an oscillating field considering only elastic collisions with atoms of mass M ($E = E_a/\sqrt{2}$ where E_a is amplitude)

$$\frac{d\varepsilon}{dt} = (\Delta\varepsilon_E - \Delta\varepsilon_{el})\,\nu_m = \left[\frac{e^2E^2}{m(\omega^2 + \nu_m^2)} - \frac{2m}{M}\varepsilon\right]\nu_m$$

Electron energy acquired from the field in one collision

$$\Delta\varepsilon_E = \frac{e^2E^2}{m(\omega^2 + \nu_m^2)} = \frac{1.75 \cdot 10^{15}\{E[\text{V/cm}]\}^2}{\omega^2 + \nu_m^2} = \frac{6.34 \cdot 10^{17} S[\text{W/cm}^2]}{\omega^2 + \nu_m^2}\ \text{eV}$$

Electron mobility

$$\mu_e = \frac{e}{m\nu_m} = \frac{1.76 \cdot 10^{15}}{\nu_m}\ \text{cm}^2/(\text{s} \cdot \text{V})$$

Skin layer thickness

$$\delta = \frac{c}{\sqrt{2\pi\sigma\omega}} = \frac{5.03}{\{\sigma[\text{Ohm}^{-1}\text{cm}^{-1}] f[\text{MHz}]\}^{1/2}}\ \text{cm}$$

Flux of rf energy into a conductor placed inside a solenoid coil (H_a and i_a are amplitudes, σ is conductivity, n is turns number per cm)

$$S = \frac{cH_a^2}{16\pi}\left(\frac{\omega}{2\pi\sigma}\right)^{1/2} = 9.94 \cdot 10^{-2}\{i_a n[\text{A} \cdot \text{t/cm}]\}^2 \left\{\frac{f[\text{MHz}]}{\sigma[\text{Ohm}^{-1}\text{cm}^{-1}]}\right\}^{1/2} \frac{\text{W}}{\text{cm}^2}$$

Magnetic field inside a solenoid coil

$$H = (4\pi/c)in = 1.26in[\text{A} \cdot \text{t/cm}]\ \text{Oe}$$

Characteristic diffusion length Λ determining the diffusion loss "frequency" $\nu_d = D/\Lambda^2$

$$\frac{1}{\Lambda^2} = \left(\frac{2.4}{R}\right)^2 + \left(\frac{\pi}{L}\right)^2 \quad \text{– cylinder of radius } R \text{ and length } L$$

$$\frac{1}{\Lambda^2} = \left(\frac{\pi}{L_1}\right)^2 + \left(\frac{\pi}{L_2}\right)^2 + \left(\frac{\pi}{L_3}\right)^2 \quad \text{– parallelepiped with sides } L_1,\ L_2, \text{ and } L_3$$

$$\frac{1}{\Lambda^2} = \left(\frac{\pi}{R}\right)^2,\ \Lambda = \frac{R}{\pi} \quad \text{– sphere of radius } R$$

Ambipolar diffusion coefficient at $T_e \gg T$

$$D_a = \mu_+ \left[\mathrm{cm}^2/(\mathrm{s}\cdot\mathrm{V})\right] T_e[\mathrm{eV}]\,\mathrm{cm}^2/\mathrm{s}$$

Rms field of a wave in vacuum, $E = 19\sqrt{S[\mathrm{W/cm}^2]}\,\mathrm{V/cm}$.

Frequency of ionization by electron impact, for the Maxwell spectrum and for the cross section being a linear function of ε at the ionization threshold I, $\sigma = C(\varepsilon - I)$:

$$\nu_i = C(I + 2kT)\bar{v}_e N \exp(-I/kT) \approx 2.2\cdot 10^7 \left\{C\,[\mathrm{cm}^2/\mathrm{eV}]\cdot 10^{17}\right\} \times \{T\,[\mathrm{eV}]\}^{1/2} I[\mathrm{eV}]\, p[\mathrm{Torr}] \exp(-I/kT)\,\mathrm{s}^{-1}$$

Relations Between Units

Energy in Electron Volts

The energy $\varepsilon = 1\,\mathrm{eV} = 1.602\cdot 10^{-12}\,\mathrm{erg}$ corresponds to

temperature $\varepsilon/k = 11,610\,\mathrm{K}$,

frequency $\varepsilon/h = 2.418\cdot 10^{14}\,\mathrm{s}^{-1}$,

wavelength $hc/\varepsilon = 1.240\cdot 10^{-4}\,\mathrm{cm} = 12,400\,\text{Å}$;

wave number $\varepsilon/hc = 8067\,\mathrm{cm}^{-1}$;

1 eV per molecule corresponds to $23.05\,\mathrm{kcal/mol} = 9.65\cdot 10^{11}/\mu\,[\mathrm{erg/g}] = 96.5/\mu\,[\mathrm{kJ/g}]$ (μ is the relative molecular mass).

Electric Units

Charge: $1\,\mathrm{C} = 3\cdot 10^9$ CGSE units $= 6.25\cdot 10^{18}$ electron charges $= 9\cdot 10^{11}\,\mathrm{V\cdot cm}$

Electron charge: $e = 1.6\cdot 10^{-19}\,\mathrm{C} = 1.44\cdot 10^{-7}\,\mathrm{V\cdot cm}$ (in the formula $E = e/r^2$)

Current: $1\,\mathrm{A} = 1\,\mathrm{C/s} = 3\cdot 10^9$ CGSE $= 6.25\cdot 10^{18}$ electron charges per second $= 9\cdot 10^{11}\,\mathrm{V\cdot cm/s}$

Voltage: $1\,\mathrm{V} = 1/300$ CGSE

Electric field strength: $E\,[\mathrm{V/cm}] = 300E$ [CGSE].

Resistance: $1\,\mathrm{Ohm} = 1/(9\cdot 10^{11})$ CGSE $= 1/30c$, $1/c = 30\,\mathrm{Ohm}$

Conductivity: $\sigma\,[\mathrm{Ohm}^{-1}\mathrm{cm}^{-1}] = 1/(9\cdot 10^{11})\sigma\,[\mathrm{s}^{-1}]$, $\sigma\,[\mathrm{s}^{-1}] = 9\cdot 10^{11}\sigma\,[\mathrm{Ohm}^{-1}\mathrm{cm}^{-1}]$

Capacitance: 1 Farad $= 9\cdot 10^{11}$ CGSE (cm), 1 picofarad (pF) $= 0.9\,\mathrm{cm}$

Inductance: 1 Henry $= 10^9$ CGSE (cm); $1\,\mu\mathrm{H} = 1000\,\mathrm{cm}$

Magnetic field strength: 1 Oersted = 1 CGSE

Energy: 1 Joule $= 10^7$ CGSE (erg)

Power: 1 Watt $= 10^7$ CGSE (erg/s)

Barometric Units and Corresponding Relations

Normal atmospheric pressure: 1 atm = $1.013 \cdot 10^6$ dyne/cm^2 or erg/cm^3

At 0° C, 1 atm = 760 mm Hg = 760 Torr = $1.013 \cdot 10^5$ Pascal $\approx$ 0.1 MPa. 1 Torr = 133.3 Pa, 1 kPa = 7.5 Torr

The number of molecules in 1 cm^3 at 0° C at 1 atm (Loschmidt's number): $2.687 \cdot 10^{19}$ cm^{-3}

The number of molecules in 1 cm^3 at 20° C (room temperature) and 1 Torr: $3.295 \cdot 10^{16}$ cm^{-3}

$$E/p\,[\mathrm{V/cm \cdot Torr}] = 3.30 \cdot 10^{16} E/N\,[\mathrm{V \cdot cm^2}] = 0.33 E/N\,[\mathrm{Td}]$$

$$E/N\,[\mathrm{V \cdot cm^2}] = 3.03 \cdot 10^{-17} E/p\,[\mathrm{V/cm \cdot Torr}] = 10^{-17} E/N\,[\mathrm{Td}]$$

The unit for E/N : 1 Townsend (Td) = 10^{-17} V·cm^2

References

Chapter 1

1.1 A. von Engel, M. Steenbeck: *Elektrische Gasentladungen. Ihre Physik und Technik*, Vol. II (Springer, Berlin 1934)
1.2 L.B. Loeb: *Basic Processes of Gaseous Electronis* (University of California Press, Berkeley CA 1960)
1.3 N.A. Kaptsov: *Electrical Phenomena in Gases and in Vacuum* (Gostekhizdat, Moscow 1950)
1.4 A. von Engel: *Ionized Gases* (Clarendon, Oxford 1965)
1.5 S.C. Brown: *Basic Data of Plasma Physics* (MIT Press, Cambridge MA 1959)
1.6 G. Francis: *Ionization Phenomena in Gases* (Butterworths, London 1960)
1.7 V.L. Granovsky: *Electric Current in Gas (Steady Current)* (Nauka, Moscow 1971)
1.8 Yu.P. Raizer: *Fundamentals of Modern Physics of Gas Discharge Processes* (Nauka, Moscow 1980)
1.9 A.M. Howatson: *An Introduction to Gas Discharges* (Pergamon, Oxford 1976)
1.10 B.E. Cherrington: *Gaseous Electronics and Gas Lasers* (Pergamon, Oxford 1982)
1.11 Yu.P. Raizer: *Physics of Gas Discharges* (Nauka, Moscow 1987) (in Russian)
1.12 Ya.B. Zel'dovich, Yu.P. Raizer: *Physics of Shock Waves and High-Temperature Hydrodynamic Phenomena* (Academic, New York 1966)
1.13 L.M. Biberman, V.S. Vorobyev, I.T. Yakubov: *Kinetics of Nonequilibrium Low-Temperature Plasma* (Plenum, New York 1987)
1.14 M.N. Hirsh, H.J. Oskam (eds.): *Gaseous Electronics*, Vol. 1, *Electrical Discharges* (Academic, New York 1978)
1.15 E. Kunhardt, L. Luessen (eds.): *Electrical Breakdown and Discharges in Gases* (Plenum, New York 1983)
1.16 J. Dutton: *A Survey of Electron Swarm Data*, J. Phys. Chem. Ref. Data **4** (1975) No. 3, pp. 577–856 (Handbook on electron processes in plasma)
1.17 M. Mitchner, C.H. Kruger: *Partially Ionized Gases* (Wiley, New York 1973)
1.18 L.A. Artsimovich, R.Z. Sagdeev: *Plasma Physics for Physicists* (Atomizdat, Moscow 1979)
1.19 V.E. Golant, A.P. Zhilinsky, S.A. Sakharov: *Fundamentals of Plasma Physics* (Wiley, New York 1979)

Chapter 2

2.1 S.C. Brown: *Basic Data of Plasma Physics* (MIT Press, Cambridge MA 1959)
2.2 A.D. MacDonald: *Microwave Breakdown in Gases* (Wiley, New York 1966)
2.3 R.B. Brode: Rev. Mod. Phys. **5**, 257 (1933)
2.4 E.W. McDaniel: *Collision Phenomena in Ionized Gases* (Wiley, New York 1964)
2.5 R.A. Nielsen: Phys. Rev. **50**, 950 (1936)
2.6 R.A. Nielsen, L. Colldi: Rev. Sci. Instr. **23**, 39 (1952)
2.7 R.A. Nielsen, N.E. Bradbury: Phys. Rev. **51**, 69 (1937)
2.8 L. Spitzer: *Physics of Fully Ionized Gases* (Wiley, New York 1962)

2.9 J.E. Allen, P.C. Stangeby: J. Phys. D: Appl. Phys. **6**, 224 (1973)
2.10 J. Dutton: *A Survey of Electron Swarm Data*, J. Phys. Chem. Ref. Data **4** (1975) No. 3, pp. 577–856
2.11 R.W. Crompton, L.C. Huxley, D.J. Sutton: Proc. Roy. Soc. **A 218**, 507 (1953); R.W. Crompton, D.J. Sutton: Proc. Roy. Soc. **A 215**, 467 (1952)
2.12 J.H. Parker, J.J. Lowke: Phys. Rev. **181**, 290, 302 (1969)
2.13 E.D. Lozansky, O.B. Firsov: *Theory of Sparks* (Atomizdat, Moscow 1975)
2.14 W.H. Cramer, J.H. Simons: J. Chem. Phys. **26**, 1272 (1957)
2.15 W.H. Cramer: J. Chem. Phys. **28**, 688 (1958); **30**, 641 (1959)
2.16 M.A. Biondi, L.M. Chanin: Phys. Rev. **94**, 910 (1954)
2.17 J.A. Hornbeck: Phys. Rev. **84**, 615 (1951)
2.18 A.D. Barkalov, A.A. Samokhin: Preprint IAE No. 4147/6 (1985)
2.19 A.M. Soroka, G.I. Shapiro: Pisma Zh. Tekh. Fiz. **5**, 129 (1979)
2.20 Ya.B. Zel'dovich, Yu.P. Raizer: *Physics of Shock Waves and High-Temperature Hydrodynamic Phenomena* (Academic, New York 1966)

Chapter 3

3.1 Yu.P. Raizer: *Laser-Induced Discharge Phenomena* (Consultants Bureau, New York 1977)

Chapter 4

4.1 J.B. Hasted: *Physics of Atomic Collisions* (Butterworths, London 1964)
4.2 E.D. Lozansky, O.B. Firsov: *Theory of Sparks* (Atomizdat, Moscow 1975)
4.3 A. von Engel: *Handbuch der Physik* Bd. 21 (Springer, Berlin 1956)
4.4 A.L. Ward: J. Appl. Phys. **33**, 2789 (1962)
4.5 A. von Engel: *Ionized Gases* (Clarendon, Oxford 1965)
4.6 D.R. Long, R. Geballe: Phys. Rev. **A 1**, 260 (1970)
4.7 L. Vriens: Phys. Lett. **8**, 260 (1964)
4.8 B.M. Smirnov: *Ions and Excited Atoms in Plasma* (Atomizdat, Moscow 1974)
4.9 Ya.B. Zel'dovich, Yu.P. Raizer: *Physics of Shock Waves and High-Temperature Hydrodynamic Phenomena* (Academic, New York 1966)
4.10 G.J. Schulz: Phys. Rev. **128**, 178 (1962)
4.11 C.E. Melton: J. Chem. Phys. **57**, 4218 (1972)
4.12 L.M. Chanin, A.V. Phelps, M.A. Biondi: Phys. Rev. Lett. **2**, 344 (1959)
4.13 A.N. Prasad, J.D. Graggs: Proc. Phys. Soc. **76**, 223 (1960)
4.14 D.R. Bates (ed.): *Atomic and Molecular Processes* (Academic, New York 1962)
4.15 V.S. Fomenko, I.A. Podchernyaeva: *Emission and Adsorption Properties of Materials. Handbook* (Atomizdat, Moscow 1975)
4.16 L.N. Dobretsov, M.V. Gomoyunova: *Emission Electronics* (Nauka, Moscow 1966)
4.17 E. Guth, C.J. Mullin: Phys. Rev. **61**, 339 (1942)
4.18 E.L. Murphy, R.H. Good: Phys. Rev. **102**, 1464 (1956)
4.19 T.H. Lee: J. Appl. Phys. **30**, 66 (1959)
4.20 S.C. Brown: *Basic Data of Plasma Physics* (MIT Press, Cambridge MA 1959)
4.21 G. Francis: *Ionization Phenomena in Gases* (Butterworths, London 1960)
4.22 F. Llevellyn-Jones, A.B. Parker: Proc. Roy. Soc. **A 213**, 185 (1952)
4.23 J.M. Meek, J.D. Graggs: *Electrical Breakdown of Gases* (Clarendon, Oxford 1953)

Chapter 5

5.1 N.L. Aleksandrov, A.M. Konchakov, E.E. Son: Fiz. Plazmy **4**, 169 (1978)
5.2 N.L. Aleksandrov, F.I. Vysikailo, R.Sh. Islamov, I.V. Kochetov, A.P. Napartovich, V.G. Pevgov: Teplofiz. Vys. Temp. **19**, 22 (1981)

5.3 N.L. Aleksandrov, E.E. Son: in *Plasma Chemistry*, ed. by B.M. Smirnov (Atomizdat, Moscow 1988) No.7,p.35
5.4 J.P. Boeuf, E. Marode: J. Phys. D., Appl. Phys. **15**, 2169 (1982)
5.5 V.A. Shveigert, I.V. Shveigert: Fizika Plazmy **14**, 347 (1988)
5.6 Yu.P. Raizer, M.N. Shneider: *Contributed Papers of the 19th ICPIG*, Belgrade, 1989, Vol. 1, p. 188; Fizika Plasmy **15**, 318 (1989); Teplofiz. Vys. Temp. **29**, 22 (1991)
5.7 M.J. Kushner, H. Pan, J.V. DiCarlo: *Invited Papers of the 19th ICPIG*, Belgrade, 1989, p. 52

Chapter 6

6.1 Yu.M. Kagan, V.I. Perel: "Probe Techniques of Plasma Analysis", Usp. Fiz. Nauk **81**, 409 (1963)
6.2 Yu.M. Kagan: in *Spectroscopy of Gas Discharge Plasma* (Nauka, Leningrad 1970)
6.3 R.H. Huddlestone, S.L. Leonard (eds.): *Plasma Diagnostic Techniques* (Academic, New York 1965)
6.4 W. Lochte-Holtgreven (ed.): *Plasma Diagnostics* (North-Holland, Amsterdam 1968)
6.5 V.L. Granovsky: *Electric Current in Gases* (Gostekhizdat, Moscow 1952)
6.6 E.O. Johnson, L. Malter: Phys. Rev. **80**, 59 (1950)
6.7 L.M. Biberman, B. Panin: Zh. Tekh. Fiz. **21**, 12 (1951)
6.8 O.V. Kozlov: *Electric Probes in Plasma* (Atomizdat, Moscow 1969)

Chapter 7

7.1 J.M. Meek, J.D. Graggs: *Electrical Breakdown of Gases* (Clarendon, Oxford 1953)
7.2 S.C. Brown: *Basic Data of Plasma Physics* (MIT Press, Cambridge MA 1959)
7.3 M. Knoll, F. Ollendorff, R. Rompe: Gasentladungstabellen (Springer, Berlin 1935)
7.4 J.G. Trump, R.J. Van de Graaff: J. Appl. Phys. **8**, 327 (1947)
7.5 A.D. MacDonald: *Microwave Breakdown in Gases* (Wiley, New York 1966)
7.6 A.D. MacDonald, D.U. Gaskell, H.N. Gitterman: Phys. Rev. **130**, 1841 (1963)
7.7 Yu.P. Raizer: *Laser-Induced Discharge Phenomena* (Consultants Bureau, New York 1977)
7.8 P.D. Maker, R.W. Terhune, C.M. Savage: Quantum Electronics III, ed. by P. Grivet, N. Bloembergen (Columbia University Press, New York 1964)
7.9 R.G. Meyerand, A.F. Haught: Phys. Rev. Lett. **11**, 401 (1963)
7.10 D.H. Gill, A.A. Dougal: Phys. Rev. Lett. **15**, 845 (1965)
7.11 Yu.P. Raizer: "Optical Discharges" (review paper), Usp. Fiz. Nauk **132**, 549 (1980)
7.12 P. Woskoboinikow, W.J. Milligan, H.C. Praddaude, D.R. Cohn: Appl. Phys. Lett. **32**, 527 (1978)
7.13 M.J. Soileau: Appl. Phys. Lett. **35**, 309 (1979)
7.14 V.N. Parfenov, L.N. Pakhomov, V.Yu. Petrunkin, V.A. Podlevsky: Pisma Zh. Tekh. Fiz. **2**, 731 (1976)
7.15 G. Francis: *Ionization Phenomena in Gases* (Butterworths, London 1960)
7.16 E.W.B. Gill, A. Engel, von: Proc. Roy. Soc. **A192**, 446 (1948)

Chapter 8

8.1 V.L. Granovsky: *Electric Current in Gas (Steday Current* (Nauka, Moscow 1971)
8.2 A. Engel, M. Steenbeck: *Elektrische Gasentladungen. Ihre Physik und Technik*, Vol. II (Springer, Berlin 1934)
8.3 A. Engel, von: *Ionized Gases* (Clarendon, Oxford 1965)
8.4 S.C. Brown: *Basic Data of Plasma Physics* (MIT Press, Cambridge MA 1959)
8.5 V.Yu. Baranov, A.A. Vedenov, V.G. Nizyev: Teplofiz. Vysok. Temperatur **10**, 1156 (1972); A.A. Vedenov: *Physic of Electric Discharge CO_2-Lasers* (Energoizdat, Moscow 1982)

8.6 G.G. Gladush, A.A. Samokhin: Prikl. Mekh. i Tekh. Fiz. No. 5, 15 (1981)
8.7 V.N. Melekhin, N.Yu. Naumov: Pis'ma v Zh. Tekh. Fiz. **12**, 99 (1986)
8.8 Yu.P. Raizer, S.T. Surzhikov: Pis'ma v Zh. Tekh. Fiz. **13**, 452 (1987); Teplofiz. Vysokikh Temperatur **26**, 428 (1988)
8.9 Yu.P. Raizer: *Invited papers of the 17th Internat. Conf. on Phenomena in Ionized Gases*, Budapest, July 1985, p. 111; Teplofiz. Vys. Temperatur **24**, 984 (1986)
8.10 A.L. Ward: Phys. Rev. **112**, 1852 (1958)
8.11 S.Ya. Bronin, V.M. Kolobov: Fizika Plasmy **9**, 1088 (1983)
8.12 J.P. Boeuf, E. Marode: J. Phys. D, Appl. Phys. **15**, 2169 (1982)
8.13 P. Gill, C.E. Webb: J. Phys. D, Appl. Phys. **10**, 229 (1977)
8.14 Yu.P. Raizer, M.N. Schneider: *Contributed Papers of the 19th IC PIG*, Belgrade, 1989 Vol. 1, p. 188; Fizika Plasmy **15**, 318 (1989); Teplofiz. Vys. Temp. **29**, 22 (1991)
8.15 V.A.Shveigert, I.V. Shveigert: Fizika Plazmy **14**, 347 (1988)
8.16 G.S. Solntsev, A.I. Orlov, V.A. Dovzhenko: Radiotekhnika i Elektronika **9**, 1980 (1970)
8.17 Yu.M. Kagan, C. Cohen, P. Avivi: J. Appl. Phys. **63** (1), 60 (1988)
8.18 A.V. Nedospasov: Zh. Tekh. Fiz. **26**, 1202 (1956)
8.19 G. Ecker, K.G. Emeleus: Ann. Phys. **15**, 53 (1965)
8.20 A.J. Davies, J.G. Evans, E. Marode, P. Segur: in *ICDGA*, Edinburgh, 1980, Vol. 2, p. 59
8.21 L.S. Polak, I.A. Sergeev, D.I. Slovetsci: Teplofiz. Vysok Temperatur **15**, 15 (1977)
8.22 Yu.B. Golubovsci, V.M. Teleshko: Teplofiz. Vysok Temperatur **22**, 428 (1984)
8.23 Yu.S. Akishev, K.V. Baidze at all: Fizika Plasmy **11**, 999 (1985)
8.24 H. Brunet, Rossa-Serra: J. Appl. Phys. **57**, 1574 (1985)
8.25 A.H. Mnazakanjan, G.V. Naidis: in *Plasma Chemistry*, ed. by B.M. Smirnov (Energoatomizdat, Moscow 1987), No. 14, p. 227
8.26 A.V. Berdishev, I.V. Kochetov, A.P. Napartovich: Fizika Plasmy **14**, 741 (1988)
8.27 L.J. Denes, J.J. Lowke: Appl. Phys. Lett. **23**, 130 (1973)
8.28 J.J. Lowke, A.V. Phelps, B.W. Irwin: J. Appl. Phys. **44**, 4664 (1973)
8.29 W.L. Nighan, W.J. Wiegand: Phys. Rev. **A10**, 922 (1974)
8.30 A.P. Napartovich, V.G. Naumov, V.M. Shashkov: Fizika Plasmy **1**, 821 (1975)
8.31 Yu.P. Raizer, G.I. Shapiro: Fizika Plasmy **4**, 810 (1978)
8.32 A.C. Eckbreth, P.R. Balszuk: AIAA Paper No. 72–723 (1972)
8.33 S.V. Pashkin, P.I. Peretyatko: Kvantovaya Elektronika **5**, 1159 (1978)
8.34 N.A. Generalov, V.D. Kosynkin, V.P. Zimakov, Yu.P. Raizer, D.I. Roitenburg: Fizika Plasmy **6**, 1152 (1980)
8.35 E.P. Velikhov, V.S. Golubev, S.V. Pashkin: "Glow Discharge in Gas Flow" (review paper), Usp. Fiz. Nauk **137**, 117 (1982)
8.36 G. Francis: "The Glow Discharge at Low Pressure", in *Encyclopedia of Physics*, ed. by S. Flugge, Handbuch der Physik, Vd. XXII (Springer, Berlin 1956) pp. 53–208
8.37 Yu.S. Akishev, A.P. Napartovich, P.I. Peretyatko, N.I. Trushkin: Teploffiz. Vysok Temperatur **18**, 873 (1980)

Chapter 9

9.1 R.A. Haas: Phys. Rev. **A8**, 1017 (1973)
9.2 W.L. Nighan: in *Principles of Laser Plasma*, ed. by G. Bekefi (New York 1976) Chap. 7
9.3 E.P. Velikhov, V.D. Pismennyi, A.T. Rakhimov: Usp. Fiz. Nauk **122**, 419 (1977)
9.4 A.V. Eletsky, A.T. Rakhimov: in *Plasma chemistry*, ed. by B.M. Smirnov (Atomizdat, Moscow 1977) No. 4, p. 123
9.5 A.P. Napartovich, A.N. Starostin: in *Plasma chemistry*, ed. by B.M. Smirnov (Atomizdat, Moscow 1978) No. 5, p. 153
9.6 G. Ecker, W. Kroll, O. Zoller: Phys. Fluids **7**, 2001 (1964)
9.7 N.G. Basov, E.M. Belenov et al.: Pis'ma v Zh. Eksp. Teor. Fiz. **14**, 421 (1971)

9.8 Yu.P. Raizer, G.I. Shapiro: Fizika Plazmy **4**, 810 (1978)
9.9 L.J. Denes, J.J. Lowke: Appl. Phys. Lett. **23**, 130 (1973)
9.10 G.D. Melnikov, A.P. Napartovich: Fizika Plasmy **1**, 891 (1975)
9.11 W.L. Nighan, W.J. Wiegand: Phys. Rev. **A10**, 922 (1974)
9.12 L. Pekarek: Usp. Fiz. Nauk **94**, 463 (1968)
9.13 A.V. Nedospasov: Usp. Fiz. Nauk **94**, 439 (1968)
9.14 A. Garscadden: "Ionization Waves", in *Gaseous Electronics I, Electrical Discharges*, ed. by M.N. Hirsh, H.J. Oskam (Academic, New York 1978)
9.15 G. Francis: "The Glow Discharge at Low Pressure", in *Encyclopedia of Physics*, ed. by S. Flugge, Handbuch der Physik, Bd XXII (Springer, Berlin 1956) pp. 53–208
9.16 A.V. Nedospasov, Yu.B. Ponomarenko: Teplofiz. Vysok Temperatur **3**, 17 (1965)
9.17 L.D. Tsendin: Zh. Tekh. Fiz. **40**, 1600 (1970)
9.18 W.P. Allis: Physica **C82**, 43 (1976)
9.19 A.B. Stewart: J. Appl. Phys. **27**, 911 (1956)
9.20 L.D. Tsendin: Zh. Tekh. Fiz. **52**, 635, 643 (1982)
9.21 Yu.B. Golubovsky, A.K. Zinchenko, Yu.M. Kagan: Zh. Tekh. Fiz. **47**, 1478 (1977)
9.22 C. Kenty: Phys. Rev. **126**, 1235 (1962)
9.23 N.A. Generalov, V.D. Kosynkin, V.P. Zimakov, Yu.P. Raizer, D.I. Roitenburg: Fizika Plasmy **6**, 1152 (1980)

Chapter 10

10.1 W. Finkelnburg, H. Maecker: "Elektrische Bogen und thermisches Plasma", *Handbuch der Physik*, Vol. XXII (1956) S. 254–444
10.2 M.F. Zhukov et al: *Electrode Processes in Arc Discharges* (Nauka, Novosibirsk 1982)
10.3 W.D. Davis, H.C. Miller: J. Appl. Phys. **40**, 2212 (1969)
10.4 J.M. Lafferty (ed.): *Vacuum Arcs. Theory and Application* (Wiley, New York 1980)
10.5 G.A. Lyubimov, V.I. Rakhovski: "Cathode Spot of a Vacuum Arc" Usp. Fiz. Nauk **125**, 665 (1978)
10.6 V.L. Granovsky: *Electric Current in Gas (Steady Current)* (Nauka, Moscow 1971)
10.7 I.I. Beilis: Dokl. Acad. Nauk **298**, 1108 (1988); Teplofiz. Vys. Temp. **25**, 1224 (1988); Pis'ma Zh. Tekh. Fiz. **14**, 1124 (1988)
10.8 T.H. Lee: J. Appl. Phys. **30**, 166 (1959)
10.9 I.I. Beilis: Pis'ma Zh. Tekh. Fiz. **16**, N10, 28 (1990)
10.10 Yu.D. Korolev, G.A. Mesyats: *Field-Emission and Explosive Processes in Gas Discharges* (Nauka, Novosibirsk 1982)
10.11 C.W. Kimblin: IEEE Trans. **PS-2**, 310 (1974)
10.12 A. von Engel: *Ionized Gases* (Clarendon, Oxford 1965)
10.13 S.V. Dresvin: *Physics and Technology of Low Temperature Plasmas* (Iowa State Univ. Press, Ames IA 1977)
10.14 J.M. Yos: *Revised Transport Properties of High Temperature Air and its Components* (AVCO, T.R. Nov. 1967)
10.15 Yu.P. Raizer: *Laser-Induced Discharge Phenomena* (Consultants Bureau, New York 1977)

Chapter 11

11.1 Yu.P. Raizer: *Laser-Induced Discharge Phenomena* (Consultants Bureau, New York 1977)
11.2 L.D. Landau, E.M. Lifshitz: *Electrodynamics of Continuous Media* (Pergamon Press, Oxford 1960)
11.3 R.E. Rovinsky, V.A. Gruzdev, A.P. Sobolev: Prikl. Mekh. i Tekh. Fiz. No. 1, 143 (1967)
11.4 R.E. Rovisnky, V.A. Gruzdev, T.M. Gutenmakher, A.P. Sobolev: Teplofiz. Vys. Temperatur **5**, 557 (1967)

11.5 L.M. Blinov, V.V. Volodko, G.G. Gontarev, G.V. Lysov, L.S. Polak: in *Generators of Low-Temperature Plasma* (Energiya, Moscow 1969)
11.6 P.L. Kapitsa: Zh. Eksp. Teor. Fiz. **57**, 1801 (1969)
11.7 Yu.P. Raizer: Pis'ma v Zh. Eksp. Teor. Fiz. **11**, 195 (1970)
11.8 N.A. Generalov, V.P. Zimakov, G.I. Kozlov, V.A. Masyukov, Yu.P. Raizer: Pis'ma v Zh. Eksp. Teor. Fiz. **11**, 447 (1970)
11.9 Yu.P. Raizer: Pis'ma v Zh. Tekh. Fiz. **7**, 938 (1981)
11.10 N.A. Generalov, V.P. Zimakov, G.I. Kozlov, V.A. Masyukov, Yu.P. Raizer: Zh. Eksp. Teor. Fiz. **61**, 1434 (1971)
11.11 D.R. Keefer, B.B. Hendriksen, W.F. Braerman: J. Appl. Phys. **46**, 1080 (1975)
11.12 G.I. Kozlov, V.A. Kuznetsov, V.A. Masyukov: Zh. Tekh. Fiz. **49**, 2304 (1979)
11.13 J. Uhlenbusch: Invited Papers of the 16th Internat. Conf. on Phenomena in Ionized Gases, Düsseldorf, 1983, p. 119
11.14 Ya.B. Zel'dovich, Yu.P. Raizer: *Physics of Shock Waves and High-Temperature Hydrodynamic Phenomena* (Academic Press, New York 1966)
11.15 Yu.P. Raizer, A.Yu. Silantyev: Kvantovaya Elektronika **13**, 593 (1986)
11.16 Yu.P. Raizer, S.T. Surzhikov: Kvantovaya Elektronika **11**, 2301 (1984); Teplofiz. Vys. Temperatur **23**, 29 (1985)
11.17 Yu.P. Raizer: "Optical Discharges" (review paper), Usp. Fiz. Nauk **132**, 549 (1980)
11.18 Yu.P. Raizer: *Fundamentals of Modern Physics of Gas Discharge Processes* (Nauka, Moscow 1980)
11.19 S.V. Dresvin: *Physics and Technology of Low Temperature Plasmas* (Iowa State Univ. Press, Ames 1977)
11.20 S.V. Kononov, M.I. Yakushin: Prikl. Mekh. i Tekh. Fiz. No. 6, 67 (1966)
11.21 M.V. Gerasimenko, G.I. Kozlov, V.A. Kuznetsov, V.A. Masyukov: Pis'ma v Zh. Tekh. Fiz. **5**, 954 (1979)
11.22 Yu.P. Raizer, A.Yu. Silantyev, S.T. Surzhikov: Pis'ma v Zh. Tekh. Fiz. **12**, 134 (1986); Teplofiz. Vys. Temperatur **25**, 454 (1987)
11.23 K.G. Guskov, Yu.P. Raizer, S.T. Surzhikov: Kvant. Elektron. **17**, 937 (1990)

Chapter 12

12.1 H. Raether: *Electron Avalanches and Breakdown in Gases* (Butterworths, London 1964)
12.2 L.B. Loeb: *Basic Processes of Gaseous Electronics* (University of California Press, Berkeley CA 1960)
12.3 J.M. Meek, J.D. Craggs: *Electrical Breakdown of Gases* (Wiley, New York 1978)
12.4 I.S. Marshak: "Electrical Discharge of Gases at Nearly Atmospheric Pressure" (review paper), Usp. Fiz. Nauk **71**, 631 (1960)
12.5 E.D. Lozansky, O.B. Firsov: *Theory of Sparks* (Atomizdat, Moscow 1975)
12.6 Yu.P. Raizer: *Laser-Induced Discharge Phenomena* (Consultants Bureau, New York 1977)
12.7 D.V. Razevig (ed.): *High-Voltage Engineering* (Energiya, Moscow 1976)
12.8 I.M. Bortnik, A.N. Kushko, A.N. Lobanov:Abstracts of Reports to the 2nd USSR Conf. on Physics of Electrical Discharge of Gases, Tartu 1984, Part II, p. 270
12.9 M.V. Kostenko (ed.): *High-Voltage Engineering* (Vysshaya Shkola, Moscow 1973)
12.10 H. Tholl: Zs. Naturforsch. **19a**, 346, 704 (1964)
12.11 I.S. Abramson, N.M. Gegechkori, S.I. Drabkina, S.L. Mandelshtam: Zh. Eksp. Teor. Fiz. **17**, 862 (1947)
12.12 S.I. Drabkina: Zh. Eksp. Teor. Fiz. **21**, 473 (1951)
12.13 M. Goldman, N. Goldman: "Corona Discharges", in *Gaseous Electronics I, Electrical Discharges*, ed. by M.N. Hirsh and H.J. Oskam (Academic Press, New York 1978)
12.14 G.A. Dawson, W.P. Winn: Zs. Phys. **183**, 159 (1965)
12.15 I. Gallimberti: J. Phys. D, Appl. Phys. **5**, 2179 (1972)

12.16 S. Badaloni, I. Gallimberti: in Proc. 11th Int. Conf. on Phenomena in Ionized Gases, Prague 1973, p. 196
12.17 R.F. Griffiths, C.T. Phelps: Quart. J. R. Math. Soc. **102**, 419 (1976)
12.18 E.M. Bazelyan, A.Yu. Goryunov: Abstracts of reports to the 2nd USSR Conf. on Physics of Electrical Breakdown of Gases, Tartu 1984, Part I, p. 42; Elektrichestvo No. 11, 27 (1986)
12.19 R.D. Klingbeil, A. Tidman, R.F. Fernsler: Phys. Fluids **15**, 1969 (1972)
12.20 E. Marode: J. Appl. Phys. **46**, 2005 (1975)
12.21 I. Gallimberti: "The Mechanism of the Long Spark Formation" (review paper), J. de Physique **40**, Coll. C7, suppl. au No. 7 (1979) p. 193
12.22 S.K. Dhali, P.F. Williams: Phys. Rev. **A31**, 1219 (1985)
12.23 A.S. Gaivoronsky, I.M. Razhansky: Zh. Tekh. Fiz. **56**, 1110 (1986)
12.24 G.N. Aleksandrov: Zh. Tekh. Fiz. **35**, 1225 (1965)
12.25 I. Gallimberti: Electra **76**, 5799 (1977)
12.26 E.M. Bazelyan, B.N. Gorin, V.I. Levitov: *Physical and Engineering Foundations of Lightning Protection* (Gidrometeoizdat, Leningrad 1978)
12.27 E.M. Bazelyan, I.M. Razhansky: *Spark Discharge in Air* (Nauka, Novosibirsk 1988)
12.28 E.M. Bazelyan: Elektrichestvo No. 5, 20 (1987)
12.29 M.M. Kekez, P. Savic: in *Electrical Breakdown and Discharges in Gases*, ed. by E. Kunhardt, L. Luessen (Plenum, New York 1983) p. 419
12.30 D.J. Malan: Ann. Geophys. **8**, 385 (1952)
12.31 Ya.I. Frenkel: *Theory of Atmospheric Electricity Phenomena* (Gostekhizdat, Moscow 1949)
12.32 M. Uman: *Lightning* (McGraw-Hill, New York 1969)
12.33 B.F. Schonland: in *Handbuch der Physik* Bd. 22, S. 576, (Springer, Berlin 1956)
12.34 Les Renardiers Group: IEEE Proc. 133, PtA No. 7, 395–483 (1986)

Chapter 13

13.1 S.M. Levitsky: Zh. Tekh. Fiz. **27**, 1001 (1957)
13.2 C.O. Brown, J.W. Davis: Appl. Phys. Lett. **21**, 480 (1972)
13.3 N.A. Generalov, V.P. Zimakov, V.D. Kosynkin, Yu.P. Raizer, D.I. Roitenburg: Pis'ma v Zh. Tekh. Fiz. **1**, 431 (1975); Fizika Plasmy **3**, 626, 634 (1977); *ibid.* **6**, 1152
13.4 Yu.P. Raizer: Fizika Plasmy **5**, 408 (1979)
13.5 S.M. Levitsky: Zh. Tekh. Fiz. **27**, 970 (1957)
13.6 A.A. Kuzovnikov, V.L.Kovalenkov, V.P. Savinov: Vestnik MGU, Ser. 3 **24**, No. 4, 28 (1983)
13.7 A.A. Kuzovnikov, V.P. Savinov: Radiotekh. i Elektronika **18**, 816 (1973)
13.8 N.A. Yatsenko: Zh. Tekh. Fiz. **51**, 1195 (1981)
13.9 N.A. Yatsenko: Zh. Tekh. Fiz. **52**, 1220 (1982)
13.10 P. Vidaud, S.M.A. Durrani, D.R. Hall: J. Phys. D: Appl. Phys. **21**, 57 (1988)
13.11 V.A. Godyak, A.A. Kuzovnikov: Fizika Plazmy **1**, 496 (1975)
13.12 N.A. Yatsenko: Teplofiz. Vys. Temperatur **20**, 1044 (1982)
13.13 Yu.P. Raizer, M.N. Shneider: Fizika Plazmy **13**, 471 (1987); *ibid* **14**, 226 (1988)
13.14 N.A. Yatsenko: Zh. Tekh. Fiz. **50**, 2480 (1980)
13.15 A.S. Smirnov: Zh. Tekh. Fiz. **54**, 61 (1984)
13.16 A.S. Kovalev, A.T. Rakhimov, V.A. Feoktistov: Fizika Plazmy **7**, 1411 (1981)
13.17 A.D. Barkalov, V.D. Gavrilyuk, G.G. Gladush *et al.*: Teplofiz. Vys. Temperatur **16**, 265 (1978)
13.18 Yu.P. Raizer, M.N. Shneider: Teplofiz. Vys. Temperatur **25**, 1008 (1987); Fizika Plazmy **16**, 878 (1990)
13.19 M.G. Gill: Vacuum **34**, 357 (1984)
13.20 *IEEE Transactions on Plasma Science*, Special Issue on the Physics of RF Discharges for Plasma Processing **PS-14**, No. 2 (1986)
13.21 B.N. Chapman: *Glow Discharge Processes – Sputtering and Plasma Etching* (Wiley, New York 1980)
13.22 D.B. Graves: AIChE Journal **35**, 1 (1989)

Chapter 14

14.1 G.A. Abilsiitov, E.P. Velikhov, V.S. Golubev, A.G. Grigoryants, F.V. Lebedev, G.A. Nikolaev: High-Power CO_2-Lasers and Their Applications in Technology (Nauka, Moscow 1984)
14.2 A.A. Vedenov: Physics of Electrical-Discharge CO_2-Lasers (Energoizdat, Moscow 1982)
14.3 G.I. Kozlov, V.A.Kuznetsov, V.A. Masyukov: Pis'ma v Zh. Tekh. Fiz. **4**, 129 (1978)
14.4 A.C. Eckbreth, J.W. Davis: Appl. Phys. Lett. **19**, 101 (1971)
14.5 N.A. Generalov, V.P. Zimakov, V.D. Kosynkin, Yu.P. Raizer, D.I. Roitenburg: Pis'ma v Zh. Tekh. Fiz. **1**, 431 (1975); Fizika Plasmy **3**, 626, 634 (1977): *ibid.* **6**, 1152 (1980)
14.6 A.E. Hill: Appl. Phys. Lett. **18**, 194 (1971)
14.7 E. Hoag, H. Pease, J. Staal, J. Zar: J. Quantum Electronics **QE-9**, 652, (1973)
14.8 N.G. Basov, I.K. Babaev, V.A. Danilychev *et al.*: Kvantovaya Elektronika **6**, 772 (1979)
14.9 E.P. Velikhov, V.S. Golubev, S.V. Pashkin: "Glow Discharge in Gas Flow" (review paper), Usp. Fiz. Nauk **137**, 117 (1982)
14.10 F.K. Kosyrev, N.P. Kosyreva, E.I. Lunev: Avtomat. Svarka **9**, 72 (1976); V.M. Andriyakhin: Nauka i Zhisn, No. 11, 86 (1977)
14.11 G.A. Abilsiitov, L.I. Antonova, A.V. Artamonov *et al.*: Kvantovaya Elektronika **6**, 204 (1979)
14.12 V.S. Aleinikov, V.V. Bibikova, O.S. Lysogorov: Elektronaya Promyshlennost No. 5–6, 71 (1981)
14.13 C.O. Brown. J.W. Davis: Appl. Phys. Lett. **21**, 480 (1972)
14.14 A.C. Eckbreth, P.R. Blaszuk: AIAA Paper No. 72–723 (1972)
14.15 Yu.P. Raizer: Fizika Plasmy **5**, 408 (1979)
14.16 N.A. Generalov, V.P. Zimakov, V.D. Kosynkin, Yu.P. Raizer, N.G. Solovyev: Kvantovaya Elektronika **9**, 1549 (1982)
14.17 Yu.P. Raizer, G.I. Shapiro: Fizika Plazmy **4**, 810 (1978)
14.18 V.D. Gavrilyuk, A.F. Glova, V.S. Golubev, F.V. Lebedev: Kvantovaya Elektronika **4**, 2034 (1977)
14.19 V.V. Antyukhov, A.I. Bondarenko, A.F. Glova, V.S. Golubev *et al.*: Kvantovaya Elektronika **8**, 2234 (1981)
14.20 V.Kh. Goikhman, V.M. Goldfarb: Zh. Prikl. Spektrosk. **21**, 456 (1974)
14.21 D. He, D.R. Hall: Appl. Phys. Lett. **43**, 726 (1983)
14.22 O.S. Akirtava, V.D. Dzhikiya *et al.*: Pis'ma v Zh. Tekh. Fiz. **43**, 1231 (1981); O.S. Akirtava, V.S. Golubev, *et al.*: in Abstracts of reports to the USSR Conf. on *Laser Applications in National Economy*, Zvenigorod, May 1985 (Nauka, Moscow 1985)
14.23 W. Schock, H. Hugel, P. Hoffman: Electro Opt. Laser **13**, 76 (1981)
14.24 W. Waidelich (ed.): Proceedings of the 7th Internat. Congress Laser 85 Optoelectronics (Springer, Berlin 1986)
14.25 H. Hügel: in *Gas Flow and Chemical Lasers* Proc. 6th. Intern. Sympos. Jerusalem, 1986, (Springer, Berlin, Heidelber 1987) p. 258
14.26 S. Yatsiv: ibid., p. 252
14.27 P. Hoffmann: in Proceedings of the 2nd Internat. Confer. Lasers Manuf., Birmingham, March 1985 (Kempston, Amsterdam 1985)
14.28 P.P. Vitruk, N.A. Yatsenko: Pis'ma Zh. Tekh. Fiz. **15**, 1 (1989)

Further Reading

1. Yu.P. Raizer, M.N. Shneider, N.A. Yatsenko: *Radio-Frequency Capacitive Discharges* (CRC Press, Boca Raton, Florida 1995)
2. M.A. Lieberman, A.J. Lichtenberg: *Principles of Plasma Discharges and Materials Processing* (Wiley, New York 1994)

Subject Index